Delft University of Technology

Analysis and Design of Lens Antenna Systems for Applications at Millimeter and Sub-millimeter Wavelengths

Zhang, H.

DOI
10.4233/uuid:5fb0dfe6-94cc-40f1-8773-91367b5e2fba

Publication date
2024

Document Version
Final published version

Citation (APA)
Zhang, H. (2024). *Analysis and Design of Lens Antenna Systems for Applications at Millimeter and Sub-millimeter Wavelengths*. [Dissertation (TU Delft), Delft University of Technology]. https://doi.org/10.4233/uuid:5fb0dfe6-94cc-40f1-8773-91367b5e2fba

Analysis and Design of Lens Antenna Systems for Applications at Millimeter and Sub-millimeter Wavelengths

Analysis and Design of Lens Antenna Systems for Applications at Millimeter and Sub-millimeter Wavelengths

DISSERTATION

for the purpose of obtaining the degree of doctor
at Delft University of Technology
by the authority of the Rector Magnificus, Prof. dr. ir. T. H. J. J. van der Hagen,
chair of the board for Doctorates,
to be defended publicly on
Monday 15 January 2024 at 10:00 o'clock

by

Huasheng ZHANG

Master of Science in Electrical Engineering,
Delft University of Technology, the Netherlands,
born in Urumqi, China.

This dissertation has been approved by the promotors.

Composition of the doctoral committee:

Rector Magnificus	Chairman
Prof. dr. N. Llombart Juan,	Delft University of Technology, promotor
Prof. dr. A. Neto,	Delft University of Technology, promotor
Independent members:	
Prof. dr. M. Ettorre,	Michigan State University, United States
Prof. dr. S. Preu,	Technische Universität Darmstadt, Germany
Prof. dr. J. J. A. Baselmans,	Delft University of Technology, Netherlands
Dr. M. Holm,	Huawei Technologies, Sweden
Reserve member:	
Prof. dr. W. A. Serdijn,	Delft University of Technology, Netherlands
Other members:	
Dr. J. Bueno,	Delft University of Technology, Netherlands

The work presented in this thesis has been performed at TU Delft and financed by the European Research Council starting grant (ERC-2014-StG LAA-THz-CC), No. 639749. Part of the work has been supported by Huawei Technologies, Sweden AB.

Keywords: Equivalent circuits, focal plane arrays, field correlation, geometrical optics, lens antennas, leaky-wave antennas, lens shaping, millimeter waves, photoconductive antennas, quasi-optical systems, sub-millimeter waves, sparse array, time-domain analysis, ultra wideband, wide field-of-view.

Cover design by: Huasheng Zhang.

Printed by: Ipskamp Drukkers B.V., Enschede, Netherlands.

An electronic version of this dissertation is available at: http://repository.tudelft.nl/

ISBN 978-94-6384-524-3

To my parents

Contents

Chapter 1

Introduction

1.1 Dielectric Lens Antennas in Quasi-optical Applications

Quasi optics is the field that exploits lens or reflector systems whose dominant dimensions are moderate or small in terms of wavelengths. Focusing on the lenses only, the history of the field could be tracked back to 1888 when Oliver Lodge used two plano-hyperbolic lenses to collimate and focus the radiation from an oscillator with 1-m wavelength [1]. After that and for a long time, lens antennas had not been widely investigated due to their bulky size at low frequencies. In recent decades, more applications have been emerging at sub-millimeter (sub-mm) wavelengths, where the acceptable physical size of lens antennas can guarantee measurable gain without the problems of excessive weight. Specifically, the field of radio astronomy has been resorting to integrated lens antennas (ILAs) since 1990's with the pioneering works of Rutledge [2] and Rebeiz [3]. Around the same time, ILAs were also considered for imaging [4,5] and spectroscopy [6,7]. More recently, lens antennas have been developed for THz passive imaging [8,9] and they can even support detector arrays with extreme sensitivity for far-infrared observatories as in [10,11]. Nowadays, as low-loss and low-cost lens materials have become available and the fabrication of lenses is becoming easier and more accurate, lens antennas have also been widely exploited for applications at millimeter (mm) wavelengths such as wireless communication [12–17] and automotive radars [18–21].

Dielectric lenses are commonly used to collimate the fields radiated by their antenna feeds to enhance the gain of the systems. There are mainly two types of configurations for lens antennas: one is to place the antenna feed away from the lens [see Fig. 1.1(a)]; the other is to integrate the feed with the lens with direct contact, as depicted in. 1.1(b). The former configuration can be commonly found in optical systems where the lenses are used for collimating/focusing purposes [22]. It is also implemented in imaging [23] or astronomical applications [24]. The latter configuration, i.e., the ILA, is more compact and is suitable for the integration with micro-electronic circuitry. After its initial introduction [2,3], it has

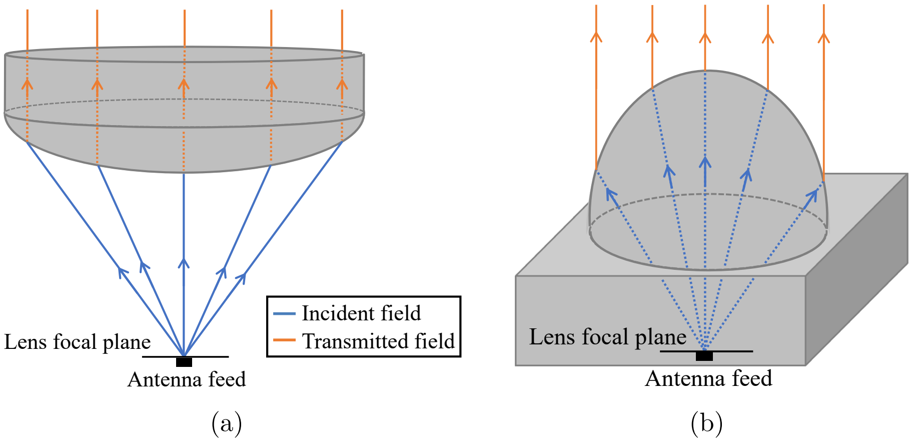

Figure 1.1: Two types of configurations for lens antennas: (a) placing the antenna feed far way from the dielectric lens, and (b) integrating the feed with the lens. The propagation of the feed radiated field is represented by the ray tracing.

been widely adopted and developed for a variety of applications mentioned before [4–21,25]. In fact, one can reasonably argue that the lens antenna system in Fig. 1.1 (b) is the only truly integrated antenna front end that has been widely adopted to date. As a case in point, the use of lenses guarantees high radiation efficiency by suppressing the most damaging loss that often hampers high-frequency integrated front ends: surface wave propagation in dielectric substrates [3, 25]. In this thesis, we mainly focus on the analysis and design of ILAs.

1.2 Integrated Lens Antennas Based on Resonant Leaky-wave Antenna Feeds

For an ILA, the most well-known feed is the double-slot antenna introduced by Filipovic in [25]. This feed can efficiently illuminate the top part of the lens surface with directive patterns, leading to high lens aperture efficiency, but over a narrow band. In recent years, a resonant leaky-wave antenna (LWA) was proposed as another efficient lens feed to achieve high lens directivity and aperture efficiency (narrow band) [26] and later some wideband designs were demonstrated at mm and sub-mm wavelengths [16, 27, 28]. This work mainly focuses on using resonant LWAs as lens feeds.

A schematic representation of a resonant LWA is shown in Fig. 1.2. The dielectric lens is represented by a semi-infinite dielectric medium and the source is placed on a ground plane. A half-wavelength resonant air cavity (Fabry-Pérot cavity) is placed in between to support the propagation of leaky waves. The main TE_1/TM_1 LW modes are nearly degenerated and propagate radially with multiple reflections along the cavity, leaking at the same time energy into the semi-infinite medium [16, 26, 29]. This effect enlarges the effective area of the antenna and thus enhances the directivity. In addition, there is an undesired TM_0 mode propagating [30], which radiates towards a larger angle (compared

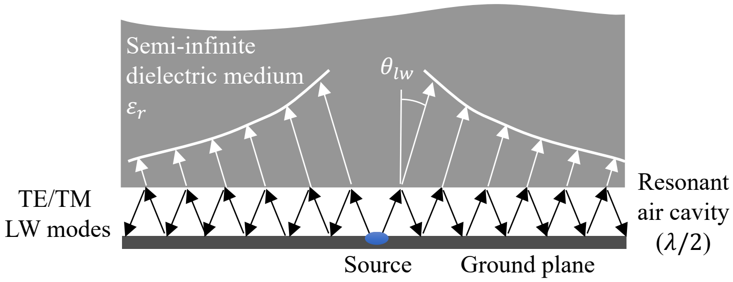

Figure 1.2: Schematic representation of a resonant LWA.

to $\mathrm{TE}_1/\mathrm{TM}_1$). In most cases, this mode can increase the cross polarization and decrease the lens aperture efficiency. To suppress this mode, one can use feed structures such as a double-slot iris [16, 26, 30], a slot-fed dipole [31], or a circular waveguide with annular corrugations [28].

1.3 Analysis of Lens Antennas

With the increasing availability of modern computing power, it is now possible to investigate entire lens antenna systems resorting to commercially available full-wave software such as CST [32], HFSS [33] and other equivalent tools. Most of these tools are capable of analyzing structures that are relatively small in terms of wavelengths: e.g. diameter $D \leq 10\lambda$. However, even such analysis would be possible, it is clear that the design of lens antennas cannot be efficiently done using full-wave techniques yet, not to mention if larger lens dimensions are considered. For this reason, a number of quasi-analytical approaches have been proposed to analyze lens antennas, all based on ray-tube field representations: geometrical optics (GO) and physical optics (PO). Specifically, the most famous optimization tool based on PO was proposed by Filipovic and Rebeiz in [25] for radiation patterns. For evaluating the effects of lenses on the input impedance, a PO based analysis was firstly introduced by Neto [34, 35]. In all cases, these approaches approximate electromagnetic (EM) fields as tubes of rays propagating from one homogenous medium to another, following Snell's law, which is applicable when the lens dimensions are electrically large in terms of wavelengths. More recently, Fourier optics (FO) tools were proposed to cope with quasi-optical (QO) focusing systems in [36–38].

These GO/PO/FO based tools are used at length in the present work. Specifically, they are adopted in a hybrid way by incorporating the asymptotic field representations with dedicated procedures aimed at characterizing the transitions from guided to radiated waves (and vice versa) which needs to be analyzed efficiently. Such hybrid technique is an extension of the method initially proposed in [39] to optimize antenna feeds for reflectors. There, the receiving antenna feed was modelled by a Thévenin equivalent circuit. The generator of the circuit is the open-circuit voltage at the feed terminal and the generator load is the antenna impedance, as depicted in Fig. 1.3(a). The open-circuit voltage was calculated by a reaction integral and then the power delivered to the external load was

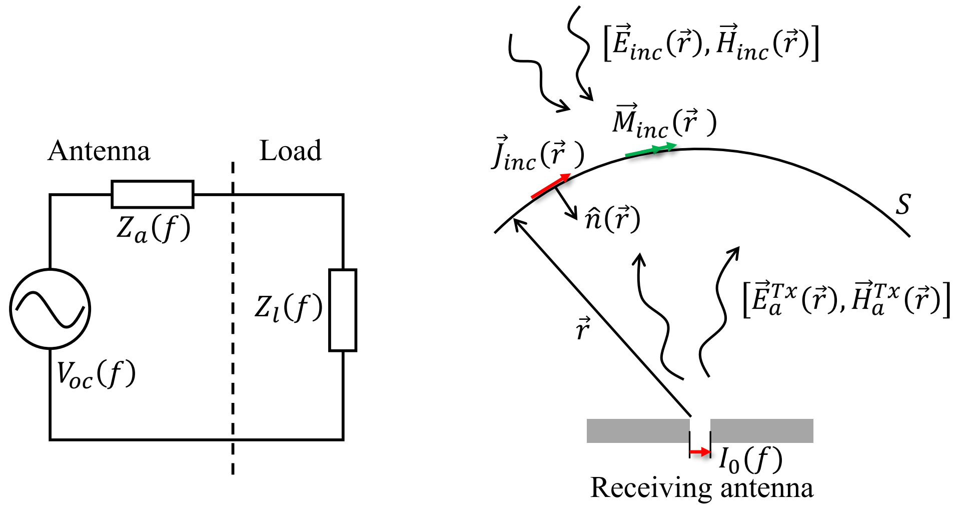

(a) (b)

Figure 1.3: (a) Thévenin equivalent circuit for a receiving antenna as proposed in [39]. (b) The considered Rx scenario for evaluating the open-circuit voltage $V_{oc}(f)$ using the reaction integral performed on an arbitrary surface S. The incident fields $\left[\vec{E}_{inc}(\vec{r}), \vec{H}_{inc}(\vec{r})\right]$ induce equivalent currents $\left[\vec{J}_{inc}(\vec{r}), \vec{M}_{inc}(\vec{r})\right]$ on S. The receiving antenna is operating in the transmission mode fed by the current I_0 and radiates the fields $\left[\vec{E}_a^{Tx}(\vec{r}), \vec{H}_a^{Tx}(\vec{r})\right]$ also on S. $\hat{n}$ is the normal vector of the surface.

evaluated. In this thesis, we use a similar methodology, referred to as the field correlation technique, to analyze lens antennas in reception (Rx) when the incident field is a plane wave or a generalized scattered field.

The reaction integral in [39] is a field correlation between two sets of sources evaluated over an arbitrary surface S, as depicted in Fig. 1.3(b). One consists of the equivalent currents $\left[\vec{J}_{inc}(\vec{r}), \vec{M}_{inc}(\vec{r})\right]$ over the surface induced by the incident EM fields $\left[\vec{E}_{inc}(\vec{r}), \vec{H}_{inc}(\vec{r})\right]$. The other includes the fields radiated by the receiving antenna over the same surface when operating in the transmission (Tx) mode, $\left[\vec{E}_a^{Tx}(\vec{r}), \vec{H}_a^{Tx}(\vec{r})\right]$. The open-circuit voltage V_{oc} at each frequency is then explicitly expressed as follows:

$$V_{oc}(f)I_0(f) = \iint_S \left[\vec{H}_a^{Tx}(\vec{r}) \cdot \vec{M}_{inc}(\vec{r}) - \vec{E}_a^{Tx}(\vec{r}) \cdot \vec{J}_{inc}(\vec{r})\right] dS, \tag{1.1}$$

where $\vec{r}$ represents a point on the surface S, $I_0(f)$ is the current at the antenna feed when it operates in the Tx mode, $\vec{M}_{inc}(\vec{r}) = \vec{E}_{inc}(\vec{r}) \times \hat{n}(\vec{r})$ and $\vec{J}_{inc}(\vec{r}) = \hat{n}(\vec{r}) \times \vec{H}_{inc}(\vec{r})$, with $\hat{n}(\vec{r})$ the normal vector of the surface at $\vec{r}$. More detailed explanation and derivation of (1.1) can be found in [16, 38].

In the case of a lens antenna, the surface S can be selected either inside or outside the lens surface. When the incident field is a simple plane wave, S is usually selected as an equivalent sphere inside the lens, referred to as the FO sphere in [16, 36, 38], with the radius of the lens rim distance. The equivalent currents $\left[\vec{J}_{inc}(\vec{r}), \vec{M}_{inc}(\vec{r})\right]$ are then associated with the fields transmitted inside the lens and propagated to the FO sphere. Such propagation can be easily evaluated using the GO/FO approach. Specially, a MATLAB tool was developed for this [38]. When the incident field is a generalized scattered field such as focal fields from a reflector, it would be more convenient to select the surface as a plane outside the lens. Because it would be numerically complex to calculate the fields transmitted inside the lens. In this case, the fields radiated by the lens antenna should evaluated, which can be done using the GO/PO approaches. This will be discussed in detail in Section 4.2 and Section 5.3.

Once $V_{oc}(f)$ is calculated, the power delivered to the load of the receiving antenna (assuming an impedance-matched condition) can be calculated as follows:

$$P_l(f) = \frac{|V_{oc}(f) I_0(f)|^2}{16 P_{rad}(f)}, \tag{1.2}$$

where $P_{rad}(f)$ is the total power radiated by the antenna feed when operating in the Tx mode. By observing (1.1) and (1.2), apparently, the maximum $P_l(f)$ can be obtained when the mentioned two types of sources, i.e. $\left[\vec{J}_{inc}(\vec{r}), \vec{M}_{inc}(\vec{r})\right]$ and $\left[\vec{E}_a^{Tx}(\vec{r}), \vec{H}_a^{Tx}(\vec{r})\right]$ are conjugately matched. This is referred to as the conjugate field-matching condition which will be an important criteria when designing the lens antennas in this thesis.

1.4 Communication Requirements at Millimeter Wavelengths

In recent years, lens antennas have gained more interests in the mm-wave regime for applications such as high-data-rate wireless communication [12–17] and automotive radars [18–21], since they can significantly enhance the gain of the systems, and in some work [12,17], with low profiles. In fact, in most applications, the research interests tend to design high-gain lens antennas with low profiles, low cost, and less feeding elements.

As an example, Table 1.1 shows the requirements for an antenna which is used for 5G point-to-point communication between a base station and a fixed access point. Such an antenna is supposed to act as a customer premise equipment (CPE) placed in a “smart home” to radiate 5G signals to other devices, as depicted in Fig. 1.4. This CPE antenna should be low-profile with only 16 elements. It should achieve high gain with dual polarization and characterized by wide bandwidth centred around 28 GHz. Antenna alignment is of great importance to ensure proper connectivity in such a communication link. Therefore, the antenna is required to support limited elevation beam steering, such as $\theta_{el} = \pm 10^\circ$ in two main planes with a scan loss less than 2 dB. In addition, a side lobe level (SLL) up to -10 dB can be accepted in communication links where the line of sight is dominating with respect to multipath effects.

To make the antenna compact and low-cost, the printed circuit board (PCB) technology is preferred to realize the antenna. The main challenge is to achieve the required high

Table 1.1: Assumed requirements for 5G CPE antennas

Items	**Requirements**
Physical size	$\leq$ 10 cm $\times$ 10 cm $\times$ 2 cm
Array elements	4×4
Dual polarization	
Frequency band	26.5-29.5 GHz
Polarization isolation	$\geq$25 dB
Steering ability	±10° in two main planes
Gain	27 dBi at broadside
Side lobe level	$\leq$-10 dB
Scan loss	$\leq$2 dB

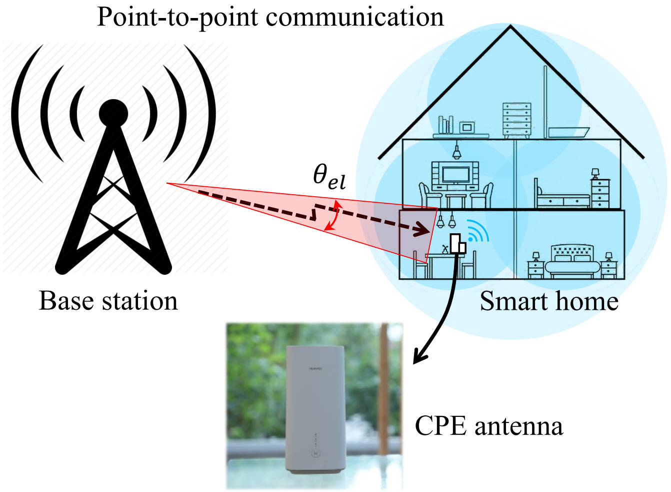

Figure 1.4: An example point-to-point communication scenario between a base station and a CPE antenna placed in a “smart home”. This antenna receive 5G signals and radiates towards other devices at home.

gain with only 16 elements. In fact, it is not possible to reach the above-mentioned gain requirement with a standard (roughly half-wavelength spacing) phased array. A possible solution is to increase the array periodicity to two wavelengths; however, the grating lobe level (GLL) will significantly increase. To reduce the GLL while maintaining a wide bandwidth, a dielectric lens array can be used in combination with this sparse phased array, as investigated in the frame of the ERC grant LAA-THz-CC [40]. When the phased array steers to a certain angle, the lens array will be displaced to suppress the GLL also in this steering case [27]. Such design will be explicitly described in Chapter 2.

1.5 Radar Imaging Requirements at Sub-millimeter Wavelengths

As anticipated, lens antennas are more widely used at sub-mm wavelengths. Besides their historical and continuous roles that have been played in astronomical observation [2, 3, 10, 11, 27], they are also widely adopted in THz imaging [8, 9, 41] and spectroscopy [42, 43]. Among these applications, a scenario that has become particularly important in the last decades is the security imaging.

Nowadays, as terroristic and criminal activities increase, secure technologies to detect potential threats are of great concerns to governments around the world. As the result, the research on advanced security imaging systems is gaining more interests. Recently, the THz Sensing Group developed a vision for the realization of a mm-resolution radar based on the use of photoconductive antennas (PCAs) [44]. In this thesis, the requirements of this ultra-wideband imaging radar have the role of pushing the development of two important breakthroughs. One is the characterization of a QO link between a PCA source and a PCA receiver; the other is the design of a focal plane array (FPA) suitable for PCA-based receivers.

1.5.1 THz Photoconductive Lens Antennas

The state-of-the-art THz radars, e.g. [45, 46], can achieve decent lateral resolution of an image due to their high operational frequency. However, they can only provide moderate range resolution in the order of a centimeter, since they only exploit limited absolute frequency bandwidth. In the past decades, THz time-domain spectroscopy (THz-TDS) systems have been attracting more interests for THz imaging since they can provide hundreds of GHz bandwidth, enabling potential very high-resolution imaging [42, 43, 47]. In such systems, PCAs are usually used to generate and detect THz pulses, when illuminated by pulsed laser sources. PCAs are less complex than heterodyne based systems since they can intrinsically down convert the optical pulses to THz pulses thanks to the non-linear properties of the used photoconductive (PC) semiconductors. Therefore, PCAs are relatively low-cost and commercially available.

A typical THz-TDS system mainly consists of a PCA source, a PCA receiver, and an in-between QO link where dielectric lenses or reflectors are used to collimate and focus THz pulses. A PCA source has been extensively studied using either full-wave finite-difference time-domain models, e.g., [48, 49], or equivalent circuit models, e.g. [50, 51]. These models can accurately calculate the photocurrents flowing across the semiconductor gap of the PCA source and further evaluate the generated THz pulses. However, the propagation of the THz pulses along the QO link has not been well modelled. In most works, it was approximated by considering far-field link conditions, e.g., [52–54], and the effect of the receiving antenna is neglected. Consequently, the detected currents of the PCA receiver can only be approximately evaluated with the amplitude of arbitrary units. Because of this, it is difficult to design an imaging system based on PCAs with accurately modelled

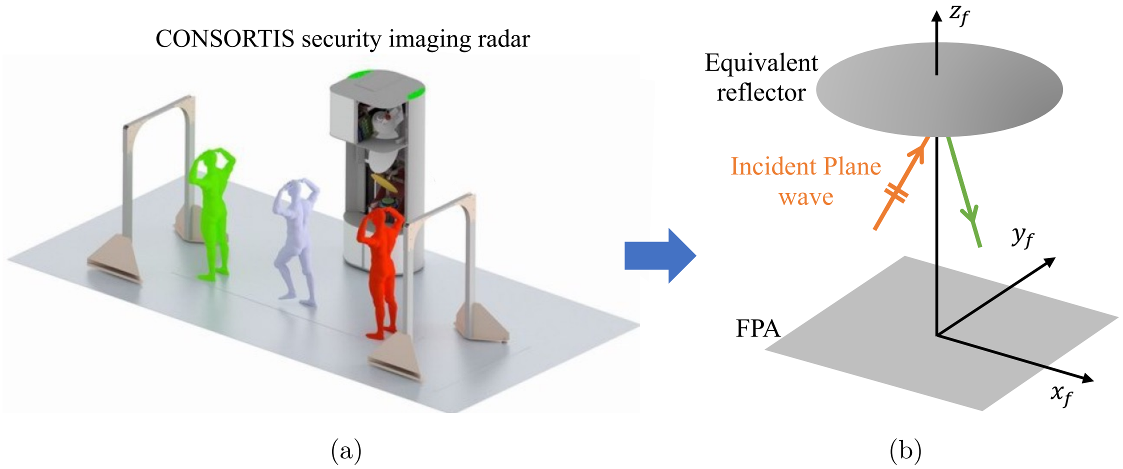

Figure 1.5: (a) Imaging scenario of the CONSORTIS security imaging radar [45]. (b) Equivalent schematic representation of the imaging scenario. The FPA is coupled to a reflector illuminated by a plane wave with an incident angle.

signal-to-noise ratio (SNR). To solve this problem, in Chapter 4, an EM methodology which combines full-wave simulations, GO/PO, and the field correlation approach will be used to accurately model the QO link, including the effect of the receiver.

1.5.2 Lens-based Focal Plane Arrays

When the modeling of the QO link between two PCAs is available, it only constitutes the basis for the analysis of a single-pixel radar system. The second important problem of such a system is the efficient design of an entire FPA of receivers. The reason why FPAs are often proposed at sub-mm wavelengths for security imaging is that they allow drastic reduction on imaging acquisition time. An example security imaging scenario is shown in Fig. 1.5(a) [45] which is equivalent to the schematic representation depicted in Fig. 1.5(b). Each array element in the FPA acts as an imaging pixel and is coupled to a reflector which is illuminated by plane waves with different incident angles. As the incident angle increases, the elements at the edges of the FPA suffer from high scan loss since they cannot couple well to the reflector. This cannot be easily solved by widely used horn-based FPAs, e.g., [45], since the horn antennas have limited pattern shaping capabilities. To achieve wide field-of-view (FoV) imaging, dielectric lens antennas are promising candidates since their shapes can be optimized to synthesize demanded radiation patterns, as discussed in [55]. The challenge is to optimize the lens surfaces to best couple to the reflector when the scanning angles are large. Besides this, the existing work, e.g. [10, 11], mostly used silicon lenses which are expensive to fabricate. To possibly reduce the fabrication cost, it is worth exploring if other materials can be used to obtain similar performance. In Chapter 5, the field correlation technique will be used to optimize lens surfaces to best couple to a reflector, and a FPA of shaped quartz lens antennas will be designed to achieve decent scanning performance.

1.6 Research Goals and Methodology

The scope of this thesis is to solve the challenges discussed in Section 1.4 and 1.5 in designing the lens antennas at mm and sub-mm wavelengths, by using the high-frequency asymptotic techniques as well as the field correlation methodology. Three relevant frequency bands are considered: 28 GHz, 180 GHz, and above 200 GHz. Lens antennas are analyzed and designed at these frequencies for applications of 5G point-to-point communication, wide FoV sub-mm imaging, and ultra-wideband imaging, respectively. The proposed methodology and design can be applied to different frequencies thus the work in this thesis provides guidelines and references for analyzing and designing lens antennas at mm and sub-mm wavelengths.

In the first scenario, a scanning lens phased array antenna will be analyzed in Rx and a prototype will be designed. This antenna can achieve the high-gain requirement for the CPE devices, with low profiles and low fabrication cost. The antenna design can be scaled to different frequencies, array size, and number of elements so it is also promising for applications beyond 5G.

Secondly, a QO link between a PCA source and a PCA receiver, including the effect of the receiver, will be accurately modelled using the field correlation technique. This will allow for accurate evaluation of the THz pulses detected at the receiver. In fact, this is the first time that the simulated detected pulses are compared to measurements for both the amplitude and the waveforms. The proposed analysis is applicable for different PCA structures and QO links. Therefore, it can be used to analyze and optimize the generation and detection of THz pulses for future imaging applications.

The last case mainly focuses on the design of shaped lens antennas in a FPA coupled to a reflector, with the goal of achieving low scan loss for large scanning angles. This provides guidelines for the future design of an entire FPA of PCA receivers. A field correlation optimization procedure on lens shaping will be proposed for synthesizing reflector's focal fields, and an optimized shaped quartz lens antenna will be demonstrated. This procedure can be easily extended to other applications if other synthesized patterns are desired.

1.7 Scientific Contribution in This Thesis

The novel aspects of this thesis are summarized in the following three items. Each of them includes theoretical contribution and novel design.

- A dual-polarized scanning lens phased array antenna at 28 GHz has been analyzed and designed. Each array element is a plastic elliptical lens fed by a LWA feed. This feed is designed in PCB structure and co-optimized with the lens using the field correlation technique combining with the GO/FO approach and the near-field analysis of the feed. Such an element achieves a relative bandwidth of 22.7% with a loss less than 0.8 dB up to 30 GHz, and a lens aperture efficiency above 75% and 70% over the required frequency band for the cases of broadside and steering to ±10°, respectively. The simulated array performance shows a 27.5 dBi broadside gain at 28 GHz and a scan loss less than 2 dB when steering up to ±20°. The array antenna was fabricated and measured, showing very good agreement with the simulations.

- A THz-TDS system, including the dispersive QO link between two PCAs, has been accurately modelled. A TD Norton equivalent circuit is used for the PCA source. A Norton resistance is then derived to simplify the time-marching evaluation of the circuit, which facilitates the PCA design according to impedance matching. Afterwards, a similar Norton circuit is developed for the receiver. To accurately evaluate the transfer function of the QO link, the field correlation technique is combined with full-wave simulations and the GO/PO approaches. Since the link is studied separately from the PCA TD analysis, the procedure can be easily extended to very different link geometries. The detected currents are then reconstructed in both waveforms and amplitude by using stroboscopic sampling of the modelled THz pulses, and compared to measurements. The agreement between the modelled and the measured pulses is of unprecedented quality.

- A FPA of shaped quartz lens antennas coupled to a parabolic reflector is designed at 180 GHz to operate over a wide FoV of 50 reflector beams (20.3°). To maximize the FoV, the FPA is divided into four regions, each containing the elements necessary to focus the energy associated to different portions of the FoV. Each quartz lens element is fed by a resonant LWA feed. The tool for analyzing and optimizing the geometry of the lens antenna is the already mentioned GO/PO based field correlation technique. A guideline on the lens antenna design at each region is discussed but specially we focus on the lens element at the edge of the FPA. The lens surface is significantly modified by means of field correlation to best couple to the reflector for the scanning angle up to 20.3°, with the directivity above 50.5 dBi and the scanning gain loss less than 2.6 dB. The shaped edge lens antenna was manufactured and measured, showing excellent agreement with the simulations.

1.8 Outline of the Thesis

A detailed description of the chapters of this dissertation is listed in the following:

- Chapter 2 presents a dual-polarized 4×4 scanning lens phased array antenna designed at 28 GHz for 5G point-to-point communication. The array is hexagonally arranged and the array element is an elliptical lens with a LWA feed. The design criteria for this feed and its PCB design is discussed. The lens geometry is designed using the field correlation technique in the near-field region of the feed. The optimized lens antenna achieves good impedance matching over the required frequency band with high broadside and steering aperture efficiency. The array shows a 27.5 dBi broadside gain at 28 GHz and less than 2 dB scan loss when scanning up to ±20°. A prototype was fabricated and measured, showing very good agreement with the simulations.

Appendix A introduces another architecture which integrates the backing reflector into an unique PCB. The simulated performance is shown and the measurements validate the proposed architecture.

- In Chapter 3, the TD modelling of a pulsed PCA source and receiver is discussed. For the PCA source, firstly its TD Norton equivalent circuit is briefly introduced. Then, an approximate Norton resistance is proposed to simplify the time-marching evaluation of the circuit. Afterwards, an approximate frequency-domain (FD) Norton circuit is proposed to analyze and design the impedance matching of the PCA source. Finally, the PCA receiver is analyzed using a non-dispersive transmission line model and a TD Norton equivalent circuit is proposed. The load photocurrent is calculated using the marching-on-time method and the detected current is evaluated using the stroboscopic sampling of the modelled THz pulses.

- Chapter 4 introduces a dispersive QO link between two PCAs. The link transfer function, including the effect of the receiver, is accurately modelled using the field correlation technique performed in the middle plane of the link. By using this transfer function, the current generator of the Norton circuit in Rx can be accurately evaluated. The detected currents are then reconstructed using the stroboscopic sampling of the modelled THz pulses. Both the amplitude and the waveforms of the detected currents are evaluated. The used QO link is then experimentally characterized to validate the proposed model. The comparison between the simulations and the measurement is excellent. Appendix B shows the full-wave simulations of the used bow-tie based PCA which is compared to a leaky-wave based PCA. Appendix C describes the design of the optical components used in the measurement setup. In addition, the alignment of the laser beams with the optical components is discussed. Finally, Appendix D presents the measurements of THz power radiated by PCA sources. This is done for two bow-tie based PCAs and two dipole-based photoconductive connected arrays (PCCAs) to characterize the material properties of the used LT GaAs substrates.

- In Chapter 5, a FPA of shaped quartz lens antennas coupled to a parabolic reflector is designed for wide FoV imaging systems. The scan loss of this system for large scanning angles is optimized via shaping lens surfaces. Firstly, the considered imaging scenario and the geometry of the used LWA feed are introduced. Then, an optimization procedure based on the field correlation technique is proposed to optimize lens geometries for different scanning angles. Finally, an example shaped quartz lens antenna at the edge of the FPA is shown. Its performance is simulated and compared to the state of the art. The lens antenna was fabricated and measured, and the measurements present excellent agreement with the simulations. Appendix E briefly discusses the design rules for the cases of plastic and silicon lens antennas.

- Chapter 6 concludes the dissertation with a review of the achieved results, and provides outlooks for possible future work.

Chapter 2

Development of a High-gain Scanning Lens Phased Array Antenna for 5G Point-to-point Communication

A dual-polarized 4×4 scanning phased array antenna with a leaky-wave (LW) enhanced lens array operating at 28 GHz is presented. Such an antenna can be used for 5G point-to-point communication that requires high gain, wide bandwidth, and limited steering ranges. The proposed array antenna has a periodicity of two wavelengths, and the resulting grating lobes are suppressed by directive and steerable lens element patterns. To achieve a low-cost and low-profile solution, the leaky-wave antenna (LWA) feeds are designed in PCB and the lenses are made of plastic. The lenses are optimized in the near-field region of the feeds, with the goal of maximizing the lens aperture efficiency. The array performance obtained from the proposed approach is validated by full-wave simulations. The latter shows a 27.5 dBi broadside gain at 28 GHz and a steering capability up to ±20° with a scan loss less than 2 dB. An antenna prototype was fabricated and measured. showing excellent agreement with the full-wave simulations. The prototype antenna, at broadside, achieves a 20% relative bandwidth and a gain of 26.2 dBi. The scan loss for 10° steering cases is less than 2 dB.

2.1 Introduction

The requirements reported in Table 1.1 for the point-to-point communication at 28 GHz are very challenging. Although great efforts have been dedicated to compact 5G architectures in recent years, arrays with such performance have not been shown to date. In Table 2.1, a summary of the state-of-the-art 5G array antennas in PCB is provided. In [56], a 1x4 dense-dielectric patch array antenna with a periodicity of $1.1\lambda_0$ (wavelength at 28 GHz) was proposed. It was designed with single polarization and achieved a relative bandwidth (BW) of 8.5% and a gain of 16.3 dBi. To improve the performance on *bandwidth*×*directivity*, a

Table 2.1: Simulated performance of the phased array antennas for 5G applications at 28 GHz band

Ref.	Elements	Periodicity (λ_0 @ 28 GHz)	BW (GHz) (Single element)	Broadside Gain @ 28 GHz (dBi)	Pol. Isolation (dB)
[56]	1×4	1.1	27.1-29.5	16.3	\
[57]	4×4	0.56	23.5-30.5	19	\
[58]	1×16	0.56	25.6-29.8	20.2	\
[59]	8×8	0.55	26.8-29.9	*21*	20
[62]	8×8	0.59	27.5-32	*22.4*	18
This work	**4×4**	**2**	**24.6-30.9**	**27.5**	**50**

(*) Gains in italic are extracted from the simulated EIRP.

4x4 phased array antenna (PAA) with a smaller periodicity of $0.56\lambda_0$ was designed in [57], where single-polarized slots and patches were used. Such a structure achieved a relative BW of 26% and a gain of 19 dBi. With the same periodicity, in [58], a 1x16 PAA with single-polarized patches achieved a relative BW of 15.2% and a gain of 20.2 dBi. In [59], a higher gain of 21 dBi was achieved by using a 8x8 PAA with patches. This PAA has a lower relative BW of 11% [60]; however, it presents dual polarization with the polarization isolation better than 20 dB [61]. Recently, a better performance was reported in [62].

In this work, differently with respect to the antennas in Table 2.1, we aim at a much larger array periodicity of $2\lambda_0$, to reach 27 dBi gain with only 4×4 active elements, from 26.5 to 29.5 GHz. In the literature, sparse arrays in combination with partially reflecting layers have been proposed in [63, 64] to suppress grating lobes and achieve high-gain steerable patterns with a small number of active elements. However, such arrays are characterized by narrow BW. In particular, only 5% relative BW was achieved for $2\lambda_0$ spacing in [31], and 10% when the periodicity is decreased to $1.5\lambda_0$ [63]. Such partially reflecting solutions would therefore, not reach the required *bandwidth*×*directivity* performance with just 16 active elements.

To achieve a wider BW, larger gain, and larger steering angles, we propose to use a scanning lens phased array architecture combined with LWA feeds, which was introduced in the framework of the ERC grant LAA-THz-CC [40], and more recently in [27]. Small lens phased arrays with limited steering ranges have been developed in mm waves [65], as well as combining with focal plane arrays in one dimension to enlarge the steering range [66]. Here, the proposed antenna architecture consists of two components: a sparse PAA fabricated on a PCB and a movable dielectric (plastic) lens array, as depicted in Fig. 2.1(a). Both arrays are arranged in a hexagonal grid with $2\lambda_0$ spacing at 28 GHz. The movable dielectric lens array, used as the add-on layer, ensures low grating lobe level (GLL) thanks to a highly directive and steerable array element pattern [27]. To illustrate the array concept, we can look to the radiation patterns in Fig. 2.1(c), with the reference

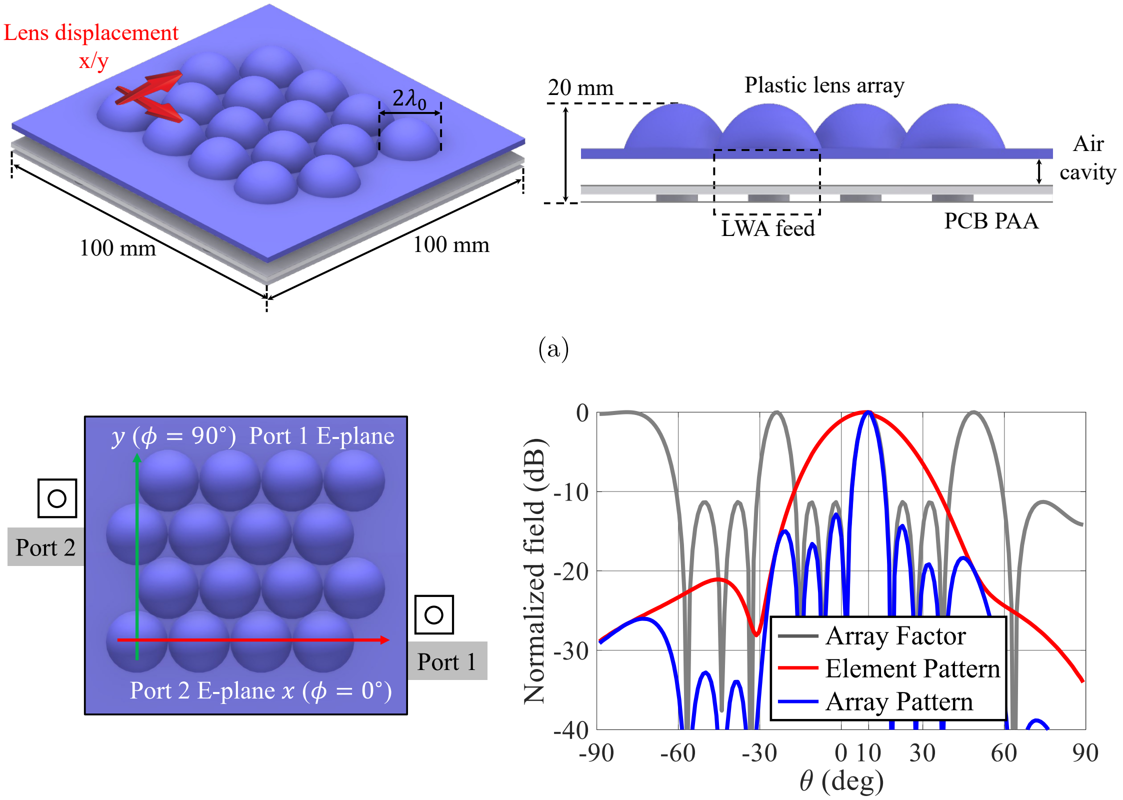

(a)

(b)

(c)

Figure 2.1: (a) Perspective and side views of the proposed array antenna architecture, showing the movable plastic lens array, one of the LWA feeds in the sparse PCB PAA, and the air cavity that supports leaky waves. (b) Top view of the hexagonally arranged lens array together with the reference system used for radiation patterns. (c) Simulated array factor of the PCB PAA (port 1), array element pattern, and array pattern at 28 GHz along the E-plane ($\phi = 90°$). The patterns are steered to 10° in the E-plane, and the lens array is displaced by 2.4 mm in the same direction.

system shown in Fig. 2.1(b). When the sparse PAA is steered to a certain angle (10°), the 16 array elements are electronically phase-shifted to steer the array factor to that angle (gray line). The grating lobes associated with this sparse array can be reduced by using a directive element pattern aligned to the same angle (red line). To achieve the dynamic steering of the directive element pattern, the lens array layer in Fig. 2.1(a) is mechanically translated with respect to the PAA along the x or y axis by a few millimeters. As a result, the array pattern, obtained as the product between the array element pattern and the array factor, shows a low GLL (blue line). To achieve such a low GLL over wide steering angles, array elements of high aperture efficiency are needed over the required frequency band and steering ranges [27].

In the proposed array antenna, each radiating element is the LWA introduced in Section 1.2 . It illuminates the corresponding lens through a $\lambda_0/2$ air cavity [see Fig. 2.1(a)], where a couple of TE/TM LW modes are excited. These modes attenuate fast because of the low contrast between the air and the plastic layer, and thereby they do not reach to the next array element. Moreover, the proposed antenna is capable to steer a dual-polarized beam. The two independent ports shown in Fig. 2.1(b) can be used for transmitting two independent signals. In [27], the proposed array, operating at sub-mm wavelengths, is based on silicon lenses excited by LW waveguide feeds. In this work, the lens array concept is adapted to the technology requirements for 5G communication. In particular, the lens array is made of high-density polyethylene (HDPE), with $\varepsilon_r = 2.34$ and $\tan\delta = 0.0003$. This type of plastic is low-cost, low-loss, and suitable for milling technique used for mass production [16]. Moreover, the proposed dual-polarized LWA feeds based on this low-contrast material will achieve a wide BW [16]. Simulations show a 22.7% -10 dB BW from 24.6 to 30.9 GHz, with the polarization isolation better than 50 dB over the entire BW.

Once the array architecture is decided, one of the biggest technological challenges is that the required performance should be guaranteed with a maximum volume occupation of 10 cm × 10 cm × 2 cm. The proposed scanning lens PAA is, in principle, scalable with the periodicity. However, the maximum vertical dimension leads to a lens diameter of $2\lambda_0$. These electrically small lenses are not usually analysed using standard physical optics (PO) method. For instance, in [66] full-wave simulations were proposed as a mean of optimization. Moreover, the lenses are in the near-field region of the LWA feeds. Consequently, we adopt the techniques developed in [38,67] for optimizing such lenses in reception (Rx) combining with geometrical optics (GO) and Fourier optics (FO) approaches. The radiation patterns of the 4×4 array antenna obtained using the proposed approach are in excellent agreement with the full-wave simulations for both the broadside and steering cases. Moreover, the simulated broadside gain is above 26.8 dBi from 26.5 to 29.5 GHz and reaches 27.5 dBi at 28 GHz. The array antenna is also capable of steering towards 20° in all planes with less than 2 dB scan loss. To validate the antenna design, the PCB PAA was fabricated with fixed phase shifts among array elements implemented in corporate feeding networks. Three separate PCBs were fabricated to validate the electronical steering performance of the proposed antenna in three static steering conditions: broadside and 10° steering in the two main planes. The measured prototype showed a -10 dB BW of 20% from 25.1 to 30.7 GHz, a gain of 26.2 dBi at broadside, and a scan loss less than 2 dB.

This chapter is organized as follows: Section 2.2 introduces the design criteria for the resonant LWA feed. Section 2.3 describes the methodology for the near-field lens design and the validation of the proposed approach. Section 2.4 describes the PCB design for the proposed antenna. Section 2.5 shows the fabricated antenna prototype and the corresponding measurement results.

2.2 Dual-polarized Resonant Leaky-wave Antenna Feed

The lenses are fed by resonant dual-polarized LWAs, as shown in Fig. 2.2. The antenna consists of two slot-fed dipoles surrounded by resonant metal cavities. The proposed geometry is similar to that used in [31], but operates over a much wider BW, from 24 to 30.5

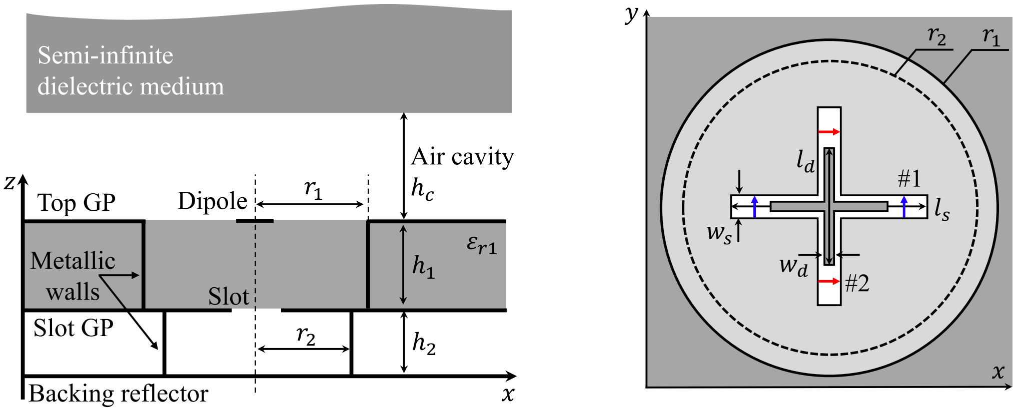

(a) (b)

Figure 2.2: Proposed resonant LWA feed. (a) Lateral view: a resonant air cavity with the height of $h_c = \lambda_0/2$ is placed below a semi-infinite dielectric medium illuminated by slot-fed dipoles. (b) Top view of the crossed dipoles (w_d, l_d) fed by crossed slots (w_s, l_s). Each slot is fed in balance by two discrete ports that are placed symmetrically at the arms of the slot. The upper and lower metal cavities are circular with the radius of r_1 and r_2, respectively. GP: ground plane.

GHz. Moreover, the LWA feed here supports dual polarization. The main criteria for the feed design and the simulated performance of the optimized structure are discussed in the following.

2.2.1 Dual-polarized Slot-fed Dipole Configuration

For a standard LWA [68], to achieve a higher directivity, a denser contrast between the lens medium and the cavity is needed, leading to narrower impedance BW as indicated in [69]. To enhance the *bandwidth*×*directivity* performance, the resonant LWA was proposed [26] and in this work its stratification is depicted in Fig. 2.2(a). In this work, wide impedance BW (in the order of 20%) with high lens illumination efficiency is targeted. Accordingly, the medium should have a low relative permittivity [16, 69].

The radiation properties of the LWA feed in Fig. 2.2 are determined by the solutions of the dispersion equation, $k_{LW} = k_0\sqrt{\varepsilon_r}(\sin\theta_{LW} + j\alpha_{LW})$, where k_{LW} is the propagation constant of the LW field: $\vec{E}_{LW}/\vec{H}_{LW} \propto e^{-jk_{LW}\rho}$, k_0 is the propagation constant in free space, θ_{LW} is the radiation angle of the LW mode, and α_{LW} is the (field) attenuation constant. For the main LW modes, θ_{LW} and α_{LW} are shown in Fig. 2.3. It can be seen that for a HDPE lens, the main TE$_1$/TM$_1$ LW modes point towards $\theta_{LW} \approx 20°$ and form a single and symmetric beam around broadside since $\sin\theta_{LW} \approx |\alpha_{LW}|$ [70]. Moreover, there is also an undesired TM$_0$ mode propagating [30], which radiates towards 40° in the E-plane of the feed. In [16], it was shown that this mode can be exploited to increase the lens aperture efficiency. However, this is not the case for the electrically small lenses in current configuration since the effective area associated to this mode is larger than the lens diameter. Therefore, the excitation of this mode must be reduced, for example, by using a

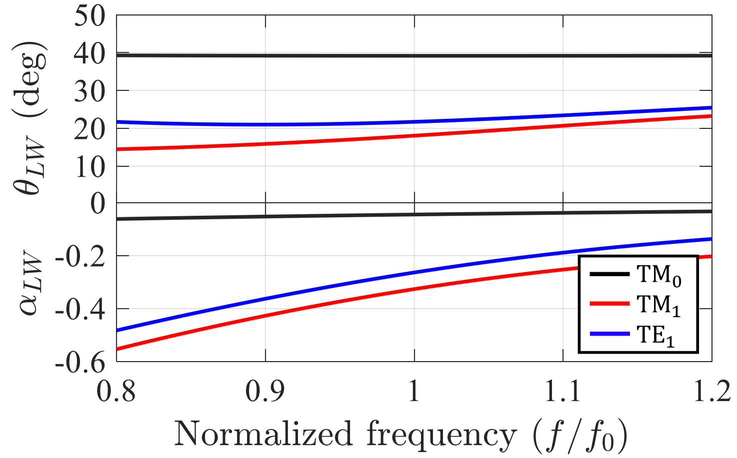

Figure 2.3: Solutions of the dispersion equation, $k_{LW} = k_0\sqrt{\varepsilon_r}(\sin\theta_{LW} + j\alpha_{LW})$, for the stratification depicted in Fig. 2.2(a), where $h_c = \lambda_0/2$ and $\varepsilon_r = 2.34$. The upper y axis shows the radiation angle θ_{LW} of each LW mode, while the bottom axis presents the (field) attenuation constant α_{LW}.

double-slot iris feed [30]. Here, to facilitate the dual-polarized feed design, a slot-fed dipole configuration [see Fig. 2.2(b)] is used, similar to what was done in [31].

The dual polarization is realized by using crossed dipoles fed by crossed slots, each one dedicated to a different polarization, as depicted in Fig. 2.2(b). The dipole oriented along the y axis is fed by slot 1 while the other orthogonal dipole is coupled to slot 2. In [71], each of the crossed slot is fed in balance by two offset feeding lines placed symmetrically at the arms of the slot. By doing so, the level of the current induced on the other unfed slot will be very low, and thus higher isolation between the two slots (or polarizations) will be achieved. Moreover, it can facilitate the impedance matching, as discussed in [72]. Here, to simplify the simulation of the proposed structure, each slot is excited by two discrete ports at their arms coherently, as shown in Fig. 2.2(b). In Section 2.4, this structure will be adapted and optimized for PCB fabrication, and the discrete ports will be replaced by microstrip lines.

2.2.2 Resonant Metal Cavities

In the stratification depicted in Fig. 2.2(a), there are three metallic layers separated by dielectric and air layers of thickness h_1 and h_2, respectively. In order to avoid the excitation of higher-order surface waves in these layers, h_1 and h_2 are designed to be less than half wavelength. With this condition, only the TM_0 surface wave mode can propagate in each of these layers. To suppress this mode, circular metallic walls placed surrounding the slots and the dipoles are used; see Fig. 2.2(b). The dimensions of the walls (radius $r_{1/2}$) are designed in such a way that most of the surface waves reflected from the walls can cancel out the outgoing surface waves excited by the slots, as discussed in [73].

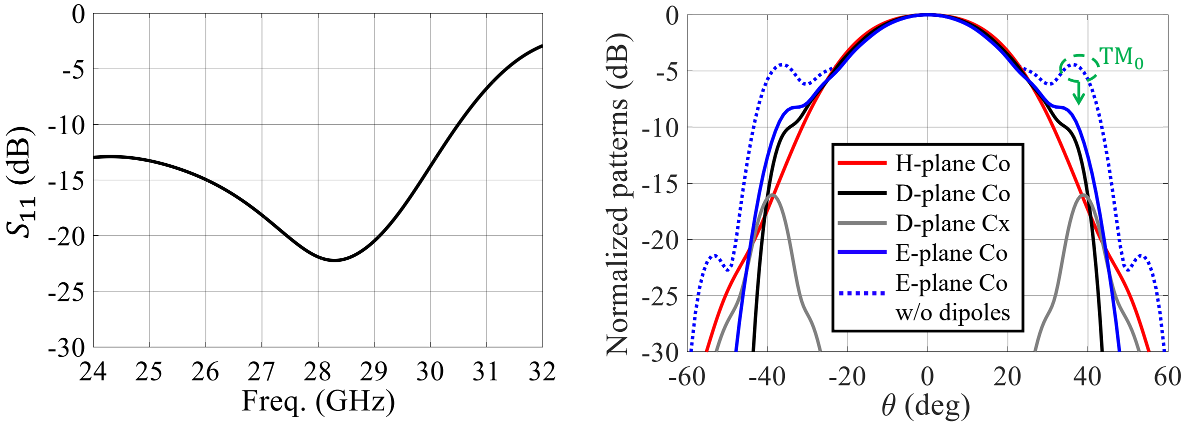

(a) (b)

Figure 2.4: Simulated performance of the LWA feed (slot 1) depicted in Fig. 2.2, when radiating into a semi-infinite HDPE medium ($\varepsilon_r = 2.34$): (a) S_{11} and (b) far fields. In the E-plane ($\phi = 90°$), the patterns with and without (w/o) using the dipoles are shown. Cx: cross polarization.

2.2.3 Simulated Performance

The structure in Fig. 2.2 is symmetric and thus the performance of only one polarization (slot 1) was optimized to have the widest BW and the lowest TM$_0$ LW mode. The optimized dimensions of the LWA feed are: $w_d = 0.2$ mm, $l_d = 2.87$ mm, $w_s = 0.34$ mm, $l_s = 5.49$ mm, $r_1 = 4.12$ mm, $r_2 = 3.64$ mm, $\varepsilon_{r1} = 3.66$, $h_1 = 1.59$ mm, and $h_2 = 1.63$ mm. The simulated S-parameter and far-field performance of the LWA feed when radiating in the semi-infinite HDPE ($\varepsilon_r = 2.34$) medium are shown in Fig. 2.4(a) and 2.4(b), respectively. As shown in Fig. 2.4(a), the -10 dB band is from below 24 to 30.5 GHz. The coupling between the two polarizations is below -90 dB and is not reported here. In Fig. 2.4(b), it is clearly shown that the TM$_0$ LW mode along the E-plane ($\phi = 90°$) is well suppressed when the dipole is introduced and optimized, i.e. from the dotted blue curve to the solid blue curve.

2.3 Near-field Lens Design

The main driver for the optimization of the lens geometry is the maximization of its aperture efficiency, since it directly impacts the level of grating lobes [27]. Therefore, we use elliptical lenses [16, 25] with the eccentricity $e = 1/\sqrt{\varepsilon_r}$, the truncation angle θ_0 seen from the lower focus of the lens [see Fig. 2.5(a)], and the fixed diameter of $D_{lens} = 2\lambda_0$.

To optimize the aperture efficiency of a single lens antenna, the analysis is performed in Rx following the field correlation approach described in Section 1.3. Here the reaction integral in (1.1) is performed over the FO sphere shown in Fig. 2.5(a) between the GO fields, $\vec{E}^{Rx}_{GO}$ and $\vec{H}^{Rx}_{GO}$, generated by an incident plane wave propagating along $\hat{k}_i$, and the field radiated by the LWA feed, $\vec{E}^{Tx}_{LWA}$ and $\vec{H}^{Tx}_{LWA}$. If we assume the transmitted GO fields

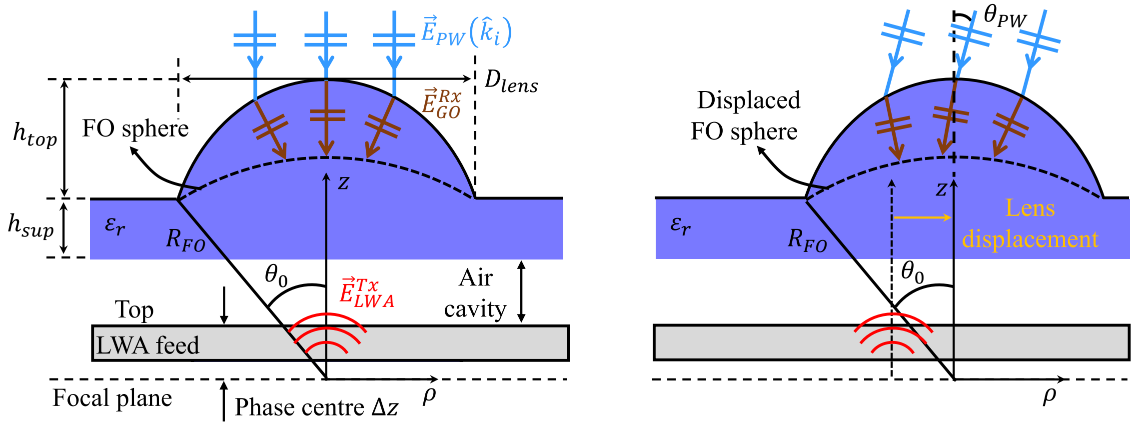

(a) (b)

Figure 2.5: Geometry of the elliptical HDPE ($\varepsilon_r = 2.34$) lens illuminated by the LWA feed in Fig. 2.2. The FO scenario is depicted when the lens is (a) aligned and (b) displaced along the ρ axis with respect to the feed. The optimized lens dimensions are: $D_{lens} = 2\lambda_0$ (at 28 GHz), $\theta_0 = 33.5°$, $R_{FO} = 1.81\lambda_0$, $\Delta z = 0.81\lambda_0$, $h_{top} = 0.85\lambda_0$, $h_{sup} = 0.2\lambda_0$, and $h_c = \lambda_0/2$.

behave as local plane waves with their propagation unit vectors normal to the FO sphere, (1.1) can be further simplified and the aperture efficiency can be calculated as follows:

$$\begin{aligned}\eta_{ap}^{Rx} &= \max\left[P_l(\hat{k}_i)/P_{inc}\right] \\ &= \frac{1}{16 P_{rad}^{LWA} P_{inc}} \left| \int_0^{2\pi} \int_0^{\theta_0} \left[\frac{1}{\zeta} \vec{E}_{GO}^{Rx}(\hat{k}_i) \cdot \vec{E}_{LWA}^{Tx} - \zeta \vec{H}_{GO}^{Rx}(\hat{k}_i) \cdot \vec{H}_{LWA}^{Tx} \right] R_{FO}^2 \sin\theta d\theta d\phi \right|^2,\end{aligned} \tag{2.1}$$

where ζ is the characteristic impedance of the lens medium, R_{FO} is the radius of the FO sphere, P_{rad}^{LWA} is the total power radiated by the LWA, and $P_{inc} = 0.5|\vec{E}_{PW}|^2 A_{lens}/\zeta_0$, where $|\vec{E}_{PW}|$ is the amplitude of the plane wave, $A_{lens} = \pi D_{lens}^2/4$ is the projected area of the lens surface, and ζ_0 is the free-space impedance. The GO fields, $\vec{E}_{GO}^{Rx}$ and $\vec{H}_{GO}^{Rx}$, are obtained following the procedures explained in [38], even though the validity of the GO approach is questionable for such small lenses. The fields radiated by the LWA feed on the FO sphere, $\vec{E}_{LWA}^{Tx}$ and $\vec{H}_{LWA}^{Tx}$, cannot be evaluated using the far-field approximation since the FO sphere is too close to the feed. Instead, the near fields are calculated using the spectral Green's function, where the equivalent magnetic currents on the top of the ground plane are taken as a source. These currents have been exported from the full-wave simulation of the LWA feed in the presence of the semi-infinite dielectric medium [see Fig. 2.2(a)] using CST [32]. It is worth mentioning that although the FO sphere is close to the feed, the fields on the FO sphere can still be considered as local spherical waves, and therefore, Eq. (2.1) can be further simplified for the on-focus feed as a field matching between the electric fields, $\vec{E}_{GO}^{Rx}$ and $\vec{E}_{LWA}^{Tx}$ only, as described in [16].

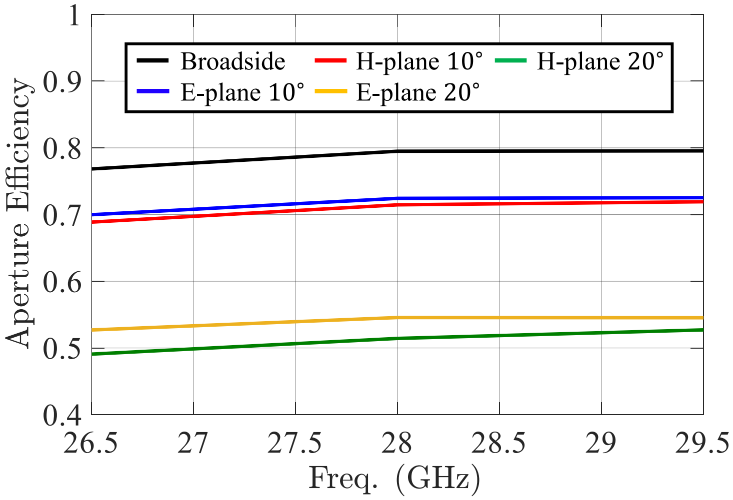

Figure 2.6: Aperture efficiency η_{ap}^{Rx} of the optimized lens illuminated by the LWA feed depicted in Fig. 2.2, calculated using (2.1) for the cases of broadside, steering towards $\theta = 10°$ and $20°$ in E- and H-planes.

2.3.1 Array Element Performance

The lens dimensions are optimized in the near-field region of the feed for one polarization (slot 1) at broadside. The optimization procedure is as follows: first, the far fields of the feed in a semi-infinite dielectric medium are calculated [see Fig. 2.4(b)], from which the phase centre is extracted. For a LWA feed, it is known that its phase centre is located below the ground plane [74]. The phase centre is then aligned with the lower focus of the lens. Second, the far-field patterns are used to calculate an initial estimate of the lens dimensions (a, b, θ_0) geometrically, by imposing $D_{lens} = 2\lambda_0$, where a and b are the semi-major and semi-minor axes, respectively. Finally, the broadside aperture efficiency is optimized iteratively by evaluating the near field, $\vec{E}_{LWA}^{Tx}$, and then performing the field correlation over the corresponding FO sphere increasing or decreasing the lens truncation angle θ_0 and the phase center location. The optimized truncation angle is 33.5°, the total height of the lens is $1.05\lambda_0$ (11.25 mm), and the phase centre is $0.81\lambda_0$ (8.68 mm) below the top ground plane. The resulting aperture efficiency is shown as a function of frequency in Fig. 2.6. As it can be seen, the broadside aperture efficiency is above 75% over the entire frequency band and reaches 80% at 28 GHz.

The broadside near field over the FO sphere radiated at 28 GHz is shown in Fig. 2.7 in co- and cross-polarizations according to Ludwig's third definition. Indeed, the amplitude of the near field differs significantly from that of the far field in Fig. 2.4(b). There is better field symmetry in ϕ up to the truncation angle and lower cross-polarization level.

In the steering cases, the lens should be displaced along the ρ axis with respect to the feed by a few millimeters to steer the element pattern of the array. To calculate the steering performance of the array elements and evaluate the optimal lens displacement, the field radiated by the feed, $\vec{E}_{LWA}^{Tx}$, should be calculated over the displaced FO sphere; see Fig. 2.5(b). The aperture efficiency can then be calculated in the same way as the broadside case. Note that in this case, the reference system is still at the lens focus, but the FO sphere

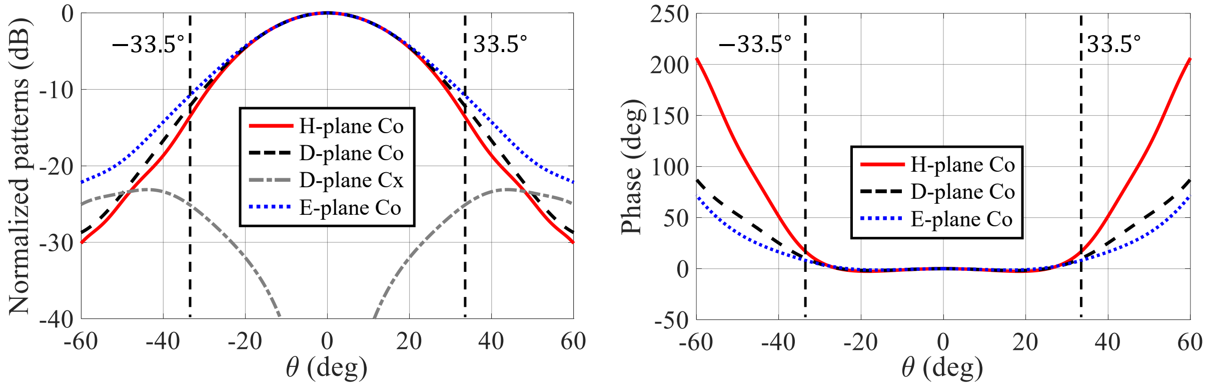

(a) (b)

Figure 2.7: Broadside near field radiated by the LWA feed in Fig. 2.2 (slot 1) at 28 GHz on the FO sphere: (a) amplitude and (b) phase. The radius of the FO sphere is $R_{FO} = 1.81\lambda_0$. The lens geometry is optimized and its truncation angle is 33.5°.

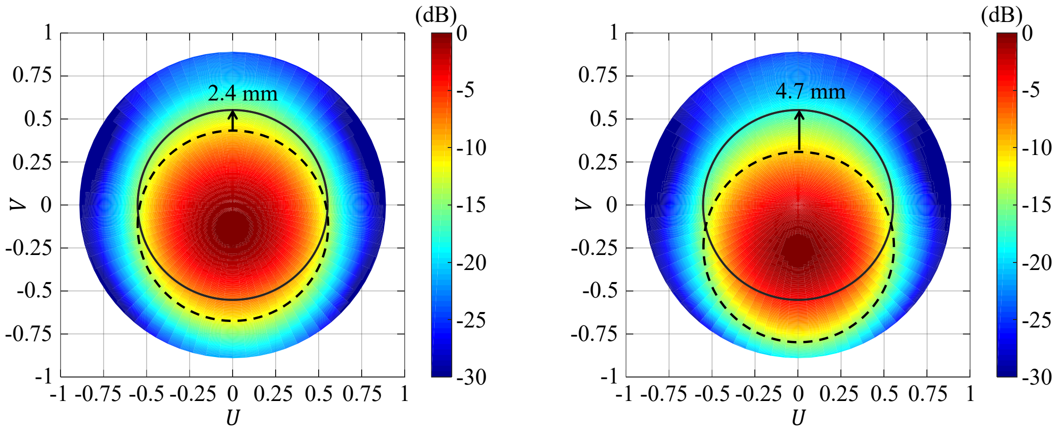

(a) (b)

Figure 2.8: Near fields radiated by the LWA feed (slot 1) at 28 GHz on the FO spheres for the displaced lenses, seen from the coordinate system in Fig. 2.5(b). Lenses are displaced by (a) 2.4 mm and (b) 4.7 mm along the E-plane ($\phi = 90°$), corresponding to $\theta = 10°$ and 20° steering, respectively. The dashed and solid black circles represent the aligned and displaced FO spheres (w.r.t the feed), respectively.

is not spherical seen from the feed position. The steering analysis is performed for steering angles of 10° and 20° in the main planes. These angles correspond to lens displacement of 2.4 and 4.7 mm along the steering directions, respectively. The amplitude of the fields over the FO sphere in these two steering cases is shown in Fig. 2.8 in the UV plane, where $U = \sin\theta\cos\phi$ and $V = \sin\theta\sin\phi$. The dashed and solid black circles represent the aligned and displaced FO spheres (with respect to the feed), respectively. It is clear that larger displacement leads to larger spillover loss. Furthermore, for larger displacement the angle between $\vec{E}^{Tx}_{LWA}$ and the lens-air interface can reach the critical angle [16], leading to reduced reflection efficiency. The aperture efficiency, shown in Fig. 2.6, is above 70% for 10° steering and above 50% for 20° steering.

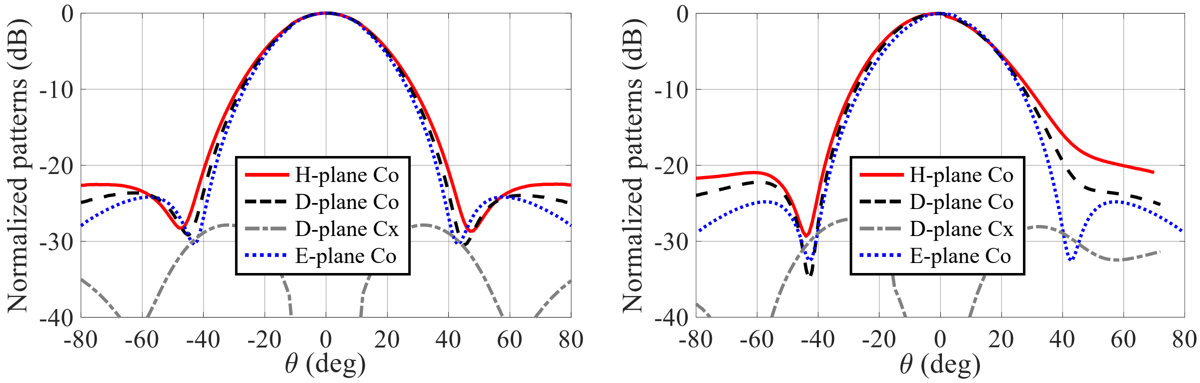

(a) (b)

Figure 2.9: Array element patterns when the lens is (a) aligned w.r.t the LWA feed, and (b) displaced by 2.4 mm along the H-plane ($\phi = 0°$), steering to $\theta = 10°$. Note that the pattern in (b) points towards 10° in H-plane when the reference system is aligned to that of (a). The reference system used in (b) is instead aligned towards 10°.

The element pattern of the array can be evaluated using (2.1) by varying the incident angle, θ_{PW} in Fig. 2.5(b), and the polarization of the incident plane wave [38]. The array element pattern when the lens is aligned to the feed is shown in Fig. 2.9(a). This broadside pattern is almost symmetric in ϕ and has a cross-polarization level below -25 dB. The array element pattern when steering in the H-plane ($\phi = 0°$) to $\theta = 10°$ is shown in Fig. 2.9(b). The steering is achieved by displacing the lens 2.4 mm in the positive x axis, and the steered pattern still shows good symmetry and high directivity.

2.3.2 Array Performance

The lens array consists of 16 lenses with $D_{lens} = 2\lambda_0$ arranged in four rows in which the uneven rows are shifted by λ_0 to form a regular triangular grid; see Fig. 2.1(b). The PAA has the same configuration with the $2\lambda_0$ periodicity, illuminating the lens array through the $\lambda_0/2$ air cavity. This hexagonal configuration is adopted since it can achieve a lower SLL with respect to a rectangular configuration. The array pattern, steered to (θ_s, ϕ_s), is obtained as the product between the array element pattern (Fig. 2.9) and the array factor $AF(\theta_s, \phi_s)$. The grating lobes in the array factor that arise from the sparse array sampling are suppressed by the directive array element pattern [27], which has been illustrated in Fig. 2.1(c).

Three radiation cases are considered here: broadside, steering to 10° and 20° in E- and H-planes, respectively. The broadside radiation patterns of the proposed scanning lens PAA, fed by port 1 and port 2 at 28 GHz, are shown by the black curves in Fig. 2.10(a) and 2.10(b), respectively. Here port 1 represents the case when all slots 1 [see Fig. 2.2(b)] are excited simultaneously, while port 2 corresponds to exciting slots 2. The first side lobe is below -13 dB for both cases. A high directivity of 28 dBi is obtained with only 16 elements due to the presence of the lenses. Moreover, the grating lobes from the

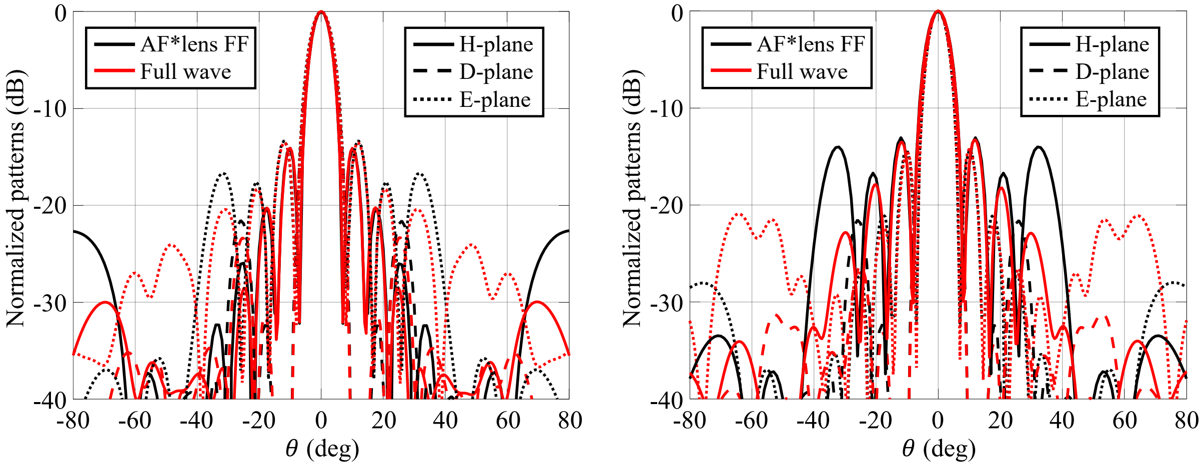

(a)

(b)

Figure 2.10: Broadside co-pol far fields (FF) radiated by the proposed scanning lens PAA at 28 GHz fed by (a) port 1 (slots 1) and (b) port 2 (slots 2). The black curves represent the far fields calculated by using the GO/FO approach. The red curves show the CST full-wave simulations. The reference system used for the patterns is shown in Fig. 2.1(b).

array factor are significantly suppressed by the directive array element pattern shown in Fig. 2.9(a). The radiation patterns of the array obtained with the GO/FO approach have been verified by the full-wave solver of CST. The simulated patterns are shown by the red curves in Fig. 2.10 for both ports. The agreement between the CST simulations and the GO/FO approach is excellent for the main lobe and the first few side lobes. Wider angles are not accurately modelled by the GO/FO approach, since the edge effect of the array and the spillover from one lens to the next is not considered in this approach.

In the steering cases, the lens array is displaced by 2.4 mm and 4.7 mm towards the steering directions, i.e., 10° and 20° in H- and E-planes, respectively. The steered radiation patterns of the array, fed by port 1 at 28 GHz, are shown in Fig. 2.11 and compared to full-wave simulations. The H-plane ($\phi = 0°$) steering is shown in Fig. 2.11(a) for 10° and 20°, while the E-plane ($\phi = 90°$) steering is shown in Fig. 2.11(b). Moreover, the simulated patterns in UV-plane are shown in Fig. 2.11(c) and 2.11(d), for the cases of H- and E-plane steering to 20°, respectively. In Fig. 2.11(a) and 2.11(b), the patterns evaluated using the GO/FO approach (solid lines) show excellent agreement with the full-wave simulations (dashed lines) for the main lobes and the first few side lobes. Moreover, the SLLs evaluated using the GO/FO approach are below -10 dB for both steering angles and both ports. It is worth mentioning that the proposed approach is quite efficient. The calculation of the array patterns is orders of magnitude faster than the full-wave simulations (ca., 4.5 hours for CST versus a couple of minutes for the GO/FO method).

The simulated array active S-parameters for port 1 (slots 1) for all radiation cases are shown in Fig. 2.12. The impedance-matching performance is very good within the required frequency band, even for the 20° steering cases. Since the feeds are far away from each other, the mutual coupling between the feeds is always lower than -20 dB.

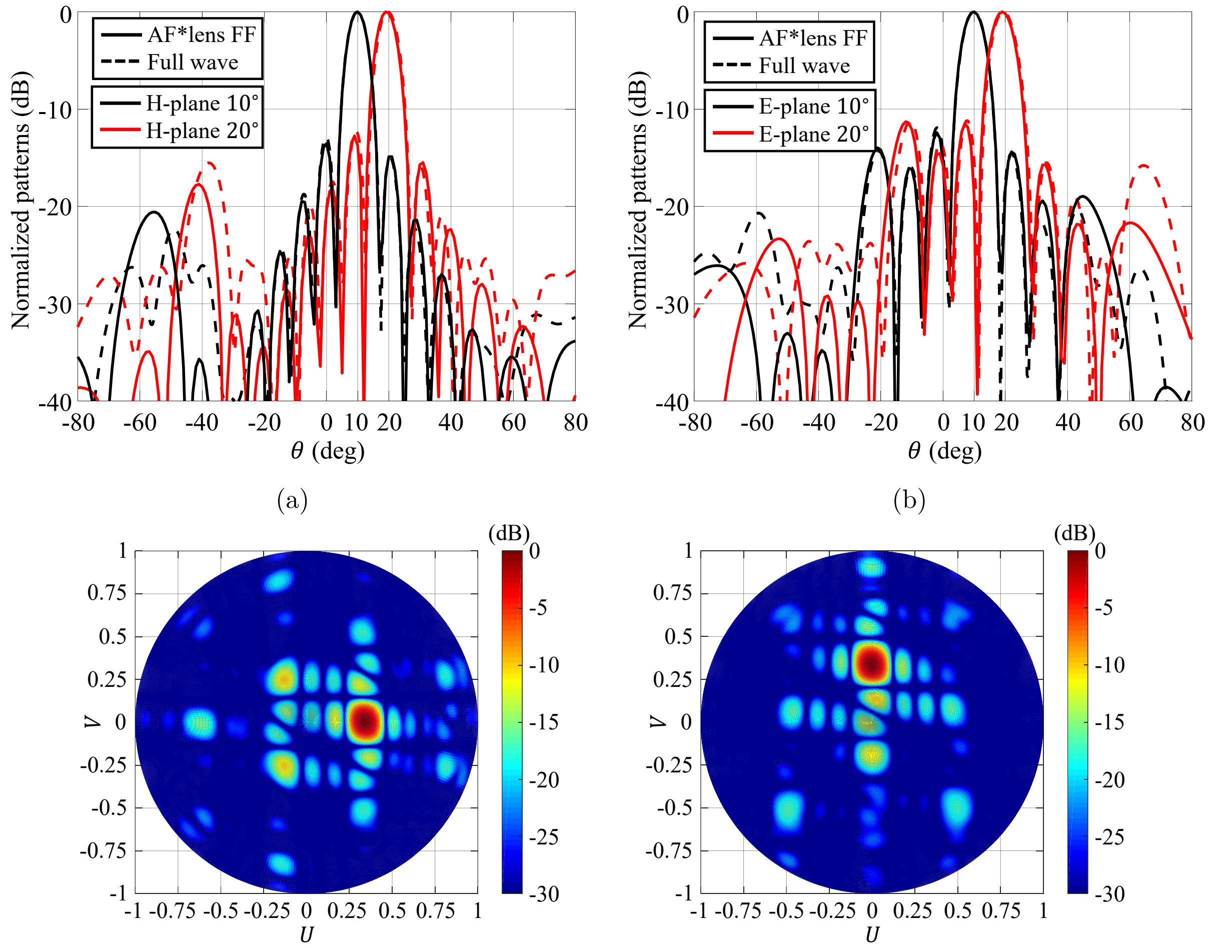

(a) (b)

(c) (d)

Figure 2.11: Co-pol far fields radiated by the proposed scanning lens PAA at 28 GHz fed by port 1 (slots 1) at (a) H-plane ($\phi = 0°$) and (b) E-plane ($\phi = 90°$), when steering towards 10° (black) and 20° (red). The solid and dashed curves represent the GO/FO approach and the CST full-wave simulations, respectively. (c) and (d) show the full-wave results of (a) and (b) when steering to 20° in UV-plane, respectively. The reference system used for the patterns is shown in Fig. 2.1(b). The lens array is displaced by 2.4 and 4.7 mm towards the steering directions, for the 10° and 20° steering cases, respectively.

Finally, the simulated directivity of the array is shown in Fig. 2.13 for both ports. The broadside directivity is 28 dBi at 28 GHz and above 27.3 dBi in the designed BW. For the cases of steering, the scan loss is below 1 and 2 dB in the whole band, when steering to 10° and 20°, respectively. The directivity evaluated using the GO/FO approach is overall 0.3 to 0.8 dB lower than the CST simulations, depending on frequencies and steering angles. This is related to the aforementioned pattern differences at the larger elevation angles ($\theta \geq 40°$). However, the accuracy of the far-field performance is good enough for design purposes.

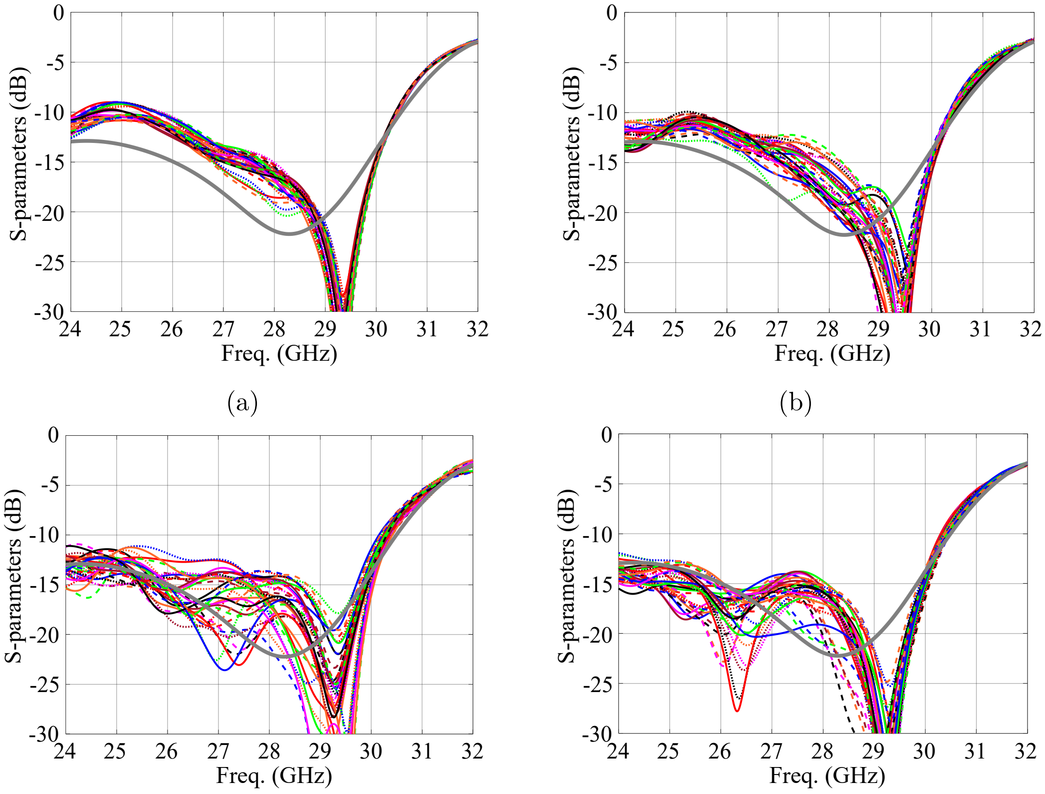

(a)

(b)

(c)

(d)

Figure 2.12: Simulated array active S-parameters (reflection coefficients) of port 1 (slots 1) for the cases of (a) broadside, (b) steering to 10° in H-plane ($\phi = 0°$), (c) 20° in H-plane, and (d) 20° in E-plane ($\phi = 90°$). The lens array is displaced by 2.4 mm and 4.7 mm for steering to 10° and 20°, respectively. The thick gray line is the S-parameter of the single LWA feed, see Fig. 2.4(a).

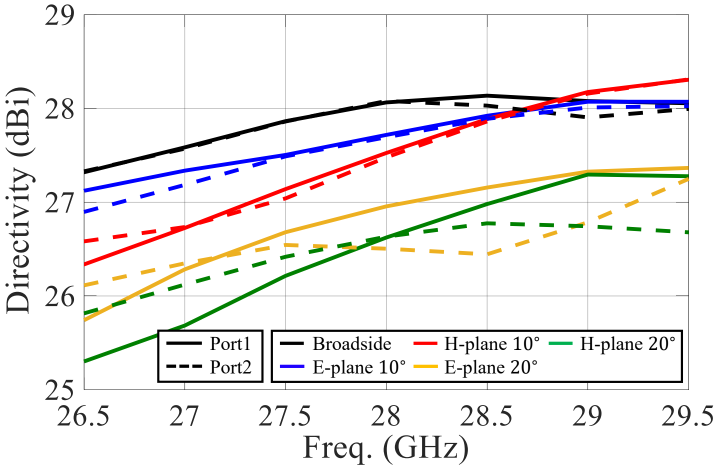

Figure 2.13: Simulated array directivity for port 1 (solid lines) and port 2 (dashed lines), and for broadside, 10°, and 20° steering in both the E- and the H-planes. The lens array is displaced by 2.4 mm and 4.7 mm for steering to 10° and 20°, respectively.

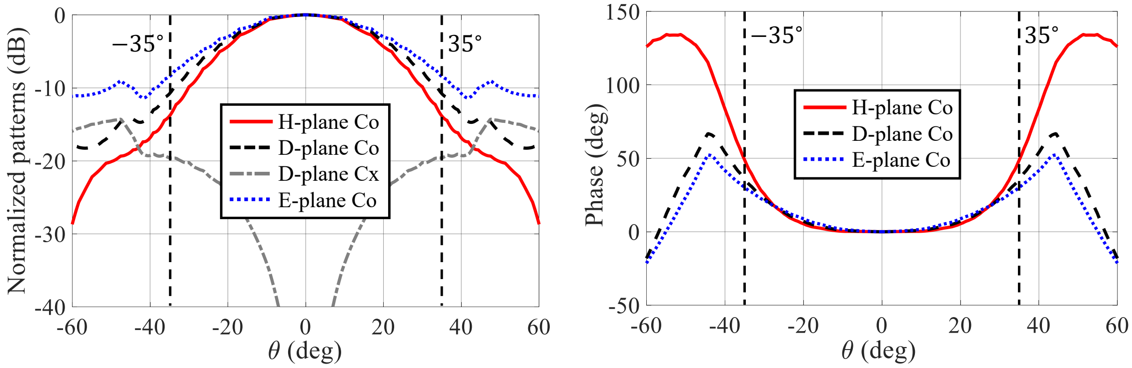

(a) (b)

Figure 2.14: Near field (at 28 GHz) radiated by the LWA feed with $l_d = 2.25$ mm inside a semi-infinite medium (Polycarbonate, $\varepsilon_r = 2.84$) at broadside: (a) amplitude, and (b) phase. The near field is plotted along the FO sphere centered at the phase center. The lens truncation angle is 35°.

2.3.3 Study on Edge Effects

If a lens array element is not well co-optimized with its antenna feed, there will be uncontrolled radiation that will eventually emerge from the array edges reducing the gain of the array. In this subsection, a study on such edge effects is reported.

One of the most important design parameters to reduce the edge radiation is the length of the dipole. The dipole length controls the amount of energy launched into the TM_0 LW mode, which will not couple well with the lenses. As an example, we show a different feed-lens design where the dipole length is only 2.25 mm, while in the proposed prototypes the length is 2.95 mm. The lens material is Polycarbonate ($\varepsilon_r = 2.84$), and its truncation angle is 35° for this different design, whereas in the proposed design the material is HDPE ($\varepsilon_r = 2.34$) and the truncation angle is 33.5°. The near field radiated by the shorter dipole at 28 GHz inside the lens is plotted in Fig. 2.14. In this case, the E-plane ($\phi = 90°$) has a side lobe at around $\theta = 50°$ because of the TM_0 mode. Moreover, the amplitude cuts along the main planes are not symmetric. At the lens truncation angle of 35°, the amplitude in the E-plane is around -8.5 dB, while that in the H-plane is around -14 dB (5.5 dB difference). Consequently, less energy will be coupled to the lens with respect to the proposed final design, leading to stronger edge effects.

To show the impact of the uncontrolled radiation, we simulated a 4 × 4 square array in CST as shown in Fig. 2.15(a). In Fig. 2.15(b), the electric field is shown when only the central lens element is excited at 28 GHz by port 1 at broadside. There appears uncontrolled power at adjacent lenses, particularly strong in the E-plane. When all of the elements in the 4 × 4 array are excited simultaneously, this uncontrolled power will impact on the array performance significantly. The simulated directivity of such an active square array is plotted in Fig. 2.16(a) for the broadside and the steering cases, in comparison with the maximum achievable directivity for the given size of the lens array. Note that the lens array is not displaced in the steering cases. We can observe significant drops in directivity. In broadside, the drop is 0.5 dB while for the E-plane scanning ($\theta = 10°, \phi = 90°$) the

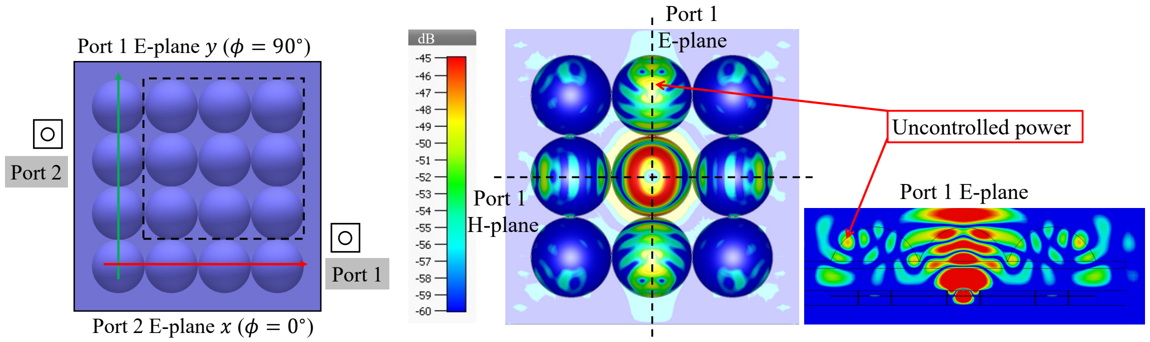

(a) (b)

Figure 2.15: Previously designed square array incident by the near field shown in Fig. 2.14: (a) reference system for the ports of the array. (b) Top and lateral views of the simulated E-field at 28 GHz of the 3×3 subarray marked in (a). Only the central lens element is excited by port 1 at broadside.

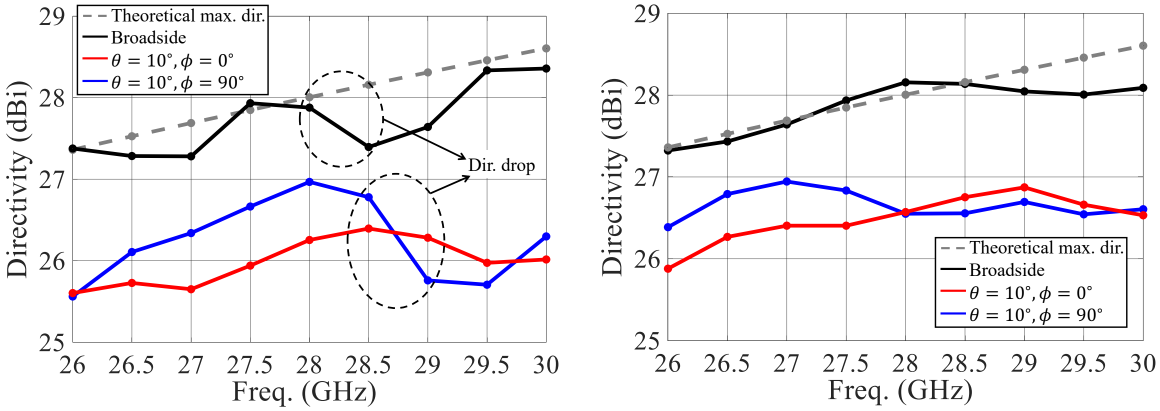

(a) (b)

Figure 2.16: Simulated directivity of the arrays. (a) Square array incident by the near field shown in Fig. 2.14. (b) Hexagonal array with the optimized lens design shown in Fig. 2.5 incident by the near field in Fig. 2.7. Note that the lens arrays are not displaced when steering in this case.

drop is 1 dB. Therefore, we changed the design and solved this issue. As mentioned before, for the final optimized feed, its near field (Fig. 2.7) is fine-tuned to solve the spillover effect in Fig. 2.14(a) and achieve the higher lens illumination efficiency. The arrays are in hexagonal configurations (Fig. 2.1), and the directivity is shown in Fig. 2.16(b). In this case, the lens array is also non-displaced when steering for comparison purposes. As it can be seen, there is less frequency variation in the achieved directivity.

2.4 PCB Antenna Design

The LWA feed shown in Fig. 2.2 is the simplified geometry used for analyzing and optimizing the performance of an array element. In this section, this geometry is optimized for the implementation in PCB technology including the proper feeding topology. The proposed

PCB design presents excellent radiation efficiency (>97%) and no back radiation in a relative BW of 22.7%. Moreover, corporate feeding networks with fixed phase shifts between array elements are designed to validate the proposed antenna architecture in pre-defined and static steering conditions.

2.4.1 Optimized Antenna Feed in PCB

Referring back to Fig. 2.2, the LWA feed consists of three metal layers and one dielectric layer. The dual polarization is realized by exciting symmetrically the crossed slots at their arms with discrete ports. In a PCB design, the stratification consists of multiple layers and the slots are excited by microstrip lines. The main challenge comes from the feeding design for the crossed slots in PCB. In [71], each of the crossed slots is fed symmetrically by a set of dual-offset microstrip lines which are connected to the input port through a reactive power combiner. However, since the two sets of microstrip lines are designed on the same dielectric layer, an air bridge is used to avoid intersection between the microstrip lines. To achieve good performance and practical implementation with standard PCB technology at 5G frequencies, the two sets of dual-offset microstrip lines are placed instead at the opposite sides of the ground plane, similar to what was done in [75].

The optimized PCB stratification is shown in Fig. 2.17(a), combined with an externally milled backing reflector. The PCB substrates are Rogers material, with the relative permittivity of 3.66, 3.52 and 2.2 for RO 4350B, RO 4450F, and RT/duroid 5880, respectively. There are four metal layers, M1-M4, in the PCB. M1 is the top ground plane where the crossed dipoles are printed; M3 is the slot ground plane; M2 and M4 are layers for microstrip feeding lines. The upper circular metallic wall between the slot plane and the top ground plane shown in Fig. 2.2(a) is made of plated-through via holes within the PCB from M1 to M4 [see Fig. 2.17(a)], with a height of 1.63 mm and a radius of 4.28 mm. While the lower metal wall is realized by a continuous milled aluminum cavity between the PCB and the backing reflector, with a height of 1.5 mm and a radius of 3.55 mm. Both cavities are fine-tuned for the best impedance matching and suppression of surface waves. The perspective and top views of the detailed antenna structure are shown in Fig. 2.17(b) and 2.17(c), respectively. Visible in the figures are two rings of metallization realized by via holes and aluminum cavity. In the top view, the crossed slot-fed dipoles are shown. Each slot is fed coherently by two offset microstrip lines that are combined together by a reactive power combiner located at the opposite sides (M2/M4) of the slot ground plane (M3). Specifically, the microstrip lines on M2 are designed with radial open stubs, while the ones on M4 are short stubs made of via holes. The short-stub design is commonly used since it makes the design more compact. However, in our case, the two stubs on M2 and M4 cannot be designed symmetrically using both short stubs, because there would be intersection between via holes and microstrip lines. Although the asymmetric stub design introduces complexity, a wideband impedance matching is best achieved using the dimension described in Fig. 2.17(c).

In the final array design, we will use corporate feeding networks located at the bottom layer M4 to excite all array elements. Therefore, the microstrip lines on M4 are directly

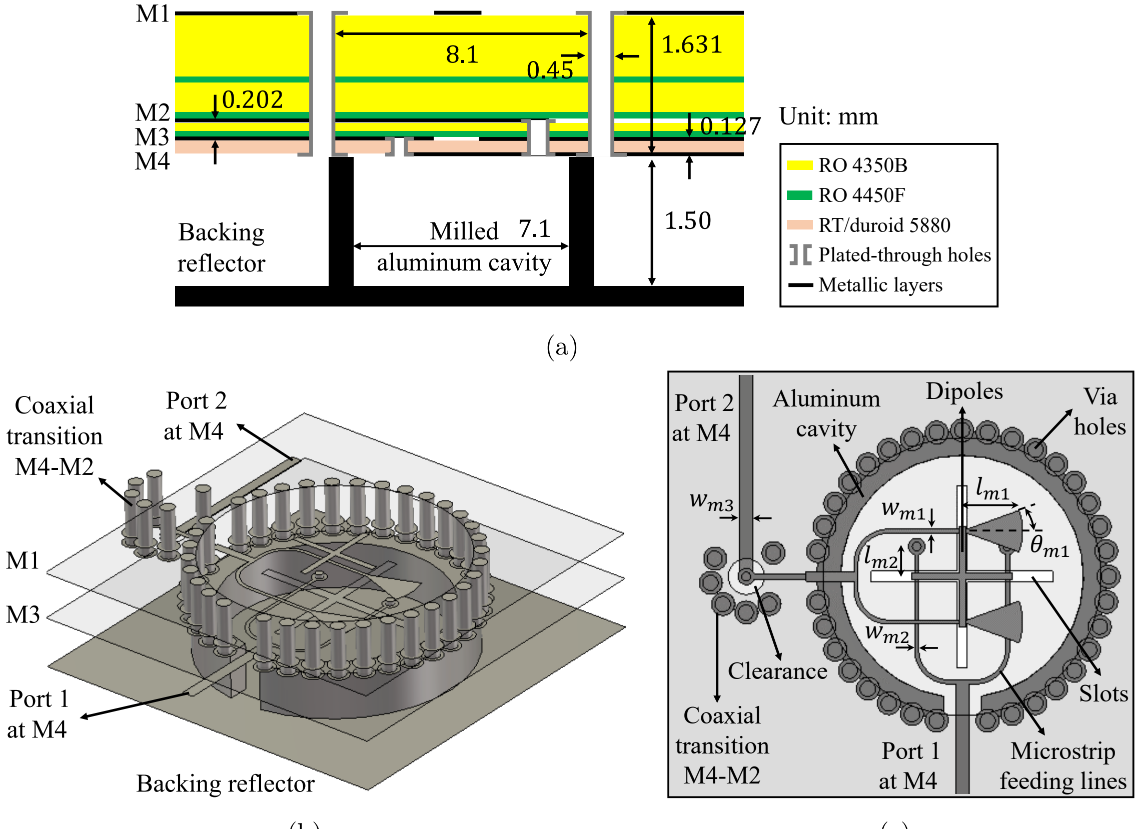

(a)

(b) (c)

Figure 2.17: PCB dual-polarized LWA feed: (a) PCB stratification. (b) Perspective and (c) top views of the detailed antenna structure. The slots are excited in balance by two sets of microstrip lines, each one dedicated to a different polarization. The lines with the radial open stubs ($w_{m1}, l_{m1}, \theta_{m1}$) are at M2, while those with the short stubs (w_{m2}, l_{m2}) are at M4. The optimized dimensions of this antenna are: $\varepsilon_{r1} = 3.66$, $w_{m1} = w_{m2} = 0.12$ mm, $w_{m3} = 0.38$ mm, $l_{m1} = 1.66$ mm, $\theta_{m1} = 20°$, $l_{m2} = 0.88$ mm, $w_s = 0.32$ mm, $l_s = 5.31$ mm, $w_d = 0.2$ mm, $l_d = 2.95$ mm, $h_1 = 1.631$ mm, $r_1 = 4.28$ mm, $h_2 = 1.5$ mm, $r_2 = 3.55$ mm.

connected to port 1 via the feeding network that will be described in Section 2.4.2. On the contrary, the microstrip lines on M2 need vertical transitions from M4 to M2 to connect to port 2 through the feeding network. Such a transition structure is made by emulating a coaxial using via holes from M4 to M2, as shown in Fig. 2.17, which is similar to what was done in [76]. This coaxial transition can significantly alter the matching performance of the feed because of the limited fabrication tolerances in standard PCB technology. To make the design more robust, we have shortened the height of the via holes and enlarged the clearance on M3 [see Fig. 2.17(c)] as much as possible. The optimized S-parameters of the proposed coaxial transition are shown in Fig. 2.18 (no lossy materials). The reflection coefficient shows a wideband behavior ($S_{11} < -25$ dB) over the entire frequency band. Moreover, S_{21} is larger than -0.3 dB, which indicates that the power launched in surface waves and effectively lost is quite low.

The matching performance of the entire PCB LWA feed is simulated and reported in Fig. 2.19(a). Here, the antenna radiates in the semi-infinite HDPE medium. The -10 dB

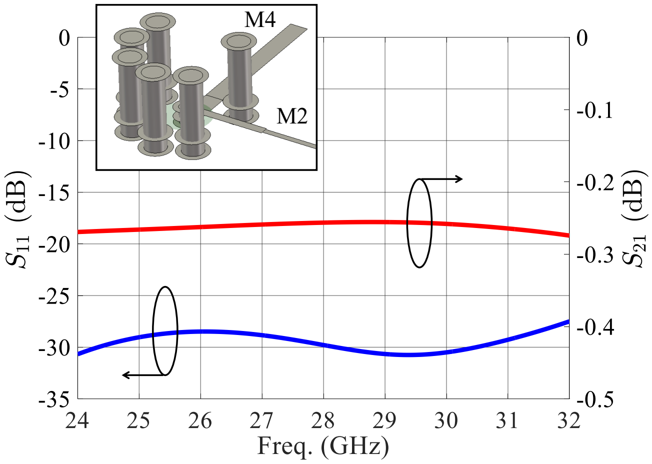

Figure 2.18: Simulated S-parameters of the vertical transitions from M4 to M2. Note that the ohmic and dielectric losses are not included in the simulation.

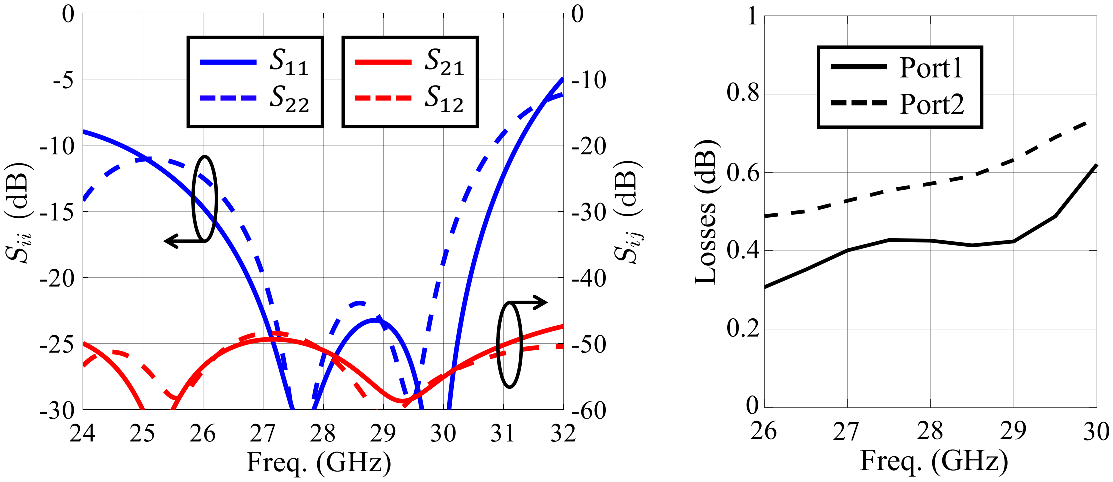

(a) (b)

Figure 2.19: Simulated performance of the dual-polarized PCB LWA feed when radiating in the semi-infinite HDPE medium: (a) S-parameters. Note that the ohmic and dielectric losses are not included in the simulation. (b) Total loss of the feed, including the excitation of surface waves, ohmic and dielectric losses (dielectric loss in the HDPE medium is not included here).

band is from 24.6 to 30.9 GHz, i.e., 22.7% relative BW. Moreover, the mutual coupling between the ports is very low, which is in the order of -50 dB. The total loss of the feeding antenna, including the excitation of surface waves, ohmic and dielectric losses, is reported in Fig. 2.19(b) for both ports. As it can be seen, the total loss is less than 0.6 dB and 0.8 dB for port 1 and port 2 up to 30 GHz, respectively. The loss in port 2 is a bit larger due to the coaxial transition structure. For the far-field performance, it is very close to the that in Fig. 2.4(b).

Another architecture with the backing reflector integrated inside the PCB is described in Appendix A. Its simulated and measured performance are reported there in details.

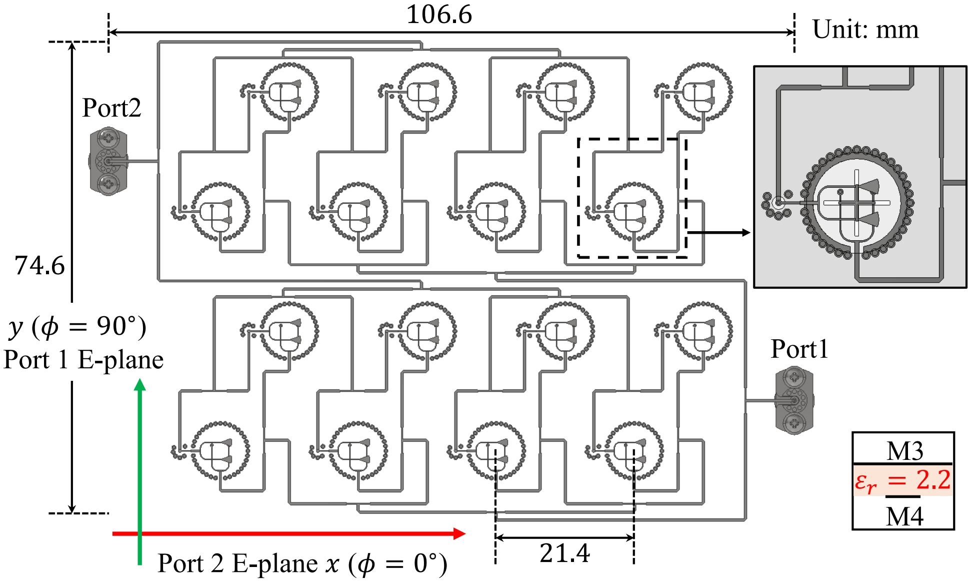

Figure 2.20: PCB feeding networks located at the bottom layer M4 used for the broadside radiation. Note that some components such as dipoles are not shown here. The reference system for both ports are also shown. The top inset shows one of the array elements, which is the same as that in Fig. 2.17(c). Here all components are shown. The bottom inset shows the lateral structure of the feeding networks.

2.4.2 Feeding Networks

To validate the array architecture discussed in Section 2.3.2, all 16 dual-polarized LWA feeds (in Fig. 2.17) are connected by two specific corporate feeding networks fed by two ports, one per polarization, as shown in Fig. 2.20. The feeding networks are done using microstrip lines fabricated on a RT/duroid 5880 layer and are located at the M4 layer of the proposed stratification in Fig. 2.17(a). The lengths of the microstrip lines are designed to guarantee uniform amplitude excitation and appropriate progressive phase shifts between the array elements that would lead to the desired steering angles. Each array element is excited by both ports through four power dividers (see Fig. 2.20). The short stubs on M4 are connected to the port 1 directly through the feeding network. While the opening stubs on M2 are first connected to M4 through the coaxial transition structures, and then excited by port 2 through the feeding network.

To demonstrate the capability of the array to electronically steer towards broadside and ±10° in the main planes, three separate PCBs were designed and fabricated with fixed progressive phase shifts between the array elements. The performance of these feeding networks in all three PCBs was simulated, showing reflection coefficients below -23 dB over the whole band and an ohmic loss of about 1.6 dB. The power division, $1 \rightarrow 1/16$, is simulated to guarantee a maximum deviation of ±1.4 dB among all array elements. The details related to the simulations are reported in Appendix A, Fig. A.4. The expected progressive phase shifts (versus frequencies) also show very little dispersion, with the phase deviating from the ideal linear phase shifts by less than 5° over the entire band.

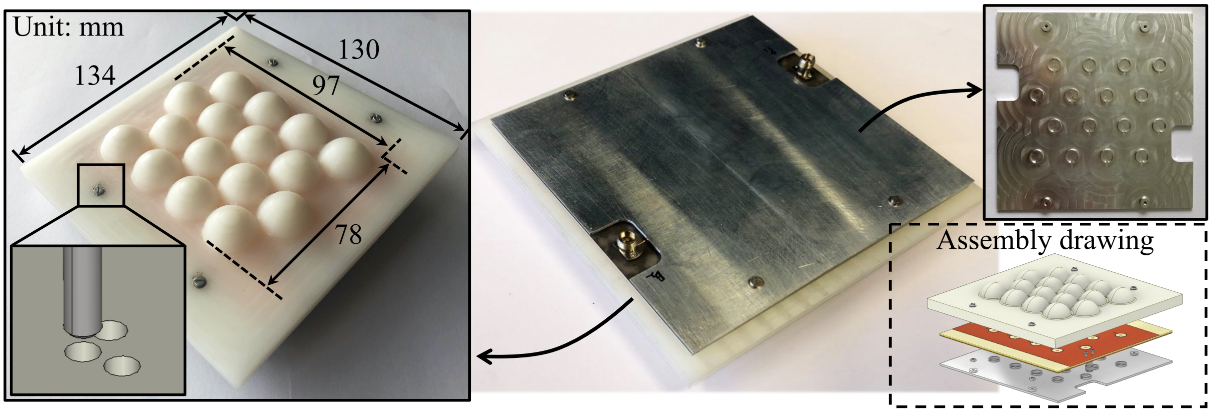

Figure 2.21: Photographs of the assembled antenna prototype. The milled HDPE elliptical lens array is shown on the left side, where the inset shows the screw holes used for the displacement of the lens layer. On the right side is the perspective view of the antenna. The milled aluminum cavity and the assembly drawing are shown in the top and bottom insets, respectively.

2.5 Antenna Prototype and Measurement

We have fabricated and measured a prototype to validate the proposed antenna architecture. The prototype consists of three parts: a HDPE lens array, three different PCBs, and a milled aluminum cavity. They were manufactured separately and then assembled together. As mentioned before, the three PCBs were fabricated with different feeding networks where the fixed phase-shifting conditions were implemented, to validate the steering capability of the antenna towards broadside, $\theta = 10°, \phi = 0°$, and $\theta = 10°, \phi = 90°$. The mechanical displacement of the lens array is implemented only for these three steering conditions, by introducing a fixed displacement of the lens layer of 0 mm and 2.4 mm along the two main planes, respectively.

The fabricated antenna prototype is shown in Fig. 2.21. In the assembly drawing shown on the right side, different parts of the prototype are aligned with screws. The milled aluminum cavity is shown on the top right side and the milled lens array is shown on the left, where the inset shows three screw holes with a spacing of 2.4 mm. These holes are used to displace and align the lens layer with respect to the PCBs used for the three steering directions. Note that the dimensions of the radiating aperture associated to the lens array are 97 mm × 78 mm, while the fabricated prototype has an area of 130 mm × 134 mm. The outer extra rim was included to facilitate the fabrication in the workshop.

The PCB for the broadside radiation is shown in Fig. 2.22. The top layer M1 is shown on the left, with the crossed dipoles shown in the inset. Moreover, the bottom feeding networks on M4 are shown on the right. In the inset is one of the 16 feeding elements, with the coaxial transition, and fed through the feeding networks by two connectors which are located at the corners of the PCB. It can be seen that the PCB size is 120 mm × 120 mm instead of 100 mm × 100 mm. The extra rim was included to facilitate the alignment with the lens array.

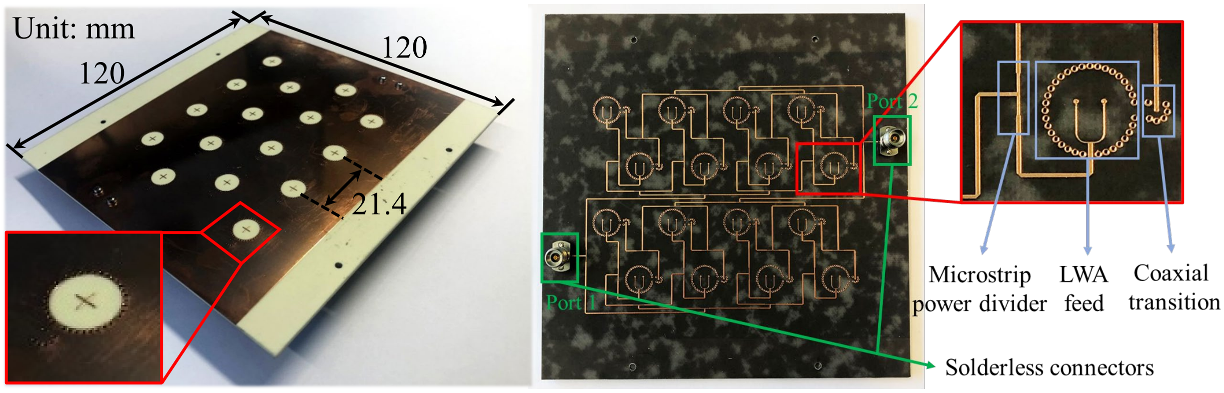

Figure 2.22: Photographs of the fabricated PCB used for the broadside radiation. The top metal layer M1 is shown on the left side, where the inset shows the crossed dipoles. The right side shows the bottom view of the PCB and the feeding networks. One of the feeding elements in the PAA is shown in the inset.

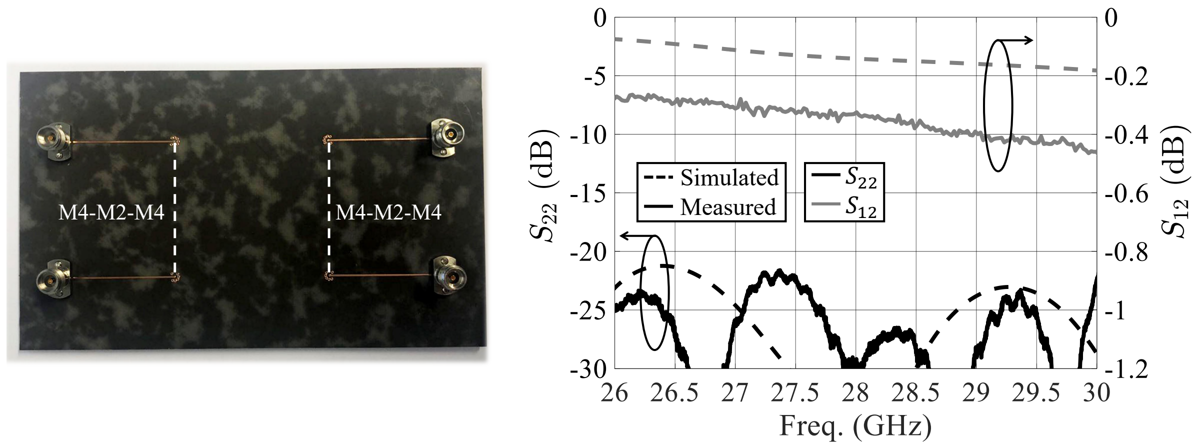

(a)

(b)

Figure 2.23: (a) PCB used for measuring the S-parameters of the coaxial transitions from M4 to M2 and then back to M4. (b) Measured S-parameters compared to the simulations. The same structure in (a) was simulated. By applying post processing, the loss S_{12} of a single transition structure from M4 to M2 is extracted from the measurement and compared to the simulation (the loss in microstrip lines is removed).

2.5.1 Characterization of S-parameters

The loss in microstrip lines is estimated using a TRL calibration kit, which is around 0.27 dB/cm at 28 GHz. This loss is higher than the one obtained using a simple surface impedance model. At higher frequencies, the effects of metal roughness and surface finish have been pointed as causes for this higher line loss [77]. The details of such effects are discussed in Appendix A.1.

The coaxial transitions were measured using the back-to-back configuration shown in Fig. 2.23(a), i.e., the structure is from M4 to M2 and then back to M4. The same structure was simulated and compared to the measurements, as shown in Fig. 2.23(b). The measured reflection coefficient matches well with the simulation. By applying post processing, the

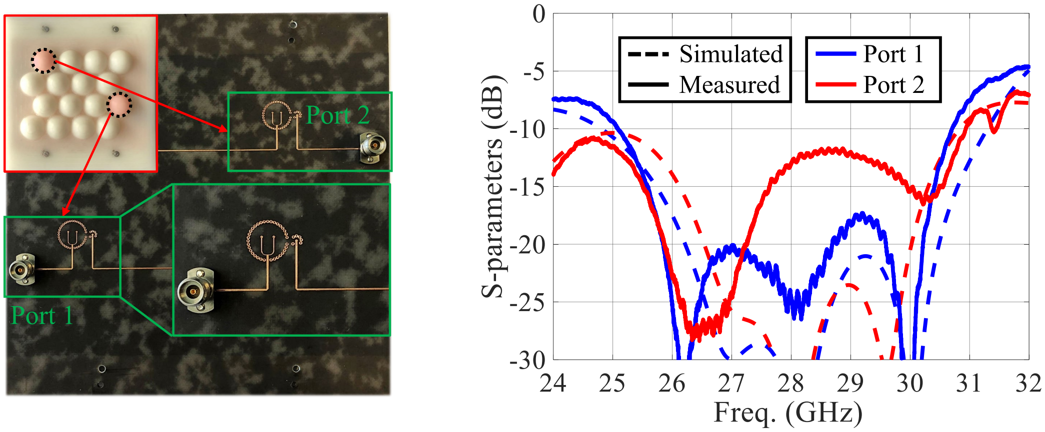

(a) (b)

Figure 2.24: Two HDPE lenses illuminated by two LWA feeds which are excited directly by two ports, each one dedicated to a different polarization: (a) photograph of the PCB. (b) Measured S-parameters compared to the simulations (all losses are included).

S_{12} of a single transition structure from M4 to M2 can be estimated (the loss in microstrip lines is removed). The agreement between the measurement and the simulation is also very good. Moreover, the matching performance of both ports of a single lens antenna was measured using a different PCB showing in Fig. 2.24(a). Two marked lenses in the lens array are illuminated by two LWA feeds which are directly excited by two ports, each one dedicated to a different polarization. The measured S-parameters are shown in Fig. 2.24(b) and compared to the simulations (all losses are included). The -10 dB band of port 1 is from 25.1 to 30.7 GHz, i.e., 20% relative BW. While for port 2, the BW is wider, but the reflection coefficient is higher (-12 dB) around the central frequency. This can be related to the limited tolerances of the fabricated PCBs, especially due to the close location of the vias in the upper cavity with respect to the microstrip lines; see Fig. 2.17(c). This tolerance problem is not present in port 1. Therefore, the matching performance of port 1 is much better than that of port 2. The matching performance of the arrays with different steering configurations was also measured. The reflection coefficients are below -10 dB over the whole band for all steering cases.

2.5.2 Far-field Performance

The far-field patterns, directivity, and gain of the fabricated array antenna were measured in an anechoic chamber. These properties were reconstructed from antenna near-field planar measurements done in front of the lens array, as depicted in Fig. 2.25. The reference system for the far-field patterns is shown in the inset which is the same as that in Fig. 2.1(b). The near fields were measured over a 160 mm × 160 mm rectangular area (step size of 2.25 mm) at 5 cm from the top of the lens array over the required frequency band.

The measured co-pol far-field patterns of both ports at 28 GHz are compared to the simulations and shown in Fig. 2.26 for the cases of broadside, steering to $\theta = 10^\circ$, $\phi = 0^\circ$,

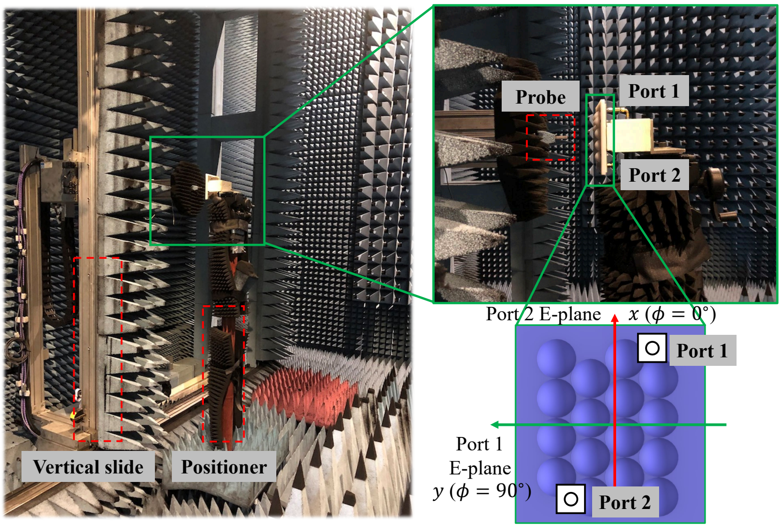

Figure 2.25: Antenna near-field measurement setup in an anechoic chamber. The antenna is placed towards the probe with port 1 pointing upwards. The bottom inset describes the E-plane of each port in this setup and the reference system to plot the radiation patterns.

and $\theta = 10°$, $\phi = 90°$. Moreover, the co-pol patterns at 26.5 GHz and 29.5 GHz for the two steering cases are shown in Fig. 2.27. In the steering cases, the lens array is displaced by 2.4 mm towards the positive x- and y-directions, respectively. In the figures, the co-pol patterns along $\phi = 0°$ and/or $\phi = 90°$ planes are plotted. The cross-pol patterns are below -20 dB at all frequency points and are not shown here. As it can be seen from Fig. 2.26 and 2.27, the agreement between the simulations and the measurements is excellent for all radiation cases. Moreover, the steered beams accurately point towards 10° in both main planes. In Fig. 2.26(f) and Fig. 2.27(c), the SLL is a bit higher (about -8.5 dB) due to the fabrication tolerances, but for other radiation cases the SLLs are below -10 dB. The measured 2D far-field patterns of port 1 at 28 GHz are shown in Fig. 2.28 for the broadside and the steering cases. In the figures, the position of side lobes and the cross-pol values are clearly shown.

The measured broadside and steering directivity and gain are shown in Fig. 2.29 and compared to the simulations. In the case of directivity, i.e., in Fig. 2.29(a), 2.29(c), and 2.29(e), the measurements are in very good agreement with the simulations for the cases of broadside and steering to $\theta = 10°$, $\phi = 0°$ and for both ports. However, when steering to $\theta = 10°$, $\phi = 90°$, port 2 performs worse than port 1, especially at 28.5 GHz. By exploring the measured near fields, it was observed that up to two lenses in the array were barely radiating, which explains the drop of 1 dB in directivity when compared to port 1. Similar case happens in Fig. 2.29(a) that the directivity of port 2 drops at 29.5 GHz since one lens element was not well radiating. This issue is most possibly related to the limited fabrication tolerances, especially in the PCB vias as mentioned in Section 2.5.1. Nevertheless, the capability of steering towards $\theta = 10°$, $\phi = 90°$ is validated by port 1.

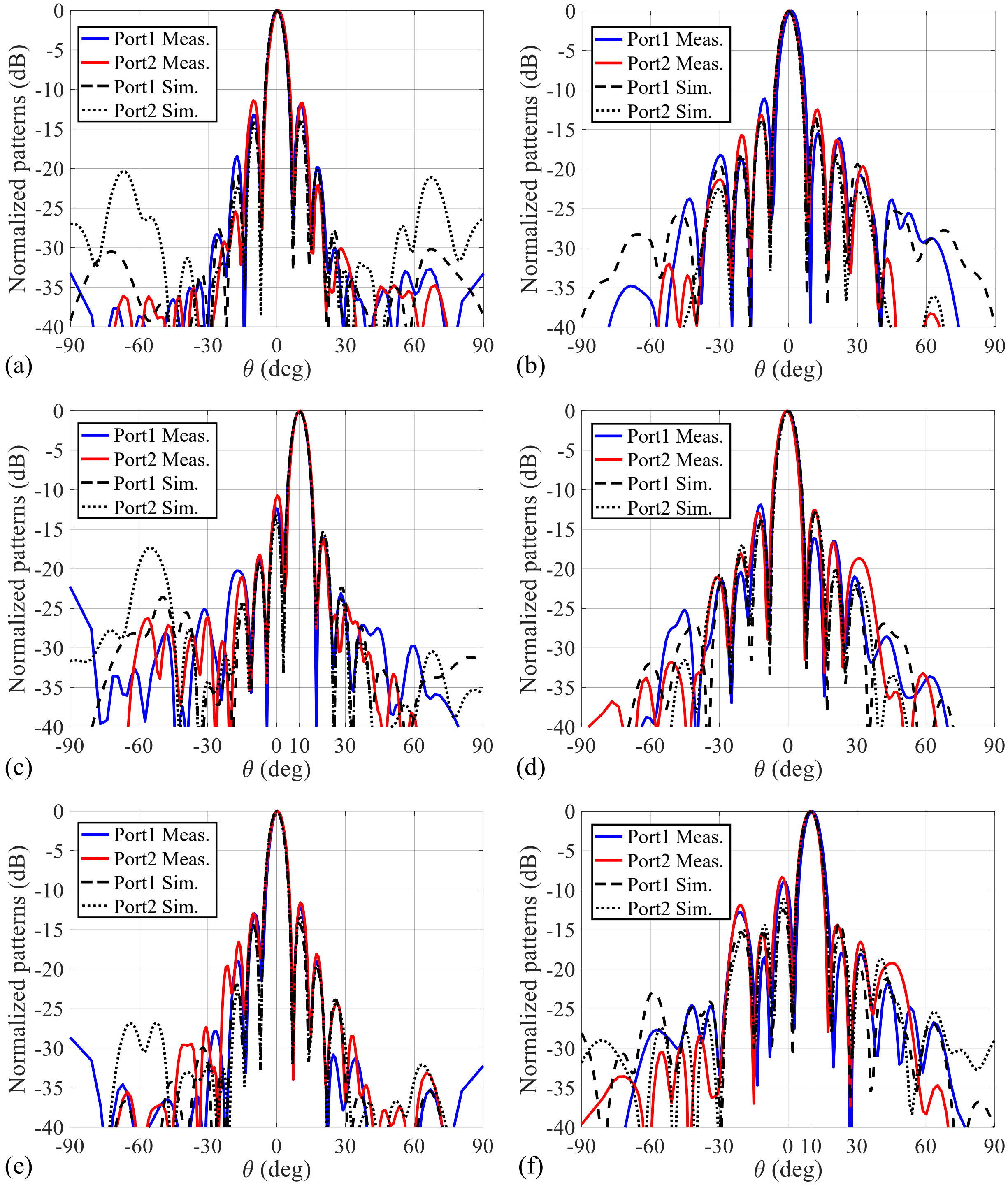

Figure 2.26: Measured co-pol far-field radiation patterns at 28 GHz, when steering to broadside: (a) and (b); $\theta = 10°$, $\phi = 0°$: (c) and (d); and $\theta = 10°$, $\phi = 90°$: (e) and (f). The first column shows the far fields along the $\phi = 0°$ plane while the second column shows the $\phi = 90°$ plane. The reference system is defined in Fig. 2.25. The lens array is displaced by 2.4 mm towards the steering directions for the steering cases.

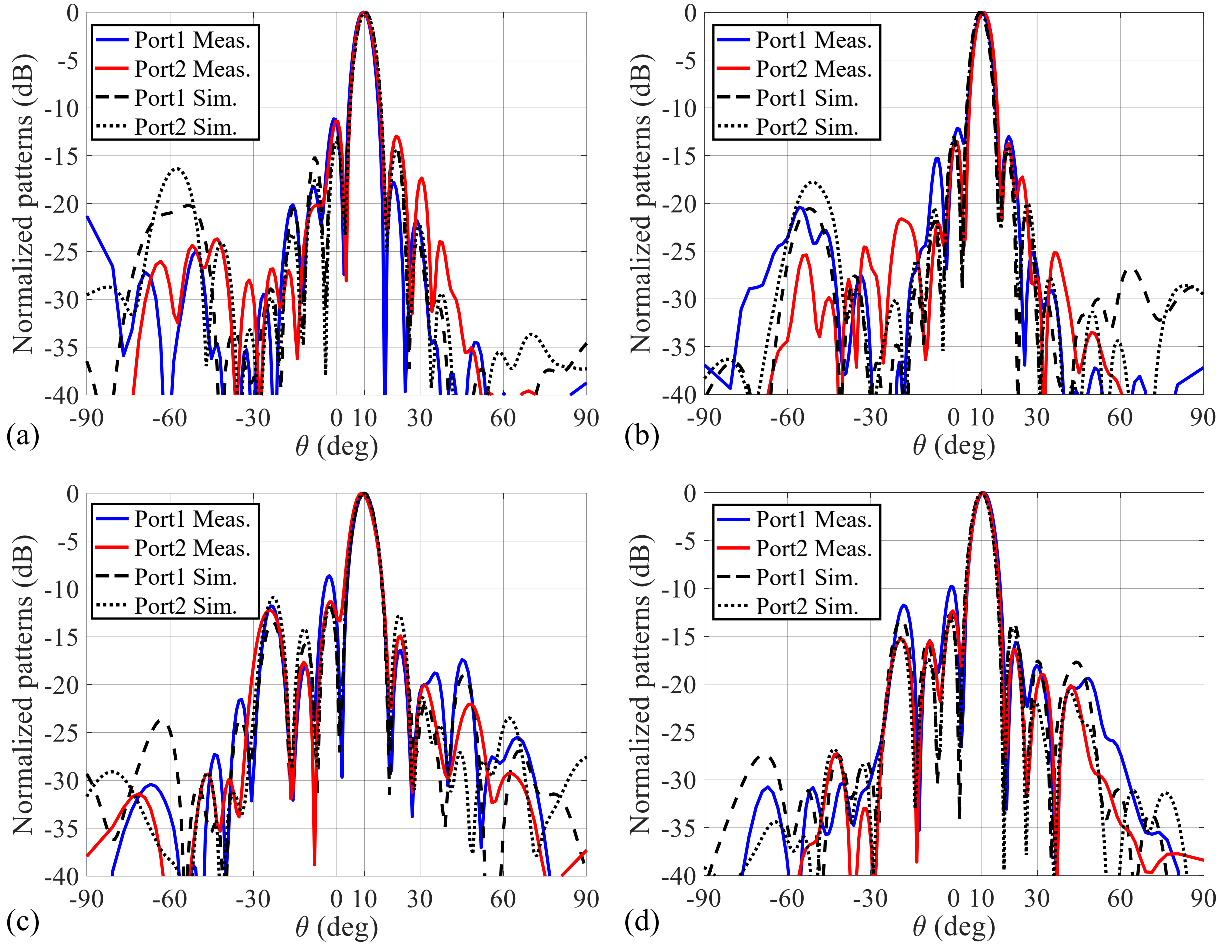

Figure 2.27: Measured co-pol far-field radiation patterns when steering to $\theta = 10°$, $\phi = 0°$ at (a) 26.5 GHz and (b) 29.5 GHz, and to $\theta = 10°$, $\phi = 90°$ at (c) 26.5 GHz and (d) 29.5 GHz. The reference system is defined in Fig. 2.25. The lens array is displaced by 2.4 mm towards the steering directions.

The calibrated gain for all radiation cases is shown in Fig. 2.29(b), 2.29(d), and 2.29(f). In the figures, the simulated broadside gain is above 26.8 dBi over the required frequency band and reaches 27.5 dBi at 28 GHz. Moreover, the scan loss is less than 1 dB when steering to 10°. For the measured gain, the losses in feeding networks (around 3.5 dB) and connectors (around 0.2 dB) are calibrated out. As it can be seen, the calibrated gain of both ports fluctuates significantly in the broadside case, while less in the steering cases. This is possibly associated with the multiple reflections in the measurement setup. For port 1, the agreement is quite good. The broadside gain is above 26.2 dBi and the steering gain is above 26 dBi over the required frequency band. While port 2 performs worse: the gain is above 25.2 dBi at broadside, 25.6 dBi when steering to $\theta = 10°$, $\phi = 0°$, and 24 dBi when steering to $\theta = 10°$, $\phi = 90°$. The gain of port 2 in Fig. 2.29(f) is about 2 dB less than that of port 1 because of the previously mentioned non-radiating elements (adding 1 dB lost in the feeding network). It is worth mentioning that the measurement of the gain (via the near-field power evaluation instead of a far-field calibrated link) can have

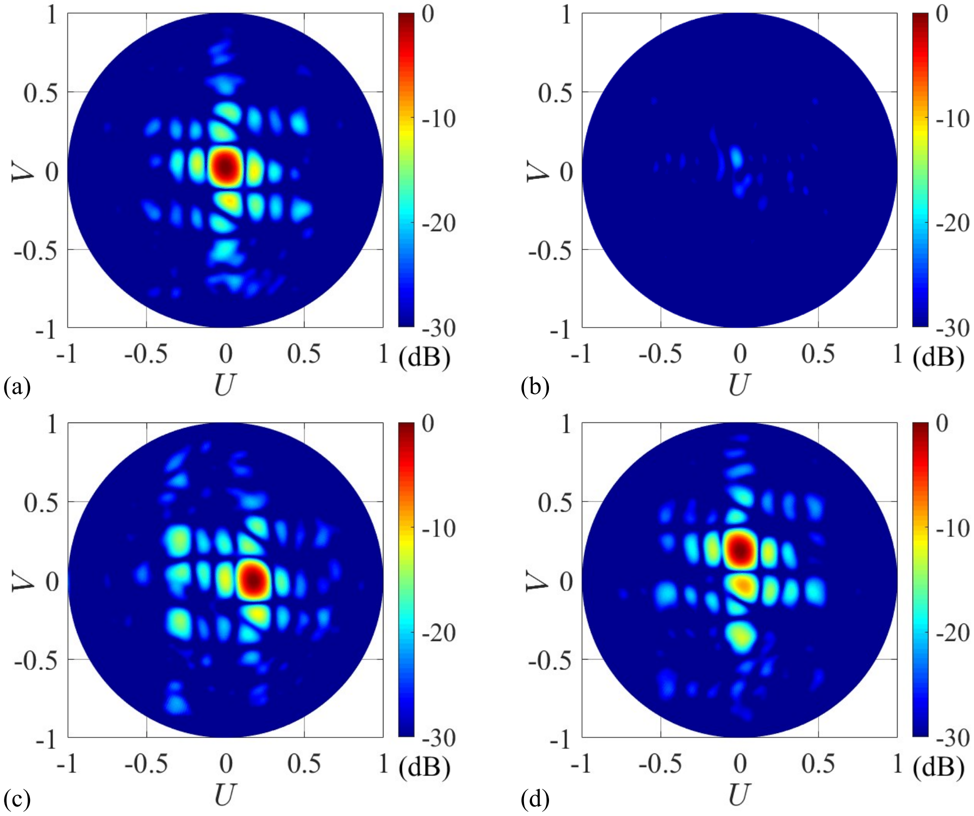

Figure 2.28: Measured 2D far-field radiation patterns of port 1 at 28 GHz: (a) broadside co-pol pattern and (b) cross-pol pattern. Co-pol patterns when steering to (c) $\theta = 10°$, $\phi = 0°$ and (d) $\theta = 10°$, $\phi = 90°$. The reference system is defined in Fig. 2.25. The lens array is displaced by 2.4 mm towards the steering directions for the steering cases.

some inaccuracy due to the multiple reflections. Moreover, the estimation of the losses in the feeding networks is done by considering a microstrip line with uniform impedance and a length approximately the same as the actual implemented networks. This introduces inaccuracy as well.

The measured far-field properties are overall in very good agreement with the simulations. Although port 2 performs a bit worse than port 1, the proposed antenna architecture is well validated. To further improve the prototype performance, the PCBs, lens array, and metal cavity should undergo a better fabrication tuning cycle.

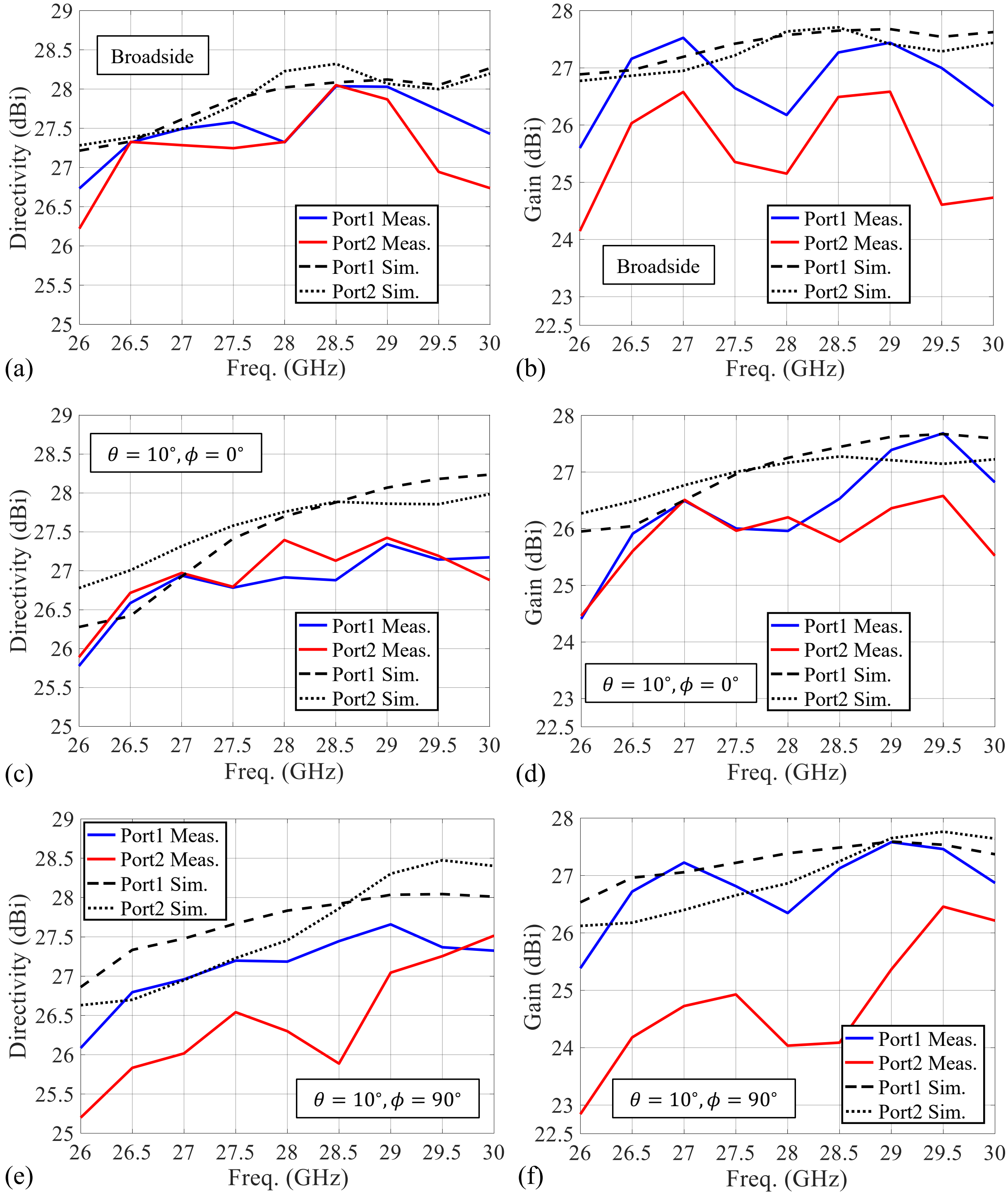

Figure 2.29: Measured directivity when steering to (a) broadside, (c) $\theta = 10°$, $\phi = 0°$, and (e) $\theta = 10°$, $\phi = 90°$; Calibrated gain when steering to (b) broadside, (d) $\theta = 10°$, $\phi = 0°$, and (f) $\theta = 10°$, $\phi = 90°$. The lens array is displaced by 2.4 mm towards the steering directions for the steering cases.

2.6 Conclusion

In this chapter, a dual-polarized high-gain 4×4 scanning lens phased array antenna is designed at 28 GHz for 5G point-to-point communication. The array is hexagonally arranged with $2\lambda_0$ periodicity and the array element is an elliptical lens fed by a LWA feed. The grating lobes caused by the array sparsity are reduced by the directive array element patterns in the broadside and the steering cases. The LWA is designed on a PCB and co-optimized with a HDPE lens via the field correlation method combined with the GO/FO approach, as discussed in Section 2.3. Since the lens is small, the field radiated by the feed is evaluated using the near-field analysis. The optimized lens antenna achieves a wide relative BW of 22.7%, with the aperture efficiency above 75% and 70% for the broadside and the 10° steering cases over the required band, respectively. The array performance evaluated using the proposed method is compared to the CST full-wave simulations, showing excellent agreement. The simulated broadside gain is larger than 26.8 dBi and can reach 27.5 dBi at 28 GHz, with the SLL lower than -13 dB. Moreover, the array is possible to steer up to 20°, with a scan loss lower than 2 dB. The designed array antenna was fabricated and measured, and the measurements validate the proposed antenna architecture. The prototype antenna can achieve 26.2 dBi gain at broadside and 26 dBi gain when steering to 10°, with a 20% relative BW, from 25.1 to 30.7 GHz. If a better fabrication tuning cycle is made, the performance could be further improved. In addition, Appendix A introduces another architecture which integrates the backing reflector into an unique PCB. The simulated performance is shown and the measurements validate the proposed architecture.

Chapter 3

Time-domain Modelling of Ultra-wideband Pulsed Photoconductive Sources and Receivers

Photoconductive antennas (PCAs) can be used to generate and receive THz pulses when excited by pulsed laser sources. Thus they are promising candidates for sensing and imaging applications. In recent years, our group has investigated the modelling of a PCA source using a time-domain (TD) Norton equivalent circuit which is solved using a marching-on-time analysis. In this chapter, firstly, a Norton resistance is proposed to simplify the time-marching evaluation. This resistance can be analytically evaluated, leading to an approximate frequency-domain (FD) Norton circuit. This circuit can also be analytically solved and is very useful for analyzing and designing the impedance matching of a PCA source. Then, a non-dispersive transmission line model is used to analyze a PCA receiver and a similar TD Norton equivalent circuit is derived. Finally, the detected currents in the receiving circuit are reconstructed using stroboscopic sampling of the modelled THz pulses. Both the amplitude and the waveforms of these currents are well evaluated.

3.1 Introduction

The last decades have experienced increasing interests in PCAs for spectroscopy and imaging applications, thanks to their ability to generate and detect THz pulses when excited by pulsed optical sources [6, 42–44, 47, 78, 79]. Examples of systems, often referred to as THz time-domain spectroscopy (THz-TDS) systems, can be found in [52–54, 80–88]. A THz-TDS system mainly consists of a PCA source, a PCA receiver, and an in-between quasi-optical (QO) link where dielectric lenses or reflectors are used to collimate and focus THz pulses.

For a PCA source, realizing an efficient coupling between the photoconductive (PC) material and the antenna has been one of the main challenges, especially when the objective is the maximization of the THz power radiated for given optical power. Moving the attention to the modelling, two types of approaches have been explored for a PCA source: full-wave finite-difference time-domain models [48, 49] and equivalent circuit models [50, 51, 89–98]. We focus on the latter approach since it is more intuitive for designing and optimizing PCAs. Recently, an accurate TD Norton equivalent circuit based on the PC constitutive (Drude) relations combined with an electromagnetic (EM) based derivation was proposed [51]. The photocurrent flowing across the PC gap was solved in TD using a marching-on-time scheme which accounts for the constitutive relations for low-temperature grown gallium arsenide (LT GaAs) [98]. However, since this time-marching evaluation is numerically complex, the TD circuit is not convenient to design a PCA source according to impedance matching.

The amplitude of the THz pulses generated by a PCA source is related to the amplitude of the THz photocurrents in the PC gap [80]. The waveforms of the emitted pulses were evaluated analytically for simple antenna geometries like short dipoles [81]. However, if the transmitting PCA structures are more complex, full-wave simulations need to be used to model these pulses accurately [54, 99]. A transfer function $H(f)$ can be introduced to characterize the QO link between PCAs [52]; but in most cases, it was approximated by the far-field link conditions, e.g., [52–54]. In [81], the transfer function was approximately modelled by a Gaussian-beam formalism instead. However, the effect of the receiving antenna is neglected in the transfer function in all cases.

At the receiver side, the arriving THz pulses induce photocurrents on the PC gap when it is illuminated by laser pulses. The receiver can be modelled by a Thévenin equivalent circuit [52, 88], where the generator was associated with the arriving THz pulses via the approximated transfer function. The Thévenin load was calculated using approximated PC constitutive relations and the detected currents were evaluated using stroboscopic sampling. Since the link between the PCAs has not been accurately modelled, the existing literature only compares the modelled detected currents to measurements using arbitrary units.

In this chapter, we consider a non-dispersive transmission line as the QO link and mainly focus on the TD modelling of a PCA source and a receiver using equivalent circuits. First, we briefly introduce the TD Norton equivalent circuit in [51, 98] and use it to analyze a PCA source. Then we simplify the time-marching evaluation of the constitutive relations by introducing a generator resistance which can be solved analytically with the parameters of the laser source, the PC material, and the gap size. An approximate FD Norton circuit is then modelled using this resistance. This circuit can be used to accurately predict the THz power radiated by its external load; therefore, it is very useful for analyzing and designing the impedance matching for a PCA source. Afterwards, by using the non-dispersive transmission line model, a similar TD Norton equivalent circuit is proposed for the receiver to characterize the photocurrents flowing across the receiving PC gap. These currents are evaluated using the PC constitutive relations. They are then used to evaluate the detected DC currents using the stroboscopic sampling of the modelled THz pulses.

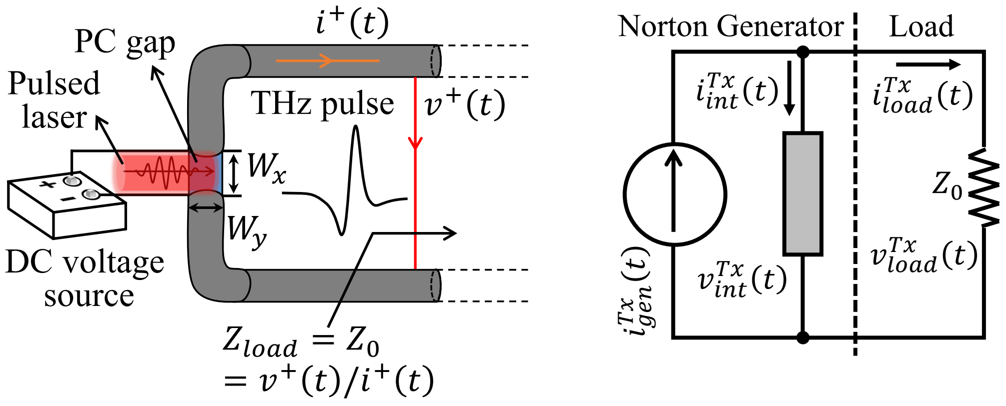

(a) (b)

Figure 3.1: (a) Schematic representation of a transmission line excited by a PC gap which is illuminated by a pulsed laser and biased by a DC voltage source. A pulsed THz forward wave, $[v^+(t), i^+(t)]$, is generated in the transmission line. The red line represents the biasing electric field while the orange line is the electric current in the presence of the laser excitation. $v^+(t)$ is opposed to the biasing electric field. (b) Corresponding TD Norton equivalent circuit used to evaluate the time-evolution of the THz voltage and current, $[v_{load}^{Tx}(t), i_{load}^{Tx}(t)] = [v^+(t), i^+(t)]$.

This chapter is structured as follows: Section 3.2 summarizes the transmission line model and the current components of the TD Norton equivalent circuit for a PCA source. An example of the currents and voltages solved using the time-marching approach is then shown. Moreover, the derivation of the approximate Norton generator resistance is discussed. The radiated energy spectral density and the radiated THz power are evaluated using the proposed Norton resistance and compared to the TD solutions. Section 3.3 describes the TD Norton equivalent circuit for a PCA receiver to calculate the photocurrents induced on the receiving PC gap. The procedure to obtain the detected currents via the stroboscopic sampling is also discussed, with some example solutions.

3.2 Time-domain Norton Equivalent Circuit in Transmission

We first consider the modelling of a PC gap excited in transmission (Tx) and connected to a non-dispersive transmission line with the characteristic impedance of Z_0, as depicted in Fig. 3.1(a). The transmission line is made of two pieces of metal printed on a photosensitive semiconductor which is biased by an external voltage source V_b. A pulsed laser with pulse width of τ_p illuminates the PC gap periodically with a repetition time of T. Within each repetition time, the laser pulse excites the electrons inside the semiconductor from their valence band to the conduction band. In response to the biasing voltage, the freed electrons form a time-varying pulsed current. This current exists roughly during the recombination time τ_c of the PC material and then gradually disappear as the electrons recombine with the holes. For a typical PC material, $\tau_p < \tau_c \ll T$, with τ_c in the order of hundreds of fs. Thus, this very short current can radiate a pulsed field in the THz regime. The generated pulsed THz field propagates along this transmission line as a forward wave with the amplitude of $v^+(t)$ and $i^+(t)$, as depicted in Fig. 3.1(a).

Such structure was first modelled using a Norton equivalent circuit in TD [51] as shown in Fig. 3.1(b). This equivalent circuit is valid to model the THz voltage, $v^{Tx}_{load}(t)$, and current, $i^{Tx}_{load}(t)$, on the PC gap (the Tx superscript indicates the voltage and current are in the transmitting/source PC gap). The forward wave will then be given by the voltage and the current: $v^+(t) = v^{Tx}_{load}(t)$ and $i^+(t) = i^{Tx}_{load}(t)$. This circuit was derived via a rigorous EM formulation that accounts for the constitutive (Drude) relations of the PC material. For the sake of completeness, the current components of the Norton circuit are summarized here:

- The generator current $i^{Tx}_{gen}(t)$ is the impressed current by the laser under a short-circuit gap condition, with a constant biasing voltage V_b. It is calculated using the PC constitutive relation as follows:

$$i^{Tx}_{gen}(t) = \frac{q_e^2}{m_e}\frac{W_yW_z}{W_x}\int_{t_0}^{t} n_p^{Tx}(t,t'')\int_{t''}^{t} e^{-\frac{t-t'}{\tau_s^{Tx}}} V_b dt'dt'', \tag{3.1}$$

  where q_e is the electron charge and m_e is the effective mass of the electrons in the PC material; W_x, W_y, and W_z are the dimensions of the PC gap; t_0 is the laser arrival time; and τ_s^{Tx} is the scattering time of the PC material. $n_p^{Tx}(t,t'')$ is the carrier density generation rate [unit: $1/(m^3s)$]. It represents the average number of electrons in the PC gap volume remaining at time t after being excited at time t'', and it is expressed as follows:

$$n_p^{Tx}(t,t'') = \frac{1}{W_xW_yW_z}\frac{\widetilde{P}^{Tx}_{opt}}{hf_c}\frac{T}{\tau_p}\sqrt{\frac{4ln2}{\pi}}e^{-4ln2\left(\frac{t''}{\tau_p}\right)^2}e^{-\frac{t-t''}{\tau_c^{Tx}}}. \tag{3.2}$$

  Here, h is the Planck constant, f_c is the laser operation frequency, and $\widetilde{P}^{Tx}_{opt}$ is the average optical power of the laser absorbed by the PC gap.

- The internal current $i^{Tx}_{int}(t)$ is the current flowing on the generator load branch. It ensures that the time-varying THz voltage $v^{Tx}_{int}(t) = v^{Tx}_{load}(t)$ verifies the constitutive relation. It can be evaluated as follows:

$$i^{Tx}_{int}(t) = \frac{q_e^2}{m_e}\frac{W_yW_z}{W_x}\int_{t_0}^{t} n_p^{Tx}(t,t'')\int_{t''}^{t} e^{-\frac{t-t'}{\tau_s^{Tx}}} v^{Tx}_{int}(t')dt'dt''. \tag{3.3}$$

  Note that this expression is the same as (3.1) except V_b is replaced by $v^{Tx}_{int}(t)$.

- The load current $i^{Tx}_{load}(t)$ represents the THz current flowing across the external load. It is thus associated with the THz radiation. The constitutive relation in this branch is given by the transmission line in Fig. 3.1(a). Assuming an infinite line, the load impedance seen from the generator will correspond to the transmission line characteristic impedance, Z_0. Then the current-voltage relation is $i_{load}^{Tx}(t) = v_{load}^{Tx}(t)/Z_0$, which is purely real.

The relations in (3.1) and (3.3) are non-linear as they depend on the laser excitation starting at t_0. Accordingly, a marching-on-time scheme was implemented to solve the time evolution of $v_{load}^{Tx}(t)$ and $i_{load}^{Tx}(t)$, as discussed in [98]. This method discretizes the involved currents and voltages in time and solves them progressively using the previously explained constitutive relations. Once the time evolutions of $v_{load}^{Tx}(t)$ and $i_{load}^{Tx}(t)$ are found, the instantaneous power delivered to the load, or carried by the THz forward wave in the present example, can be calculated as $p_{load}^{Tx}(t) = i_{load}^{Tx}(t)v_{load}^{Tx}(t)$. The average THz power over the laser repetition time is then

$$\widetilde{P}_{load}^{Tx} = \frac{1}{T}\int_{t_0}^{t_0+T} p_{load}^{Tx}(t)dt. \tag{3.4}$$

3.2.1 Example Solutions of the Circuit

An example of the solved currents and voltages is shown in Fig. 3.2. Here we consider LT GaAs ($\varepsilon_r = 12.94$) as the PC material, with a typical gap volume of 10 µm ×10 µm ×2 µm, biased by $V_b = 30$ V. The material is characterized by a scattering and recombination time of $\tau_s^{Tx} = 2$ fs and $\tau_c^{Tx} = 700$ fs, respectively. The transmission line impedance is assumed as $Z_0 = 70\ \Omega$. The pulsed laser operates at $f_c = 384.6$ THz (wavelength of 780 nm) and has a width of $\tau_p = 100$ fs and a repetition time of $T = 12.5$ ns. This laser behaves like a Gaussian beam with the full width at half maximum (FWHM) of 10 µm and the average optical power absorbed by the gap of $\widetilde{P}_{opt}^{Tx} = 30$ mW. These parameters are relevant for the measurements that will be discussed in Section 4.3. In Fig. 3.2(a), when a laser pulse arrives, the generator current $i_{gen}^{Tx}(t)$ starts to increase and then it gradually drops due to the recombination process. The time-varying THz current $i_{load}^{Tx}(t)$ in Fig. 3.2(b) shows the same behavior as $i_{gen}^{Tx}(t)$ and its waveform is similar to that of $i_{gen}^{Tx}(t)$. In Fig. 3.2(c), the time-varying voltage $v_{load}^{Tx}(t)$ behaves similarly to $i_{load}^{Tx}(t)$ and its amplitude is $i_{load}^{Tx}(t) \cdot Z_0$. This voltage is opposite to the biasing voltage (due to the movement of the free electrons). Therefore, the net voltage on the PC gap is $v_{gap}^{Tx}(t) = V_b - v_{load}^{Tx}(t)$ which is also shown in the figure. Note that $v_{gap}^{Tx}(t)$ is not the output voltage in the circuit since the proposed Norton circuit does not model the DC components [51]. In the same figure, an example with much higher optical power, $\widetilde{P}_{opt}^{Tx} = 160$ mW, is also shown. It can be observed that the amplitude of $i_{gen}^{Tx}(t)$ is proportional to $\widetilde{P}_{opt}^{Tx}$ and its waveform remains the same. The amplitude of $i_{load}^{Tx}(t)$ and $v_{load}^{Tx}(t)$ also increases as $\widetilde{P}_{opt}^{Tx}$ increases; however, their waveforms start to get distorted when $\widetilde{P}_{opt}^{Tx}$ is very high and $v_{gap}^{Tx}(t)$ almost reaches zero value. This effect is related to the saturation of the THz power, $\widetilde{P}_{load}^{Tx}$, being generated.

Fig. 3.3 shows the power delivered to the transmission line, $\widetilde{P}_{load}^{Tx}$ (solid curves), versus the laser optical power, $\widetilde{P}_{opt}^{Tx}$. For this case, we observe that when $\widetilde{P}_{opt}^{Tx}$ is high, $\widetilde{P}_{load}^{Tx}(Z_0 =$

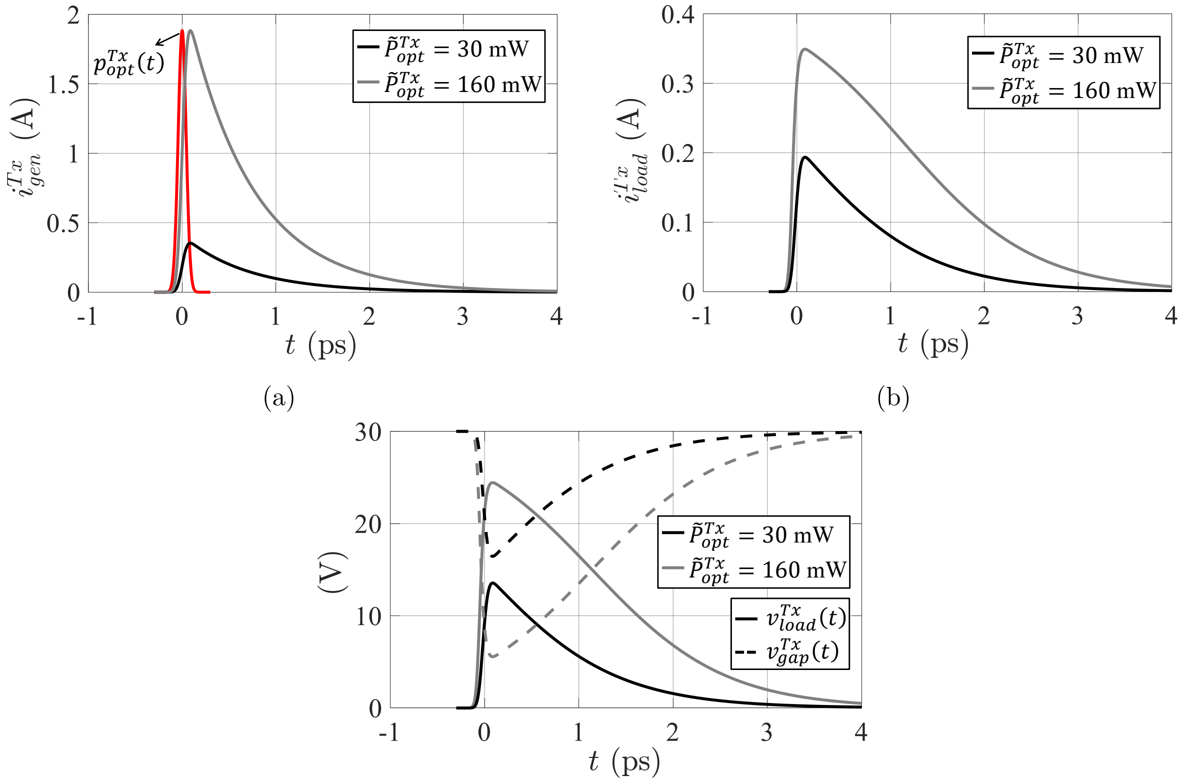

(a) (b)

(c)

Figure 3.2: (a) Norton generator current $i_{gen}^{Tx}(t)$. The laser pulse is also shown with its amplitude normalized to that of $i_{gen}^{Tx}(t)$. (b) Time-varying current $i_{load}^{Tx}(t)$ on the load. (c) Corresponding time-varying voltage $v_{load}^{Tx}(t)$ on the load. The gap voltage $v_{gap}^{Tx}(t)$ is also shown. Here we consider two optical power levels: $\widetilde{P}_{opt}^{Tx} = 30$ mW and 160 mW. The biasing voltage is $V_b = 30$ V and the load impedance is $Z_0 = 70\ \Omega$. $\tau_c^{Tx} = 700$ fs and $\tau_s^{Tx} = 2$ fs.

70 Ω) starts to saturate. This effect can be well explained by the used Norton equivalent circuit in terms of the impedance matching. If we apply Fourier transform (FT) on the TD current and voltage in the generator load branch from Fig. 3.1(b), we obtain their FD representation: $I_{int}^{Tx}(f)$ and $V_{int}^{Tx}(f) = V_{load}^{Tx}(f)$. We can now evaluate the internal generator impedance as $Z_{int}^{Tx}(f) = V_{int}^{Tx}(f)/I_{int}^{Tx}(f)$. This impedance is shown in Fig. 3.4 for the same case as in Fig. 3.2. When the laser optical power $\widetilde{P}_{opt}^{Tx}$ is low; see Fig. 3.4(a), $Real[Z_{int}^{Tx}(f)]$ is comparable to Z_0 (70 Ω). Thus for low power levels $\widetilde{P}_{load}^{Tx}$ is increasing linearly in the scale shown in Fig. 3.3. As $\widetilde{P}_{opt}^{Tx}$ increases to 160 mW; see Fig. 3.4(b), $Z_{int}^{Tx}(f)$ drops significantly and $Real[Z_{int}^{Tx}(f)] < Z_0$. Thus Z_0 cannot match with $Z_{int}^{Tx}(f)$ and $\widetilde{P}_{load}^{Tx}(Z_0 = 70\ \Omega)$ does not follow the same linear growth in Fig. 3.3.

We also calculate $Z_{int}^{Tx}(f)$ for other two different values of Z_0: 20 Ω and 300 Ω, plotted in Fig. 3.4. For very low Z_0, since it is always lower or comparable to $Z_{int}^{Tx}(f)$ below $\widetilde{P}_{opt}^{Tx} = 160$ mW, $\widetilde{P}_{load}^{Tx}$ does not show any power saturation (see the red curve in Fig. 3.3). On the other hand, for very high Z_0, it cannot match with $Z_{int}^{Tx}(f)$ even at low power level

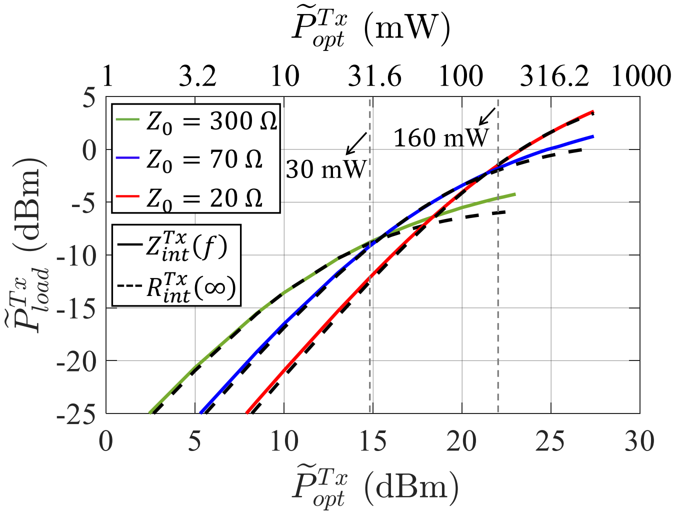

Figure 3.3: Power delivered to the load $\widetilde{P}_{load}^{Tx}$ versus the laser optical power on the gap, $\widetilde{P}_{opt}^{Tx}$, when $V_b = 30$ V for different loading conditions. The solid curves correspond to the results of the time-marching solution of the constitutive relations whereas the dotted curves correspond to the results calculated using the analytical generator resistance $R_{int}^{Tx}(\infty)$.

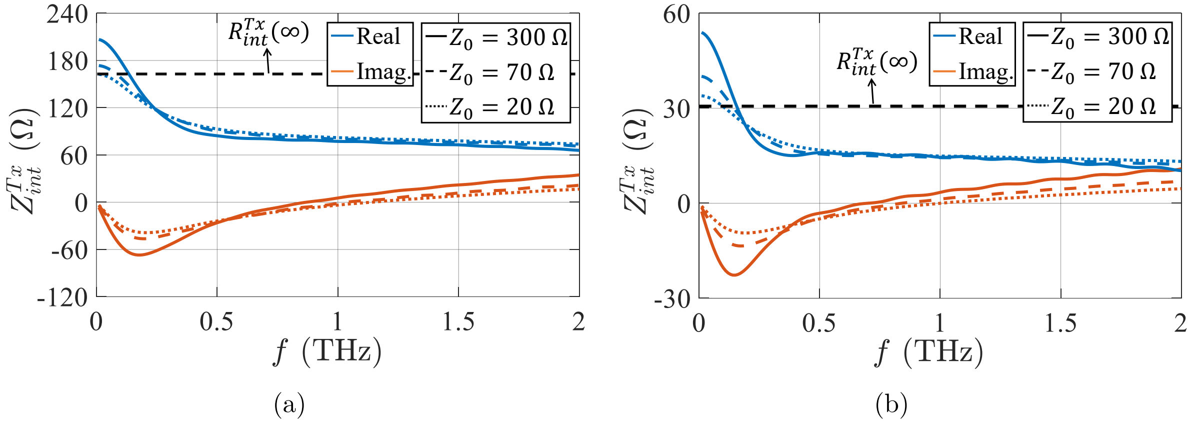

(a)

(b)

Figure 3.4: Norton generator impedance $Z_{int}^{Tx}(f)$ when three values of the the load impedance are used: $Z_0 = 20\ \Omega$, $70\ \Omega$, and $300\ \Omega$. The optical power $\widetilde{P}_{opt}^{Tx}$ is (a) 30 mW and (b) 160 mW. The biasing voltage is $V_b = 30$ V. In the same figures, the analytical generator resistance $R_{int}^{Tx}(\infty)$ calculated using (3.11) is also plotted for reference.

as shown in Fig. 3.4(a), and thus $\widetilde{P}_{load}^{Tx}$ is already saturated at $\widetilde{P}_{opt}^{Tx} = 30$ mW, as shown by the green curve in Fig. 3.3. Therefore, the impedance matching is directly associated with the power saturation and should be considered when designing the load impedance Z_0. In our laboratory system, $\widetilde{P}_{opt}^{Tx}$ has a limit of 80 mW; therefore, we designed the PCA with an impedance close to 70 Ω to achieve the optimal delivered power between 0-80 mW. To achieve such an optimal design, one must use the marching-on-time method to iteratively calculate $Z_{int}^{Tx}(f)$ for different $\widetilde{P}_{opt}^{Tx}$ and Z_0 until the best impedance matching is achieved. Unfortunately, such a process is time-consuming and not intuitive.

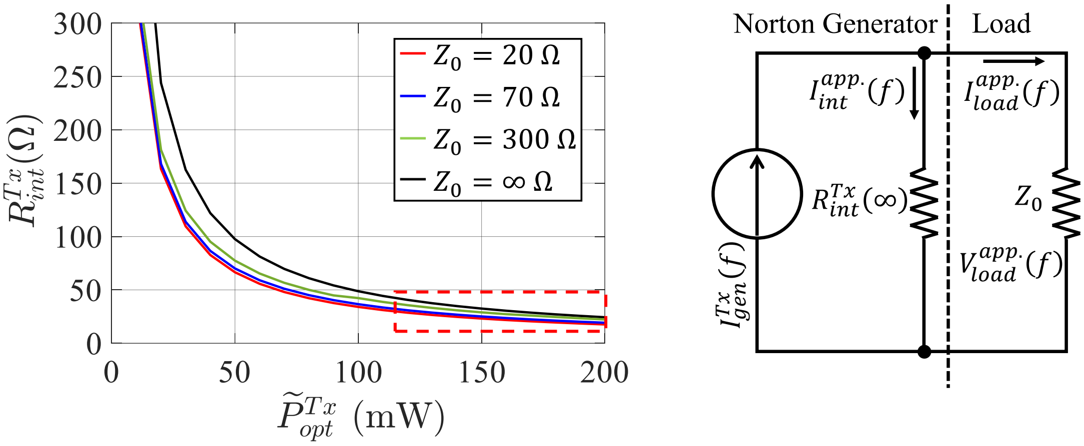

(a) (b)

Figure 3.5: (a) Numerical solution of $R_{int}^{Tx}(Z_0)$ calculated using (3.6) versus $\widetilde{P}_{opt}^{Tx}$. We consider $Z_0 = 20$ Ω, 70 Ω, and 300 Ω. The dashed red box indicates the power saturation region. (b) Proposed FD Norton equivalent circuit with constant generator resistance $R_{int}^{Tx}(\infty)$ calculated using (3.11). Its value is shown in (a) by the black curve.

3.2.2 Norton Resistance

To better consider the impedance matching and simplify the numerical time-marching solution of the TD Norton circuit, we approximate the calculation of the non-linear constitutive relation of the internal generator current in (3.3) as a simple resistance. To achieve this, we introduce an auxiliary quantity defined as the *pseudo energy* dissipated in the Norton generator load branch, which can be evaluated as follows:

$$E_{pseudo}^{Tx}(Z_0) = \int_{t_0}^{t_0+T} v_{int}^{Tx}(t, Z_0) i_{int}^{Tx}(t, Z_0) dt. \tag{3.5}$$

Here, E_{pseudo}^{Tx} is indicated as pseudo energy because it does not represent the actual energy dissipated in the PC gap since the proposed Norton circuit does not model the DC components [51]. It is convenient to introduce an equivalent generator resistance $R_{int}^{Tx}(Z_0)$ that is constant in time and would provide the same energy dissipation as in the internal generator branch in (3.5):

$$\begin{aligned} E_{pseudo}^{Tx}(Z_0) &= \int_{t_0}^{t_0+T} R_{int}^{Tx}(Z_0) \left[i_{int}^{Tx}(t, Z_0)\right]^2 dt \\ \Rightarrow R_{int}^{Tx}(Z_0) &= \frac{\int_{t_0}^{t_0+T} v_{int}^{Tx}(t, Z_0) i_{int}^{Tx}(t, Z_0) dt}{\int_{t_0}^{t_0+T} \left[i_{int}^{Tx}(t, Z_0)\right]^2 dt}. \end{aligned} \tag{3.6}$$

Fig. 3.5(a) shows the values of $R_{int}^{Tx}(Z_0)$ calculated using the time-marching method versus the laser optical power $\widetilde{P}_{opt}^{Tx}$ when different loads are considered, i.e., $Z_0 = 20\ \Omega$, 70 Ω, and 300 Ω. The corresponding $R_{int}^{Tx}(Z_0)$ is comparable to $Z_{int}^{Tx}(f)$ in Fig. 3.4 at low frequencies. Moreover, the curves of $R_{int}^{Tx}(Z_0)$ for all Z_0 values are quite close to each other so we can assume that $R_{int}^{Tx}(Z_0)$ is independent from the load value. It suggests that we can solve the circuit for $Z_0 = \infty$. In this case, the load plays no role and the voltage to the current relation can be evaluated analytically without the marching-on-time procedures, using the approximations discussed in the following.

Very Short Carrier Scattering Time

When the carrier scattering time τ_s^{Tx} is very short (for LT GaAs, τ_s^{Tx} is in the order a few fs), the exponential term in (3.3), i.e., $e^{-(t-t^{'})/\tau_s^{Tx}}$, decreases very rapidly with respect to the voltage evolution $v_{int}^{Tx}(t')$. In such situation, we can assume that $v_{int}^{Tx}(t')$ is constant in the time interval where the exponential term is significantly different from zero, so that the inner integral in (3.3) can be approximated as follows:

$$\int_{t''}^{t} e^{-\frac{t-t'}{\tau_s^{Tx}}} v_{int}^{Tx}(t')dt' \cong v_{int}^{Tx}(t)\int_{t''}^{t} e^{-\frac{t-t'}{\tau_s^{Tx}}}dt' = v_{int}^{Tx}(t)\tau_s^{Tx}\left(1-e^{-\frac{t-t''}{\tau_s^{Tx}}}\right). \tag{3.7}$$

Accordingly, the current $i_{int}^{Tx}(t)$ in (3.3) can be approximated as follows:

$$i_{int}^{Tx}(t) \cong \frac{\tau_s^{Tx} q_e^2}{m_e}\frac{W_y W_z}{W_x} v_{int}^{Tx}(t)\int_{t_0}^{t} n_p^{Tx}(t,t'')\left(1-e^{-\frac{t-t''}{\tau_s^{Tx}}}\right)dt''. \tag{3.8}$$

If we next consider LT GaAs as the photoconductor material, i.e., we assume $\tau_c^{Tx} \gg \tau_s^{Tx}$, (3.8) can be further approximated as follows:

$$i_{int}^{Tx}(t) \cong \frac{\tau_s^{Tx} q_e^2}{m_e}\frac{T}{W_x^2}\frac{\widetilde{P}_{opt}^{Tx}}{hf_c} v_{int}^{Tx}(t)\int_{t_0}^{t} \frac{1}{\tau_p}\sqrt{\frac{4ln2}{\pi}}e^{-4ln2\left(\frac{t''}{\tau_p}\right)^2}\left(e^{-\frac{t-t''}{\tau_c^{Tx}}} - e^{-\frac{t-t''}{\tau_s^{Tx}}}\right)dt''. \tag{3.9}$$

Equation (3.9) is similar to the corresponding expression (7) in [100], but here (3.9) retains the dependence of the current at time t that accounts for the history of the voltage on the gap.

Instantaneous Laser Pulses

The integral in (3.9) can be easily evaluated numerically; however, to acquire deeper physical understanding, one can further assume that the laser pulse duration is instantaneous, i.e., $\tau_p \to 0$. Under this hypothesis, the term $\frac{1}{\tau_p}\sqrt{\frac{4ln2}{\pi}}e^{-4ln2\left(\frac{t''}{\tau_p}\right)^2}$ becomes a Dirac delta function $\delta(t'')$. Thus, for $t > 0$, $i_{int}^{Tx}(t)$ can be written as follows:

$$i_{int}^{Tx}(t) \cong \mu_{dc}^{Tx} q_e \frac{T}{W_x^2}\frac{\widetilde{P}_{opt}^{Tx}}{hf_c} v_{int}^{Tx}(t)\left(e^{-\frac{t}{\tau_c^{Tx}}} - e^{-\frac{t}{\tau_s^{Tx}}}\right), \tag{3.10}$$

where $\mu_{dc}^{Tx} = \tau_s^{Tx} q_e / m_e$ is the DC mobility of the PC material. It is worth noting that in the time interval $t = (2\tau_s^{Tx}, \infty)$, $e^{(-t/\tau_s^{Tx})}$ in (3.10) becomes negligible with respect to $e^{(-t/\tau_c^{Tx})}$ since we assume $\tau_c^{Tx} \gg \tau_s^{Tx}$. Thus the value of $i_{int}^{Tx}(t)$ is mainly related to the recombination rate of the excited electrons.

For the LT GaAs discussed in this paper, the single integral approximation that leads to (3.9) is well justified, while the approximation resulting in (3.10) is rougher since the pulse duration could be comparable to the recombination time. Nevertheless, expression (3.10) can be used to estimate the current $i_{int}^{Tx}(t, Z_0)$ in (3.6) to obtain $R_{int}^{Tx}(Z_0)$. Here, since $R_{int}^{Tx}(Z_0)$ is almost independent from the load, we can assume that $Z_0 = \infty$. This corresponds to an open-circuit case and thus the voltage on the gap is assumed to remain constant as equal to the biasing voltage V_b. By substituting $v_{int}^{Tx}(t) = v_{load}^{Tx}(t) = V_b$ (implying no biasing field screening) into (3.10), we obtain an analytical expression for $i_{int}^{Tx}(t)$. Then, the Norton resistance in (3.6) can be directly calculated with the parameters of the laser source, the PC material, and the gap size as follows:

$$R_{int}^{Tx}(\infty) = \frac{2hf_c W_x^2}{\mu_{dc}^{Tx} q_e T \widetilde{P}_{opt}^{Tx}} \frac{\tau_c^{Tx} + \tau_s^{Tx}}{\tau_c^{Tx} - \tau_s^{Tx}}. \tag{3.11}$$

The use of this resistance simplifies the evaluation of the PC constitutive relation and introduces a Norton equivalent circuit in FD as shown in Fig. 3.5(b). The notations of the currents and the voltage have additional "app." superscripts indicating that they have been approximated. Since the generator current $I_{gen}^{Tx}(f)$ can also be analytically calculated, as discussed in [97], the whole circuit in Fig. 3.5(b) can be solved analytically without any time-marching evaluation. A similar idea was discussed in [101] for the materials design.

This resistance is plotted in Fig. 3.5(b) by the black curve which is compared to the results $R_{int}^{Tx}(Z_0)$ numerically calculated using (3.6). We can notice that $R_{int}^{Tx}(\infty)$ is close to the numerical evaluation of $R_{int}^{Tx}(Z_0 = 300\Omega)$. Moreover, as $\widetilde{P}_{opt}^{Tx}$ increases, $R_{int}^{Tx}(\infty)$ tends to converge to a constant, which indicates the power saturation via the impedance mismatched to a load. Therefore, we should design our load before the saturation region shown by the dashed red box in Fig. 3.5(a) . In the case of $Z_0 = 70\ \Omega$, the impedance-matched condition can be fulfilled when $\widetilde{P}_{opt}^{Tx} \approx 50$ mW which is before the saturation, as shown in Fig. 3.3.

To evaluate the applicability of the circuit in Fig. 3.5(b), we can calculate the THz power generated in the load and compare it to the numerical results (time-marching results) in Fig. 3.3. As expected, the agreement is excellent before power saturation. This is because $\widetilde{P}_{load}^{Tx}$ is highly dominated by the low-frequency components where $Z_{int}^{Tx}(f)$ is comparable to $R_{int}^{Tx}(\infty)$, as shown in Fig. 3.4. However, when $\widetilde{P}_{opt}^{Tx}$ increases to the level where saturation occurs and Z_0 is high, it becomes more inaccurate to approximate $Z_{int}^{Tx}(f)$ by $R_{int}^{Tx}(\infty)$. As the result, the numerical evaluation of $\widetilde{P}_{load}^{Tx}$ ($Z_0 = 300\ \Omega$) in Fig. 3.3 is higher for high $\widetilde{P}_{opt}^{Tx}$.

From Fig. 3.4 we can also find that $R_{int}^{Tx}(\infty)$ cannot well approximate the high-frequency parts of $Z_{int}^{Tx}(f)$. Therefore, the energy spectral density could be different when evaluated

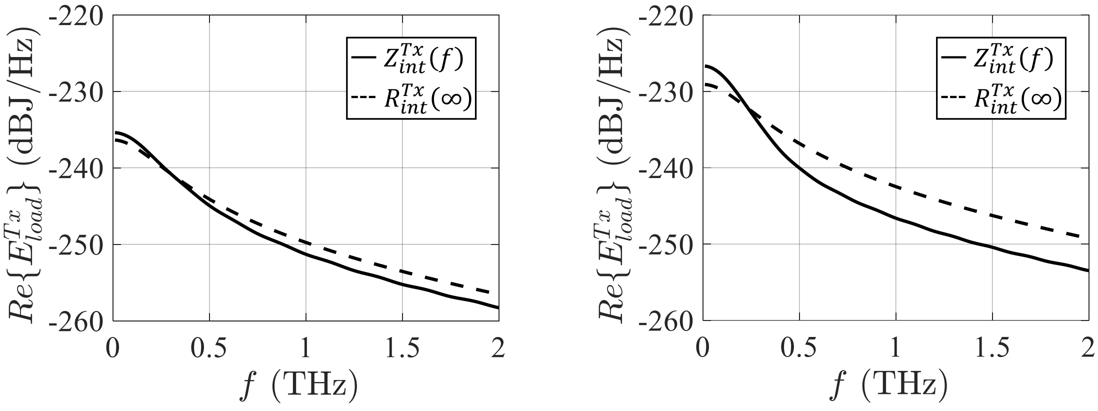

(a) (b)

Figure 3.6: Energy spectral density of the load when $\widetilde{P}_{opt}^{Tx}$ is (a) 30 mW and (b) 160 mW, $V_b = 30$ V, and $Z_0 = 70\ \Omega$. The results are evaluated using the Norton circuits in Tx in Fig. 3.1(b) and Fig. 3.5(b).

using the Norton circuits in Fig. 3.1(b) and Fig. 3.5(b). Fig. 3.6(a) and 3.6(b) show the energy spectral density $E_{load}^{Tx}(f) = |I_{load}^{Tx}(f)|^2 Z_0$ for $Z_0 = 70\ \Omega$ when $\widetilde{P}_{opt}^{Tx} = 30$ mW and 160 mW, respectively. When $\widetilde{P}_{opt}^{Tx}$ is low [see Fig. 3.6(a)], the agreement is very good until 0.7 THz where most of the energy is contained. Whereas at higher frequencies, the spectrum calculated from $R_{int}^{Tx}(\infty)$ is becoming different (2 dB at 2 THz). However, when $\widetilde{P}_{opt}^{Tx}$ increases and enters the saturation region, we can observe more significant difference between the spectra, as shown in Fig. 3.6(b). This is because $Z_{int}^{Tx}(f)$ varies more dramatically with high $\widetilde{P}_{opt}^{Tx}$, as shown in Fig. 3.4(b). Thus, we can use $R_{int}^{Tx}(\infty)$ to characterize the spectra in the relevant frequency band only before the power saturation.

3.3 Norton Equivalent Circuit in Reception

In this section, we present the modeling of the current detected at a receiving PC gap via its corresponding Norton equivalent circuit. We consider the problem shown in Fig. 3.7(a) where a THz forward pulse wave $[v^+(t), i^+(t)]$ is propagating along an infinite transmission line. This wave can be, for instance, the one generated by the source geometry in Fig. 3.1(a). The transmission line is loaded with a PC gap excited by a pulsed laser. In this case, the derivation of the generator of the Norton circuit is standard by evaluating the transmission line when the load is short-circuited, as shown in Fig. 3.7(c). At $z = 0$, the voltage amplitude of the forward wave and that of the reflected wave have the relation $v^+(t) = -v^-(t)$. Therefore, the generator current $i_{gen}^{Rx}(t)$ (with the Rx superscript used to indicate the receiver) is the same as the total (short-circuited) current at $z = 0$, i.e., $i_{gen}^{Rx}(t) = i_{sc}(t, z = 0)$, which is calculated as follows:

$$i_{gen}^{Rx}(t) = 2i^+(t) = 2v^+(t)/Z_0, \tag{3.12}$$

and the generator load is the impedance of the transmission line, i.e., Z_0.

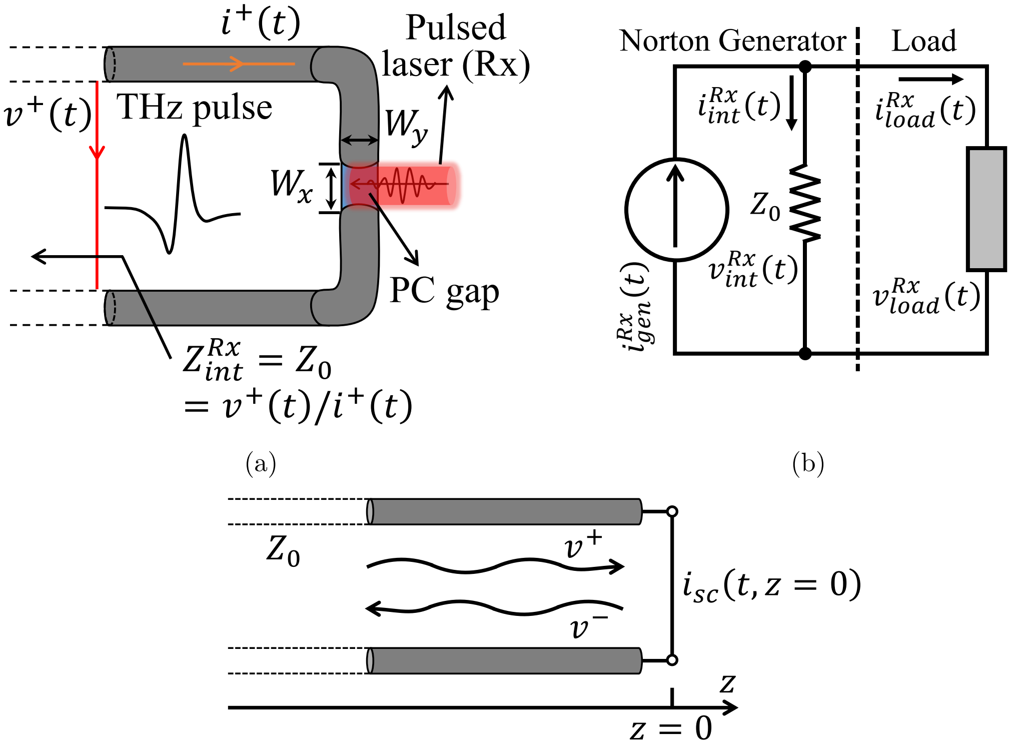

(a) (b)

(c)

Figure 3.7: (a) Schematic representation of a transmission line loaded with a PC gap. It is excited by a laser pulse, and at the same time, by a THz forward wave, $[v^+(t), i^+(t)]$, propagating along the transmission line. (b) Corresponding TD Norton equivalent circuit used to evaluate the time-evolution of the THz voltage and current, $[v_{load}^{Rx}(t), i_{load}^{Rx}(t)]$. (c) Short-circuited transmission line model. $v^-(t)$ represents the reflected wave and $i_{sc}(t, z = 0) = 2v^+(t)/Z_0$ is the total current at $z = 0$.

The laser pulses in Rx illuminate the PC gap periodically and free the electrons inside the gap. If the incoming THz wave is synchronized in time with a laser pulse, this wave will induce a time-varying current flowing across the PC gap. Such process can be modelled by a load that has a time-varying constitutive relation related to the pulsed illumination on the PC gap. Accordingly, a TD Norton equivalent circuit is derived for the receiving PCA and is shown in Fig. 3.7(b), where the load current $i_{load}^{Rx}(t)$ is evaluated using the Drude constitutive relation of the PC material:

$$i_{load}^{Rx}(t) = \frac{q_e^2}{m_e} \frac{W_y W_z}{W_x} \int_{t_1}^{t} n_p^{Rx}(t, t'') \int_{t''}^{t} e^{-\frac{t-t'}{\tau_s^{Rx}}} v_{load}^{Rx}(t') dt' dt'', \tag{3.13}$$

where t_1 is the time when the laser pulse arrives, and t is the current time. $n_p^{Rx}(t, t'')$ has the same expression as (3.2) but with $\widetilde{P}_{opt}^{Rx}$ as the optical power. The current and voltage in the generator load branch are indicated as $i_{int}^{Rx}(t)$ and $v_{int}^{Rx}(t) = v_{load}^{Rx}(t)$, respectively. The constitutive relation in this branch is given by the transmission line as $i_{int}^{Rx}(t) = v_{int}^{Rx}(t)/Z_0$.

The load current $i_{load}^{Rx}(t)$ exists only when the periodic THz waves are synchronized with

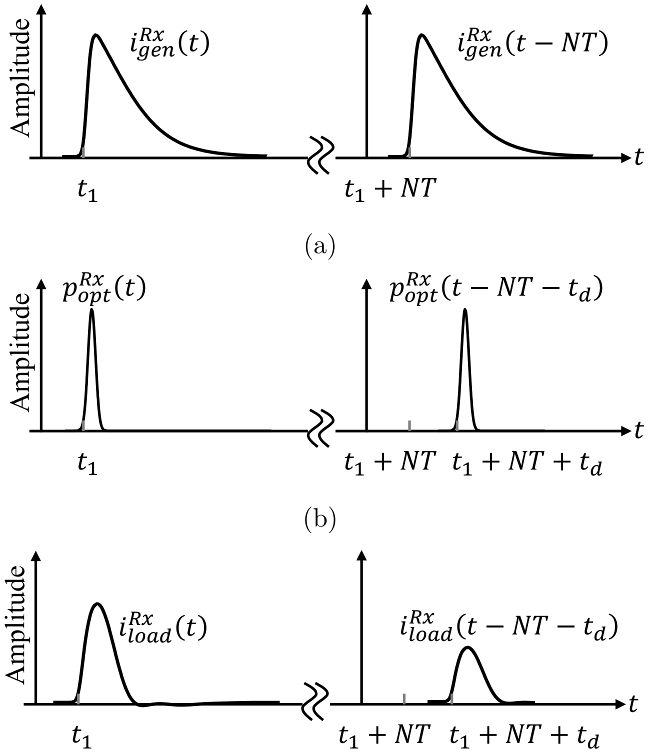

(a)

(b)

(c)

Figure 3.8: Time evolution of the pulses in the Rx circuit for two periods: (a) generator currents $i_{gen}^{Rx}(t)$, (b) optical power pulses $p_{opt}^{Rx}(t)$, and (c) currents in the PC gap $i_{load}^{Rx}(t)$.

the laser pulses in Rx. Fig. 3.8 illustrates such synchronization for different time-delayed laser pulses. Let us first focus on the left column of the figure: a THz wave induces $i_{gen}^{Rx}(t)$ at time t_1, as shown in Fig. 3.8(a). We then assume the laser pulse $p_{opt}^{Rx}(t)$ is synchronized to arrive at the PC gap at also t_1, as depicted in Fig. 3.8(b). Since the amplitude of $i_{gen}^{Rx}(t)$ reaches its maximum at the laser arrival, we obtain $i_{load}^{Rx}(t)$ with also a high amplitude after t_1; see Fig. 3.8(c). Then we examine the right column of Fig. 3.8 when several repetition time has passed and the time is at $t_1 + NT$ ($N = 1, 2$). The periodic THz wave induces $i_{gen}^{Rx}(t - NT)$ shown in Fig. 3.8(a). At the same time, we add additional time delay t_d to the laser pulse to synchronize it with $i_{gen}^{Rx}(t - NT)$ at different time $t_1 + NT + t_d$; see Fig. 3.8(b). The amplitude of $i_{gen}^{Rx}(t - NT)$ already starts to drop when the laser arrives; therefore, a lower $i_{load}^{Rx}(t - NT - t_d)$ is obtained; see Fig. 3.8(c). Of course, if the laser pulse is synchronized with the tail of $i_{gen}^{Rx}(t)$, $i_{load}^{Rx}(t)$ will be close to zero.

3.3.1 Marching-on-time Solution of the Norton Circuit in Reception

Let us then solve the proposed TD Norton circuit for a specific period of the laser pulses and a specific time delay for the laser pulse, t_d. We impose the continuity of the currents

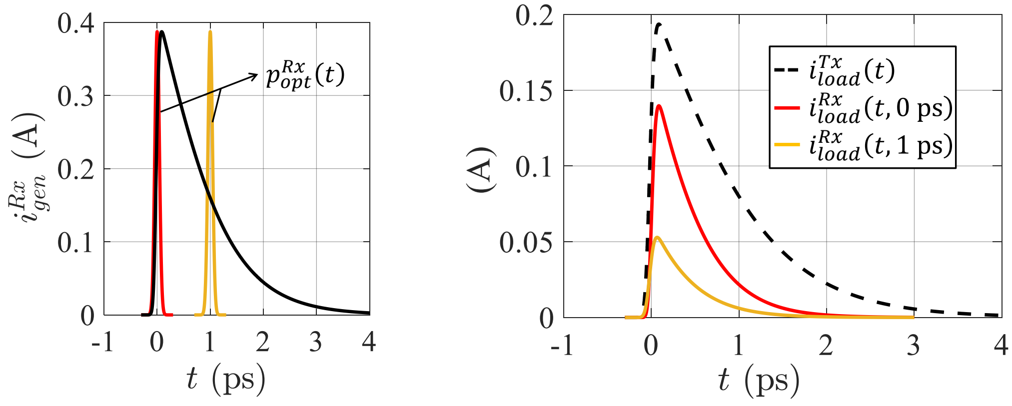

(a) (b)

Figure 3.9: (a) Generator current in Rx $i_{gen}^{Rx}(t)$ synchronized with the laser pulses in Rx with different time delay, $t_d = 0$ ps and 1 ps. (b) Load current in Rx $i_{load}^{Rx}(t, t_d)$ for different t_d and compared to the load current in Tx, $i_{load}^{Tx}(t)$. Here $\tau_c^{Tx} = \tau_c^{Rx} = 700$ fs, $\tau_s^{Tx} = 2$ fs, $\tau_s^{Rx} = 1.3$ fs, $\widetilde{P}_{opt}^{Tx} = \widetilde{P}_{opt}^{Rx} = 30$ mW and $V_b = 30$ V.

at the node in the Rx Norton circuit in Fig. 3.7(b) as follows:

$$i_{gen}^{Rx}(t) = i_{int}^{Rx}(t, t_d) + i_{load}^{Rx}(t, t_d). \tag{3.14}$$

Before the laser arrival, i.e., $t \le t_1$, we have the initial conditions that $i_{load}^{Rx}(t_1, t_d) = 0$, and $v_{load}^{Rx}(t_1, t_d) = 0$. We then use the current continuity to calculate the voltage at the following time $t_2 = t_1 + dt$, as follows:

$$v_{load}^{Rx}(t_2, t_d) = \left[i_{gen}^{Rx}(t_2) - i_{load}^{Rx}(t_1, t_d) \right] Z_0, \tag{3.15}$$

where dt is an infinitesimal time step. By substituting (3.15) into (3.13), we can obtain $i_{load}^{Rx}(t_2, t_d)$, and then we use the marching-on-time technique to progressively solve the complete $i_{load}^{Rx}(t, t_d)$ and $v_{load}^{Rx}(t, t_d)$.

An example is shown here to highlight the currents in the proposed Rx circuit. Let us consider a case when the THz forward wave is the one generated in Fig. 3.2(b) with $\widetilde{P}_{opt}^{Tx} = 30$ mW, i.e., $i_{load}^{Tx}(t)$. Fig. 3.9(a) shows the generator current $i_{gen}^{Rx}(t)$ which is the same as $i_{load}^{Tx}(t)$ but with the factor of 2 from (3.12), i.e., $i_{gen}^{Rx}(t) = 2i^{+}(t) = 2i_{load}^{Tx}(t)$. The PC gap and the laser source in Rx are the same as those in Tx. But the material properties are different: $\tau_c^{Rx} = 700$ fs and $\tau_s^{Rx} = 1.3$ fs. These values are in line with the measurements which will be explained in detail in Section 4.3. We consider two cases of the laser delay in Rx, $t_d = 0$ ps and 1 ps, and the synchronization is shown in Fig. 3.9(a) with the laser amplitude normalized to $i_{gen}^{Rx}(t)$. Fig. 3.9(b) shows the solutions of the marching-on-time evaluation for $i_{load}^{Rx}(t, t_d)$ with the corresponding time delay. It is compared to $i_{load}^{Tx}(t)$ and we can notice $i_{load}^{Rx}(t, 1\text{ ps}) < i_{load}^{Rx}(t, 0\text{ ps}) < i_{load}^{Tx}(t)$. This is because the impedance of the PC gap in Rx is also inversely proportional to $\widetilde{P}_{opt}^{Rx}$, similar to the case in Tx shown in Fig. 3.5(a). For our specific case, the load impedance is mismatched with the generator impedance (70 Ω).

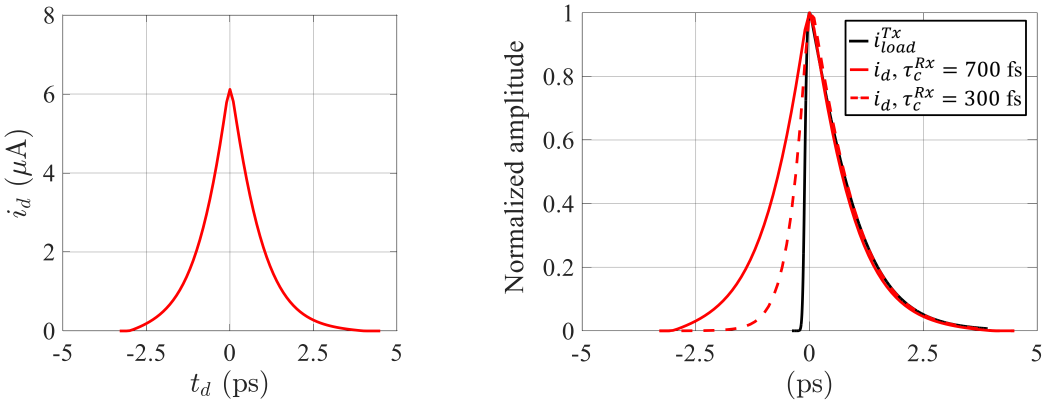

(a) (b)

Figure 3.10: Detected current $i_d(t_d)$: (a) amplitude and (b) waveform. $i_d(t_d)$ is compared to the load current in Tx $i_{load}^{Tx}(t)$. For the transmitter, $\tau_c^{Tx} = 700$ fs and $\tau_s^{Tx} = 2$ fs; while for the receiver, $\tau_c^{Rx} = 700$ fs and 300 fs are considered and $\tau_s^{Rx} = 1.3$ fs. $\widetilde{P}_{opt}^{Tx} = \widetilde{P}_{opt}^{Rx} = 30$ mW and $V_b = 30$ V.

3.3.2 Detected Currents in the Receiving PC Gap

For a specific time delay t_d, the load current $i_{load}^{Rx}(t, t_d)$ lasts in the order of τ_c^{Rx} as shown in Fig. 3.9(b), so it cannot be easily detected instantaneously. Only the net charges $Q(t_d)$ associated with each pulse period can be measured. Accordingly, one can define the detected current $i_d(t_d)$ as the average of $Q(t_d)$ over the laser repetition time as follows:

$$i_d(t_d) = \frac{Q(t_d)}{T} = \frac{1}{T}\int_{t_1+t_d}^{t_1+t_d+T} i_{load}^{Rx}(t, t_d)dt. \tag{3.16}$$

Note that for each t_d, we only obtain a single DC value. If we sweep t_d and define a series of time delays as $t_d(\Delta t) = 0$, Δt, ..., $N\Delta t$ for $N + 1$ laser repetition time, with Δt the resolution of the time delay. Then for each repetition, the laser pulse synchronizes with a different section of $i_{gen}^{Rx}(t)$. We assume Δt is small enough and N is large enough so that the complete $i_{gen}^{Rx}(t)$ can be swept by the laser pulses. Typical values for Δt are in the order of 0.1 ps. We thus can obtain a curve for the detected current for different time delay, i.e., $i_d(t_d)$ which is almost continuous.

An example of $i_d(t_d)$ is shown in Fig. 3.10 where its amplitude is plotted in Fig. 3.10(a) and its waveform is shown in Fig. 3.10(b) compared to that of $i_{load}^{Tx}(t)$. Thanks to the use of the Norton circuit, the actual amplitude of $i_d(t_d)$ can be evaluated. Moreover, we can notice that $i_d(t_d)$ is almost symmetric with respect to $t = 0$ and the waveform of $i_d(t_d \geq 0)$ is very close to that of $i_{load}^{Tx}(t \geq 0)$. The pulse width of $i_d(t_d)$ is doubled compared to $i_{load}^{Tx}(t)$ because of the long τ_c^{Rx} in Rx. During the recombination process in Rx, once a THz wave arrives at the PC gap in Rx, the remaining free electrons flow across the PC gap and form a time-varying current $i_{load}^{Rx}(t, t_d)$. Therefore, even when the laser is synchronized with $i_{gen}^{Rx}(t)$, for instance, at $t_d = -2.5$ ps, there is still a certain value of $i_d(t_d)$ and thus the complete $i_d(t_d)$ shows a symmetric behavior. According to this explanation, the shorter τ_c^{Rx}

is, the better reconstruction can be achieved. If we use $\tau_c^{Rx} = 300$ fs while keeping other parameters the same, $i_d(t_d)$ is shown in Fig. 3.10(b) by the dashed curve. Apparently, in this case, $i_d(t_d)$ is much closer to $i_{load}^{Tx}(t)$. Ideally, if $\tau_c^{Rx} \to 0$, $i_{load}^{Tx}(t)$ can be completely reconstructed without distortion.

3.3.3 Fidelity Factor

We have seen that even if we have considered a non-dispersive link based on a transmission line, the detected current $i_d(t_d)$ is still distorted when compared to $i_{load}^{Tx}(t)$ due to the use of long τ_c^{Rx} . If we further consider the use of antennas and QO components, the distortion could be worse. To quantify the pulse distortion from the Tx side to the Rx side, we evaluate the fidelity factor which is typically used for ultra-wideband antennas [102, 103]. It quantifies the distortion of a current $i_1(t)$ compared to a reference current $i_{ref}(t)$, and is expressed as follows:

$$F(i_1, i_{ref}) = \max_{\tau} \frac{\int_{-\infty}^{+\infty} i_{ref}(t) i_1(t-\tau) dt}{\sqrt{\int_{-\infty}^{+\infty} \left| i_{ref}(t) \right|^2 dt \int_{-\infty}^{+\infty} \left| i_1(t) \right|^2 dt}}, \tag{3.17}$$

where τ is a certain time delay.

Let us first consider the fidelity factor in Tx between the load current $i_{load}^{Tx}(t)$ and the generator current $i_{gen}^{Tx}(t)$, i.e., $F(i_{load}^{Tx}, i_{gen}^{Tx})$. We use the case shown in Fig. 3.2 and the fidelity factor is $F(i_{load}^{Tx}, i_{gen}^{Tx}) = 99\%$ and 93.3% for $\widetilde{P}_{opt}^{Tx} = 30$ mW and 160 mW, respectively. This mens as long as $\widetilde{P}_{opt}^{Tx}$ is not in the saturation region, $i_{load}^{Tx}(t)$ should have very similar waveform as $i_{gen}^{Tx}(t)$. Then, for a non-dispersive link, $F(i_{gen}^{Rx}, i_{load}^{Tx}) = 100\%$ according to (3.12). Finally, the fidelity factor between the detected current $i_d(t_d)$ and the load current in Tx $i_{load}^{Tx}(t)$ is calculated. For the case in Fig. 3.10(b), $F(i_d, i_{load}^{Tx}) = 90\%$ and 96.1% for $\tau_c^{Rx} = 700$ fs and 300 fs, respectively.

3.4 Conclusion

In this chapter, the TD equivalent circuits for a pulsed PCA source and a receiver are introduced. Firstly, the TD Norton circuit for a PCA source is briefly summarized. To simplify the marching-on-time evaluation of the TD circuit, an approximate Norton resistance is proposed to represent the active component. This resistance can be solved analytically and then an approximate FD Norton circuit is modelled. It can be used to accurately predict the power radiated by the PCA, thus it is a very useful tool for analyzing and designing the impedance matching for a PCA source. Then, a PCA receiver is modelled by a non-dispersive transmission line connected to a PC gap, illuminated by a pulsed laser. This model leads to a similar Norton equivalent circuit in Rx. The photocurrent flowing across the load is solved using the marching-on-time method and the detected current is evaluated by the stroboscopic sampling of the modelled THz pulses. Example solutions are shown to illustrate the detection process.

Chapter 4

Theoretical and Experimental Characterization of a Quasi-optical Link Between Two Pulsed Photoconductive Antennas

In this chapter, we consider a dispersive QO link between two PCAs and model its transfer function. Specifically, a field correlation approach based on high-frequency techniques is used to evaluate the spectral transfer function between two bow-tie based PCAs including the QO link and the effect of the receiving antenna. The detected currents in the receiving circuit are reconstructed using stroboscopic sampling of the modelled THz pulses, equivalent to what is actually performed by THz-TDS systems. Both the amplitude and the waveforms of these currents are evaluated. The QO link is then experimentally characterized to validate the proposed methodology. The comparison between the simulations and the measurements is excellent.

4.1 Introduction

A non-dispersive transmission line is used in Section 3.3 to model the THz pulses arriving at the receiver. Here we extend the analysis to a more common scenario where two PCAs are integrated with dielectric lenses and coupled to each other via two free-standing plano-convex lenses as shown in Fig. 4.1. We then characterize the coupling between two PCAs, including the QO link, by accurately modeling the link transfer function $H(f)$ (instead of using an approximation of it). We use an EM methodology which combines full-wave simulations, the GO/PO approaches, and the field correlation approach discussed in Section 1.3. This procedure can be easily extended to very different link geometries since the link is studied separately from the PCA time-domain analysis.

The current generator in the Rx circuit is calculated using the link transfer function

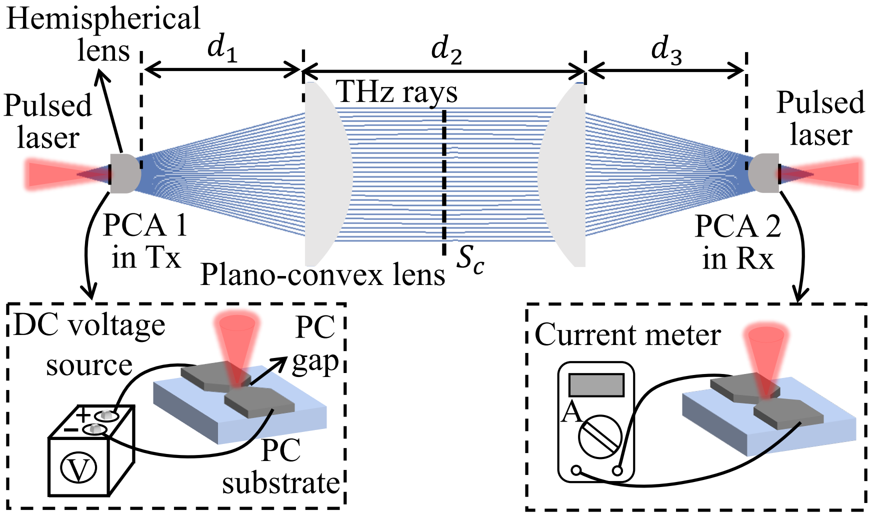

Figure 4.1: Schematic representation of the QO link between two PCAs. The insets show the PCAs at the Tx and the Rx sides. The ray tracing of the field propagation along the link is shown by the blue rays.

and the photocurrents are evaluated using the PC constitutive relation. The detected currents are then reconstructed by simulating the stroboscopic sampling which is achieved in the actual TD instruments by changing the optical delay of the laser pulses in Rx. In this respect, the modelling reconstructs the sampling process performed in the commercial Menlo System [104] which is available in our laboratory. We replace the fiber-coupled PCAs [105] by our own free-space excited bow-tie based PCAs [98]. The measured currents are compared to the simulations, showing excellent agreement in both the waveforms and the amplitude.

This chapter is structured as follows: Section 4.2 discusses the theoretical modelling of the dispersive QO link between two PCAs using the field correlation approach. Bow-tie based PCAs are used as examples to demonstrate the link transfer function and the detected currents. Section 4.3 shows the experimental characterization of the used PCAs to validate the proposed methodology.

4.2 Theoretical Characterization of the Link Transfer Function and the Detected Currents

Here we use the bow-tie based PCAs in [98], as shown in Fig. 4.2. The bow-tie antenna (BTA) is processed on a substrate made of LT GaAs and integrated with a silicon ($\varepsilon_r = 11.9$) extended hemispherical lens. This lens has a diameter of 10 mm and an extension of 1.45 mm, and its phase center is 16 mm below the lens. Moreover, it is coated with a quarter-wavelength matching layer which is made of parylene ($\varepsilon_r = 2.72$) at 400 GHz. The inset shows the detailed bow-tie geometry which has the width and length of 2 mm × 2 mm, the gap size of 10 µm × 10 µm, and the taper angle of 45°.

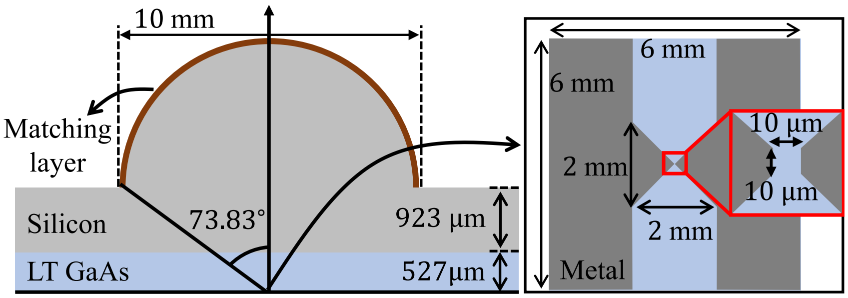

Figure 4.2: BTA integrated with an extended hemispherical lens. The inset shows the detailed geometry of the BTA.

This BTA presents almost constant and real input impedance below 1 THz, which can be approximated as a resistance, i.e., $Z_a(f) \approx R_a = 70\ \Omega$, as discussed in [98]. Therefore, we can use the similar Norton equivalent circuits in Tx and Rx as explained in the previous sections, where the load in Fig. 3.1(b) is $Z_0 \approx R_a = 70\ \Omega$, and the generator impedance in Fig. 3.7(b) is also R_a. It is worth mentioning that the main limitation of these assumption is that we would not properly model the low frequencies where the PCAs become small in terms of wavelengths and stop working as broadband antennas (i.e., their input impedance will change significantly).

4.2.1 Norton Current Generator in Reception

The QO link in Fig. 4.1 is similar to the scenarios in Fig. 3.1(a) and Fig. 3.7(a). However, now the transmitting THz wave will suffer from dispersion due to the propagation through this link, in contrast to the non-dispersive transmission line assumption taken previously. In terms of modelling, the main difference is that the current generator of the Norton circuit in Rx will not be two times the load current in Tx as in (3.12) anymore. To evaluate this current generator in the presence of the QO link, we resort to the antenna in Rx analysis introduced in Section 1.3, which is very similar to that in [52]. The Thévenin open-circuit voltage $V_{oc}^{Rx}(f)$ is then expressed as the field correlation on a decided surface S_c as follows:

$$V_{oc}^{Rx}(f) I_0(f) = \frac{2}{\zeta_0} \int_{S_c} \vec{E}_{PO-Tx}^{S_c}(\vec{r}, f) \cdot \vec{E}_{PO-Rx}^{S_c}(\vec{r}, f) d\vec{r}, \tag{4.1}$$

where ζ_0 is the free-space impedance, $\vec{E}_{PO-Tx}^{S_c}(\vec{r}, f)$ is the spectral field amplitude radiated by the PCA in Tx from Fig. 4.1 on the surface S_c, $\vec{E}_{PO-Rx}^{S_c}(\vec{r}, f)$ is the field radiated by the PCA in Rx from Fig. 4.1 on S_c when it is operated in the Tx mode, and $I_0(f)$ is the current input at this receiving antenna when used in the Tx mode. Once the spectral Thévenin voltage $V_{oc}^{Rx}(f)$ is calculated, we can derive the corresponding spectral Norton current simply as $I_{gen}^{Rx}(f) = V_{oc}^{Rx}(f)/R_a$ and then resort to its TD representation as follows:

$$i_{gen}^{Rx}(t) = Re\left[2 \int_0^{\infty} I_{gen}^{Rx}(f) e^{j2\pi f t} df\right]. \tag{4.2}$$

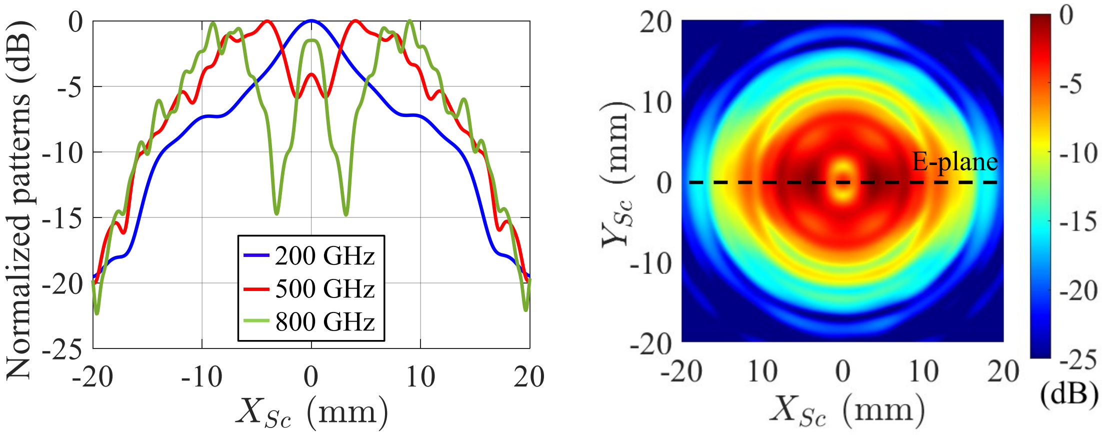

(a) (b)

Figure 4.3: Co-pol PO fields propagated to S_c evaluated using GRASP, $\vec{E}^{S_c,GRASP}_{PO-Tx}(\vec{r}, f)$, in (a) E-plane at 200 GHz, 500 GHz, and 800 GHz, and in (b) XY plane at 500 GHz.

Here one-sided inverse FT (IFT) is implemented since we only consider positive frequencies. The Norton circuit in Rx is then solved using the marching-on-time method in (3.15).

4.2.2 Numerical Simulations of the Quasi-optical Link

In order to evaluate (4.1), we the use simulations done in two commercial software: CST [32] to obtain the PCA fields radiated into a semi-infinite silicon medium, and the PO solver of TICRA GRASP [106] to perform the field propagation from the silicon lens to the surface S_c. For convenience, S_c is taken in the middle of the link shown in Fig. 4.1. The fields radiated by both PCAs, $\vec{E}^{S_c}_{PO-Tx}(\vec{r}, f)$ and $\vec{E}^{S_c}_{PO-Rx}(\vec{r}, f)$, are the same at this plane because of the link symmetry thus only one needs to be numerically evaluated.

In CST, the BTA is excited with an impressed current in the gap with the amplitude of $I_{CST}(f)$. The far-field performance of this BTA, when radiating inside the semi-infinite silicon medium, was discussed in [107] and is shown in Appendix B, Section B.1. The patterns at all frequencies oscillate significantly and their maxima are not at broadside. Therefore, they cannot efficiently illuminate the lens as explained in [99]. By using an in-house PO tool [38], the secondary fields radiated by the silicon lens in free space are evaluated. These fields are shown in Appendix B, Section B.1 (also discussed in [107]) and present non-broadside and oscillating behaviors, especially at high frequencies.

The secondary fields are then propagated towards the left-side plano-convex lens shown in Fig. 4.1 and collimated by it. This lens (TPX 50) has a diameter of 35.5 mm, an effective focal length (EFL) of 50 mm, a thickness of 8.5 mm, and a refractive index of 1.46. The focus of this TPX lens is aligned with the phase center of the hemispherical lens. This setup was simulated in GRASP with the distance $d_1 = d_3 = 22.5$ mm and $d_2 = 150$ mm, and the ray tracing is shown by the blue rays. The simulated PO fields are defined as $\vec{E}^{S_c,GRASP}_{PO-Tx}(\vec{r}, f)$ and $\vec{E}^{S_c,GRASP}_{PO-Rx}(\vec{r}, f)$, which are identical in our case. The amplitude

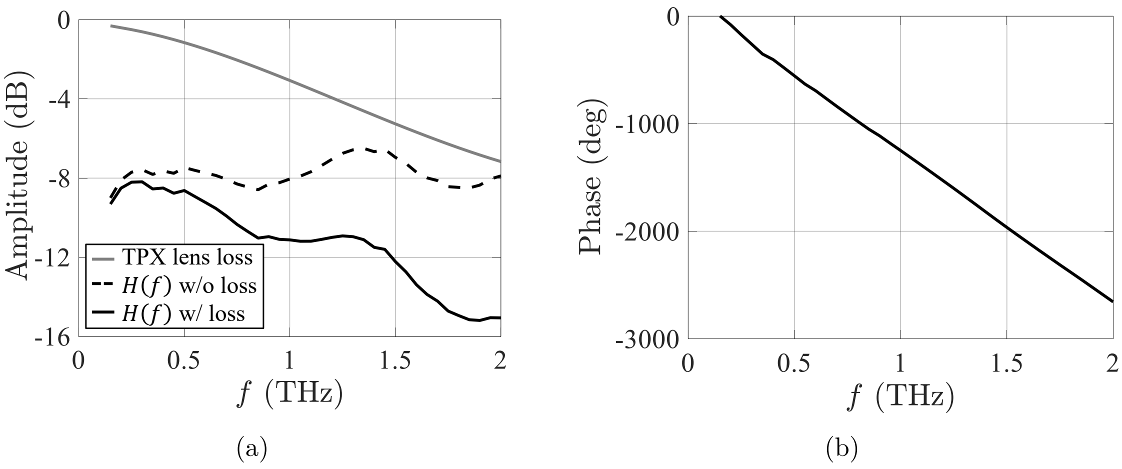

(a) (b)

Figure 4.4: Simulated link transfer function $H(f)$. (a) Amplitude. The total dielectric loss of the used two TPX lenses is also shown. (b) Phase. The linear phase term is removed.

pattern of $\vec{E}^{S_c,GRASP}_{PO-Tx}(\vec{r},f)$ is shown in Fig. 4.3(a) in the E-plane and in Fig. 4.3(b) in the XY plane (at 500 GHz). Here the cartesian coordinate system with X_{Sc} and Y_{Sc} is used to represent the plane S_c. We also observe significant oscillation in the PO fields.

The PO field $\vec{E}^{S_c,GRASP}_{PO-Tx}(\vec{r},f)$ is proportional to the CST impressed current $I_{CST}(f)$. Therefore, this field can be related to the PO field in (4.1) i.e. $\vec{E}^{S_c}_{PO-Tx}(\vec{r},f)$, via the amplitude renormalization between $I_{CST}(f)$ and the load current in Tx, $I^{Tx}_{load}(f)$, as follows:

$$\vec{E}^{S_c}_{PO-Tx}(\vec{r},f) = \frac{I^{Tx}_{load}(f)}{I_{CST}(f)}\vec{E}^{S_c,GRASP}_{PO-Tx}(\vec{r},f). \tag{4.3}$$

If we substitute (4.3) into (4.1), the generator current $I^{Rx}_{gen}(f)$ can be calculated numerically. Using the normalization described in (4.3), the amplitude of $I^{Rx}_{gen}(f)$ is well modelled without introducing approximations as in [52].

Before evaluating the current detected at the receiving PCA, we can analyze the amplitude and phase dispersion of the QO link itself by means of the link transfer function $H(f)$. It only quantifies the field propagation between two PCAs and does not include the spectral properties of the PC gaps. This means that $H(f)$ is independent from the Norton circuits discussed before and it is calculated as follows:

$$H(f) = \frac{\int_{S_c} \vec{E}^{S_c,GRASP}_{PO-Tx}(\vec{r},f)\cdot\vec{E}^{S_c,GRASP}_{PO-Rx}(\vec{r},f)d\vec{r}}{2\zeta_0 P^{CST}_{acc}(f)}, \tag{4.4}$$

where $P^{CST}_{acc}(f) = 1/2\,|I_{CST}(f)|^2\,R_a$ is the accepted power in CST simulations. $H(f)$ is always smaller than one and independent from the actual current amplitude in the PC gaps. For the analyzed QO link and BTAs, the resulting amplitude of $H(f)$ is shown in Fig. 4.4(a). The total dielectric loss of the used two TPX lenses is also shown. Note that for the mentioned PCA lens diameter (10 mm), the PO approach is not accurate when the frequency is below 150 GHz since the lens is too small in terms of wavelengths. Therefore,

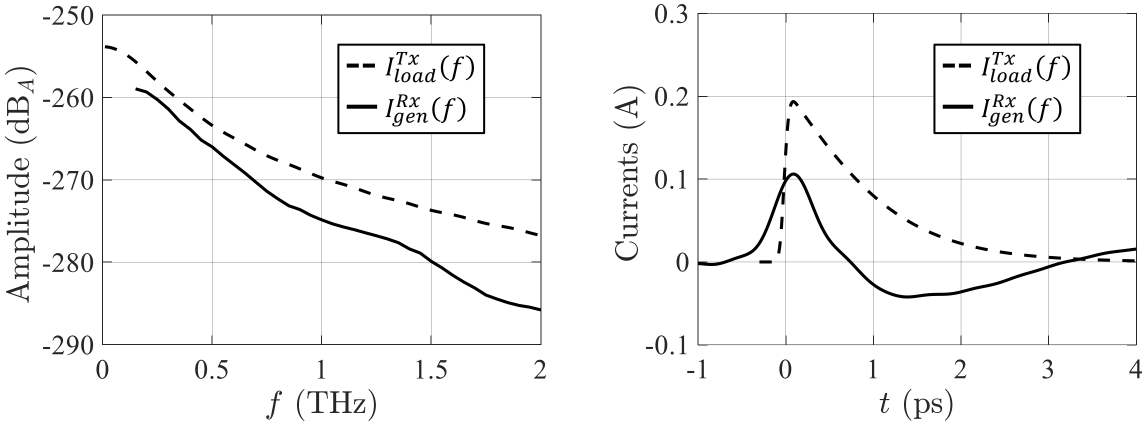

(a) (b)

Figure 4.5: Comparison between the generator current in Rx $I_{gen}^{Rx}(f)$ and the load current in Tx $I_{load}^{Tx}(f)$ in (a) FD and (b) TD.

the simulated $H(f)$ cannot be accurately estimated at low frequencies and we truncate it for $f < 150$ GHz. This truncation will be performed for all frequency-related figures in the following. Due to the high dielectric loss and the poor radiation of the BTA mentioned before, the amplitude of $H(f)$ is quite low. The peaks in $H(f)$ are caused by the matching layer which is resonant around 400 GHz and multiple frequencies. The phase of $H(f)$ is shown in Fig. 4.4(b). It presents a linear behavior which corresponds to the forward-wave propagation along the QO link. Since $H(f)$ represents the dispersion of the QO link, by considering the field normalization in (4.3), the generator current in Rx, $I_{gen}^{Rx}(f)$, can be related to the load current in Tx, $I_{load}^{Tx}(f)$, via $H(f)$ as:

$$I_{gen}^{Rx}(f) = 2I_{load}^{Tx}(f)H(f). \tag{4.5}$$

4.2.3 Currents Detected at the PCA Receiver

Let us now evaluate the detected currents of the receiving PCA shown in Fig. 4.1. Here we consider a biasing voltage of $V_b = 30$ V for the PCA in Tx, and the laser optical power of $\widetilde{P}_{opt}^{Tx} = \widetilde{P}_{opt}^{Rx} = 30$ mW. The recombination time is $\tau_c^{Tx} = \tau_c^{Rx} = 700$ fs and the scattering time is $\tau_s^{Tx} = 2$ fs and $\tau_s^{Rx} = 1.3$ fs for the transmitter and the receiver, respectively.

By implementing the current relation in (4.5), the generator current in Rx, $I_{gen}^{RX}(f)$, is calculated. It is shown in Fig. 4.5(a) and compared to the load current in Tx, $I_{load}^{Tx}(f)$. Here $I_{gen}^{RX}(f)$ is truncated for $f < 150$ GHz as mentioned before while $I_{load}^{Tx}(f)$ is not truncated since it corresponds to $i_{load}^{Tx}(t)$ in Fig. 3.2(b). Due to the link propagation, $I_{gen}^{RX}(f)$ is distorted and its amplitude follows the relation in (4.5). We then perform IFT on the spectral currents to obtain their time evolution which are shown in Fig. 4.5(b). The waveform of $i_{gen}^{RX}(t)$ is also distorted and the amplitude drops in line with the spectral difference. Note that besides the link propagation, the truncation of the spectral current also introduces distortion.

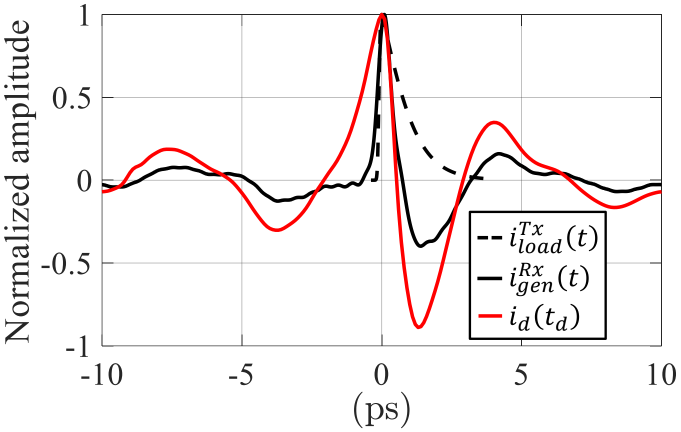

Figure 4.6: Detected current $i_d(t_d)$ compared to the generator current in Rx $i_{gen}^{RX}(t)$ and the load current in Tx $i_{load}^{Tx}(t)$ when the QO link in Fig. 4.1 is used. $\tau_c^{Tx} = \tau_c^{Rx} = 700$ fs, $\tau_s^{Tx} = 2$ fs, $\tau_s^{Rx} = 1.3$ fs, $\widetilde{P}_{opt}^{Tx} = \widetilde{P}_{opt}^{Rx} = 30$ mW and V_b=30 V.

Finally, the detected current $i_d(t_d)$ is estimated using (3.16) and it is shown in Fig. 4.6 compared to $i_{gen}^{Rx}(t)$ and $i_{load}^{Tx}(t)$. Due to the use of the BTAs and the dispersive QO link, the THz pulse in Tx, i.e., $i_{load}^{Tx}(t)$, is distorted when arriving at the receiver. Such distortion (including the truncation distortion) is quantified by $F(i_{gen}^{Rx}, i_{load}^{Tx}) = 57.5\%$. Then, $i_{gen}^{Rx}(t)$ is reconstructed by $i_d(t_d)$. The waveform of $i_d(t_d)$ has wider pulse width and higher side lobes compared to $i_{gen}^{Rx}(t)$ and the fidelity factor is $F(i_d, i_{gen}^{Rx}) = 90.8\%$. Such pulse distortion is mainly related to the very long recombination time of the receiver ($\tau_c^{Rx} = 700$ fs), which is similar to the case shown in Fig. 3.10(b). Finally, the total distortion of the link is calculated as $F(i_d, i_{load}^{Tx}) = 43.1\%$.

4.3 Experimental Characterization of the Detected Currents

The proposed QO link shown in Fig. 4.1 with the above-mentioned bow-tie based PCAs was measured in our laboratory at TU Delft. Fig. 4.7 shows a photograph of the measured PCA. The PCA is mounted on a holder as explained in [108]. The PCA holder has a SMA connector which is used either to bias the PCA source or to read out the current detected by the PCA receiver. A schematic representation of the measurement setup, together with a photograph of it, is shown in Fig. 4.8. This setup uses the free-space 780-nm laser output of a commercial THz spectrometer TERA K15 from Menlo Systems [104] to optically illuminate our PCAs. We split the output laser power equally for both laser ports and the maximum output power (not the laser optical power) is about 100 mW per port. The PCA source is biased by a DC power supply with the voltage V_b whereas the PCA receiver is connected to a DC current meter.

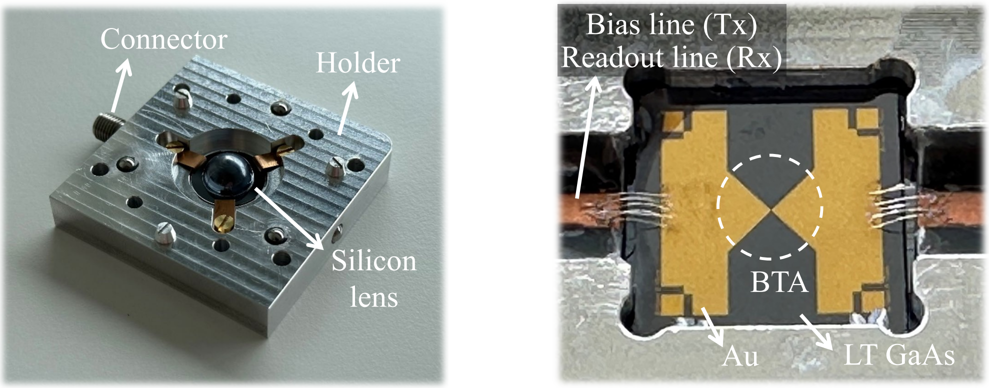

(a) (b)

Figure 4.7: Photographs of the measured bow-tie based PCA: (a) perspective view and (b) bottom view.

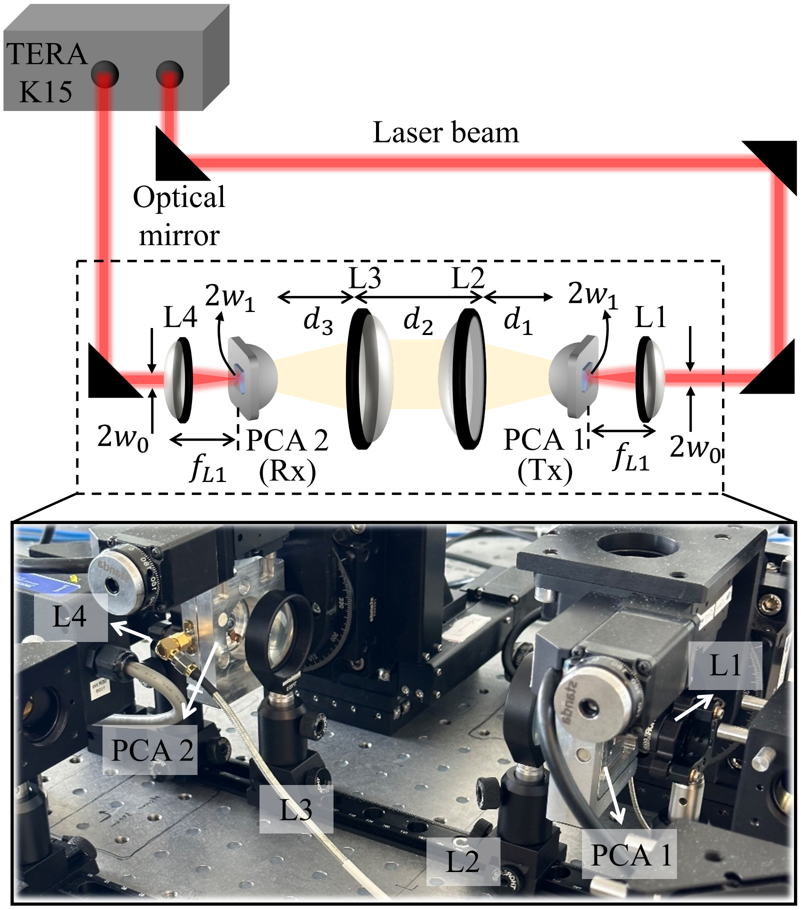

Figure 4.8: Schematic representation of the measurement setup with the photograph shown in the inset. The laser beams are represented by the red rays while the THz pulses are the yellow rays. The indicated distance is $f_{L1} \approx 20.1$ mm, $d_1 = d_3 \approx 22.5$ mm, and $d_2 \approx 150$ mm.

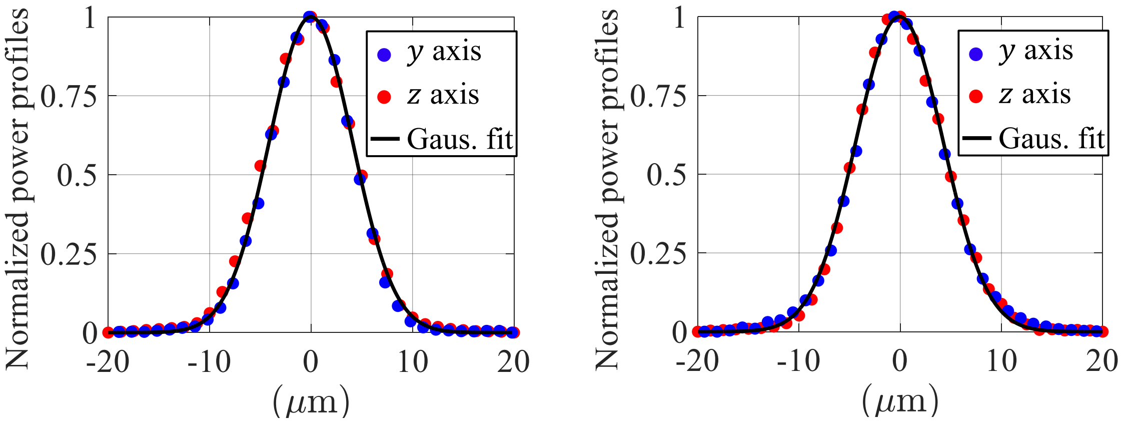

(a) (b)

Figure 4.9: Measured power profiles of the focused laser beams at the gaps of the PCAs in (a) Tx and (b) Rx. The black curves are the Gaussian fits of the measured points.

4.3.1 Laser Power Profiles

The output laser beam arriving at L1 has a $1/e^2$ radius of $w_0 \approx 0.7$ mm. To achieve the ideal illumination on the gap of the PCA, we use a plano-convex lens L1 to focus the incoming laser beams; see Fig. 4.8. This lens is LA1074-B-ML from Thorlabs and has a diameter of 12.7 mm and an EFL of 20 mm. The reason to choose this lens is described in Appendix C.1. The focused laser beam has a radius of $w_1 = 8.5$ μm. This corresponds to the FWHM of 10 μm which is the same as the gap size of the PCA, i.e., FWHM=W_x=W_y. Note that the free-space optical path for the transmitter in Fig. 4.8 is longer than that of the receiver. This is because the optical path of the port in Tx is shorter than that in Rx inside TERA K15 and we need to add this extra length to assure that the detected THz signal is within the range of the optical delay unit (ODU) of the TERA K15.

The spot sizes of the focused laser beams in both Tx and Rx were measured along two orthogonal axes (y and z axes) using the knife-edge technique with two metal blades [108]. The results are shown in Fig. 4.9(a) and 4.9(b) for the transmitter (PCA 1) and the receiver (PCA 2), respectively. Thanks to the extensive alignment procedures described in Appendix C.2, the profiles have excellent Gaussian shapes for both laser ports. The FWHM of the transmitter is 9.3 μm (y axis) and 10 μm (z axis), which leads to an average spillover efficiency on the PC gap of 60.5%. By considering also the absorption of the LT GaAs substrate, the optical efficiency is $\eta_{opt}^{Tx} = \widetilde{P}_{opt}^{Tx}/\widetilde{P}_{L}^{Tx} \approx 35.7\%$, where $\widetilde{P}_{L}^{Tx}$ is the power of the measured profile. While for the receiver, the FWHM is 10.1 μm for both axes, thus the average spillover efficiency is 57.1% and $\eta_{opt}^{Rx} = \widetilde{P}_{opt}^{Rx}/\widetilde{P}_{L}^{Rx} \approx 33\%$.

4.3.2 Measured Currents at the Receiver

We then measure the currents detected at the receiver using the setup in Fig. 4.8. To synchronize the receiver with the transmitter, we fix the optical path of the laser pulses

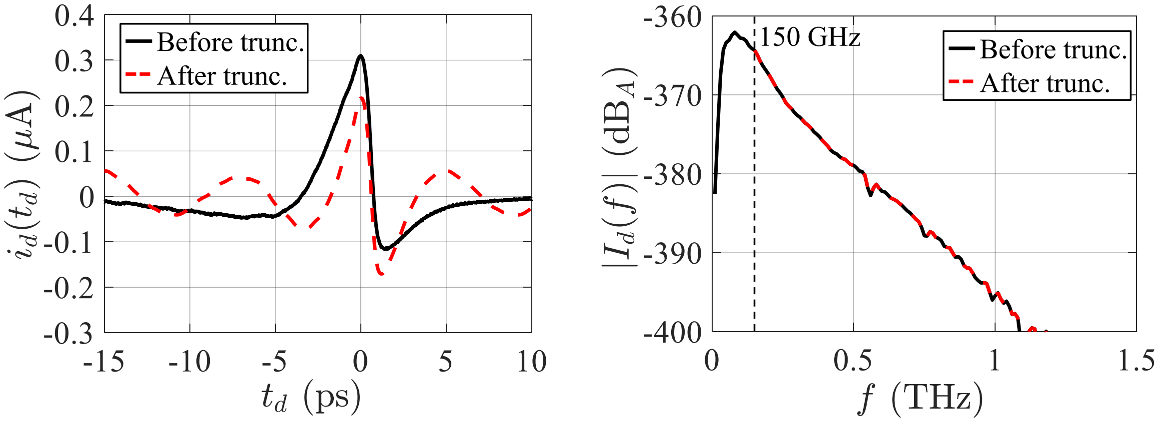

(a) (b)

Figure 4.10: Measured current of the PCA receiver (PCA 2) when $V_b = 30$ V for the transmitter (PCA 1) with $\widetilde{P}_{opt}^{Tx} = 10$ mW and $\widetilde{P}_{opt}^{Rx} = 9$ mW: (a) time signal and (b) spectrum. The spectrum truncated for $f < 150$ GHz is shown by the dashed curve in (b).

in Tx and change the one in Rx by using the ODU inside the TERA K15. The measured $i_d(t_d)$ is shown in Fig. 4.10(a) when $V_b = 30$ V for the PCA transmitter with $\widetilde{P}_{opt}^{Tx} = 10$ mW and $\widetilde{P}_{opt}^{Rx} = 9$ mW, and its corresponding spectrum $I_d(f)$ is plotted in Fig. 4.10(b). The amplitude of $i_d(t_d)$ is measured using a Keithley 2000 multimeter with an integration time of 200 msec. We obtain a fidelity factor of $F(i_d, i_{load}^{Tx}) = 65\%$ when comparing the waveform of $i_d(t_d)$ to the load current in Tx $i_{load}^{Tx}(t)$. Since the PO approach is not accurate when the frequency is below 150 GHz, we need to truncate the measured spectrum for $f < 150$ GHz [see Fig. 4.10(b)] to have a fair comparison with our simulations. We then perform the IFT on the truncated spectrum to obtain the corresponding time signal which is plotted in Fig. 4.10(a) by the dashed curve. This curve shows that the low-frequency spectrum has a strong impact on the detected current. After the truncation, the width of $i_d(t_d)$ significantly decreases with higher side lobes and lower main lobe. The fidelity factor now becomes 46.5% (including the truncation distortion). This current and its truncated spectrum are referred to as the measured current and spectrum in the following.

Following the procedures discussed in Section 3.3, we can solve the Rx circuit for different time delays and obtain the simulated detected current $i_d(t_d)$. To best fit the waveform of the measured pulse in Fig. 4.10(a), the recombination time of both PCAs are found to be the same, and their values are $\tau_c^{Tx} = \tau_c^{Rx} = 700$ fs. In Appendix D, we have shown that the PCA transmitter (PCA 1) radiates more power than the receiver (PCA 2) due to the different material properties. In our modelling, we assume a unitary value for the quantum efficiency with which one electron is freed for every photon absorbed. Thus the differences between PCAs are represented by different values of the scattering time. To best match our simulations with the power measurements, the scattering time of PCA 1 is set to be $\tau_s^{Tx} = 2$ fs whereas that of PCA 2 is $\tau_s^{Rx} = 1.3$ fs.

Then we substitute these parameters into simulations and compare to the measurements. The comparison is shown in Fig. 4.11(a) and 4.11(b) for $\widetilde{P}_{opt}^{Tx} = 10$ mW and

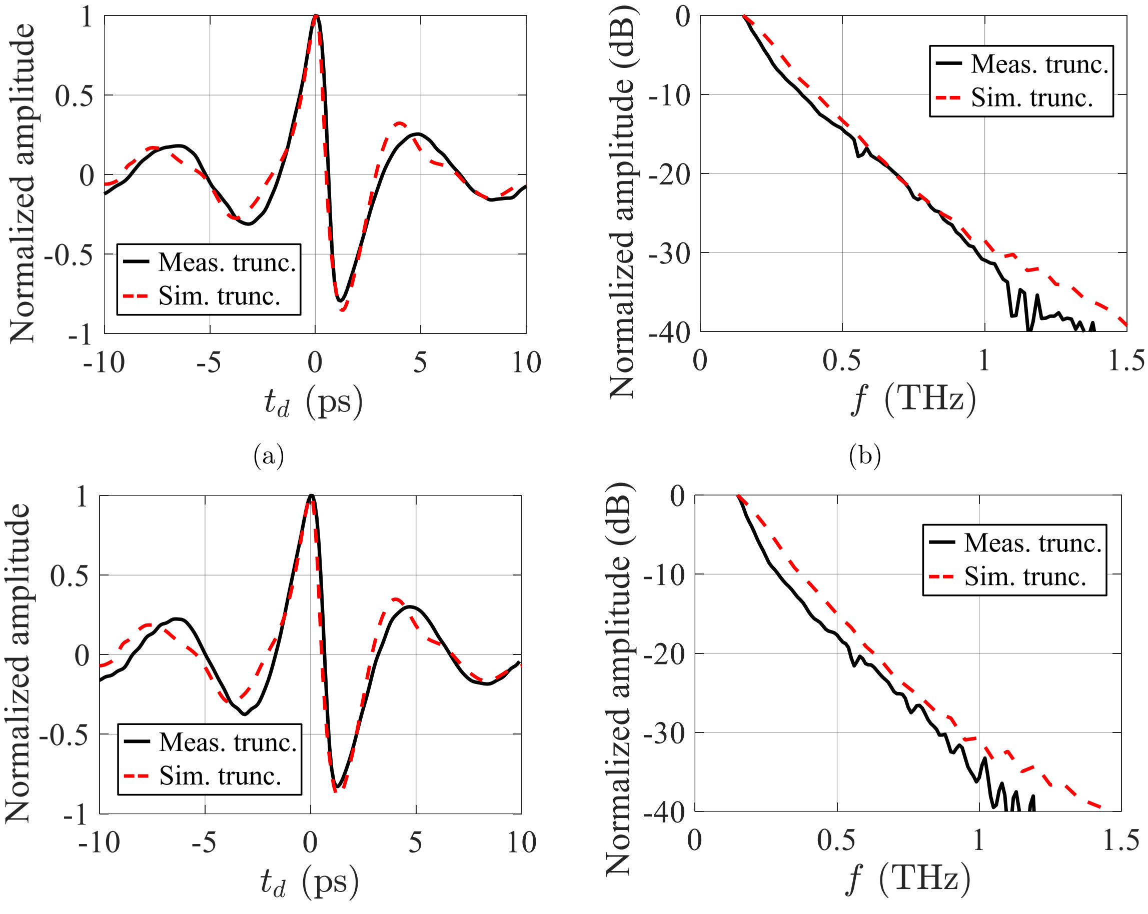

(a) (b)

(c) (d)

Figure 4.11: Measured detected currents (after truncation) of the receiver compared to the simulations. (a) and (b) correspond to $\widetilde{P}_{opt}^{Tx} = 10$ mW and $\widetilde{P}_{opt}^{Rx} = 9$ mW; (c) and (d) are $\widetilde{P}_{opt}^{Tx} = 30$ mW and $\widetilde{P}_{opt}^{Rx} = 28$ mW. The amplitude of the time signals is normalized to the maxima values (at $t_d = 0$). The spectra are normalized to $f = 150$ GHz and the loss of the TPX lenses in Fig. 4.4(a) is included in the simulations.

$\widetilde{P}_{opt}^{Rx} = 9$ mW, and in Fig. 4.11(c) and 4.11(d) for $\widetilde{P}_{opt}^{Tx} = 30$ mW and $\widetilde{P}_{opt}^{Rx} = 28$ mW. The simulated spectra are also truncated for $f < 150$ GHz and the agreement with the measurements in both cases is excellent. These spectra decrease fast because τ_c of both PCAs is very long. By performing IFT, the simulated detected currents are also in excellent agreement with the measurements. Furthermore, we measured the maximum detected DC currents when the laser pulses in Rx are synchronized with the peaks of the THz pulses. These peaks correspond to the maxima position ($t_d = 0$) shown in Fig. 4.11(a) and 4.11(c). These DC currents are calculated when the spectra are truncated and are plotted in Fig. 4.12 versus $\widetilde{P}_{opt}^{Rx}$. The simulations were done under the same conditions and they match well with the measurements for different V_b. Such good matching further confirms that τ_s^{Tx} and τ_s^{Rx} are properly evaluated. As a reference, when using the transmitter and the receiver from Menlo Systems [105], the measured DC current is less than 0.4 µA when

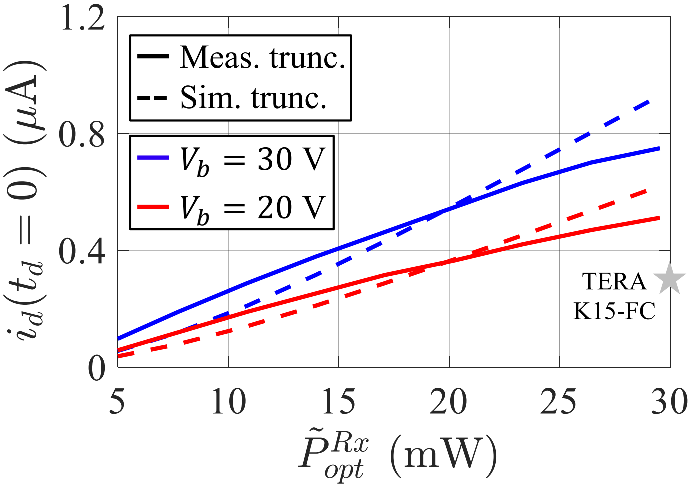

Figure 4.12: Measured DC currents at the maxima position ($t_d = 0$) in Fig. 4.11 compared to the simulations. Two biasing voltages $V_b = 20$ V and 30 V are considered for the transmitter. The current measured using TERA K15-FC from Menlo Systems [105] is also shown.

$\tilde{P}_{opt}^{Rx} \approx 30$ mW and $V_b = 100$ V. To our best knowledge, this is the first time that the detected currents are simulated in a link between PCAs and compared to the measurements in both waveforms and amplitude.

4.4 Conclusion

In this chapter, the transfer function of a dispersive QO link between two PCAs is modelled. This function is evaluated using the field correlation technique which is performed in the middle plane of the link. The fields propagated to this plane are evaluated using full-wave simulations combined with the GO/PO approaches. By using this transfer function, the current generator of the Norton circuit in Rx can be accurately calculated. The detected currents are then evaluated using the stroboscopic sampling of the modelled THz pulses. The proposed methodology is validated by the measurements of the detected currents using the proposed QO link. Extensive alignments are performed between the laser beams and the optical components in the link, as described in Appendix C. Afterwards, the THz pusles are measured by a current meter connected to the receiver. The measured pulse width indicates that the used PCAs have long recombination time of 700 fs. While the power measurements discussed in Appendix D indicate a short scattering time of 2 fs and 1.3 fs for the source and the receiver, respectively. By truncating the low-frequency components of the measured spectra (for $f < 150$ GHz), the resulting measured time signals are in excellent agreement with the simulations in both amplitude and waveforms.

Chapter 5

Focal Plane Array of Shaped Quartz Lens Antennas for Wide Field-of-view Sub-millimeter Imaging Systems

Large format focal plane arrays (FPAs) of dielectric lens antennas are promising candidates for wide field-of-view (FoV) sub-millimeter imagers. They are especially suitable for designing a photoconductive-antenna-based receiver for future security imaging. In this work, we optimize the scanning gain of such imagers via shaping lens surfaces. We develop an optimization procedure using the field correlation technique between the fields generated by a reflector on the top of the lenses and those generated by the lens feeds. Based on this procedure, an FPA of quartz lens combined with leaky-wave feeds is designed to efficiently illuminate the reflector, achieving a directivity of 50.5 dBi up to scanning 20.3°. The obtained scanning gain loss of 2.6 dB is much lower than that associated with the direct fields coming from the reflector (about 6 dB). The proposed FPA is validated by full-wave simulations with excellent agreement. We have fabricated and measured an example shaped quartz lens antenna optimized for scanning 20.3° at 180 GHz. The comparison between the simulations and measurements also shows excellent agreement.

5.1 Introduction

FPAs are widely considered in the (sub-)THz regime for imaging applications in the areas of astronomy and security [8–11, 41, 45, 46, 109–113] due to their ability to significantly reduce imaging acquisition time. Specially, they are very suitable for designing photoconductive-antenna-based receiver for future mm-resolution security imaging as indicated in [44]. FPAs commonly consist of horn arrays, e.g., [45, 109], or lens arrays, e.g., [10, 11], which are coupled with reflectors. The size of reflector apertures depends on the required resolution and is limited by the need for performing mechanical scanning [114]. In most cases, high aperture efficiency is needed, limiting the possibility of improving the scanning performance via the optimization of shapes of main reflectors [113]. Here we consider the application scenario of a state-of-the-art imaging radar discussed in [45]. This imager has a horn-based FPA with an equivalent aperture of $141.4\lambda_0$ (λ_0 is the wavelength) which leads to an estimated broadside directivity of 52 dBi. Because of the limited field shaping capabilities of horns, such a system suffers from a scan loss (SL) of 3 dB at 14°. To further improve the scanning performance, dielectric lens antennas are promising candidates since their shapes can be optimized to synthesize demanded radiation patterns.

Several studies have been carried out to investigate axisymmetric or arbitrarily shaped lenses to synthesize desired radiation patterns [55, 115–122]. In these works, lens surfaces were optimized locally or globally using geometrical/physical optics (GO/PO), spherical wave expansions, or finite-difference time-domain approaches, depending on the lens size. However, these methods require complex numerical optimization procedures which cannot provide much insight into the analysis of the lens itself. Recently, a coherent Fourier optics (CFO) based method was presented in [123] to shape silicon lenses coupled to a parabolic reflector. These lenses are analysed in reception (Rx) and designed according to a direct solution of a field correlation technique. The achieved SL is 1.6 dB at 20.3° which is much lower than that predicted by the direct fields coming from the reflector. However, such study was done only for shallow silicon lenses, which are costly to fabricate.

In this work, we instead explore if similar performance can be achieved by lenses with lower permittivity, in particular made of quartz with $\varepsilon_r = 3.75$. In [123], the optimized shapes of the shallow silicon lenses were derived directly from the plane wave spectrum of the reflector-lens combination without the need of optimization. However, in the case of non-shallow lenses, due to more significant effects associated with the total reflection beyond the critical angle, an optimization procedure is needed. Therefore, in this work, we have developed a specific method that correlates the reflector's focal fields and the radiated fields of the lens antennas over the lens aperture planes. This choice allows for evaluating the reflector's focal fields only once outside the optimization cycle leading to faster optimization.

The lens feed is a resonant leaky-wave antenna (LWA) with a double-slot iris [26]. Such a feed is particularly efficient in illuminating dielectric lenses and can be easily integrated with lenses. We first briefly discuss the lens optimization with this feed for moderate scanning angles, and then mainly focus on the optimization procedure for large scanning angles by shaping lens surfaces. Shaped lens surfaces can compensate the higher-order phase aberrations present in reflector's focal fields and achieve better field correlation. We present an example design of the shaped quartz lens antenna at the edge of the FPA for a scanning angle of 20.3° at 180 GHz. The optimized lens antenna couples well to the reflector and the system achieves a scanning directivity of 50.5 dBi with a scanning gain loss of 2.6 dB. This performance is compared to the state of the art showing low SL while maintaining high broadside aperture efficiency. A prototype of this shaped quartz lens antenna was fabricated using the same waveguide feed as in [16]. We have measured the lens radiation performance and it is in excellent agreement with the simulations.

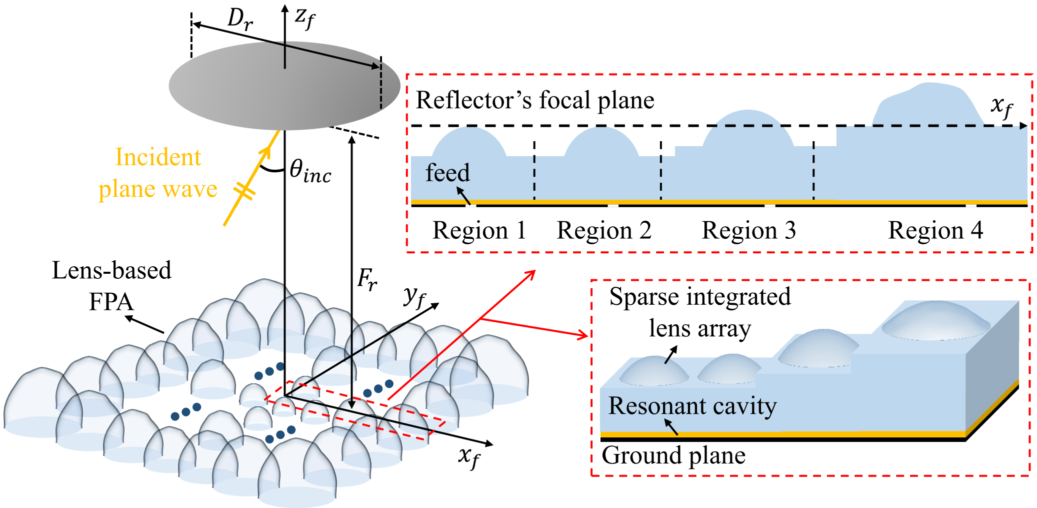

Figure 5.1: Architecture of the proposed lens-based FPA. The top inset shows the lens elements in the four regions identified in [123]. The bottom inset depicts the structure of the integrated lens array.

This chapter is organized as follows: Section 5.2 introduces the considered imaging scenario and the geometry of the lens feed. Section 5.3 describes the proposed field correlation method and the optimization procedures for different scanning angles. Section 5.4 discusses the optimization of the lens geometries when the scanning angle is moderate. Section 5.5 discusses the procedures to modify lens surfaces when the scanning angles are large and shows an example design of the edge lens element. Its performance is analysed, validated, and compared to the state of the art. Section 5.6 shows the prototype and the measurement results.

5.2 Imaging Scenario

Let us consider the imaging scenario shown in Fig. 5.1. An array of quartz lens antennas is placed at the focal plane of a main reflector which is illuminated by an incident plane wave (PW) with the incident angle of $(\theta_{inc}, \phi_{inc})$. For simplicity, the main reflector aperture is modelled as a symmetric non-oversized parabola, but it can be easily extended to more practical components. We consider the central frequency as 180 GHz. The reflector has a diameter of $D_r = 141.4\lambda_0$, focal distance of $F_r = 282.8\lambda_0$, and f-number of $f_{\#}^{r} = F_r/D_r = 2$, which are in line with the reflector dimensions in [45, 123].

For the described FPA, the antenna feeds are placed over a flat surface, enabling monolithic integration at high frequencies, as shown in the top inset in Fig. 5.1. The lens feeds remain the same across the array while the lens geometries change for different scanning angles. To facilitate the design of lenses in a large format FPA, we discretized the FPA into four regions as suggested in [123]. The corresponding lens geometries are depicted in the top (side view) and bottom (perspective view) insets in Fig. 5.1. In the first three regions, lens surfaces are elliptical. As the scanning angle increases, the lens diameters increase,

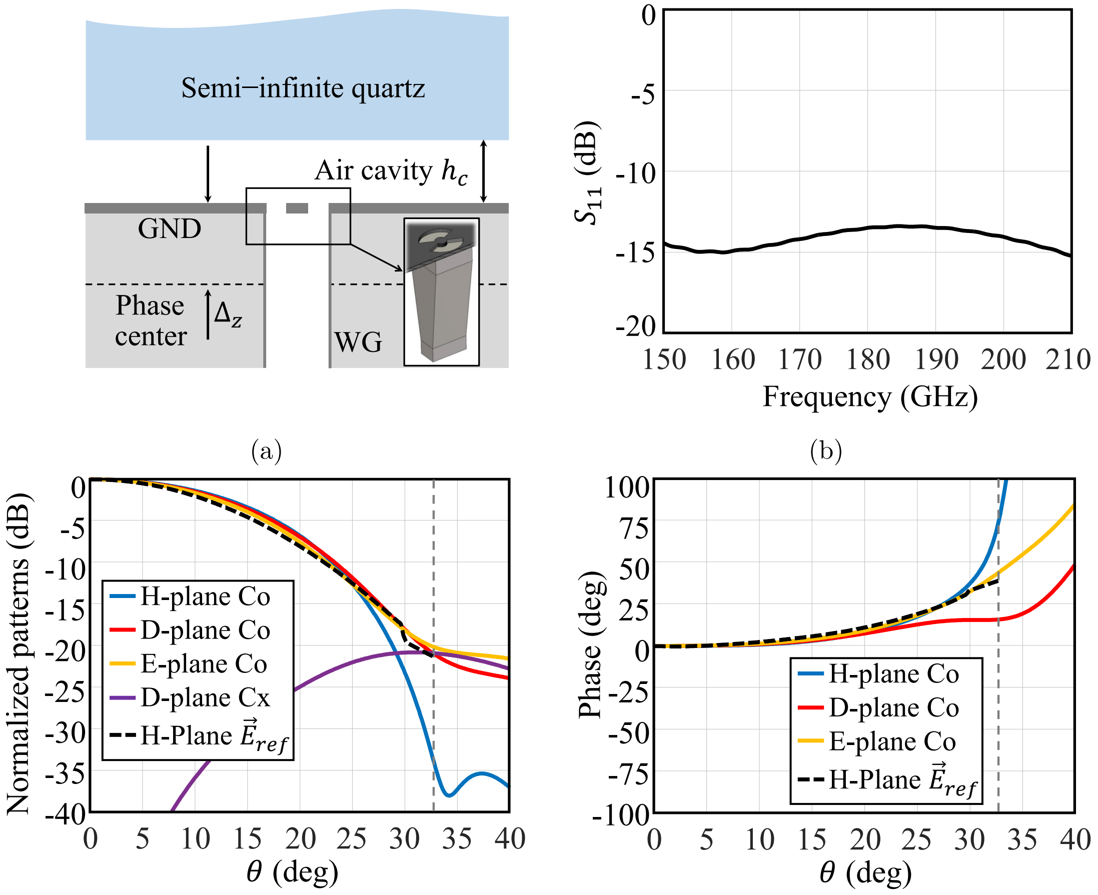

(a) (b)

(c) (d)

Figure 5.2: (a) Structure of the lens feed for the FPA: a resonant LWA. A double-slot iris is fed by a waveguide and radiated towards the semi-infinite quartz medium through an air cavity. The inset shows the feed geometry in [16]. WG: waveguide. (b) The simulated S-parameter of the feed. (c) and (d) are the amplitude and phase of the field radiated by the LWA feed, respectively. This field is plotted at 180 GHz inside the quartz medium on a sphere with the radius of $8\lambda_d$. The dashed black curve represents the reflector's scattered field, $\vec{E}_{ref}$, on the same sphere for the broadside incidence case. The dashed grey lines represent the optimized lens truncation angle θ_0^l.

and the lens feeds are displaced with respect to lens focuses. While in the fourth region, the shapes of lens surfaces need to be modified to compensate the higher-order phase terms present in the reflector's focal fields. The FPA is not fully sampled, and its sampling size follows that used in [45] where a mechanical scanner was used to fulfill the complete FoV.

In this work, we consider a resonant LWA as the lens feed, and its stratification is shown in Fig. 5.2(a). A resonant air cavity is placed between the ground plane and the lens material to enable the excitation of leaky waves. On the ground plane, a double-slot iris is excited by a square waveguide. To facilitate the fabrication and measurement, here we use the same iris and waveguide dimensions as discussed in [16]. In our case, the stratification dimensions are different: $h_c = 0.48\lambda_0$ and $\Delta z = 0.87\lambda_0$. This LWA was

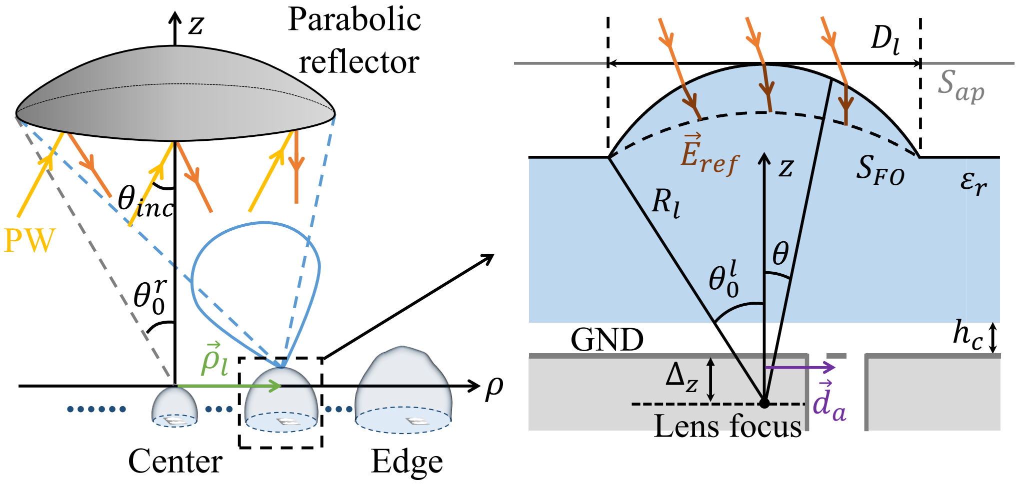

(a) (b)

Figure 5.3: Schematic representation of a scenario when a PW illuminates the reflector and couples to one of the lens elements in the FPA. The blue beam represents the radiated field of the lens antenna in the transmission mode. (b) Detailed structure of the lens antenna.

simulated in CST [32] full-wave simulator when radiating toward a semi-infinite quartz medium; see Fig. 5.2(a). The S-parameter of the antenna is shown in Fig. 5.2(b) and it shows very good impedance matching over a wide bandwith. Fig. 5.2(c) and 5.2(d) show the field radiated by the feed inside the lens medium at 180 GHz over a sphere with the radius of $8\lambda_d$ (λ_d: wavelength inside the medium). This radiated field will be used to decide the lens truncation angle and will be discussed in detail in Section 5.4.

5.3 Field Correlation Optimization Technique

To find the optimized lens geometry for each scanning direction, we propose to use the field correlation technique introduced in Section 1.3 between the reflector's focal fields and the lens radiated fields, similar to the method discussed in [124]. Let us consider the scenario depicted in Fig. 5.3(a). An incident PW is coming from a certain direction $(\theta_{inc}, \phi_{inc})$. It is scattered by the reflector and couples to the lens antenna located at $\vec{\rho_l}$ in the focal plane of the reflector. The detailed lens geometry is shown in Fig. 5.3(b). Here we consider an elliptical lens with the diameter D_l, the rim distance R_l (corresponds to the truncation angle θ_0^l), and the lens f-number $f_{\#}^l = R_l/D_l$. The phase center of the feed is placed at the lens focal plane and the feed lateral position is displaced $\vec{d_a}$ with respect to the lens focus.

Each lens antenna in the FPA is optimized to maximize the aperture efficiency η_{ap} of the reflector for a specific PW direction. This efficiency can be defined as the ratio of the power received by the lens feed, $P_r(\theta_{inc}, \phi_{inc})$, under the impedance-matched condition, to the power incident onto the reflector, P_{inc}^{PW}, at broadside:

$$\eta_{ap}(\theta_{inc}, \phi_{inc}) = \frac{P_r(\theta_{inc}, \phi_{inc})}{P_{inc}^{PW}}, \tag{5.1}$$

where $P_{inc}^{PW} = 0.5 \left|E_0\right|^2 A_{ref}/\zeta_0$, A_{ref} is the physical area of the reflector and E_0 is the amplitude of the PW electric fied. The power $P_r(\theta_{inc}, \phi_{inc})$ in (5.1) can be evaluated using the reaction integral in (1.1) between the incident field scattered from the reflector to an arbitrary surface S and the field radiated by the lens feed on the same surface. This power is expressed as follows:

$$P_r(\theta_{inc}, \phi_{inc}) = \frac{\left| \iint_S \vec{H}_{LWA}(\vec{r}) \cdot \vec{M}_{inc}(\vec{r}, \theta_{inc}, \phi_{inc}) - \vec{E}_{LWA}(\vec{r}) \cdot \vec{J}_{inc}(\vec{r}, \theta_{inc}, \phi_{inc}) dS \right|^2}{16 P_{rad}^{LWA}}, \tag{5.2}$$

where $\left[\vec{E}_{LWA}(\vec{r}), \vec{H}_{LWA}(\vec{r})\right]$ is the field radiated by the LWA on the surface S in the transmission (Tx) mode. $\vec{M}_{inc} = \vec{E}_{ref} \times \hat{n}$ and $\vec{J}_{inc} = \hat{n} \times \vec{H}_{ref}$ are the equivalent currents evaluated using the field scattered by the reflector on the same surface, i.e., $\left[\vec{E}_{ref}(\vec{r}), \vec{H}_{ref}(\vec{r})\right]$.

To maximize η_{ap} in (5.1), we need to optimize the integrand in (5.2), and this can be done by conjugately matching $\left[\vec{E}_{LWA}, \vec{H}_{LWA}\right]$ with $\left[\vec{M}_{inc}, \vec{J}_{inc}\right]$. In previous works [16, 38, 123], this field correlation was performed on an equivalent sphere inside the lens, i.e., S_{FO} in Fig. 5.3(b). Particularly in [123], the scattered reflector's fields have to be propagated to this sphere using a GO method in combination with a FO method. Such procedures are useful to design the lens geometries in region 1; however, for larger scanning angles, it is more convenient to use an equivalent aperture on the top of the lens surface for evaluating (5.1), i.e., S_{ap} in Fig. 5.3(b). In this way, the scattered fields of the reflector are only computed once outside the multi-parametric optimization loop. In different regions (see Fig. 5.1), different parameters of lens antennas are optimized as follows.

- Region 1: elliptical lens geometry $(D_l, f_{\#}^l)$. The same geometry is used in the entire region.
- Region 2: the location of the feed inside the lens, $\vec{d_a}$. The elliptical lens geometry is kept the same.
- Region 3: $\vec{d_a}$ increases and D_l is enlarged (a limit is set to $10\lambda_0$). The same $f_{\#}^l$ is kept.
- Region 4: $\vec{d_a}$, D_l, and the shape of the lens surface (via Zernike polynomials) change. The same $f_{\#}^l$ is kept.

This procedure is done in MATLAB using its global optimization tool which runs parametric analysis for all the mentioned parameters, with the goal of maximizing (5.1). The explicit optimization for each region and the corresponding results will be shown in Section 5.4 and 5.5.

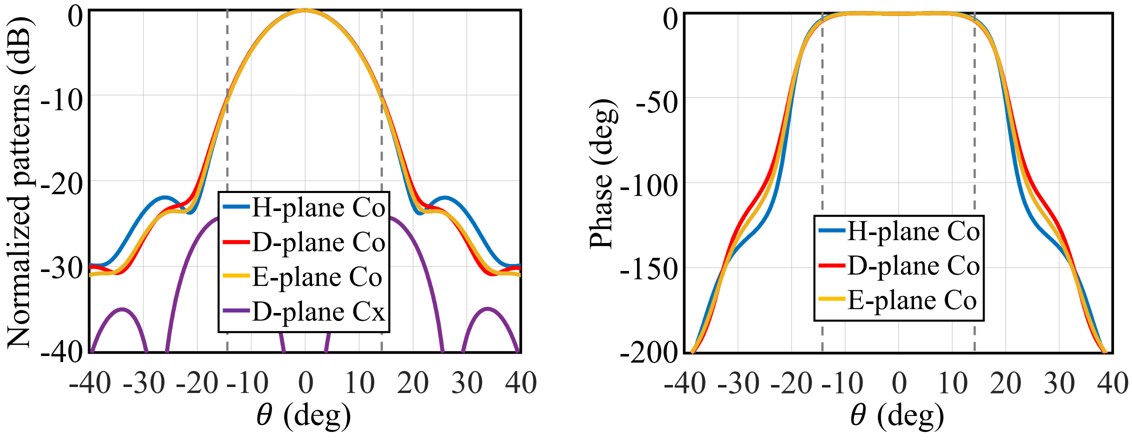

(a) (b)

Figure 5.4: Secondary far field radiated by the lens antenna towards the reflector: (a) amplitude and (b) phase. The dashed grey lines represent the reflector truncation angle θ_0^r. A quarter-wavelength matching layer ($\varepsilon_r = 2.62$) is used.

5.4 Lens Antenna Optimization for Moderate Scanning Angles

The above-mentioned regions in Fig. 5.1 are only related to the geometry of the reflector and approximate formulas were given in [123] for the region limits. For our considered imaging scenario, the region limits defined in terms of the number of beams (half-power beam width) are: $N_1 = 8.8$, $N_2 = 15.5$, and $N_3 = 23.6$, which corresponds to the scanning angles of $\theta_{inc} = N\lambda_0/D_r = 3.6°$, $6.3°$, and $9.6°$. In the first three regions, the lenses have elliptical shapes and the optimization of their geometries are discussed in this section.

5.4.1 Lens Antenna Design in Region 1

In the first region, all lenses are identical so we only consider the central lens design. The diameter of the lens is designed to be $D_l = 4.4\lambda_0$ which corresponds to -20 dB truncation of the reflector's focal field on the lens FO sphere, S_{FO}. The f-number of the lens $f_\#^l$ is obained by maximizing (5.2) when the field correlation surface is S_{FO}. The optimal $f_\#^l = 0.925$ ($\theta_0^l = 32.7°$) leads to an excellent field matching between the field radiated by the LWA on S_{FO}, i.e., $\vec{E}_{LWA}$, and the reflector's scattered field on S_{FO}, i.e., $\vec{E}_{ref}$, as shown in Fig. 5.2(c) and 5.2(d). Note that $\vec{E}_{LWA}$ has to be evaluated in the near field with $R_l = 8\lambda_d$ since the lens is small [67]. The amplitude is symmetric in all planes and the phase is almost constant until 25°. Here we implement a quarter-wavelength matching layer made of parylene ($\varepsilon_r = 2.62$) on the lens surface to improve the transmission between the quartz-air interface by about 0.5 dB.

We also evaluate the far field radiated by this lens antenna. This field is calculated using an in-house PO code [38] and shown in Fig. 5.4. The pattern is symmetric and illuminates

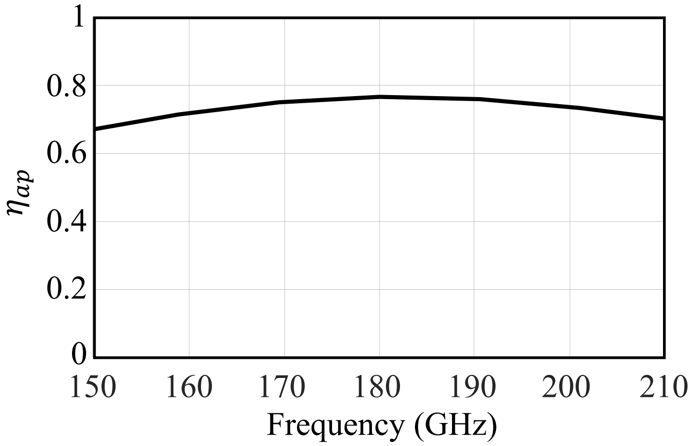

Figure 5.5: Optimized aperture efficiency η_{ap} of the reflector coupled to the central lens antenna with $D_l = 4.4\lambda_0$ and $f_{\#}^l = 0.925$. A quarter-wavelength matching layer ($\varepsilon_r = 2.62$) is used.

the reflector with the -10 dB amplitude taper at the reflector's rim where $\theta_0^r = 14.25°$ (shown by the dashed grey lines). Moreover, the phase within the relevant angle is almost constant. The resulting aperture efficiency of the lens-reflector system, η_{ap}, is plotted in Fig. 5.5 versus frequencies. It shows broadband behaviour and the value at 180 GHz is 76.7% which is comparable to the performance of the design based on silicon lenses [123].

The design rules of such lens antennas for other lens materials (plastic and silicon) are briefly discussed in Appendix E.

5.4.2 Lens Antenna Design in Region 2 and 3

The lens f-number remains the same as $f_{\#}^l = 0.925$ for lenses in all regions. In region 2, the lens diameters are still $D_l = 4.4\lambda_0$ but in region 3 they are enlarged to follow the reflector's focal fields [123] (with a limitation on the maximum lens diameter of $10\lambda_0$). Fig. 5.6 shows the variation of D_l as a function of the number of beams scanned.

Starting from region 2, the phase term introduced by the non-broadside PW in the reflector aperture presents a significant linear term in $\vec{E}_{ref}$. Therefore, the feed should be displaced along the focal plane of the lens to add an extra phase term in $\vec{E}_{LWA}$ to compensate the incident linear phase. An estimation of the feed displacement $\vec{d}_a$ can be obtained using the ray tracing approximation. We can consider a PW arriving at the lens with an incident angle of $(\theta_{inc}, \phi_{inc})$. Using Snell's law, the position where these transmitted rays are focused, also referred to as the flash point, can be estimated as follows:

$$\vec{\rho}_{fp} = \frac{f_{\#}^l D_l}{1-e}\left[1 - e\cos\left(\sin^{-1}\frac{1}{2f_{\#}^l}\right)\right] \cdot \tan\left[\sin^{-1}\left(e\sin\theta_{inc}\right)\right]\left(\cos\phi_{inc}\hat{x} + \sin\phi_{inc}\hat{y}\right), \quad (5.3)$$

where $e = 1/\sqrt{\varepsilon_r}$ is the lens eccentricity. $\vec{\rho}_{fp}$ is also plotted in Fig. 5.6 and it increases significantly as the scanning beam increases. By parametrically sweep $\vec{d}_a$ and D_l around their estimated values, we can obtain the optimal lens geometries in region 2 and 3.

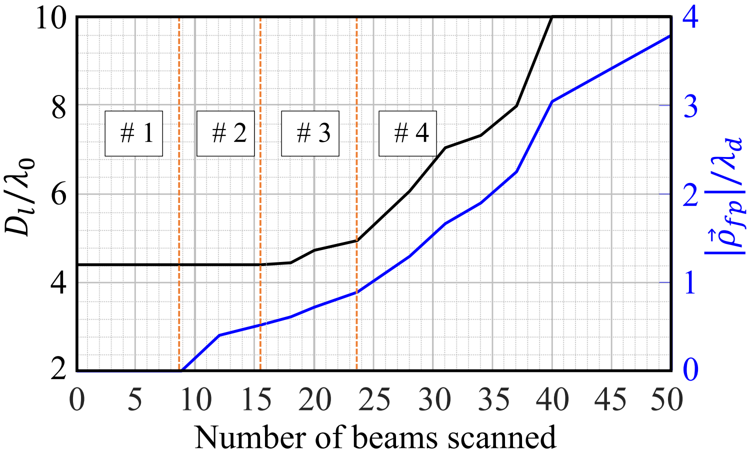

Figure 5.6: Flash point $\vec{\rho}_{fp}$ and lens diameter D_l versus the number of beams scanned. The orange lines show the borders of the four regions of the FPA.

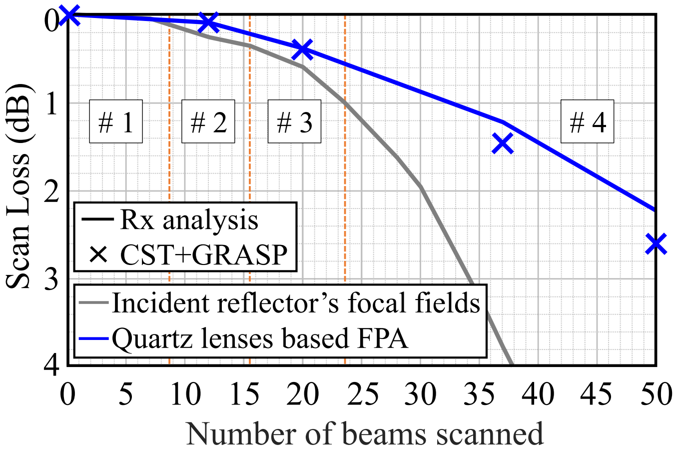

Figure 5.7: SL of the lens-coupled reflector versus the number of beams scanned. The solid line represents the SL calculated using the Rx analysis in (5.2), while the crosses are the results obtained from the full-wave simulations in the Tx mode. As a reference, the SL associated to the reflector's focal fields is shown by the grey curve. The orange lines show the borders of the four regions of the FPA.

For the optimized lens antennas in region 1-3, we have evaluated their SL when coupled to the reflector, as shown by the solid blue curve in Fig. 5.7. The crosses in the figure represent the results obtained using the full-wave simulations in CST for the respective quartz lens antennas and TICRA tools, GRASP [106], for the reflector. The agreement between the full-wave simulations and our method is excellent within the first three regions. As a reference, one can evaluate the intrinsic SL associated to the reflector's focal fields. In this case we assume $S \to 0$ and neglect any effect from the lens antennas. This is equivalent as evaluating the decay of the directivity of the incident focal fields [123]. These fields are evaluated using a PO code and their scanning directivity loss is shown by the grey curve in Fig. 5.7. As the scanning beam increases, the SL of the focal fields is becoming higher than the lens case.

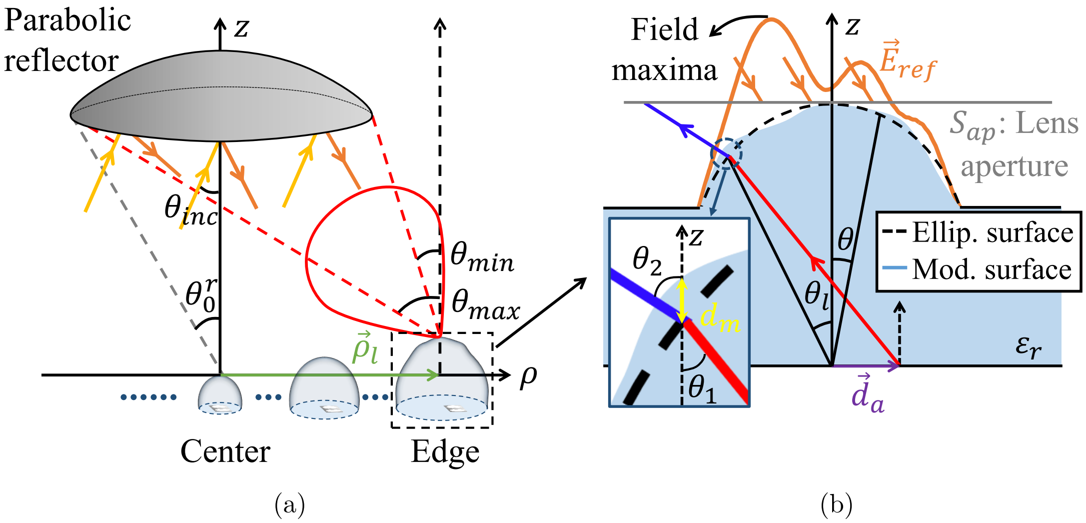

Figure 5.8: (a) Edge lens element of the FPA couples to the reflector illuminated by a PW with a large scanning angle. The red beam represents the radiated field of the lens antenna in the Tx mode. (b) Geometry of the shaped edge lens, with an illustration of the ray propagation from the feed. The reflector's focal field $\vec{E}_{ref}$ is also illustrated by the orange curve and rays.

5.5 Lens Antenna Optimization for Large Scanning Angles

In region 4 ($\theta_{inc} \geq 9.6°$), the incident PW can be scattered and focused outside the reflector's rim, as shown in Fig. 5.8(a). In this region, the focal fields are severely distorted and present severe phase aberrations. Let us consider a PW with an incident angle of $\theta_{inc} = 50\lambda_0/D_r = 20.3°$ (scanning 50 beams) as an illustrative example. The reflector's focal field on the lens aperture plane, $\vec{E}_{ref}$, is shown in Fig. 5.9. The lens diameter is enlarged to $10\lambda_0$ and its area is marked by the black dashed circle. Fig. 5.9(b) shows the zoomed-in phase pattern of the focal field in Fig. 5.9(a). We can see the amplitude is quite distorted with almost two maxima, and the phase varies significantly over the lens aperture. Thus, it would be very difficult for an elliptical lens to generate a matched pattern. For such a case, the elliptical lens surface must be modified to compensate the phase distortion in $\vec{E}_{ref}$, as graphically illustrated in Fig. 5.8(b). In this section, the optimization procedures for shaping the lens surfaces in region 4 are discussed.

5.5.1 Lens Surface Modification

The main objective of the lens surface modification is the phase matching between the fields $\left(\vec{E}_{LWA}, \vec{H}_{LWA}\right)$ and the currents $\left(\vec{M}_{inc}, \vec{J}_{inc}\right)$ in (5.2). The phase difference between these fields, i.e., the phase of the entire integrand in (5.2), is referred to as the hologram phase, Φ_{holo}^{ellip}. Here we consider an elliptical lens with its feed displaced according to Fig. 5.6. In

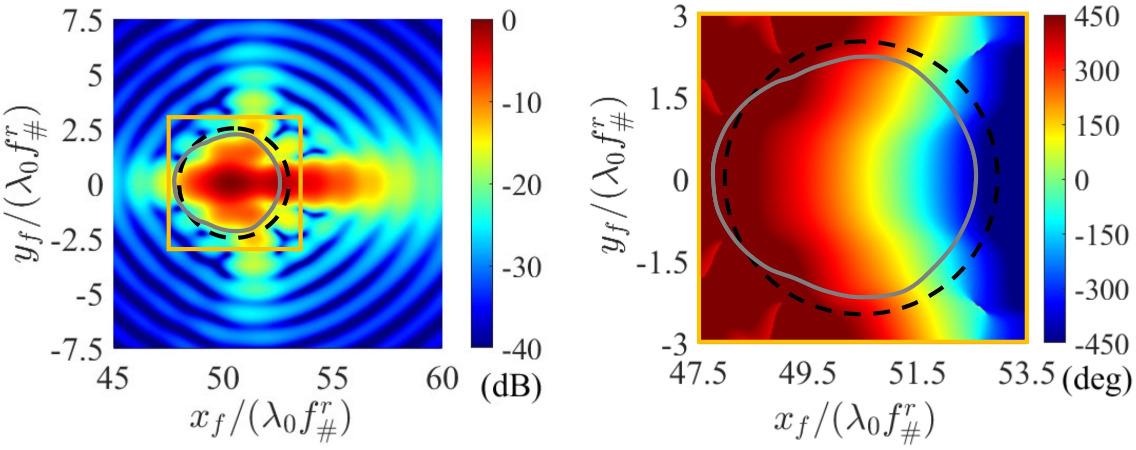

(a) (b)

Figure 5.9: Reflector's focal field $\vec{E}_{ref}$ at the top of the lens for an incident angle of $\theta_{inc} = 20.3°$: (a) amplitude and (b) phase. The dashed black circle represents the lens area, while the solid grey curve is the lens aperture plane S_{ap}. The area within the orange box in (a) is zoomed in and shown in (b) for the phase variation.

this case, a linear phase is already achieved in $\left(\vec{E}_{LWA}, \vec{H}_{LWA}\right)$ by the feed displacement. Therefore, Φ^{ellip}_{holo} mainly represents the higher-order phase aberrations.

To compensate such phase aberrations, we can change the phase distribution of the field $\left(\vec{E}_{LWA}, \vec{H}_{LWA}\right)$ by adding a certain thickness d_m in the vertical axis $\hat{z}$ to the original elliptical surface, as depicted in the inset in Fig. 5.8(b). Such surface modification leads to extra phase propagation of $\left(\vec{E}_{LWA}, \vec{H}_{LWA}\right)$ in the vertical direction: $\Delta\Phi^{a}_{ap} = -k_d \cos\theta_1 d_m + k_0 \cos\theta_2 d_m$, where k_0 and k_d are the propagation constants in free space and the lens medium, respectively; θ_1 and θ_2 are the incident and transmitted angles with respect to the $\hat{z}$ axis, repectively. By imposing the new hologram phase to be 0, i.e., $\Phi^{ellip}_{holo} + \Delta\Phi^{a}_{ap} = 0$, the lens surface modification is derived as follows:

$$d_m(\theta,\phi) = \frac{\Phi^{ellip}_{holo}(\theta,\phi)}{k_d \cos\theta_1 - k_0 \cos\theta_2}. \tag{5.4}$$

Note that d_m represents the ideal surface modification and it will lead to 100% phase matching in (5.2). However, directly using (5.4) can lead to lens modification with rapid changes in the vertical direction due to the jump of phase, especially for non-shallow lenses. This behavior is illustrated by an example shown in Fig. 5.10(a). Here the lens modification is optimized for the case of $\theta_{inc} = 20.3°$. We can observe significant height (phase) variation at the edge of the E-plane. This will have strong distortion of the far field radiated by the lens.

To obtain a smoother surface with an unique tangent plane at every point, we approximate d_m using a Zernike polynomial expansion with a certain number of modes M and N, Z^M_N [125]. This Z^M_N is then added on the top of the the elliptical surface Z^{ellip}_l to obtain

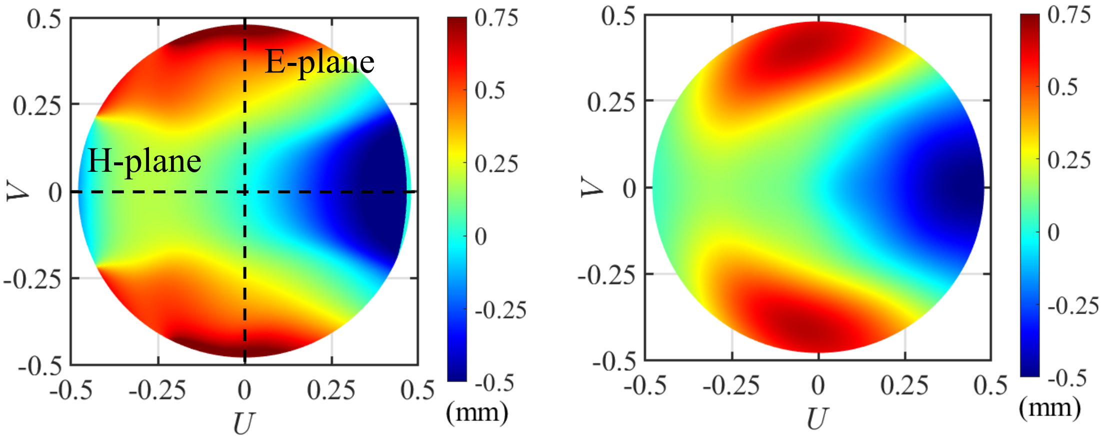

(a) (b)

Figure 5.10: Optimized lens surface modification: (a) the ideal one and (b) the smoothed Zernike surface.

the shaped lens surface Z_l^{mod} as follows:

$$\begin{aligned} Z_l^{mod}(\theta,\phi) &= Z_l^{ellip}(\theta) + Z_N^M(\theta,\phi) \\ &= \frac{a(1-e^2)\cos\theta}{1-e\cos\theta} + \sum_{m=0}^{M}\sum_{n=m}^{N}\left[A_n^m O_n^m(\sin\theta,\phi) + B_n^m E_n^m(\sin\theta,\phi)\right], \end{aligned} \tag{5.5}$$

where a is the semi-major axis of the elliptical lens; O_n^m and E_n^m are the odd and even Zernike polynomials, respectively; A_n^m and B_n^m are the corresponding weights which are calculated by projecting $d_m(\sin\theta,\phi)$ on these orthogonal polynomials. For a specific d_m, we can tune the values of (M,N) to obtain a more accurate expansion. For d_m in Fig. 5.10(a), the optimized Zernike modes are $M = 24$, $N = 2$, and the approximate surface is shown in Fig. 5.10(b). This surface is smoother and leads to 93% phase matching efficiency.

In region 4, the optimization procedures are described as follows. For each set of D_l and $\vec{d}_a$, we first evaluate the ideal modification d_m using (5.4), and then smooth d_m with a Zernike expansion Z_N^M to create a modified surface Z_l^{mod} using (5.5). We parametrically optimize the mode number $(M,\ N)$ to maximize η_{ap} with the modified lens antenna. Note that here we only change the mode number. The weights A_n^m and B_n^m are decided according to d_m and they are not optimized individually. Finally, we change the combination of D_l and $\vec{d}_a$ and redo the steps, until a maximum η_{ap} is obtained.

5.5.2 Application Case of 50 Beams' Scanning

Let us consider the most challenging lens design for our imaging scenario, i.e., the edge lens element of the FPA coupled to the PW with $\theta_{inc} = 20.3°$. This lens is located outside the reflector's rim with the displacement of $\vec{\rho}_l = +50.47\lambda_0 f_\#^r\ \hat{x}$ from the reflector's focus which corresponds to the rim angles of $\theta_{min} = 6.2°$ and $\theta_{max} = 31.5°$; see Fig. 5.8(a). The

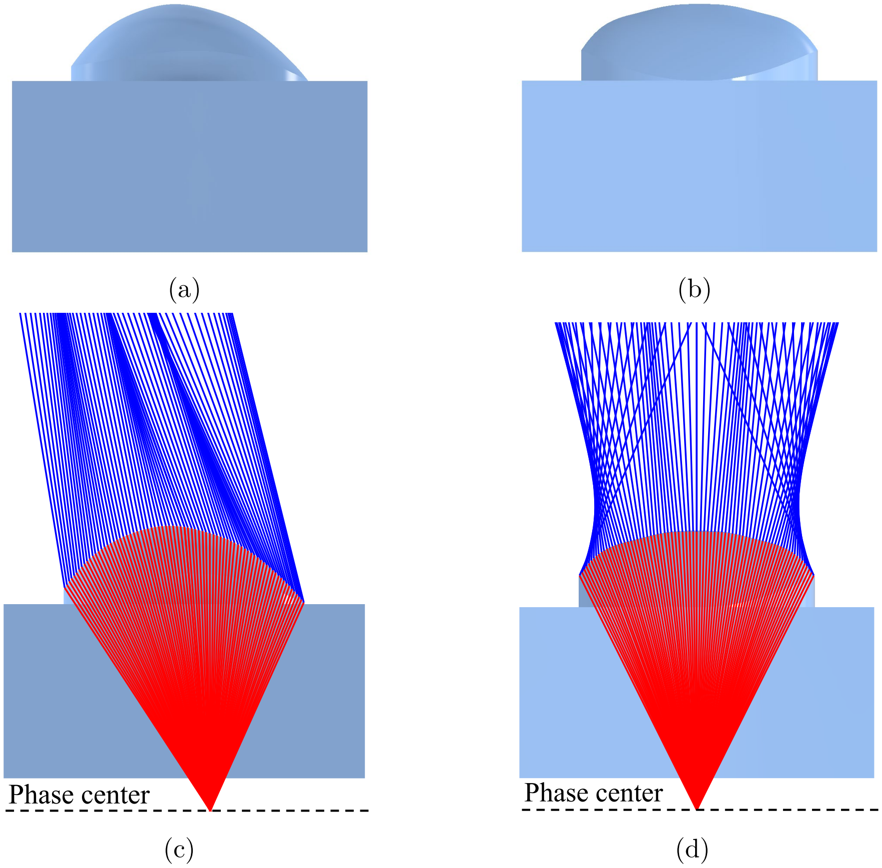

Figure 5.11: Optimized shaped lens surface: (a) and (b) represent the surfaces viewed in the H- and E-planes, respectively. (c) and (d) show the corresponding ray tracing when the antenna is in the Tx mode. The red and blue rays correspond to the rays inside and outside of the lens, respectively.

optimized lens antenna parameters are $D_l = 10\lambda_0$, $\vec{d_a} = +2.11\lambda_d\ \hat{x}$, and $M = 24$, $N = 2$ and the modified lens surface is shown in Fig. 5.11(a) and 5.11(b) for the H- and E-plane side views, respectively. The shaped surface is asymmetric and significantly different from the original ellipsoid. We also plot the ray tracing in Fig. 5.11(c) and 5.11(d) where the red and blue rays correspond to the radiation of the antenna feed inside and outside the lens in the Tx mode, respectively. The transmitted rays outside the lens point towards 16.2° as shown in Fig. 5.11(c), but due to the lens modification, the rays are not well collimated in Fig. 5.11(d) and those at the lens edge radiate towards unexpected directions.

Moreover, the lens radiated electric field, $\vec{E}_{LWA}$, on the lens aperture, S_{ap}, is plotted in Fig. 5.12. Here we use the same zoomed-in orange area in Fig. 5.9 to show the field. The lens area is marked by the black dashed circle and the plane S_{ap}, where the field correlation in (5.2) is performed, is marked by the solid grey area. This area is not circular due to the tilted propagation of the field by the displaced feed through the modified lens surface. Compared to the reflector's focal field $\vec{E}_{ref}$ in Fig.5.9, the amplitude of $\vec{E}_{LWA}$ matches well with that in Fig. 5.9(a) and its phase is conjugate to that in Fig. 5.9(b). As the result,

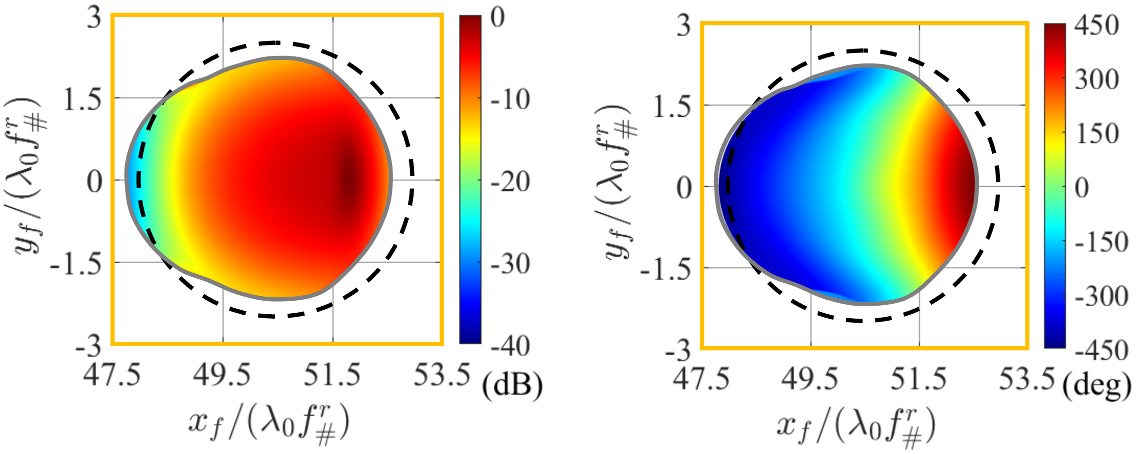

(a)

(b)

Figure 5.12: Lens GO field on the lens aperture S_{ap} within the orange area depicted in Fig. 5.9: (a) amplitude and (b) phase.

this shaped lens can couple best to the reflector with the optimized $\eta_{ap} = 46\%$ and the SL of this case is 2.2 dB which is shown in Fig. 5.7. This value is much lower than that of the reflector's focal field which is about 6 dB.

5.5.3 Far Field of the Lens-coupled Reflector for 50 Beams' Scanning

The far field radiated by the mentioned shaped lens antenna is calculated using the in-house PO code in Tx and is compared to the full-wave simulation where the complete lens plus feed geometries were modelled and simulated. Here, the dielectric loss of quartz is not included in the simulation. The gain of the lens antenna is the product between its directivity and the lens radiation efficiency which includes the feed spillover efficiency within the lens angular domain and the reflection efficiency through the lens surface. Fig. 5.13(a) plots the co-pol lens secondary fields along the H- (scanning plane) and the E-planes at 180 GHz. Fig. 5.13(b) and 5.13(c) show the co-pol and cross-pol fields (from CST) in the UV plane, respectively. We can observe excellent agreement between the PO approach and the full-wave simulation within the reflector's rim, i.e., the grey dashed lines. The patterns are asymmetric in the scanning plane and point towards 16.2°. The maximum cross-pol level normalized to the co-pol maxima is below -18 dB (largest value) at 150 GHz and -21 dB at 180 GHz, similar to the values reported in [16]. The optimization via the field correlation method ensures this pattern illuminates and couples well to the reflector. For comparison, the pattern of an elliptical lens (without the surface modification) with the same diameter is also shown. It is more directive and has a much higher gain because this shape couples better to the LWA feed; however, this field does not couple well to the reflector, as predicted by the field correlation and will be shown in the following. It is worth mentioning that the full-wave simulation took about 5 hours to simulate this shaped

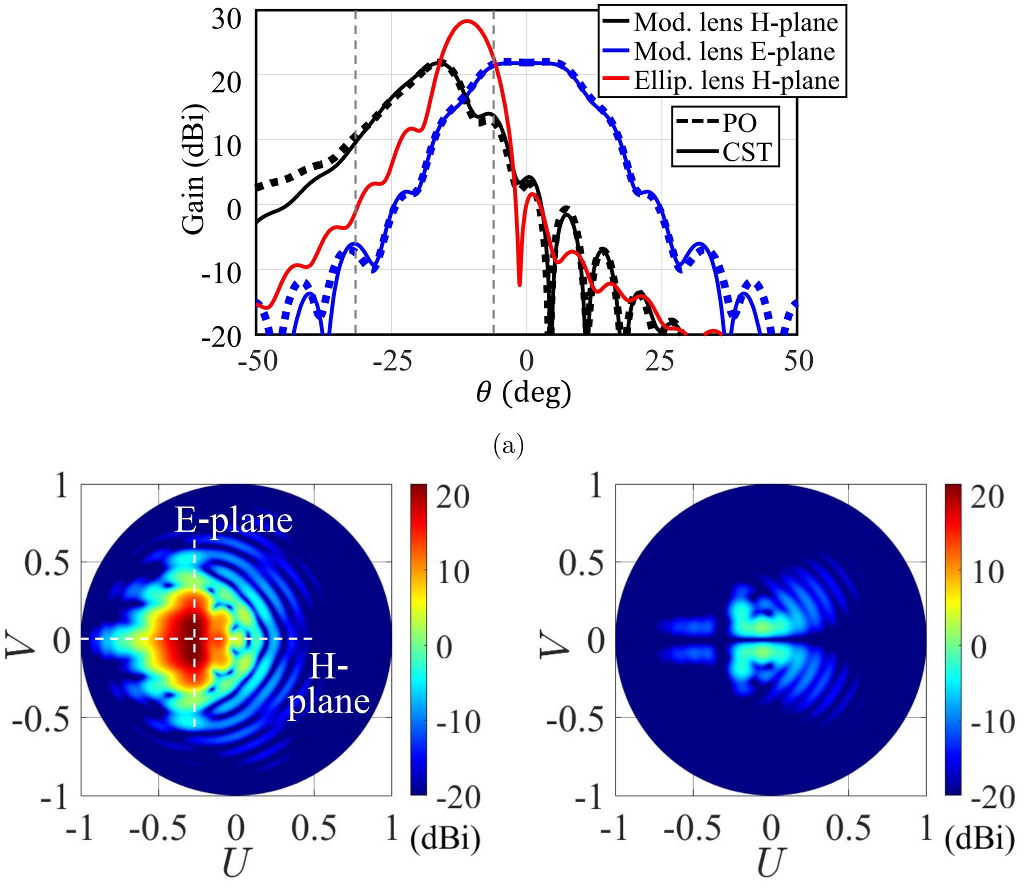

(a)

(b)

(c)

Figure 5.13: Secondary far field radiated by the optimized shaped lens antenna towards the reflector at 180 GHz: (a) comparison of the co-pol patterns between the PO approach and the full-wave simulation in the H- (scanning plane) and the E-planes; The field radiated by an elliptical lens with the same diameter is also shown as a reference. The dashed grey lines mark the rim angles $\theta_{min} = 6.2°$ and $\theta_{max} = 31.5°$ of the reflector in the H-plane. (b) Full-wave co-pol pattern shown in the UV plane, and (c) cross-pol pattern.

lens antenna, while our method took about 5 minutes on the same PC, i.e., 60 times faster.

The far field of the reflector is evaluated using the commercial PO code in GRASP. We import the lens secondary field into GRASP as a tabulated source and radiate it towards the reflector. The resulting reflector's far field at 180 GHz is shown in Fig. 5.14 where 5.14(a) plots the co-pol patterns in the H- (scanning) plane; 5.14(b) and 5.14(c) plot the co-pol and cross-pol patterns (CST+GRASP) in the UV plane, respectively. The maximum cross-pol level normalized to the co-pol maxima is below -25 dB (largest value) at 150 GHz and -30 dB at 180 GHz. As expected, the shaped lens antenna achieves a more directive beam and its gain is about 4 dB higher than that of the elliptical lens. Moreover, the reflector with the shaped lens antenna points towards 20.3° which corresponds to the intended scanning angle θ_{inc}. The agreement between the PO method and the full-wave simulation is excellent. From these far fields we can also evaluate the directivity and the aperture efficiency of the reflector. With the shaped lens antenna, $Dir^{PO} = 50.6$ dBi,

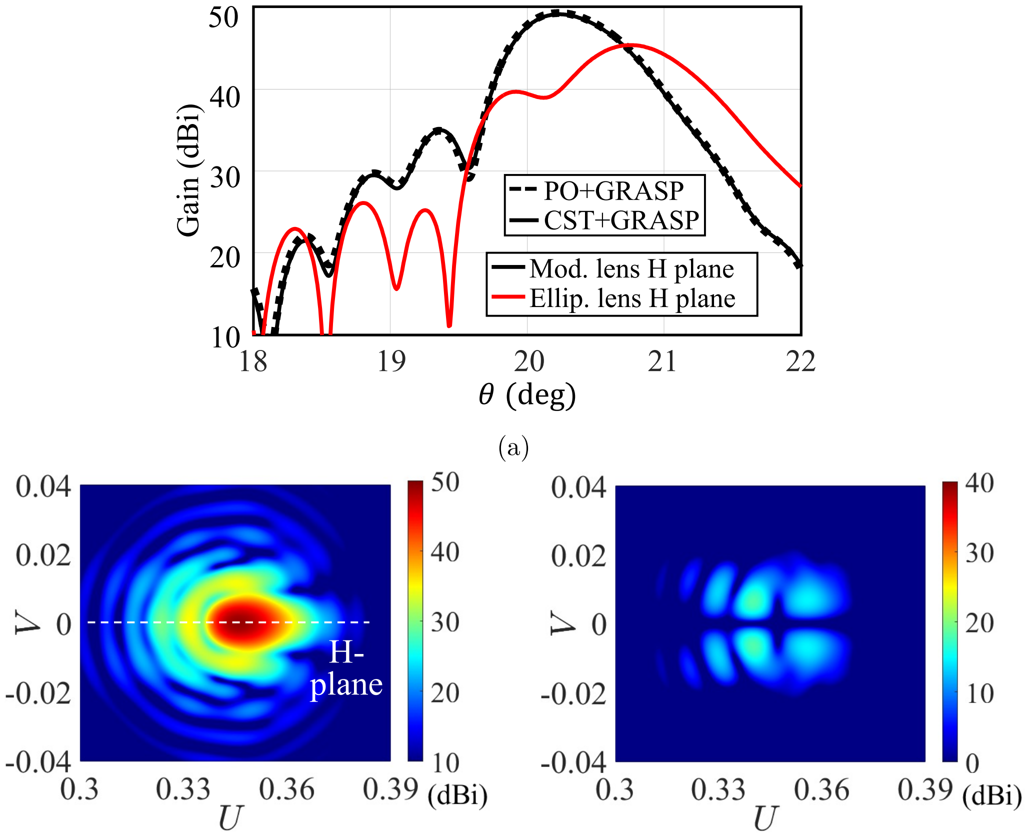

(a)

(b)

(c)

Figure 5.14: Far field radiated by the lens-coupled reflector at 180 GHz: (a) comparison of the co-pol patterns between the PO approach and the full-wave simulation in H-plane, (b) full-wave co-pol pattern shown in the UV plane, and (c) cross-pol pattern.

$\eta_{ap}^{PO} = 42.8\%$, $Dir^{CST+GRASP} = 50.5$ dBi, and $\eta_{ap}^{CST+GRASP} = 41.3\%$; while for the elliptical lens antenna $Dir^{CST+GRASP} = 46.2$ dBi and $\eta_{ap}^{CST+GRASP} = 17.4\%$ which are much lower. The corresponding SL for the shaped lens antenna is $SL^{CST+GRASP} = 2.6$ dB and is shown in Fig. 5.7 by the cross at 50 beams.

5.5.4 Scan Loss Versus the Number of Scanned Beams

By following the described optimization procedures, we have designed the lens antennas in all regions and plotted the SL of the FPA in Fig. 5.7. The agreement between our Rx analysis and the full-wave simulations is excellent in all regions. The full-wave SL is slightly higher in region 4 because of the significant surface modification of the quartz lenses. Such modification leads to shadow regions which slightly decrease the lens radiation efficiency, and makes the field correlation more difficult. Even though, this FPA achieves much better SL than the reflector's incident focal fields when scanning at large angles. We also plot the far fields radiated by the reflector in Fig. 5.15 (H-plane) for different lens elements. We can see the far fields become more and more distorted as the scanning angle increases. This

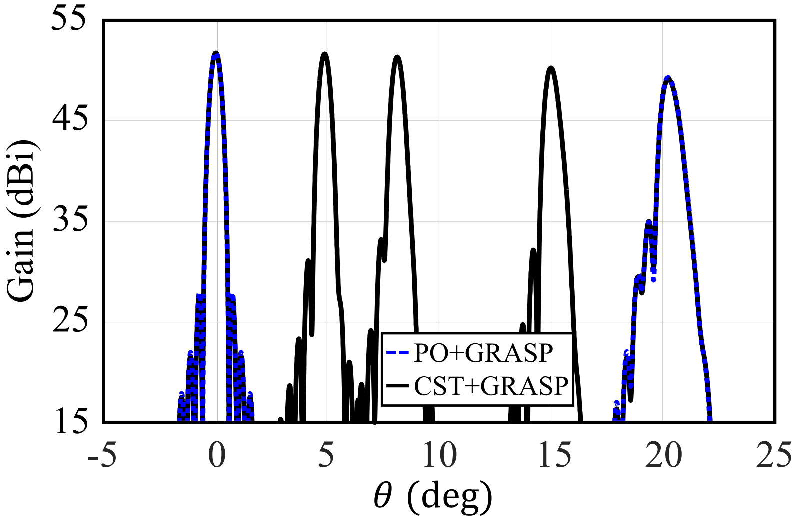

Figure 5.15: Far fields radiated by the reflector in H-plane for different scanning angles. The reflector is illuminated by the optimized quartz lens antennas placed in H-plane. Comparison between the PO results and the full-wave results is also shown for the broadside and the 20.3° scanning cases.

distortion leads to a drop of the gain of the scanned beams with respect to the broadside beam which is equivalent to the reported SL values. In addition, the agreement between the PO results and the full-wave results is excellent.

As a comparison, the simulated/measured performance of the state-of-the-art FPAs is listed in Table 5.1. For a horn-based FPA, if the surfaces of the primary reflectors are not modified, the horns need to be tilted and arranged along a curved focal plane to better couple to the reflector [113]. This will lead to a high broadside aperture efficiency η_{ap} of the reflector, but the SL is limited by the shapes of the horn's radiation patterns. To further improve the scanning performance, a commonly used approach is to modify the shapes of the primary reflectors according to a ray tracing or a GO-based method [23, 112, 126, 127]. At the same time, the curved focal planes are optimized for the shaped reflectors. This will indeed lead to very low SL when scanning to large angles [23, 126]; however, the compromise is the much lower η_{ap}. On the contrary, the proposed shaped lens antenna achieves a low SL of 2.6 dB when scanning to 20.3° while keeping a high broadside η_{ap} of 75%, without shaping the primary reflector. Moreover, in this work, the lenses are placed on a flat focal plane, enabling easier monolithic integration at high frequencies.

Table 5.1: Simulated/measured performance of the state-of-the-art FPAs

References	**This work** **sim./meas.**	**[112]** **sim.**	**[113]** **sim./meas.**	**[126]** **sim.**	**[23]** **sim./meas.**	**[127]** **sim./meas.**
Frequency (GHz)	180	30	220	12.75	500	76.5
$\boldsymbol{D_r}$ **(**$\boldsymbol{\lambda_0}$**)**	141.4	80	168.7	195×186	223.3	23
Broadside Dir. (dBi)	52.5	46	≈ 54	54.3	55.3	≈ 35.9
Scan loss (dB)	2.6/2.6 at 20°	≈ 3.7 at 15°	3 at 12.3°	0.25 at 20°	1.2 at 25.4°	0.54/$\approx$ 1.1 at 13.5°
Broadside $\boldsymbol{\theta_{3dB}}$ **(deg)**	0.46	≈ 2.1	0.5/0.5	≈ 0.4	0.25/0.25	$\approx 3/\approx 3.2$
Broadside $\boldsymbol{\eta_{ap}}$	0.75	0.8	≈ 0.8	0.58	≈ 0.36	0.67
Method	- Shaped lenses - Flat FPA	- Shaped reflectors - Flat horn FPA	- Dragonian reflectors - Curved horn FPA	- Shaped reflectors - Curve horn FPA	- Shaped reflectors -Flat FPA (tilted horns)	- Reflect arrays - Curved horn FPA

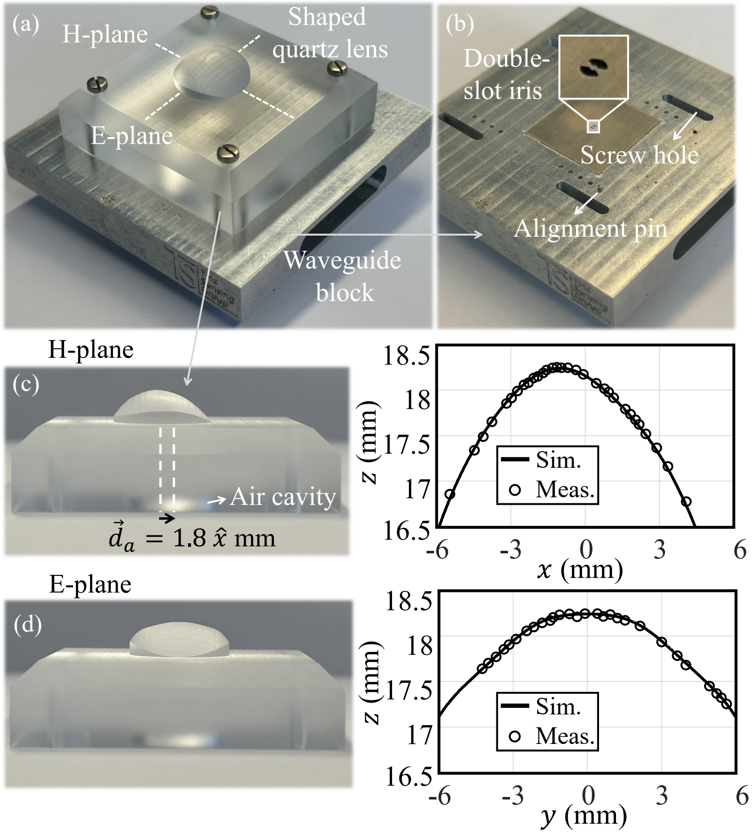

Figure 5.16: (a) Photographs of the fabricated quartz lens antenna. (b) Details of the waveguide block, including the double-slot iris feed, the alignment pins and the screw holes. (c) and (d) show the side views of the shaped quartz lens and the corresponding surface profiles compared to the designed shapes. The air cavity and the feed displacement are also shown.

5.6 Antenna Prototype and Measurement

We have fabricated and measured a prototype to validate the proposed concept of lens shaping. Here we consider the edge lens design discussed in Section 5.5.2 and shown in Fig. 5.11, and the LWA feed described in Section 5.2.

5.6.1 Antenna Prototype

The fabricated quartz lens antenna is shown in Fig. 5.16(a). It consists of three parts: the double-slot iris feed [see Fig. 5.16(b)], the waveguide block which is tapered from a square waveguide to a standard WR5 waveguide flange, and the shaped quartz lens with the air cavity [see Fig. 5.16(c) and 5.16(d)]. The waveguide block and the double-slot iris are the same as those in [16] and operate from 140 GHz to 220 GHz. The feed is displaced $\vec{d}_a = +1.8\hat{x}$ mm with respect to the lens apex as shown in Fig. 5.16(c), and it is aligned with the lens using two metal pins. The whole structure is assembled using four screws at the lens edges.

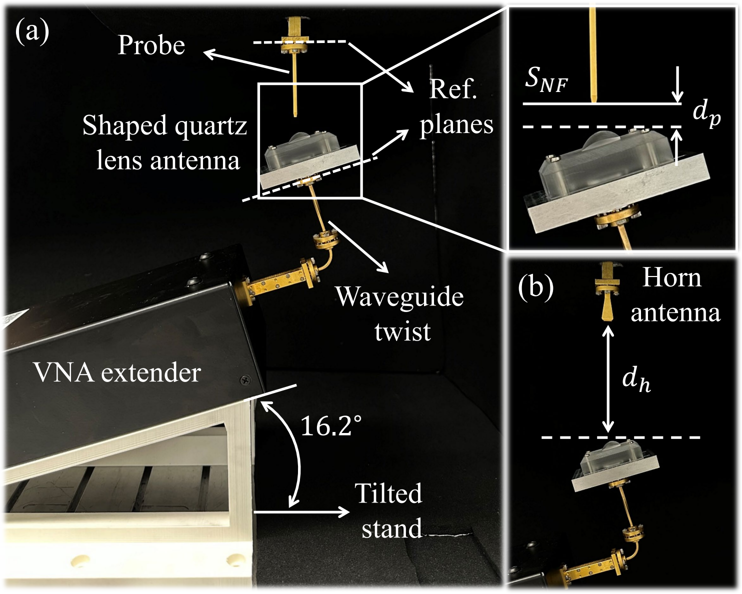

Figure 5.17: (a) Measurement setup for the shaped quartz lens antenna. The antenna is fed by a VNA extender through a waveguide twist. The extender is mounted on a stand tiled 16.2°. A WR5 probe is used to measure the near fields on the plane S_{NF} which is d_p away from the top of the lens (see the inset). (b) Gain measurement: a standard WR5 horn antenna is placed d_h from the top of the lens. In both measurements, absorbers were installed around the lens antenna, the probe, and the horn antenna to suppress multiple reflections, but they are not visible in the figure.

The quartz material (fused silica) was provided by Heraeus Group [128] (Suprasil 3001 Quartz material series) with homogeneous permittivity of $\varepsilon_r = 3.75$ and dielectric loss of $\tan\delta = 4.2 \times 10^{-4}$, over the considered frequency band. These values were measured for various quartz samples using our antenna near-field measurement setup before the fabrication. The shaped quartz lens was fabricated by LouwersHanique using their selective laser etching technique [129]. The lens surface was measured by the same company using an interferometer. The lens profiles along the main planes are shown in Fig. 5.16(c) and 5.16(d), compared to the designed ones in Fig. 5.11. The agreement is excellent and the surface difference meets the expectation within ±40 µm. Here to facilitate the fabrication of the first prototype, the matching layer is not included. As will be discussed in the following, this will decrease the system aperture efficiency by about 0.5 dB, but the SL remains the same. The measured reflection coefficient is below -10 dB over the considered frequency band with small oscillations. Therefore, it may not be necessary to implement a matching layer for certain applications.

5.6.2 Antenna Near-field Measurement

The prototype was measured at TU Delft using the measurement setup shown in Fig. 5.17. The lens antenna is fed by a VNA extender from Virginia Diodes (WR5.1-VNAX) through a waveguide twist (to rotate the polarization). The extender is mounted on a 3D-printed plastic stand which has a tilt angle of 16.2°. This angle corresponds to the main beam

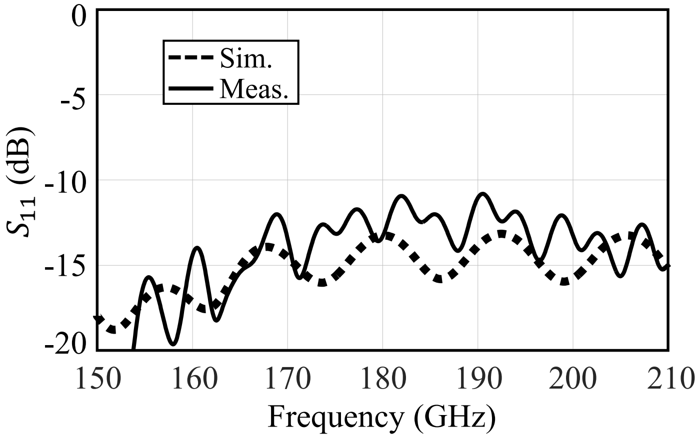

Figure 5.18: Measured S_{11} of the fabricated quartz lens antenna compared to the simulation where the same structure was modelled.

angle of the lens secondary field at 180 GHz (see Fig. 5.13). By using such a stand, the secondary field will point at 0° and its polarization will be parallel to the ground. This facilitates the antenna near-field measurement over a plane parallel to the ground.

This setup was calibrated using a TRL kit and the reference planes of both waveguide ports are shown in Fig. 5.17(a). The measured reflection coefficient of the lens antenna is shown in Fig. 5.18 and compared to the simulation where the same structure was modelled. The measured S_{11} is below -10 dB over the considered frequency band agreeing very well with the simulation. If a matching layer is implemented, the oscillations in S_{11} will be further reduced; see Fig. 5.2(b).

The far-field patterns of the lens antenna are obtained from the planar near-field measurement where a WR5 probe is used. The probe scans a square plane S_{NF} at the top of the lens with the area of 40 mm × 40 mm and the distance of $d_p = 11.5$ mm, as depicted in the inset in Fig. 5.17(a). The position of the probe is controlled by a CNC scanner with the step size of 0.3 mm. During the measurement, the probe and the lens antenna were surrounded by absorbers to suppress the multiple reflections between the lens and the lab's surroundings. By implementing the transformation from near fields to far fields at each frequency, the corresponding co-pol far-field patterns at 160 GHz, 180 GHz, and 200 GHz are shown in Fig. 5.19(a)-(c) along the main planes and compared to the simulations. The agreement is excellent in both planes at all frequencies and the difference in the main beam position is less than 0.8°.

The realized gain is quantified resorting to Friis equation and the measured coupling coefficient S_{12} between the lens antenna and a standard WR5 horn antenna shown in Fig. 5.17(b). The horn is placed $d_h = 96.5$ mm away from the lens top and was surrounded by absorbers during the measurement. The realized gain considers the measured S_{11} in Fig. 5.18, the dielectric loss in quartz, and the conductor loss in the waveguide, which are listed in Table 5.2. The dielectric loss is estimated to be 0.2-0.3 dB from 150-210 GHz. The waveguide was fabricated at the workshop at TU Delft with very high metal roughness, leading to an equivalent low metal conductivity of 3.6×10^5 S/m, as discussed in [16]. The

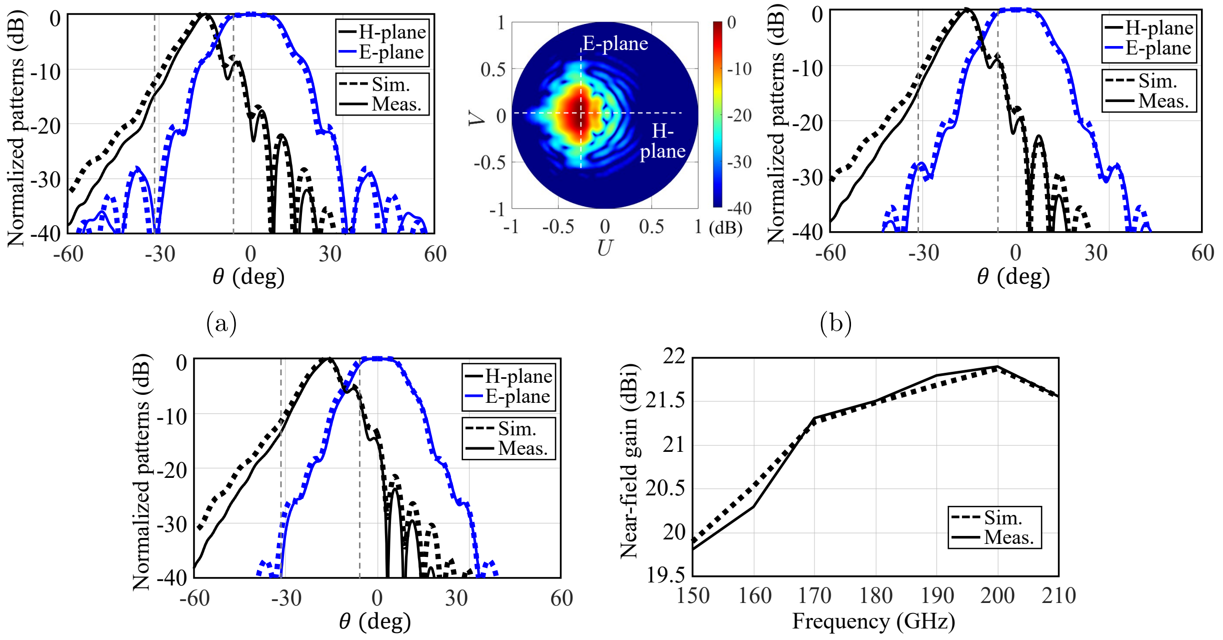

(a) (b)

(c) (d)

Figure 5.19: Measured co-pol far fields at (a) 160 GHz, (b) 180 GHz (the pattern in the UV plane is also shown), and (c) 200 GHz. The dashed grey lines mark the rim angles of the reflector in the H-plane. (d) Measured near-field gain when $d_h = 96.5$ mm. The impedance mismatch loss and the conductor loss in the waveguide are not included in the gain.

Table 5.2: Loss terms relevant to the prototype from 150 GHz to 210 GHz

Frequency (GHz)	Waveguide (dB) 3.6×10^7 S/m	Waveguide (dB) 3.6×10^5 S/m	Dielectric (dB)	Mismatch (dB)
150	0.14	1.38	0.19	0.16
180	0.11	1.06	0.23	0.2
210	0.1	0.99	0.27	0.14

total length of the waveguide is about 1.4 cm and the simulated waveguide loss is from 1.4 to 1 dB (150-210 GHz). This loss can be significantly decreased by using a low-roughness metallization with a much higher equivalent conductivity, e.g., 3.6×10^7 S/m, as shown in Table 5.2. By removing the measured impedance mismatch loss and the conductor loss from the realized gain, we can obtain the near-field gain of the lens antenna evaluated at $d_h = 96.5mm$. It is shown in Fig. 5.19(d) as a function of frequencies and is compared to the simulation. The measured gain is comparable to the simulated one with maximum difference of 0.2 dB over the entire frequency band. This difference is associated with the fabrication and measurement tolerances, and the estimation of the conductor loss.

Moreover, we import the measured far fields into GRASP as a tabulate source to

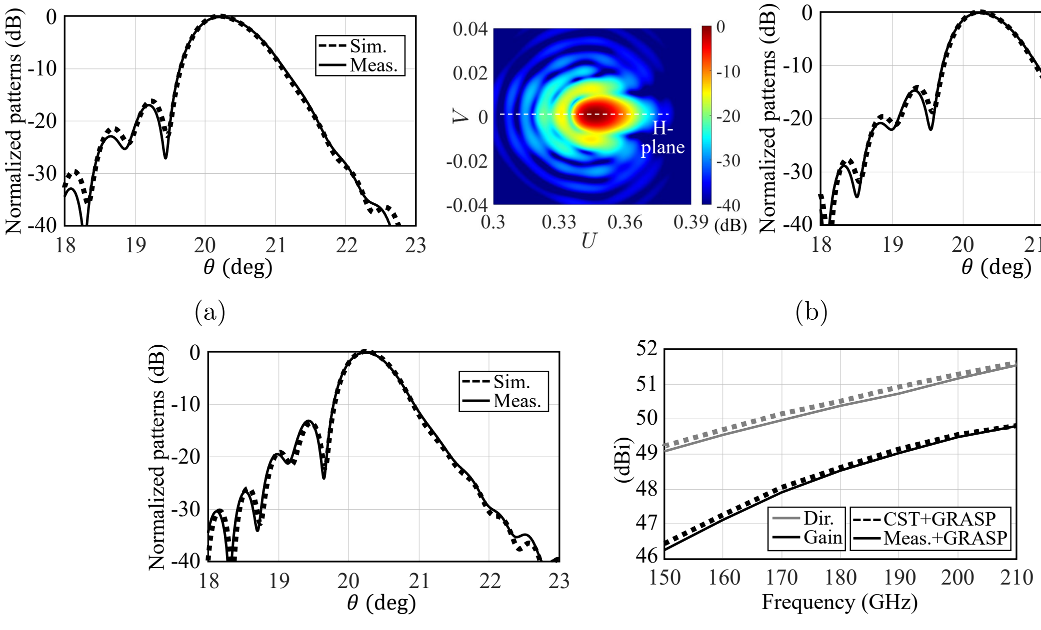

(a) (b)

(c) (d)

Figure 5.20: GRASP simulations of the reflector's co-pol far fields in the H-plane at (a) 160 GHz, (b) 180 GHz (the pattern in the UV plane is also shown), and (c) 200 GHz. In GRASP, the measured and simulated lens far fields are imported as a tabulated source. (d) Directivity and gain of the lens-coupled reflector.

evaluate the far fields radiated by the reflector. The source position is the same as that in the measurement setup. Fig. 5.20(a), 5.20(b), and 5.20(c) show the reflector's co-pol far fields in the H-plane at 160 GHz, 180 GHz (the pattern in the UV plane is also shown), and 200 GHz, respectively. The measured far fields almost overlap with the simulations, showing excellent agreement. The directivity and the gain of the reflector is plotted in Fig. 5.20(d). The measurement is less than 0.2 dB different from the simulation. Note that the simulated gain at 180 GHz is slightly lower than that in Fig. 5.14 since the matching layer is not implemented (the directivity remains the same). In this case, the simulated aperture efficiency drops about 0.5 dB to $\eta_{ap}^{CST+GRASP} = 37.1\%$, which corresponds to the drop in the lens radiation efficiency. For lenses without the matching layers, their simulated SL remains the same as that in Fig. 5.7.

5.7 Conclusion

In this chapter, a wide FoV FPA of shaped quartz lens antennas coupled to a parabolic reflector is designed. The focus is to optimize the scanning gain of the lens-reflector system when the scanning angles are large, via shaping the quartz lens surfaces. An optimization procedure is proposed for this purpose. This procedure is based on the field correlation technique introduced in Section 1.3 and is performed on the lens aperture plane. The lowest SL of the system can be achieved when the reflector's focal field and the lens radiated field on the lens aperture are conjugately matched. To achieve this, the lens surface is modified according to the phase matching (hologram phase) between the mentioned fields. An example shaped lens antenna operating at 180 GHz is discussed for an extreme case when the reflector scans 20.3° (50 beams). The far-field performance obtained from the proposed methodology is in excellent agreement with the full-wave simulations. The latter achieves a directivity of 50.5 dBi and a scanning gain loss of 2.6 dB. The optimized shaped quartz lens antenna was fabricated and measured, showing excellent agreement with the simulations. The proposed FPA can provide design rules for future photoconductive-antenna-based radar systems.

Chapter 6

Conclusion and Future Outlooks

This thesis describes the research work carried out over a period of four and a half years (from April 2019 to October 2023) in the THz Sensing Group at Delft University of Technology, Delft, the Netherlands. This project was supported by the ERC Starting Grant (ERC-2014-StG LAA-THz-CC), No. 639749. The prototype of the mm-wave antenna was developed under a contract with Huawei Technologies, Sweden AB.

The scope of this thesis is to provide guidelines for analyzing and designing lens antennas at mm and sub-mm wavelengths. Dielectric lenses are commonly used to collimate the patterns radiated by their feeds and thus enhance the gain of the systems. However, the co-optimization between the lenses and their feeds is a challenge. This work proposes to use the field correlation technique to optimize the aperture efficiency of lens antennas. First, a high-gain scanning lens phased array antenna is designed at 28 GHz for 5G point-to-point communication. Secondly, a QO link between a PCA source and a PCA receiver is accurately modelled. The detected THz pulses are then theoretically and experimentally characterized, which facilitates the design of future mm-resolution imaging systems. Finally, a FPA based on shaped quartz lens antennas is designed at 180 GHz for wide FoV imaging. This provides guidelines for the future design of an entire focal plane of PCA receivers.

In this chapter, the conclusion and the most significant results of the research are summarized. Furthermore, the outlooks for possible future work are discussed.

6.1 Field Correlation Optimization Methodology

A lens antenna can be either analyzed in Tx or Rx, being equivalent according to the reciprocity theorem. In this thesis, the analysis in Rx is proposed to optimize the aperture efficiency of a lens antenna via the field correlation reaction integral. This integral is performed on an arbitrary surface and correlates the field incident on the surface and the field radiated by the antenna feed on the same surface. Therefore, the maximum aperture efficiency can be achieved when these two sets of fields are conjugately matched. These fields can be efficiently evaluated using the GO/PO approaches, enabling an optimization procedure for the feed and the lens geometries.

In Chapter 2, the methodology is used to design the lens geometry by optimizing the broadside lens aperture efficiency when fed by a LWA. Moreover, the feed displacement for the steering cases is evaluated using this method. The surface to perform the field correlation is inside the lens as the FO sphere and the incident field is a plane wave. The lens is in the near-field region of the feed so the feed radiated field is evaluated using the near-field analysis; while the field transmitted inside the lens is calculated using the GO/FO approaches.

In Chapter 4, this methodology is used to evaluate the transfer function of a QO link between two pulsed PCAs. The field correlation surface in placed at the middle of the link for simplicity. The fields propagated on this surface are evaluated using full-wave simulations combined with the GO/PO approaches. Once the link transfer function is calculated, the current generator of the receiving Norton circuit can be accurately evaluated.

In Chapter 5, this methodology is applied for optimizing the geometries of lens elements in a FPA when coupled to a parabolic reflector. For the broadside case, the lens truncation angle is designed by optimizing the field correlation on the FO sphere. While for larger scanning cases, lens surfaces need to be modified to fulfill the conjugate field-matching condition. In fact, the field correlation method directly provides the hologram phase to be synthesized by the surface modification. The method is performed on the lens aperture plane to improve the efficiency of the involved numerical calculation. An optimization procedure is then proposed to maximize the aperture efficiency of the lens-reflector system.

The field correlation methodology for the case of plane wave incidence was published in paper J1 (see page 151).

6.2 High-gain Scanning Lens Phased Array Antenna

In Chapter 2, a hexagonally arranged scanning lens phased array antenna, with two-wavelengths spacing, has been proposed and demonstrated to provide 27 dBi gain over the frequency band from 26.5 GHz to 29.5 GHz, with just 16 active feeding elements. The grating lobes caused by the array sparsity can be reduced by designing a directive array element pattern. When the phased array steers towards an angle, the lens array will be displaced, in order to steer simultaneously the element pattern towards the same angle, and thus achieving also low GLL while steering.

The challenges of the design emerge due to the simultaneous requirements of high efficiency over a wide bandwidth while also implementing dual polarization. To meet these challenges while maintaining a low-cost structure, a dual-polarized LWA feed in PCB was co-designed with a plastic elliptical lens. It achieves a wide relative bandwidth of 22.7%, from 24.6 to 30.9 GHz, and a polarization isolation better than 50 dB. It is worth mentioning that the analysis of the lens with a diameter of only two wavelengths would have been a challenge even in absence of the other challenges. We implemented the field correlation methodology, combined with the near-field evaluation of the LWA feed and the

GO/FO approach for the elliptical lens. The optimized lens antenna shows above 75% and 70% aperture efficiency for the cases of broadside and 10° steering over the required band, respectively. The array performance obtained from the proposed approach was validated by CST full-wave simulations for both polarizations and all steering cases. The latter shows that the broadside gain is larger than 27 dBi and can reach 27.5 dBi at 28 GHz, with SLL lower than -13 dB. Moreover, the design procedure is well validated even for steering up to 20°, with a scan loss lower than 2 dB.

The proposed array antenna was fabricated and measured and the measurement validated the proposed antenna architecture. The array can achieve 26.2 dBi gain at broadside and 26 dBi gain when steering to 10°, with a 20% relative BW, from 25.1 to 30.7 GHz. If a better fabrication tuning cycle is made, the performance could be further improved. Moreover, the proposed array antenna can be easily expanded into more elements such as 8×8 within 20 cm × 20 cm × 2 cm. A gain around 33.5 dBi would then be achieved.

Moreover, in Appendix A, another architecture is proposed to integrate the backing reflector into an unique PCB. The simulated performance is shown and compared to measurements. The measured impedance matching of the array element indicates limited fabrication tolerances of the long coaxial transition structures. Although the measured far-field performance is not as good as the architecture discussed in Chapter 2, we consider the experiment successful in validating the proposed architecture.

The work described in Chapter 2 of this thesis was published in paper J2 (see page 151).

6.3 Time-domain Equivalent Circuits for the Link Modelling Between Pulsed Photoconductive Sources and Receivers

In Chapter 3 we characterize the generation and detection of THz pulses between a pulsed PCA source and a receiver via the TD Norton equivalent circuits. We first briefly introduce the Norton circuit for a PCA source. To simplify the numerical time-marching evaluation of the TD circuit, we introduce a constant generator resistance and propose an approximated FD circuit. This circuit can be solved analytically and is capable of accurately predicting the radiated power. Therefore, it is a powerful tool to analyze and design PCA sources in terms of the impedance matching, especially when the goal is to maximize their radiated power, without spending more optical power than necessary. We then consider an ideal case that the PCA receiver is connected to the source by a non-dispersive transmission line. A similar TD Norton equivalent circuit is proposed to characterize the photocurrents in the receiving PC gap. Afterwards, a stroboscopic sampling process is implemented to evaluate the detected currents. It is found that the reconstruction quality (fidelity factor) of the detected currents with respect to the load currents in Tx is directly related to the recombination time of the receiver.

Finally in Chapter 4, we characterize a dispersive QO link between two PCAs via the link transfer function which is evaluated using the field correlation approach. The fields radiated by the PCAs are evaluated in the middle plane of the link using full-wave simulations combined with the GO/PO approaches. The current generator of the receiving Norton circuit is then accurately calculated using the link transfer function and the detected currents are reconstructed in both amplitude and waveforms. To validate our proposed modelling methodology, we measured the detected currents at the PCA receiver using the proposed QO link. The design of the optical components used in this link and the alignment of the laser beams with these components are described in Appendix C. The measured pulse width indicates that the used PCAs have long recombination time of 700 fs. While the power measurements discussed in Appendix D indicate a short scattering time of 2 fs and 1.3 fs for the source and the receiver, respectively. After truncating the measured spectra for $f < 150$ GHz, the corresponding time signals are in excellent agreement with the simulations. We also compare the peak amplitude of the detected currents, showing also very good agreement. The proposed methodology is validated and is applicable for different PCA structures and QO links. Therefore, it can be used to analyze and optimize the generation and detection of THz pulses for future PCA-based imaging applications.

The work described in Chapter 3 and 4 of this thesis has been submitted (see paper J5 in page 151).

6.4 Wide Field-of-view Focal Plane Array of Shaped Quartz Lens Antennas

FPAs based on dielectric lens antennas are promising for designing PCA-based radar systems for future mm-resolution security imaging. In Chapter 5, we focus on optimizing the scanning gain of a lens based FPA coupled to a reflector when the scanning angles are large, via shaping the lens surfaces. We consider the array elements as quartz lenses with LWA feeds (Appendix E briefly discusses the design rules for plastic and silicon lens antennas). We propose an optimization procedure using the field correlation technique on the top of the lens. Once the incident reflector's focal fields and the lens radiated fields on the same plane are conjugately matched, we can obtain the lowest scan loss for the system.

When the scanning angles are large, lens elements can be located outside the rim of the reflector and the reflector's focal fields can present significant higher-order phase terms. To match with these phase terms, we have derived a formula to modify the shape of the lens surface and thus modify the phase propagation of the lens radiated fields. In fact, the field correlation method directly provides the hologram phase to be synthesized by the surface modification. The shaped lens is then expanded into Zernike polynomials leading to a smoother practical surface. We present an example of the shaped quartz lens antenna operating at 180 GHz for an extreme case when the reflector scans 20.3° (50 reflector's beams). The far-field performance obtained from our approach is in excellent agreement with the full-wave simulations. The latter achieves 50.5 dBi directivity with 2.6 dB scanning gain loss which is much lower than that of the reflector's focal field (about 6 dB).

To validate the simulations, we have fabricated and measured this shaped quartz lens antenna. The fabricated lens surface presents very good surface difference (±40 µm) compared to the designed one. The measured reflection coefficient is less than -10 dB from 150 GHz to 210 GHz. The measured lens near fields, when propagated to the far-field region, point towards the expected angular position and are in excellent agreement with the full-wave simulations over the entire frequency band. We have also evaluated the reflector's far fields when using the lens far fields calculated from the measured near-field data as the source in GRASP. The resulting reflector's far fields also present excellent agreement with the simulations, validating the proposed method for shaping dielectric lens surfaces.

The work described in Chapter 5 of this thesis will be published in paper J6 (see page 151).

6.5 Future Outlooks

The future outlooks for this thesis are summarized in the following:

- In the context of the 5G point-to-point communication, we have demonstrated that the scanning lens phased array antenna discussed in Chapter 2 and Appendix A can achieve high gain with less feeding elements. However, we have only investigated the fixed beams at broadside and 10°. The designed PCBs are not suitable for continuous electronical steering due to the use of the fixed-delay feeding networks. In addition, the prototypes cannot fully fulfill the requirements due to the limited fabrication tolerances on the PCBs. In the future design, the PCB feed and the lens array can be modified to support continuous beam steering. The architecture in Appendix A can be further investigated to include low-cost active components at the back of the PCB to achieve continuous phase shifting for each array element. Advanced PCB technology with better tolerances should be adopted to achieve better performance. The lens array can be integrated with a low-cost and low-power piezomotors to achieve continuous displacement which is synchronized with the phased array steering.

- The THz time-domain system with PCAs has been investigated for future mm-resolution security imaging applications. Its modelling has been done in this thesis; however, there are still three problems that need to be further solved. The first is to achieve high detected currents (or high signal-to-noise ratio). In Chapter 4, the used bow-tie based PCAs have poor radiation performance and thus the link transfer function has a low value. To solve this, we can use leaky-wave based PCAs for future link measurements due to their more directive radiated patterns and better coupling to the used QO components. The silicon lenses and the focusing lenses should be co-designed to achieve the best link transfer function.

  The second problem is related to the fabrication of the designed PCAs. According to the measurements, the used LT GaAs substrates of the bow-tie PCAs have long recombination time and short scattering time. However, to obtain more broadband spectra of the detected THz pulses, lower recombination time is needed. Therefore, it would be necessary to have a stricter control of the material recombination time (or an accurate estimation) during the fabrication process.

Finally, one should consider how to achieve an imaging scenario using the optimized PCAs. This requires proper dimensioning of the system on a top level. A rigorous loss budget should be investigated and a proper setup should be designed. Afterwards, as the final goal, the design of an entire array of PCA receivers may be considered.

- The design of the shaped lens antennas in Chapter 5 can be further investigated in the following aspects. The lens surface is now smoothed by Zernike polynomials in terms of the mode number. But it may be possible to optimize each Zernike coefficient to obtain better lens surfaces which can achieve higher reflector's aperture efficiency.

  Moreover, the lens radiation efficiency can be further improved by realizing tilted primary fields when the lens feeds are displaced. Since all feeds are printed on a flat plane, they cannot be physically tilted. The stratification of the lens antennas should be designed to support electrically tilt, which is challenging. Furthermore, the lens feed is now single-polarized. It could be worthy to explore if dual polarization can be achieved.

  Finally, the designed FPA mainly focuses on optimizing its field of view but has not been analyzed as a radar system. We did not consider a real imaging scenario with specific requirements such as imaging distance, power budget, array sampling, and etc. Not all array elements are investigated and the reflector system is not designed. These should be further considered if a complete imaging system is required in the future.

6.6 Impact of the Research

The work described in this dissertation has led to a number of journal and conference publications; see "List of Publications" in page 151. Four first-author peer-reviewed journal papers have been published or submitted, together with 18 conference papers. The work discussed in Chapter 3 was nominated for the "Best Electromagnetics Award" in the European Conference on Antennas and Propagation (EuCAP), Florence, Italy, 2023.

Appendix A

Integrated PCB Design for the Scanning Lens Phased Array Antenna

In Chapter 2, we have introduced a dual-polarized scanning lens phased array antenna used for 5G point-to-point communication. There, the lens array is fed by a phased array antenna which consists of two separate parts: a PCB and an externally machined metallic backing reflector. This architecture ensures that the feeding network is placed very close to the array feeding elements, avoiding the need for electrically long vertical transitions inside the PCB. But the disadvantages are the lack of the antenna integration and the limited assemble accuracy since the PCB and the metallic cavity are aligned using screws. Therefore, in this Appendix, we propose another architecture that integrates the PCB and the backing reflector into a single PCB. This architecture is referred to as Architecture II while the design in Chapter 2 is Architecture I.

A.1 Feed Structure

The design of the PCB for Architecture II is very similar to that discussed in Section 2.4. The main difference is that here the metalic backing cavity is realized using PCB vias, as depiected in Fig. A.1. Fig. A.1(a) shows the PCB stratification. Fig. A.1(b) and A.1(c) show the perspective and top views of the detailed feeding structure, respectively. We introduce two more metal layers M5 and M6 for the implementation of the feeding networks at M6. The big metal cavity shown in Fig. 2.2 is achieved by vias from M1 to M6 , while the small cavity is from M2 to M6, also formed by vias. Since now the feeding networks cannot directly feed the slots compared to the design in Fig. 2.17, two integrated coaxial transitions are designed to connect the power dividers on M2 and M4 with the feeding networks at M6; see Fig. A.1(b) and A.1(c). To achieve the best impedance matching, both power dividers are fine-tuned by radial open stubs. The dimensions of the

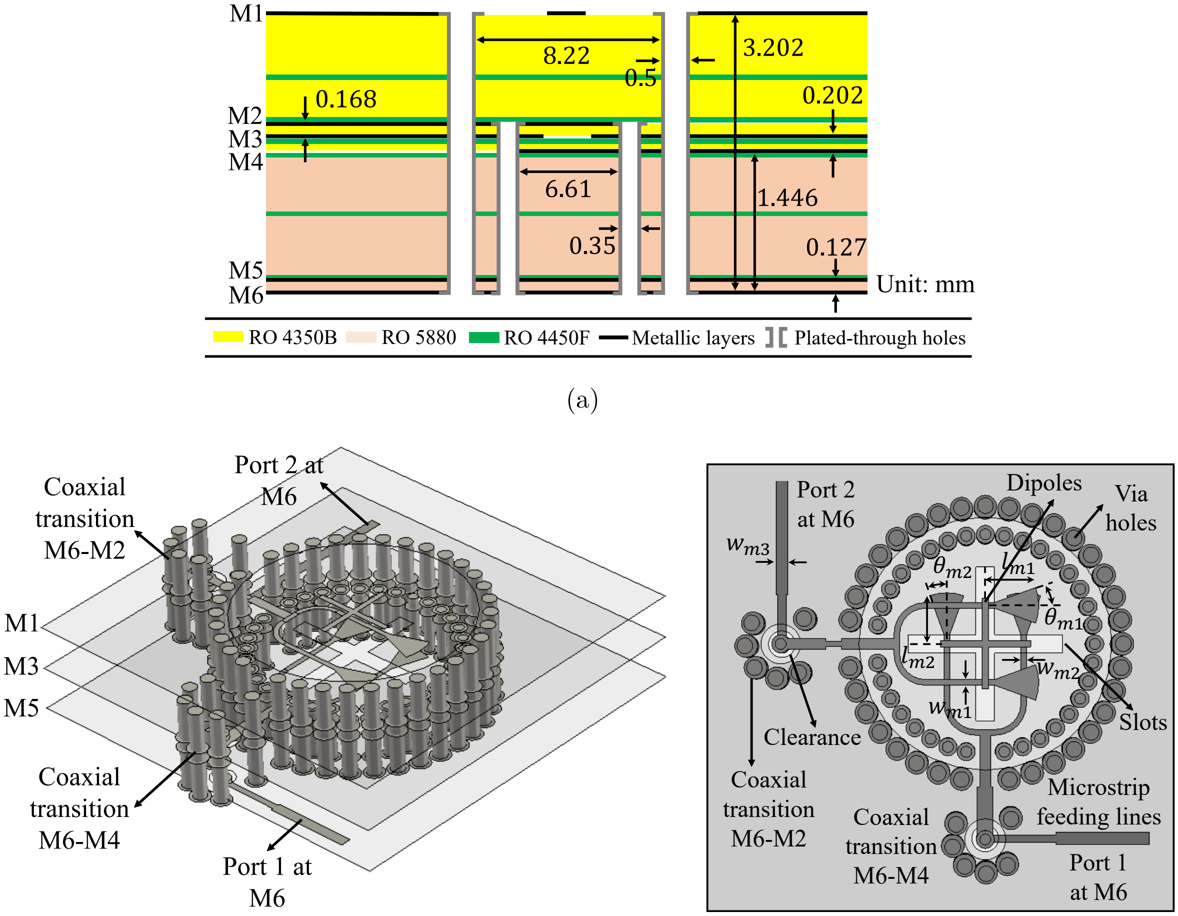

(a)

(b) (c)

Figure A.1: PCB dual-polarized LWA feed: (a) PCB stratification. (b) Perspective and (c) top views of the detailed antenna structure. The slots are excited in balance by two sets of microstrip lines, each one dedicated to a different polarization. The radial open stubs at M2 has the dimensions $(w_{m1}, l_{m1}, \theta_{m1})$, while those at M4 are $(w_{m2}, l_{m2}, \theta_{m2})$. The optimized dimensions of this antenna are: $w_{m1} = w_{m2} = 0.18$ mm, $w_{m3} = 0.38$ mm, $l_{m1} = 1.6$ mm, $l_{m2} = 1.53$ mm, $\theta_{m1} = \theta_{m2} = 20°$, $w_s = 0.6$ mm, $l_s = 4.9$ mm for the slots, and $w_d = 0.2$ mm, $l_d = 2.85$ mm for the dipoles.

feeding antenna are marked in Fig. A.1(c) for Architecture II. Although Architecture I and II have different PCB designs, their near-field patterns inside the lens are essentially the same. Therefore, we use the same lens design and lens array for both architectures.

Integrated Coaxial Transitions

The coaxial transitions in Fig. A.1 are optimized to achieve the best impedance matching which is shown in Fig. A.2. Note that the metal and dielectric are not lossy in the simulations. Both transitions achieve the reflection coefficients S_{11} lower than -25 dB over the required frequency band (26.5-29.5 GHz). Moreover, the loss in surface waves, implied by S_{21} shown by the red curves, are smaller than 0.3 dB. Compared to Architecture I, due

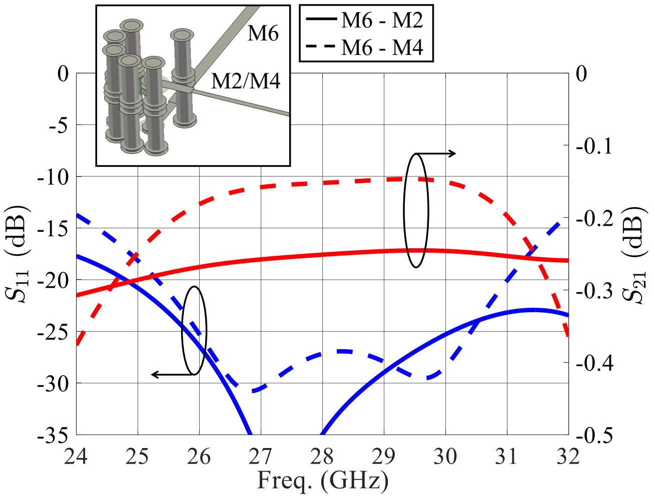

Figure A.2: Simulated S-parameters of the vertical transitions in Architecture II from M6 to M4 and M2. Note that the ohmic and dielectric losses are not included in the simulations.

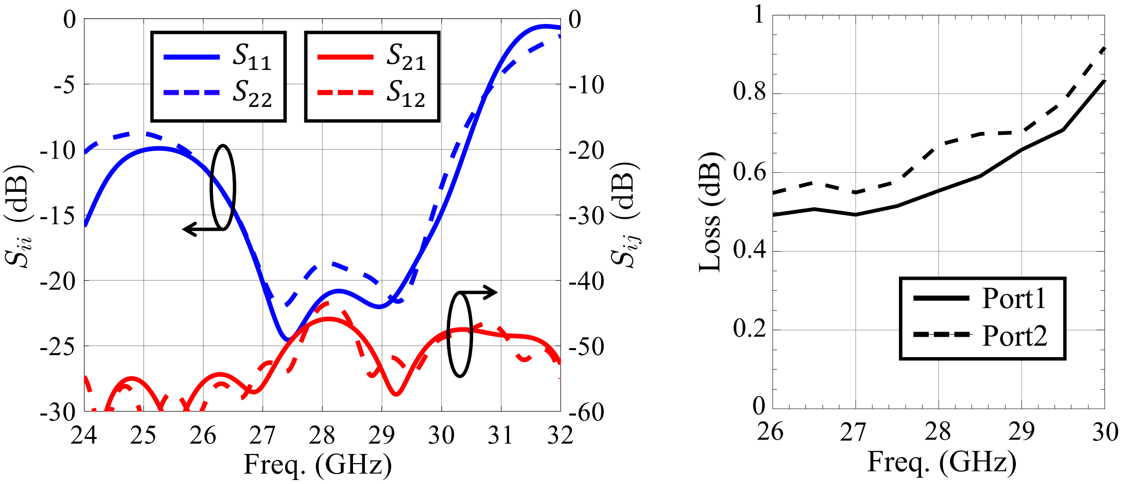

(a) (b)

Figure A.3: Simulated performance of the dual-polarized PCB LWA feed of Architecture II when radiating inside the semi-infinite HDPE medium: (a) S-parameters. Note that the ohmic and dielectric losses are not included in the simulations. (b) Total loss of the feed, including the excitation of surface waves, ohmic and dielectric losses (dielectric loss in the HDPE medium is not included here).

to the use of the long transitions, the S-parameters of Architecture II are more resonant. This means that Architecture II is less robust against fabrication tolerances.

When the transition structures are combined with the feeding antenna, the simulated reflection coefficients are shown in Fig. A.3. The -10 dB bandwidth (BW) is from 25.5 GHz to 30.3 GHz, i.e., 17.2% relative BW, which is narrower than that of Architecture I shown in Fig. 2.19(a). This is due to the resonant behaviors happened in Architecture II as shown in Fig. A.2.

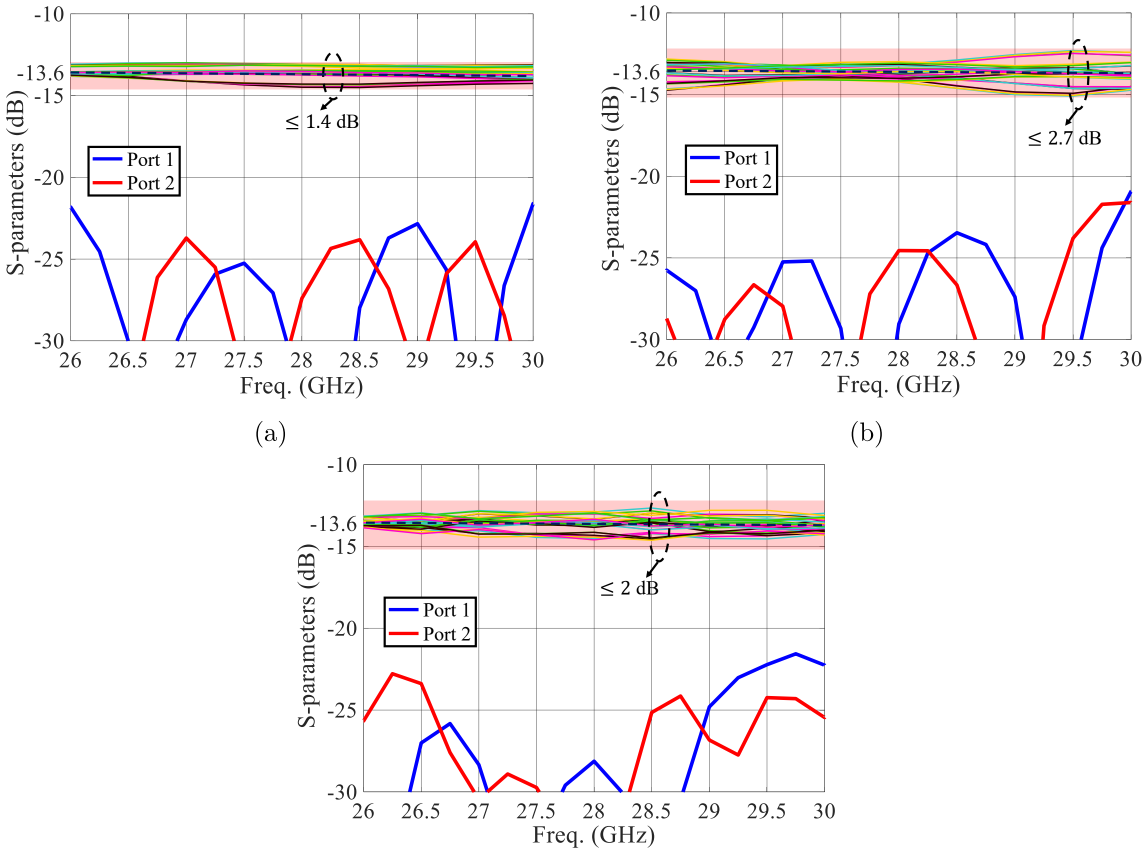

(a) (b)

(c)

Figure A.4: Simulated S-parameters of the feeding networks in Architecture II for the cases of: (a) broadside radiation, (b) $\theta = 10°, \phi = 0°$ steering, and (c) $\theta = 10°, \phi = 90°$ steering. The blue and red curves represent the reflection coefficients for port 1 and 2, respectively. The other curves within the red regions represent the power delivered from port 1/2 to other elements.

Performance of the Feeding Networks

In both architectures, all 16 feeding elements are connected to the feeding networks on the bottom layers of the respective PCBs, as shown in Fig. 2.20. The design and the performance of the feeding networks for both architecture are essentially the same. Thus here we only show the simulated S-parameters of Architecture II as examples which are shown in Fig. A.4 for three radiation cases. The blue and red curves represent the reflection coefficients of port 1 and port 2, respectively; and the curves in the red regions show the ratio between the power at the elements and the corresponding ports, at each element.

All feeding networks are well matched over the required frequency band, and have a loss approximately 1.6 dB in the microstrip lines. This loss is estimated using a simple surface impedance model. The power division, $1 \rightarrow 1/16$ (-12 dB, plus 1.6 dB loss and thus -13.6 dB) is also quite equal among all antenna elements, with a maximum deviation of ±1.4 dB in the case of steering $\theta = 10°, \phi = 0°$. The expected progressive phase shift versus

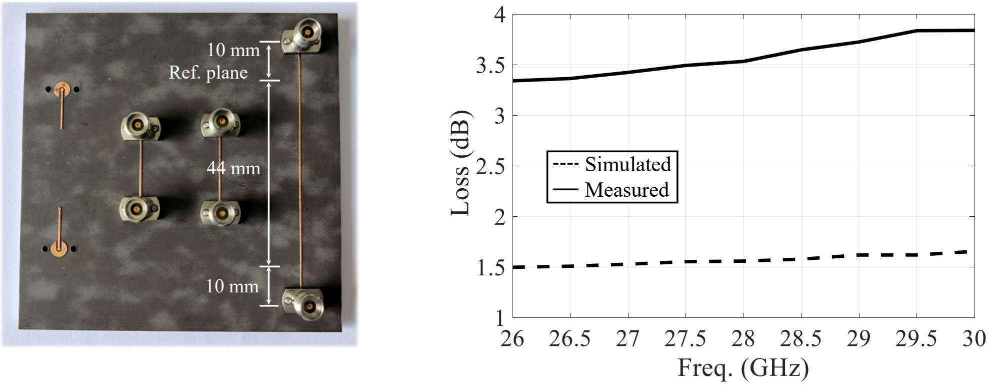

(a) (b)

Figure A.5: (a) Photograph of the fabricated TRL kit in PCB. (b) Estimated microstrip loss in the feeding network compared to the simulation. The total length of the microstrip lines is 123 mm for port 1, and 126 mm for port 2. The average value of the loss is shown here.

frequencies is not reported here but it also shows very little dispersion, with the phase deviating from ideal linear phase shift by less than 5° over the entire band, for all three networks. It is worth noting that in the eventual utilization for Architecture II, the feeding networks can be replaced by the connection to separate signal lines coming from central or multiple transmitting/receiving modules. This is not very feasible for Architecture I due to the use of the external backing reflector.

A.2 Antenna Prototype and Measurement

The fabricated lens array and PCBs for Architecture I have been introduced in Section 2.5. Architecture II uses the same lens array but with different PCBs which look very similar to those in Fig. 2.22 so they are not shown here. Instead, we show some other components which were fabricated for verification purposes. Fig. A.5(a) shows the through-reflect-line (TRL) kit used to calibrate out the impact of connectors. The reference planes are also shown in the figure.

After the TRL calibration, the long microstrip line shown in Fig. A.5(a) is measured to quantify the microstrip loss in the feeding networks, which is plotted in Fig. A.5(b) and compared to the simulations. The simulated attenuation in transmission lines is based on the dielectric properties suggested by the provider ($\varepsilon_r = 2.2$, $\tan\delta = 0.0009$, Rogers Corporation) and a simple surface impedance model. The total loss in the feeding networks is then calculated as the product between the attenuation and the total length of the microstrip lines in the feeding networks. The length is 123 mm for port 1 and 126 mm for port 2. The measured loss is in the order of 3.4 dB (0.27 dB/cm), which is twice as large than the simulated one, 1.7 dB (0.13 dB/cm). At this point, we can conclude that the loss discrepancy is most likely associated with the roughness of the copper microstrip lines. It is well known that the roughness of high-frequency lines affects the losses [77], and

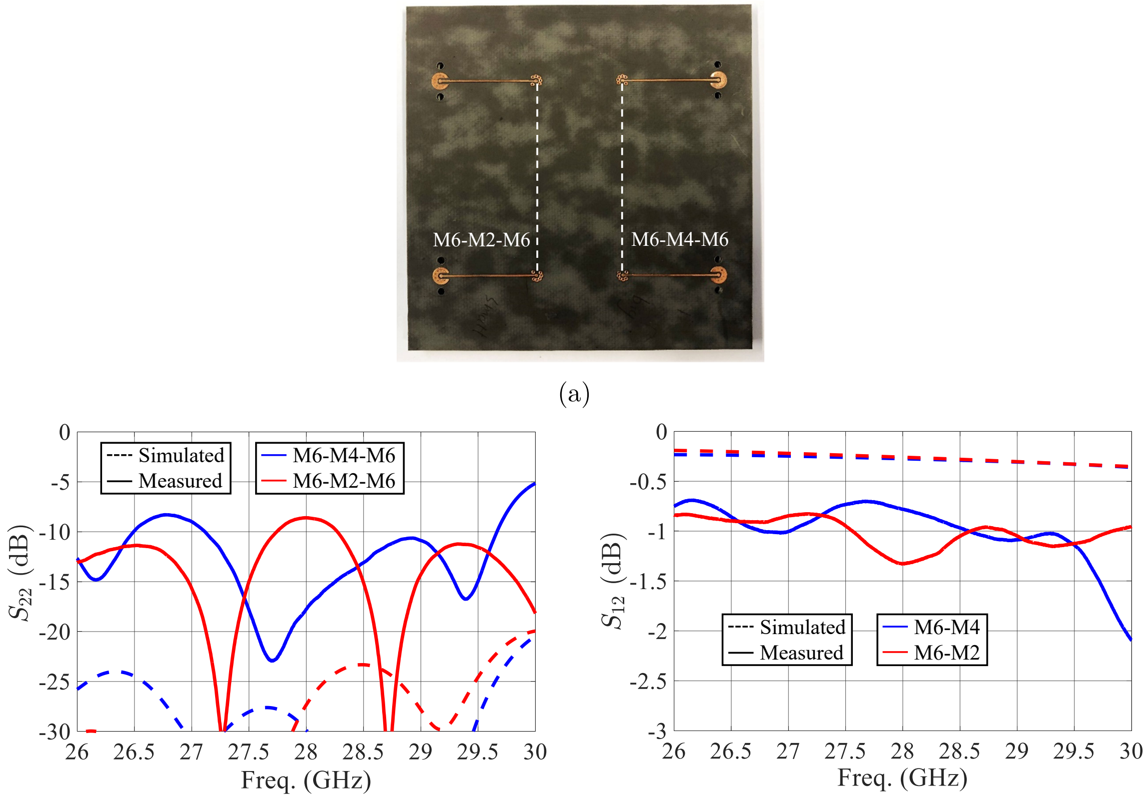

(a)

(b)

(c)

Figure A.6: (a) Fabricated PCB for measuring the S-parameters of the coaxial transitions from M6 to M2/M4 and then back to M6. (b) and (c) show the measured S-parameters compared to the simulations. The same structures in (a) were simulated. By applying post processing, the S_{12} of a single transition from M6 to M2/M4 is extracted from the measurement and compared to the simulation.

different surface finishes can be used to mitigate this problem. The fabricated microstrip lines were done with bare copper without any surface finish. Therefore, they can get oxidized very soon after fabrication, which will increase the surface roughness as copper oxide is thick. When working at 28 GHz the signals travel much closer to the copper top as opposed to running through the center or near the track laminate interface, leading to higher loss. This measurement result is in line with the analysis in [77] and the measured loss described in [130]. In latter, the substrate is Isola AstraMT ($\varepsilon_r = 3$, $\tan\delta = 0.0017$), with the thickness of 0.254 mm, and the copper has a very low roughness with nickel free surface finish. Even in this case, the resulting loss in microstrip line was 0.35 dB/cm, which is much higher than the one obtained with a surface impedance model (0.13 dB/cm). To solve this problem, using gold flash as a surface finish could be a feasible way.

Characterization of S-parameters

The coaxial transitions of Architecture II were measured using the back-to-back configuration shown in Fig. A.6(a), i.e., the structure is from M6 to M2/M4 and then back to

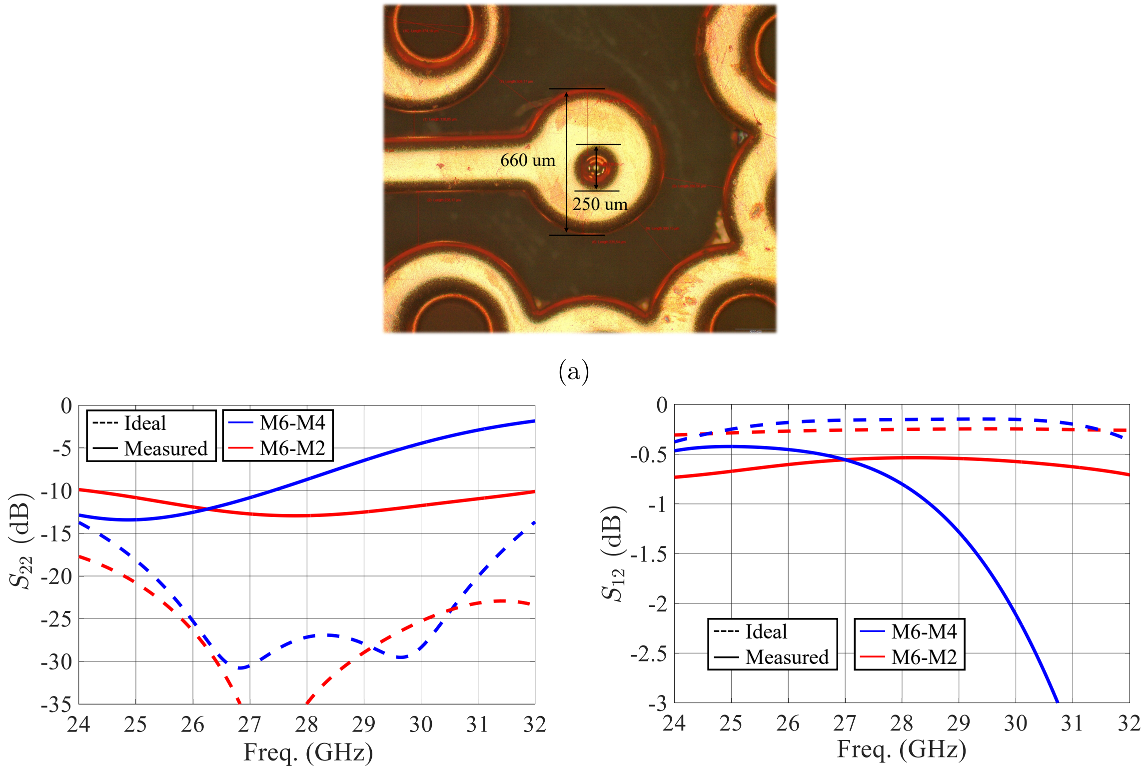

(a)

(b)

(c)

Figure A.7: Vertical transitions in Architecture II from M6 to M4 and M2: (a) dimensions of via holes and pads measured under a microscope. (b) Simulated reflection coefficients of the transitions with the ideal and the measured dimensions. (c) Simulated S_{12} of the transitions with the ideal and the measured dimensions. The ideal case corresponds to the simulations shown in Fig. A.2(a). Note that the ohmic and dielectric losses are not included in the simulations.

M6. The same structures were simulated and compared to the measurements, as shown in Fig. A.6(b) and A.6(c). The measured reflection coefficients of both transitions are not as good as the simulations would have suggested. By applying post processing, the S_{12} of a single transition structure from M6 to M2/M4 is estimated, and its values are lower than those predicted by the simulations. To find the reason for the poor matching of the transitions, we measured the dimensions of the vias in the transitions under a microscope, as shown in Fig. A.7(a). It was found that the outer diameter of the via holes from M2 to M6 was around 250 µm, which is smaller than the expected value of 350 µm. Moreover, the outer diameter of the vias pads were measured as 660 µm, which is bigger than the simulated value of 570 µm. In Fig. A.7(b) and A.7(c), the simulated S-parameters of the transitions from M6 to M4 and M2 are shown. Here we study the single transition case instead of the back-to-back case, and the transitions with the ideal dimensions are compared to those using the measured dimensions. The metal and dielectric are not lossy in the simulations. We can notice that the impedance matching becomes much worse when using the measured dimensions (with about 100 µm tolerance), which is in line with the measurement results shown in Fig. A.6. The design of the transitions is very sensitive

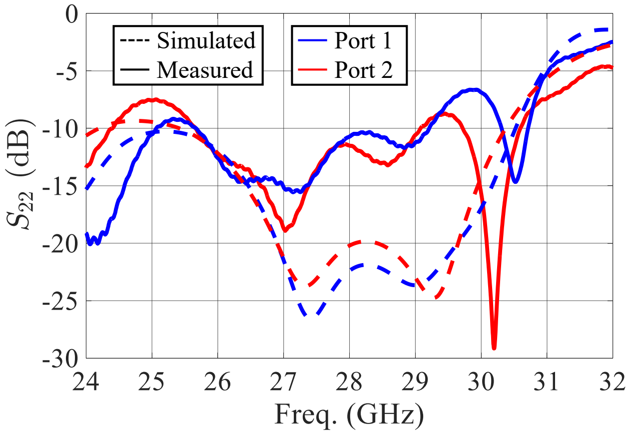

Figure A.8: Measured reflection coefficients of the single feeding antenna (in Architecture II) shown in Fig. A.1. The measurement setup is similar to that in Fig. 2.24(a).

to the fabrication tolerances of vias; therefore, in our prototype, neither of the vertical transitions, from M6 to M4 and M2, can support a good propagation of signals. Specially, the one from M6 to M4 is more sensitive, and has a worse matching than that from M6 to M2. It is important to reduce such sensitivity and make the transitions realizable for PCB technology. The solution chosen was to shorten the vias when designing the Architecture I, and the resulting measurements are in excellent agreement with the simulations.

Finally, the single feeding antenna (in Architecture II) shown in Fig. A.1 is measured and compared to the simulations, as reported in Fig. A.8. As expected, the measured reflection coefficients are worse than the simulations, especially at higher frequencies, congruent with the poor matching in the vertical transitions mentioned before.

Far-field Performance

The far-field patterns, directivity, and gain of this architecture is also evaluated via the antenna near-field measurements discussed in Section 2.5.2. The near-field area is 200 mm × 200 mm with the step size of 4.5 mm. The reference system for the far-field radiation patterns is shown in Fig. 2.25.

The co-pol far-field patterns of both ports at 28 GHz are shown in Fig. A.9 for the cases of broadside, steering to $\theta = 10°$, $\phi = 0°$, and $\theta = 10°$, $\phi = 90°$, respectively. Moreover, the co-pol patterns at 26.5 and 29.5 GHz for the two steering cases are shown in Fig. A.10 compared to the simulations. In the steering cases, the lens array is displaced 2.4 mm in the positive x-direction when steering to $\theta = 10°$, $\phi = 0°$; and 2.4 mm towards positive y-direction when scanning to $\theta = 10°$, $\phi = 90°$. The cross-pol patterns are below -23 dB at all frequency points and are not shown here. It can be seen that the agreement between the simulations and the measurements is quite good for all radiation cases at all frequency points, except when steering to $\theta = 10°$, $\phi = 90°$ at 29.5 GHz, as shown in Fig. A.10(d). In that case, the side lobe of port 1 is much higher than the simulated one. This can be attributed to the limited fabrication tolerances in the coaxial transitions, leading

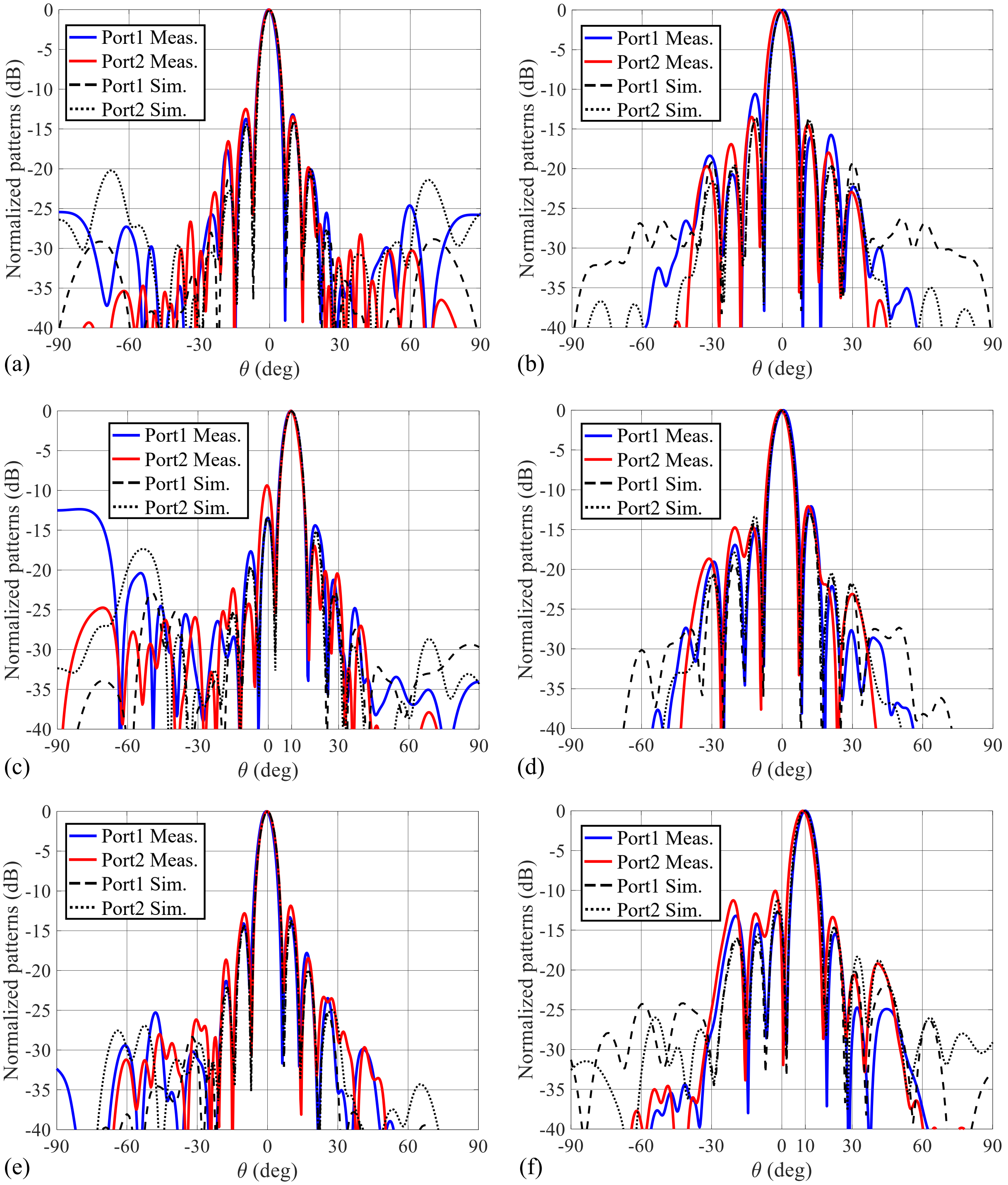

Figure A.9: Measured co-pol far-field patterns at 28 GHz, when steering to broadside: (a) and (b); $\theta = 10°$, $\phi = 0°$: (c) and (d); and $\theta = 10°$, $\phi = 90°$: (e) and (f). The first column shows the far fields along the $\phi = 0°$ plane while the second column shows the $\phi = 90°$ plane. The reference system is defined in Fig. 2.25. The lens array is displaced by 2.4 mm towards the steering directions for the steering cases.

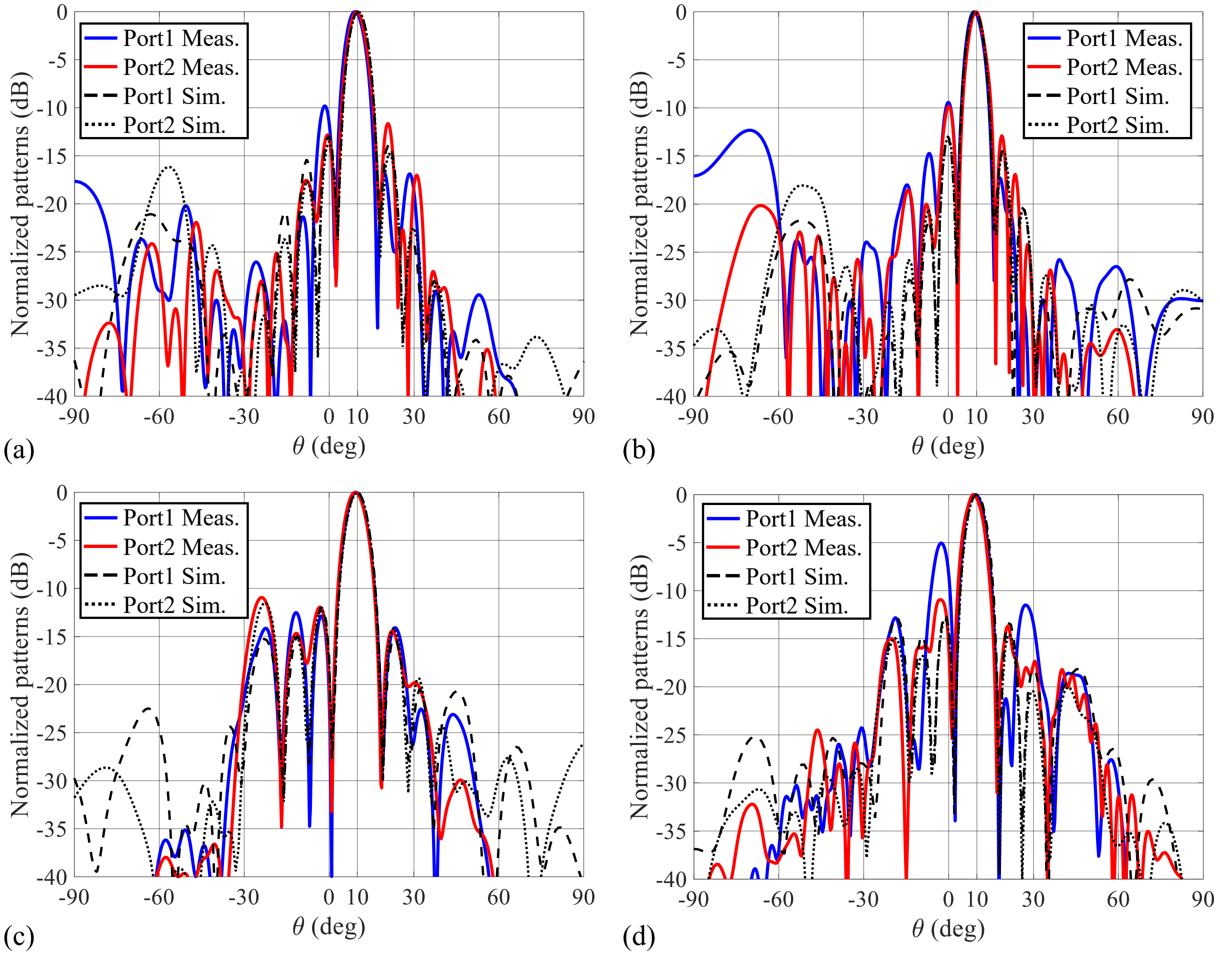

Figure A.10: Measured co-pol far-field patterns when steering to $\theta = 10°$, $\phi = 0°$ at (a) 26.5 GHz and (b) 29.5 GHz, and to $\theta = 10°$, $\phi = 90°$ at (c) 26.5 GHz and (d) 29.5 GHz. The reference system is defined in Fig. 2.25. The lens array is displaced by 2.4 mm towards the steering directions.

to poor impedance matching of the array elements at the higher part of the frequency band, as shown in Fig. A.8. As the result, when the feeding networks are connected to the array elements, some amplitude and phase errors also emerge in the networks due to the mismatch of the coaxial transitions. The errors propagate differently in the feeding lines corresponding to different elements, especially for the configurations dedicated to the steering. The measured 2D far-field patterns of port 1 at 28 GHz are shown in Fig. A.11 for the cases of broadside and steering. In the figures, the position of the side lobes and the cross-pol values are clearly shown.

The measured broadside and steering directivity and gain, as a function of frequencies, are shown in Fig. A.12 and compared to the simulations. In the case of directivity, the measured results are in reasonably good agreement with the simulations, as shown in Fig. A.12(a), A.12(c), and A.12(e). There are drops at higher frequencies, especially for port 1, since the far fields of port 1 are significantly affected by the poor-performance transitions, leading to several non-radiating lens elements as explained in Section 2.5.2. The calibrated

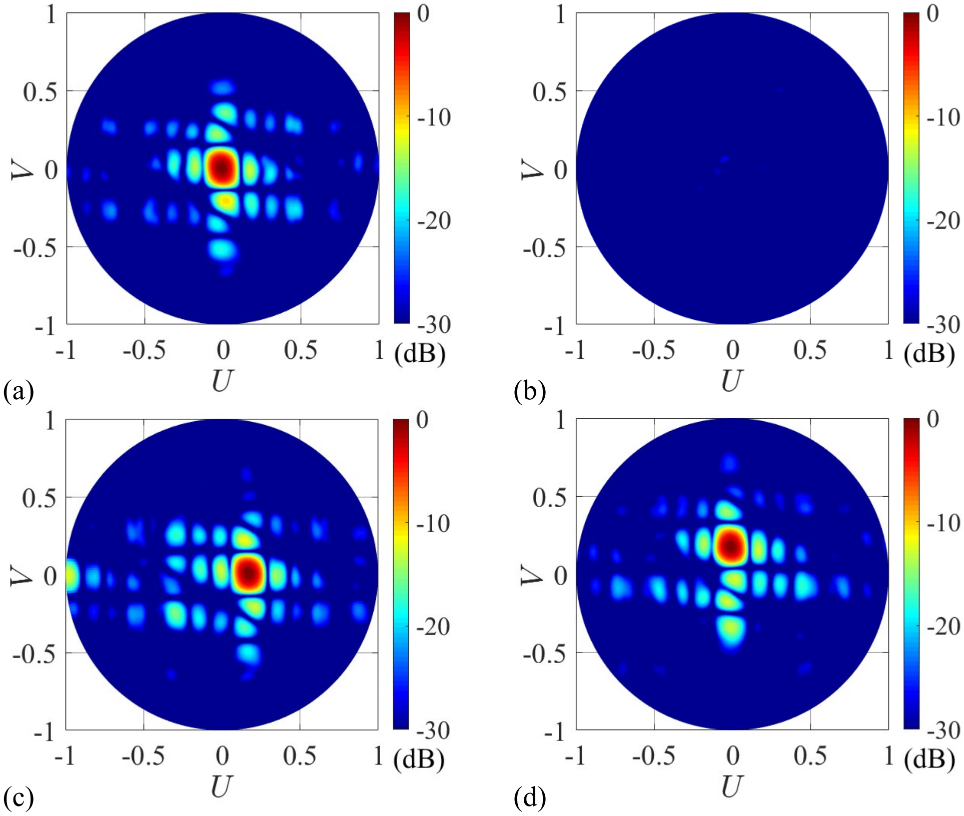

Figure A.11: Measured 2D far-field patterns of port 1 at 28 GHz. (a) Broadside co-pol pattern and (b) cross-pol pattern. Co-pol patterns when steering to (c) $\theta = 10°$, $\phi = 0°$ and (d) $\theta = 10°$, $\phi = 90°$. The reference system is defined in Fig. 2.25. The lens array is displaced by 2.4 mm towards the steering directions for the steering cases.

gain is shown in Fig. A.12(b), A.12(d), and A.12(f). The simulations and the measurements have only moderate agreement, also due to the mentioned tolerances and thus the poor matching in the transitions. Nevertheless, the gain requirements are in fact achieved for the steering configurations and missed by less than 2 dB for the broadside radiation.

Conclusion

To conclude, Architecture II gives us promising measurement results and its structure is more integrated than Architecture I. The fabrication tolerances in PCB technology is a constrain if one really wants to fully achieve the requirements. However, we consider the experiments completely successful in validating the proposed architecture. If the feeding networks are replaced by transmitting/receiving modules, and the PCBs undergo a better fabrication tuning circle, the eventual array performance could reach the predicted results.

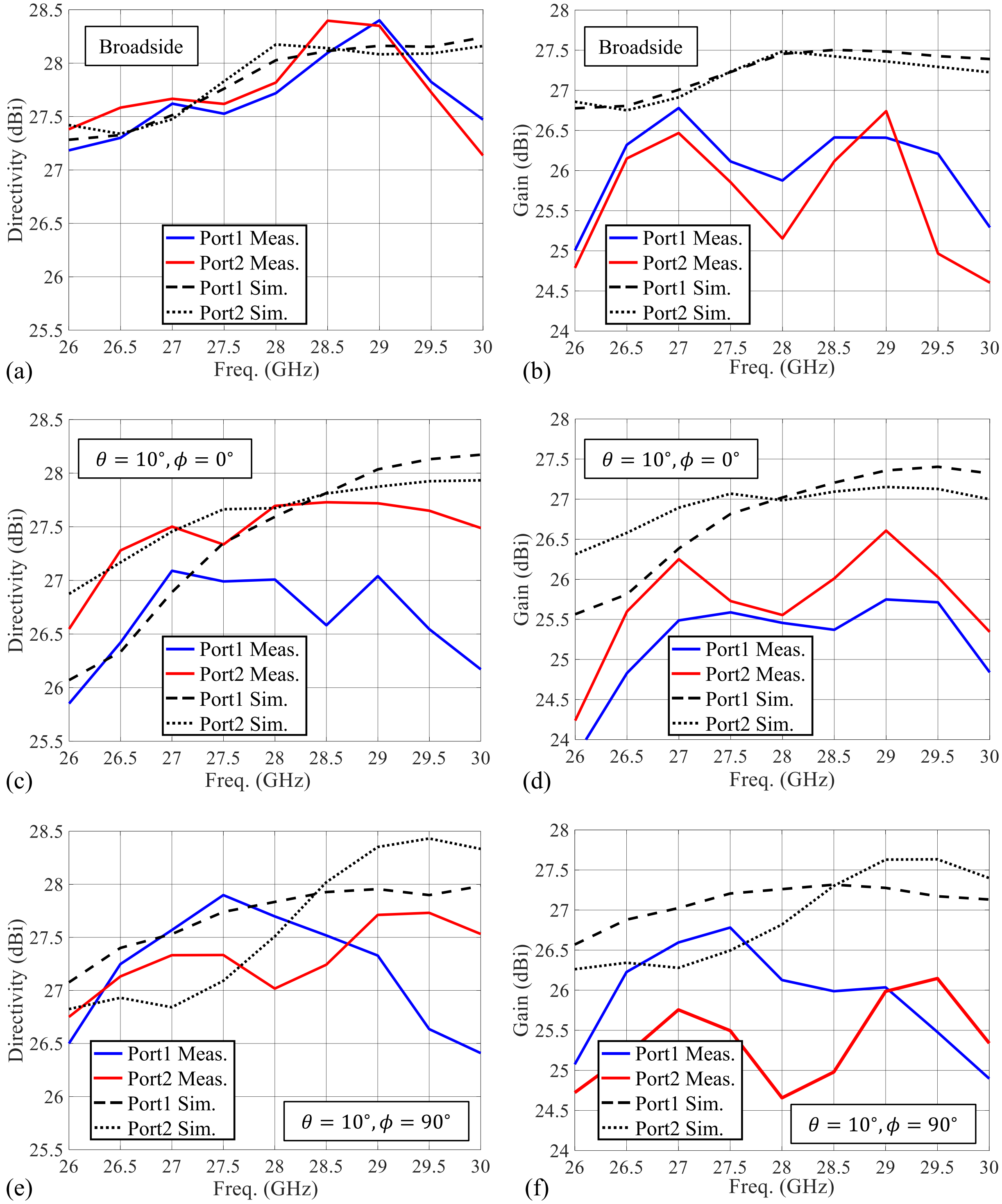

Figure A.12: Measured directivity at (a) broadside, (c) $\theta = 10°$, $\phi = 0°$, and (e) $\theta = 10°$, $\phi = 90°$; Calibrated gain at (b) broadside, (d) $\theta = 10°$, $\phi = 0°$, and (f) $\theta = 10°$, $\phi = 90°$. The lens array is displaced by 2.4 mm towards the steering directions for the steering cases.

Appendix B

Simulated Far-field Performance of Pulsed Photoconductive Antennas

In Chapter 4, bow-tie based photoconductive antennas (PCAs) are used for the link measurements. Besides this type of PCA, there are other commonly used geometries such as Auston switches [78], spiral antennas [97], and strip line antennas [131]. A review of different types of PCAs is shown in [132] and thorough studies have been done to compare their performance [82, 133]. In most cases, these PCAs are integrated with high resistivity silicon lenses to collimate the emitted electromagnetic fields and improve their radiation performance. In this appendix, the radiation performance of two types of PCAs is simulated and reported. One is the bow-tie antenna (BTA) used in Chapter 4 [98]. The other is a novel leaky-wave antenna (LWA) which was proposed in [99] and characterized in [107], showing better coupling to quasi-optical (QO) components when compared to the BTAs.

CST full-wave simulator is used to simulate these PCA structures to obtain their input impedance and primary fields radiated inside a semi-infinite silicon medium. The primary fields are then collimated and radiated by silicon lenses. These radiated fields are referred to as the lens secondary fields and are evaluated using an in-house physical optics (PO) codes [38]. Note that in CST, an antenna is excited by an impressed current in the PC gap with the amplitude of $I_{CST}(f)$. This current is independent from the photocurrents which are generated when a PCA is biased by an external voltage and illuminated by laser pulses. Accordingly, the amplitude of the simulated fields are independent from the PCA time-domain analysis, which is explicitly discussed in Section 4.2.2. Here we only focus on the radiation performance of the PCAs when excited by $I_{CST}(f)$.

B.1 Analysis of Bow-tie Based Photoconductive Antennas

The geometry of the used bow-tie based PCA is shown in Fig. 4.2 and its photograph is shown in Fig. 4.7. The simulated antenna input impedance $Z_a(f)$ is shown in Fig. B.1(a).

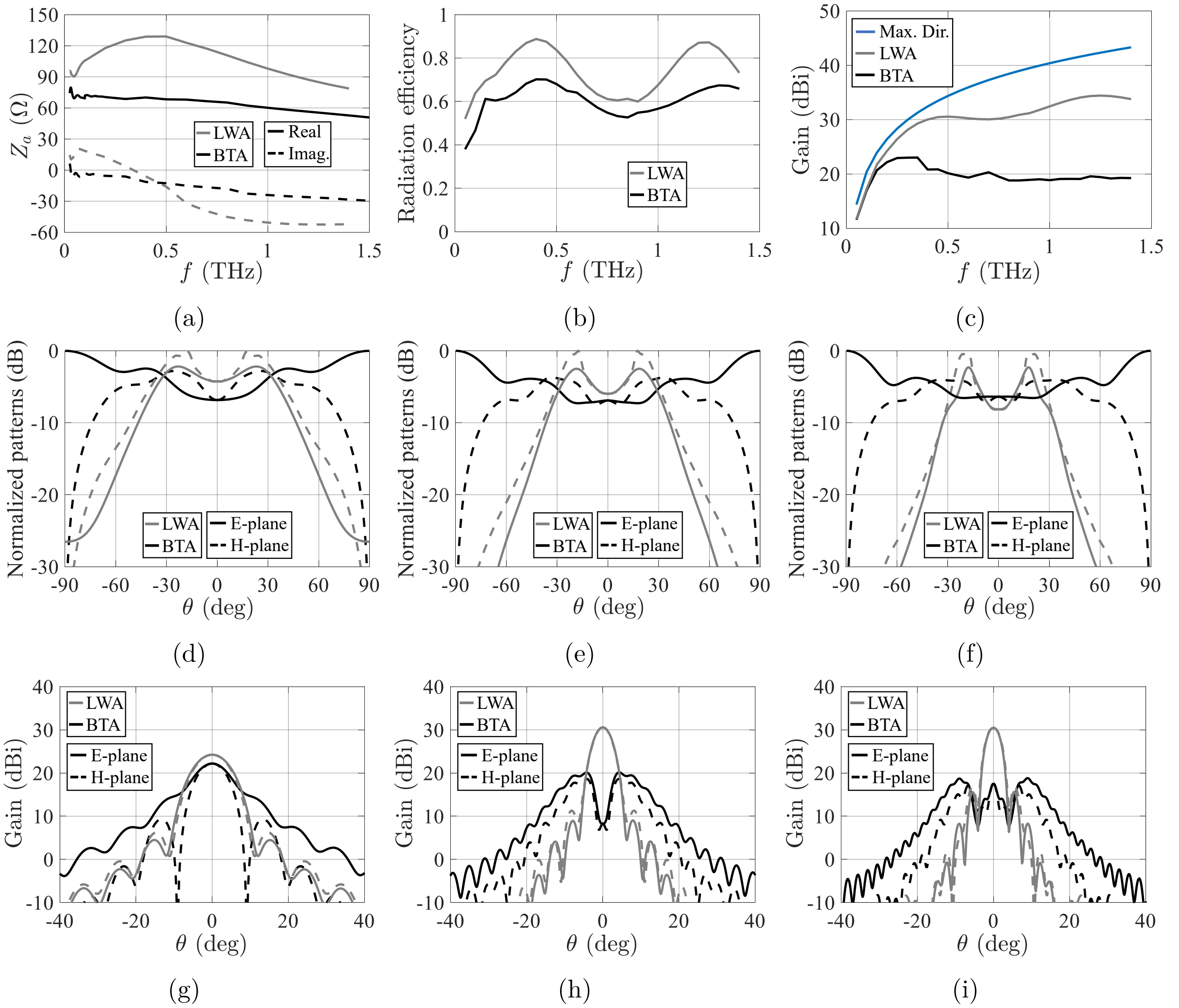

(a)

(b)

(c)

(d)

(e)

(f)

(g)

(h)

(i)

Figure B.1: Simulated antenna radiation performance for the BTA in [98] and LWA in [107]. (a) Input impedance; (b) Lens radiation efficiency; (c) Antenna far-field gain. The blue curve represents the maximum achievable directivity for the given lens diameter; (d)-(f) Normalized co-pol far fields radiated inside the semi-infinite silicon medium at 0.2 THz, 0.5 THz, and 0.8 THz, respectively; (g)-(i) Co-pol far fields radiated by the silicon lens at 0.2 THz, 0.5 THz, and 0.8 THz, respectively.

It presents almost constant real impedance below 1 THz, which can be approximated as a resistance, i.e., $Z_a(f) \approx R_a = 70\ \Omega$. The simulated co-pol primary fields radiated inside the silicon medium are shown in Fig. B.1(d)-B.1(f) along the main planes at 0.2 THz, 0.5 THz, and 0.8 THz, respectively. The patterns at all frequencies are not well focused at broadside. Therefore, they cannot illuminate the lens efficiently as explained in [99].

By using the in-house PO tool, the corresponding secondary fields radiated by the silicon lens are evaluated from the phase center of the lens (16 mm below the lens) to a far-field sphere. Theses fields (co-pol) are shown in Fig. B.1(g)-B.1(i) in the main planes. For $f \leq 0.35$ THz, the patterns are still focused at broadside; however, as the frequency increases, the patterns become distorted and non-broadside, with significant oscillation

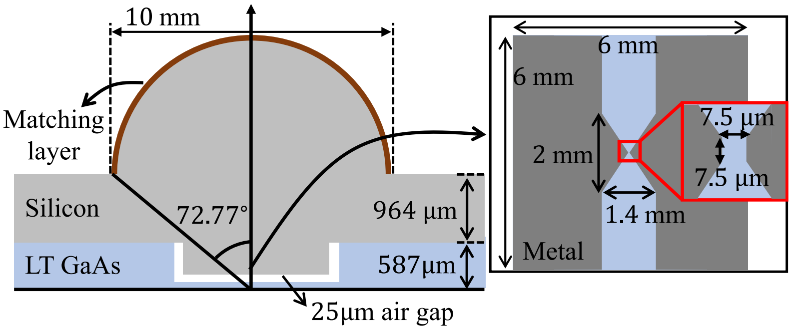

Figure B.2: LWA integrated with an extended hemispherical silicon lens. The inset shows the detailed antenna geometry.

and undesired radiation at about 10°, as shown in Fig. B.1(h) and B.1(i). By integrating the secondary fields, we can evaluate the power radiated by the lens antenna and then calculate the lens radiation efficiency as the ratio between the lens radiated power and the feed radiated power. This efficiency term is shown in Fig. B.1(b) and it includes the front-to-back ratio of the BTA, the spillover of the feed with respect to the lens truncation angle, and the reflection at the lens-air interface. The average value of the radiation efficiency is about 60% and the peaks in the figure are caused by the matching layer which is resonant around 0.4 THz and multiple frequencies. Furthermore, we calculate the gain of the lens antenna and show it in Fig. B.1(c). We can notice that the gain decreases after 0.35 THz and remains at 19 dBi for $f \geq 0.8$ THz. This is associated with the very low taper efficiency of the poorly radiated secondary fields. The blue curve in the figure represents the maximum achievable directivity for the given lens diameter.

B.2 Analysis of Leaky-wave Based Photoconductive Antennas

The structure of the used leaky-wave based PCA is shown Fig. B.2. The lens feed also has a bow-tie geometry but with the width and length of 2 mm × 1.4 mm and the gap size of 7.5 µm × 7.5 µm. The lens now has a mushroom-like shape, with a “stalk” sticking out of the flat side of it. This allows the introduction of a 25 µm air cavity between the lens bottom and the LT GaAs substrate to support the propagation of leaky waves. Such a LWA is particularly efficienct at illuminating dielectric lenses, as discussed in [26, 99]. A full description of the fabrication process is discussed in [107].

The simulated antenna impedance is shown in Fig. B.1(a). It has a higher value than the BTA and varies more significantly. The co-pol primary fields of this LWA radiated inside the silicon lens are shown in Fig. B.1(d)-B.1(f) and compared to those of the BTA. We can observe a typical leaky radiation (two peaks around broadside) which is more symmetric and more focused at broadside compared to that of the BTA. Consequently, the lens radiation efficiency is higher than that of the BTA, as shown in Fig. B.1(b), and the corresponding lens secondary fields [see Fig. B.1(g)-B.1(i)] have well-focused broadside patterns with much higher gain which is reported in Fig. B.1(c). Therefore, this type of lens antenna can couple better to a QO component, as discussed in [99, 107].

Appendix C

Design and Alignment of the Optical Components Used in the THz Time-domain System

In this appendix, we first describe how to choose the dimensions of the focusing lenses in the measurement setup shown in Fig. 4.8. Afterwards, we discuss the alignment of the laser beams with the optical components to achieve the best illumination on a photoconductive antenna (PCA).

C.1 Dimensions of the Focusing Lenses

In our laboratory, we use a commercially available pulsed laser source, Tera K15, from Menlo system [104], as shown in Fig. C.1(a). It can be used for spectroscopy by using two fiber-coupled PCAs [105] shown in Fig. C.1(b). Both the emitter and the detector are excited by in-fiber laser pulses. The former is biased by an external voltage while the latter is connected to an amplifier and electronic devices. This system also has two free-space ports, see C.1(a), which are used for our own PCAs. One port has a fixed optical path while the other has an optical delay unit (ODU) which is used to electronically control the optical delay of the port. The fixed port is used to illuminate a PCA source while the delayed port for a PCA receiver.

The output laser beam of each port behaves as a Gaussian beam and has a waist of 0.605 mm at the port position. The beam will then diverge as it propagates, and for the measurement setup shown in Fig. 4.8, the laser beam arriving at the focusing lens L1 has a $1/e^2$ radius about $w_0 \approx 0.7$ mm. To achieve the best illumination of the laser on the gap of the PCAs, we use L1 to focus the laser beam with its full width at half maximum (FWHM) the same as the gap size of the PCA, i.e., FWHM$= W_x = W_y = 10$ µm. The ideal effective

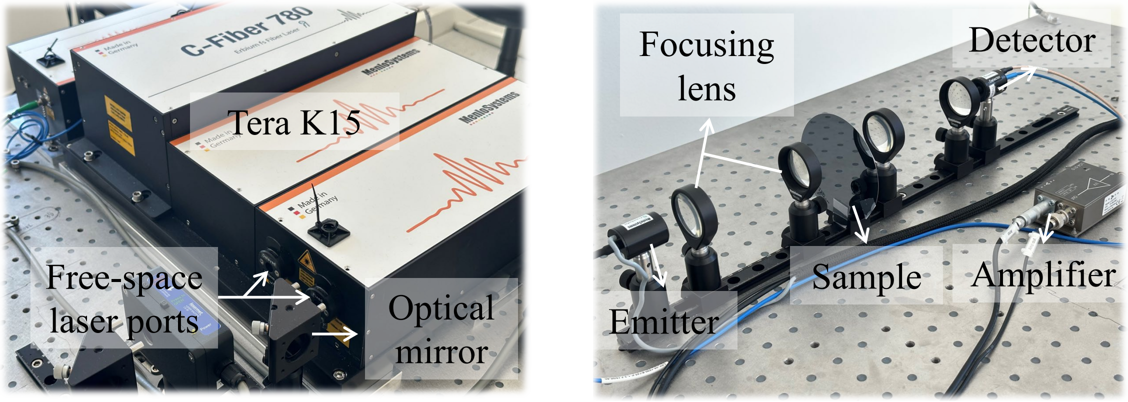

(a) (b)

Figure C.1: Photographs of the used pulsed lase source, Tera K15, with (a) two free-space laser ports and (b) two fiber-coupled PCAs as the emitter and the detector.

focal length (EFL) of L1 can then be calculated using the expression as follows:

$$EFL_{ideal} = \frac{\pi w_0 \cdot \mathrm{FWHM}}{\lambda_c \sqrt{2ln2}}, \tag{C.1}$$

where $\lambda_c = 780$ nm is the laser wavelength. The resuling ideal EFL is 24 mm thus we use the commercially available focusing lens LA1074-B-ML from Thorlabs which has a diameter of 12.7 mm and an EFL of 20 mm.

Focusing Lenses for the Used Photoconductive Connected Arrays

In Appendix D, we characterize the raidated power of two types of photoconductive connected arrays (PCCAs), and part of the measurement setup is depicted in Fig. C.2. Here we use a beam expander to enlarge the diameter of the output laser beams since the used optical path is so long that the unexpanded laser beams will diverge significantly. The $1/e^2$ radius of the laser beam arriving at the focusing lens L1 is $w_{BE} \approx 3.125$ mm. To best illuminate the PCCA, the laser beam arriving at the PCCA should be collimated and has the FWHM of $D_L^{FWHM} = 500$ µm, which is the same size as the micro lens array (500 µm × 500 µm). To achieve this, we use two focusing lenses, L1 and L2, to first focus and then collimate the incoming laser beams, as depicted in Fig. C.2. The EFL of each lens can be calculated using (C.1). The first lens L1 is LA1608-B-ML (Thorlabs) which has a diameter of 25.4 mm and an EFL of 75 mm. The second lens L2 is LA1540-B-ML (Thorlabs) with a diameter of 12.7 mm and an EFL of 15 mm.

C.2 Laser Alignment

The used laser source outputs collimated laser beams with their propagation vectors parallel to the ground. However, if they interact with non-aligned optical components, their

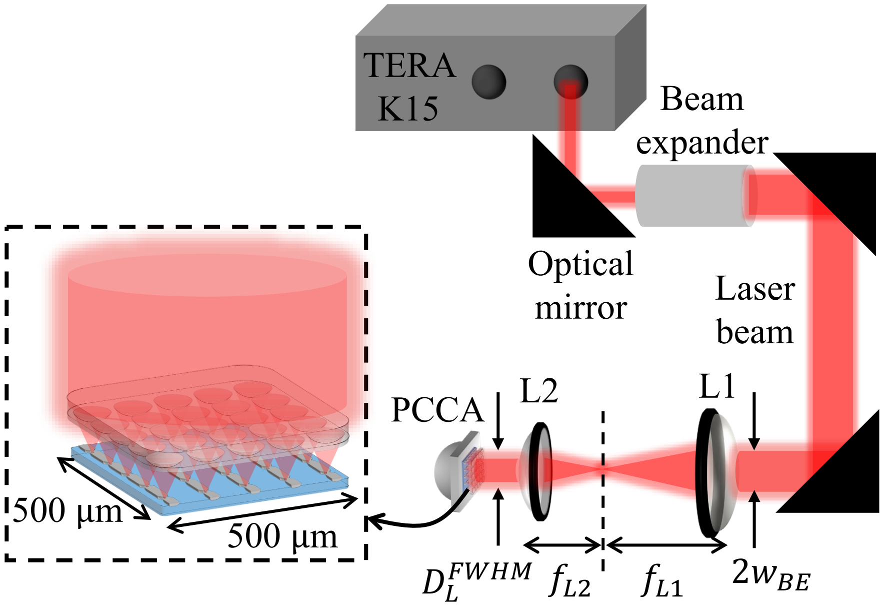

Figure C.2: Schematic representation of the setup for characterizing a PCCA. The inset shows the zoomed-in laser illumination on the PCCA. The indicated distance is $f_{L1} \approx 75$ and $f_{L2} \approx 15$ mm, respectively.

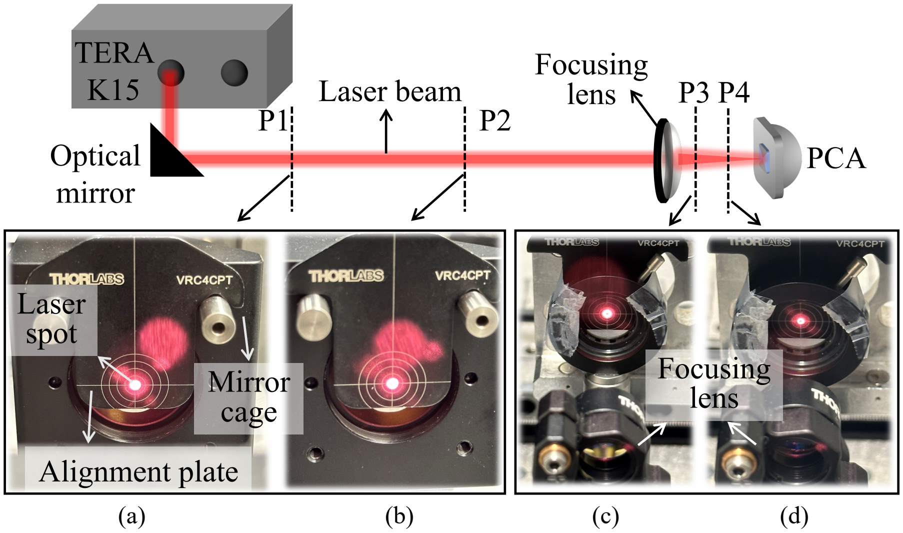

Figure C.3: Illustration of the laser alignment with the optical components. (a) and (b): alignment of the optical mirror. (c) and (d): alignment of the focusing lens. The laser beams are visualized by the camera of a smartphone.

propagation direction can be tilted, which leads to poor illumination on the PCAs. Here we propose to use a near-far beam checking approach to ensure good alignment of the optical components with the laser beams.

Let us consider the scenario shown in Fig. C.3. The output laser beams are reflected by an optical mirror and focused by a focusing lens on a PCA. The first step is to collimate the beams reflected by the mirror. We place an alignment plate at a near position P1, as

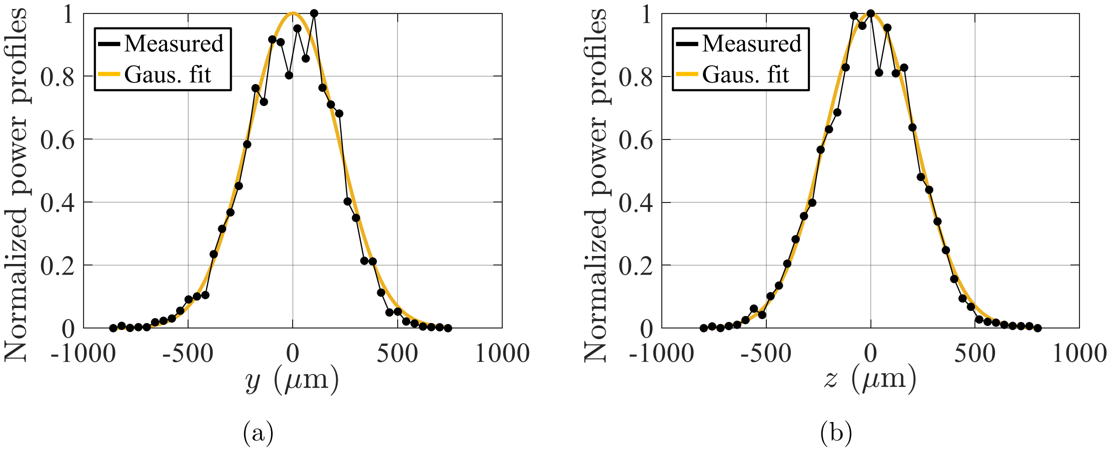

(a) (b)

Figure C.4: Power profiles of the focused laser beam illuminating the micro-lens array of the PCCA along (a) y axis and (b) z axis, measured using the setup in Fig. C.2. The yellow curves are the Gaussian fits of the measured points.

shown in Fig. C.3(a), and then we can tune the mirror to reflect the laser beams on the center of the plate. This can be achieved by visualizing the laser beams using the camera of a smart phone. Afterwards, we move the plate to a far position P2 and check if the laser beams are still located at the the plate center. If so, it means the beams are collimated, as shown in Fig. C.3(b); otherise, the beams are tilted so we need to re-tune the mirror until the beams are collimated between P1 and P2.

A similar procedure can be done for the alignment of the focusing lens. If the laser beams remain at the plate center at both P3 and P4, the lens is aligned. The tuning of the lens is more difficult than that of the mirror since the beam width is different at P3 and P4, as shown in Fig. C.3(c) and Fig. C.3(d), respectively. It is worth mentioning that this alignment approach has a tolerance between $200 - 500$ µm since the centering of the laser beams is judged by human eyes and photographs, which is subjective. The accuracy can be improved if one performs this alignment procedure several times.

We have achieved great alignment for the bow-tie based PCAs, as indicated by the measurements of the laser profiles shown in Fig. 4.9. This is also done for the mentioned PCCAs, as shown by the laser profiles in Fig. C.4.

Appendix D

Measurement of THz Power Radiated by Photoconductive Sources

In this appendix, we experimentally characterize two types of photoconductive antenna (PCAs) in term of their radiated THz power: a bow-tie based PCA and a photoconductive connected array (PCCA). The measurements are then used to determine the material properties of the used LT GaAs substrates.

D.1 Bow-tie Based Photoconductive Antennas

In Chapter 4, PCA 1 (the transmitter) and PCA 2 (the receiver) have identical geometries; however, since they were fabricated from different locations on the same LT GaAs wafer, their recombination (τ_c) and scattering time (τ_s) could be 2-3 times different. To quantify τ_c and τ_s for the used PCAs, we measured the THz power radiated by each PCA using the setup shown in Fig. D.1. Such power measurements are useful to assess the material properties of the used LT GaAs substrates as done in [98]. We use a PM5 power meter (Virginia Diodes) connected to a conical WR10 horn antenna to capture the THz fields focused by the focusing lens L3.

The measured power is shown in Fig. D.2 for a biasing voltage of $V_b = 30$ V versus the optical power $\widetilde{P}_{opt}^{Tx}$ in the gap. We can observe that even if the used PCAs and the measurement setups are identical, different radiated power is detected. From this we can conclude that the used LT GaAs substrates of each PCA have different material properties. The recombination time of the PC material is mainly associated with the width of the radiated THz pulses, thus the integration time for the power. We estimate its value according to the measurements of the detected currents discussed in Section 4.3.2 and $\tau_c^{Tx} = \tau_c^{Rx} = 700$ fs. In our modelling, we assume a unitary value for the quantum efficiency with which one electron is freed for every photon absorbed. Thus the differences between PCAs are represented by different values of the scattering time. Since PCA 1 radiates about 4 dB higher power than PCA 2, we can assume that $\tau_s^{Tx} \approx 1.6\tau_s^{Rx}$. We then apply the same procedures

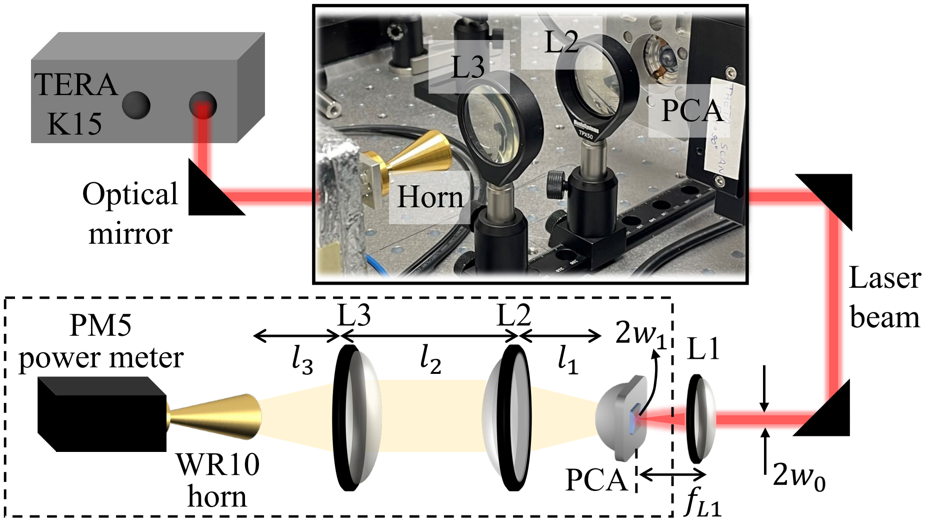

Figure D.1: Schematic representation of the setup for the power measurement with the photograph shown in the inset. The laser beams are represented by the red rays while the THz pulses are yellow rays. The indicated distance is $f_{L1} \approx 20.1$ mm, $l_1 \approx 22.5$ mm, $l_1 \approx 63$ mm, and $l_3 \approx 20$ mm.

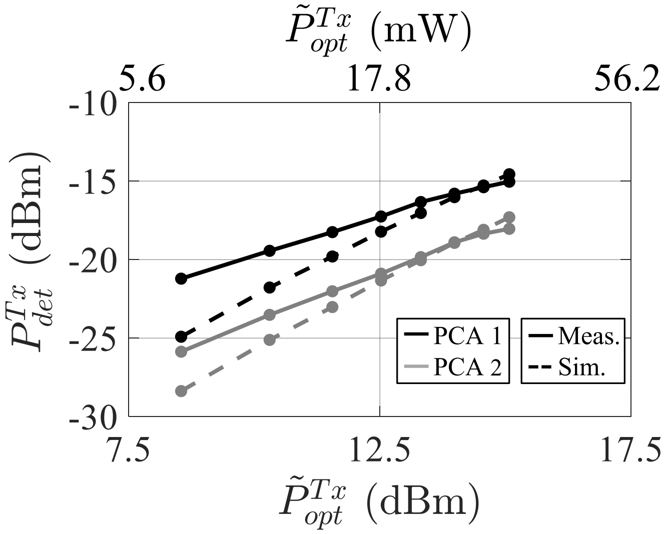

Figure D.2: Measurements and simulations of the radiated THz power P_{det}^{Tx} for both PCAs when using the setup in Fig. D.1. PCA 1 is later used as the transmitter while PCA 2 is the receiver. In the simulations, $V_b = 30$ V, $\tau_c^{Tx} = \tau_c^{Rx} = 700$ fs, $\tau_s^{Tx} = 2$ fs and $\tau_s^{Rx} = 1.3$ fs.

described in [98] to obtain the electromagnetic simulations of the setup. The accuracy of the simulations for the QO link is limited below 150 GHz, as explained in Section 4.3.2. We estimate the values of τ_s^{Tx} and τ_s^{Rx} for both PCAs by matching the power simulations with the measurements. Eventually we set $\tau_s^{Tx} = 2$ fs and $\tau_s^{Rx} = 1.3$ fs for the best fit shown in Fig. D.2. Although the values of these scattering time are somewhat lower than those used in [98], these values possibly correspond to a lower quantum efficiency, for instance, if the LT GaAs is not properly annealed [133–136].

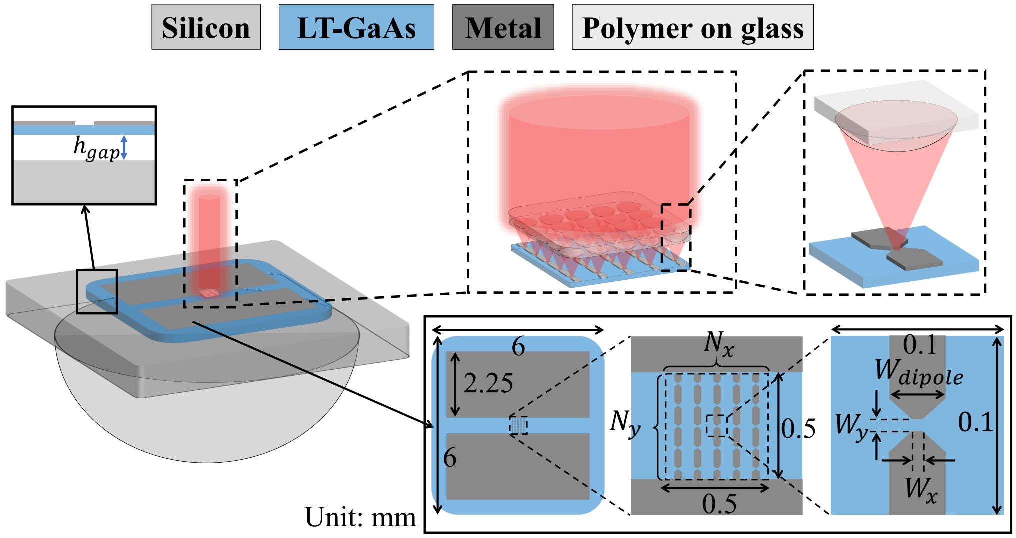

Figure D.3: Schematic representation of the connected dipole array presented in [137] coupled to a silicon lens under pulsed laser illumination. The array dimensions are marked in the figure. The array elements are $N_x = N_y = 5$ and the dipole dimensions are $W_x = W_y = 7.5$ µm, $W_{dipole} = 20$ µm. Here we consider the gap height $h_{gap} = 0$ and 25 µm.

D.2 Photoconductive Connected Arrays

As the optical power absorbed by a PCA increases, the THz power radiated by it suffers from saturation, as already shown in Fig. 3.3. One can increase the feeding gap size of the PCA to mitigate this problem. However, making the feeding gap too large in terms of the THz wavelengths will cause a dramatic drop in the antenna efficiency due to dispersion effects. To solve this problem, a photoconductive connected array (PCCA) was proposed in [137]. The advantage of this solution is that the PC area serving as the antenna feed is distributed over multiple elements, which allows smaller individual gap sizes. This mitigates the dispersion associated with large gap sizes. Here we characterize the radiated power of two types of PCCAs: one is the connected dipole array from [137]; the other is the leaky-wave based PCCA where an air gap of 25 µm is maintained between the dipole array and the silicon lens, similar to the leaky lens antenna discussed in Appendix B.

Fig. D.3 shows the geometry of the used PCCA and illustrates how it works. The incoming laser beam first impinges on a micro-lens array. This array divides and focuses the laser beam on each PC gap of the connected array. The connected array then radiates the generated THz fields towards the silicon hemispherical lens with/without the air gap. The used micro lenses are commercially available with a diameter of 100 µm and f-number of 9.5 [138]. The detailed geometry of the connected array is shown in the bottom inset in Fig. D.3, with the corresponding dimensions. The array elements are $N_x = N_y = 5$ and the dipole dimensions are $W_x = W_y = 7.5$ µm, $W_{dipole} = 20$ µm. Two PCCAs with $h_{gap} = 0$ and 25 µm were simulated in CST when radiating towards a semi-infinite silicon medium and the results were reported in [139]. Here we mainly focus on the measurement of the radiated THz power. The measurement setup is essentially the same as that depicted in Fig. D.1, but with different focusing lenses as discussed in Appendix C. Thanks to the extensive alignment, the power profiles of the laser beams have decent Gaussian shapes and their FWHM are 509 µm (y axis) and 514 µm (z axis), as shown in Fig. C.4(a) and Fig. C.4(b), respectively. This leads to an average spillover efficiency for illuminating the micro-lens array of the PCCA of $\eta_{so}^{ML} = 56.6\%$. The spillover efficiency of the micro lenses on the PC gaps is calculated as $\eta_{so}^{gap} = 53.7\%$. Therefore, the optical efficiency is $\eta_{opt}^{Tx} = 17.9\%$ (total spillover times the absorption of the LT GaAs gap). Note that the oscillation at the centers of the profiles is most likely associated with the non-perfect alignment of the optical path.

To maximize the detected power, the position of the focusing lenses and the horn were fine-tuned for both arrays: for $h = 0$ µm, $l_1 \approx 43.5$ mm, $l_2 \approx 56.5$ mm, and $l_3 \approx 14.5$ mm; for $h = 25$ µm, $l_1 \approx 61$ mm, $l_2 \approx 43.5$ mm, and $l_3 \approx 13$ mm. The detected power P_{det}^{Tx} was measured and is plotted in Fig. D.4(a) versus the optical power $\widetilde{P}_{opt}^{Tx}$ when the biasing voltage V_b is 30 V, 75 V, and 150 V. We can observe power saturation as $\widetilde{P}_{opt}^{Tx}$ increases for both arrays. When $V_b = 30$ V, P_{det}^{Tx} of both arrays is quite close; however, as the voltage increases to 150 V, the difference becomes more significant. To better understand this behaviour, we also measured P_{det}^{Tx} versus V_b when the optical power is fixed as $\widetilde{P}_{opt}^{Tx} = 32$ mW, as shown in Fig. D.4(b). We can notice when $10\log_{10}(V_b) \leq 20$ ($V_b \leq 100$ V), both arrays have similar P_{det}^{Tx}, but as V_b increases, the difference becomes larger. The array with the air gap appears to have a higher saturation voltage compared to the array without the gap. Consequently, for higher V_b, the array with the air gap can achieve a higher P_{det}^{Tx}.

We also compare the measurements to the simulations for both arrays, as shown in Fig. D.4(c) and D.4(d). The details associated with the simulations were reported in [139]. There, the recombination and scattering time were assumed as $\tau_c^{Tx} = 300$ fs and $\tau_s^{Tx} = 8$ fs in the simulations, respectively. However, these values need to be confirmed by future current measurements similar to what was done in Section 4.3.2. The agreement is reasonable but is not as good as that shown in Fig. D.2. The measured power saturates earlier than what is predicted by the simulation. This discrepancy is most likely related to the approximations made on the array impedance. In the proposed model, when evaluating P_{det}^{Tx}, the element impedance is assumed as constant resistance (100 Ω and 200 Ω for the arrays without and with the air gaps, respectively), but this impedance in fact shows strong frequency dependence [139]. Moreover, the active impedance of the arrays is calculated assuming the array elements are terminated by matched loads. However, the PC gaps are conductive only for a short time after excitation, which is in the order of the propagation time between two neighboring elements. Due to this highly time-dependent behavior of the PC feeding gaps, the mutual-coupling effects between the array elements are not accurately modeled by the proposed formulation.

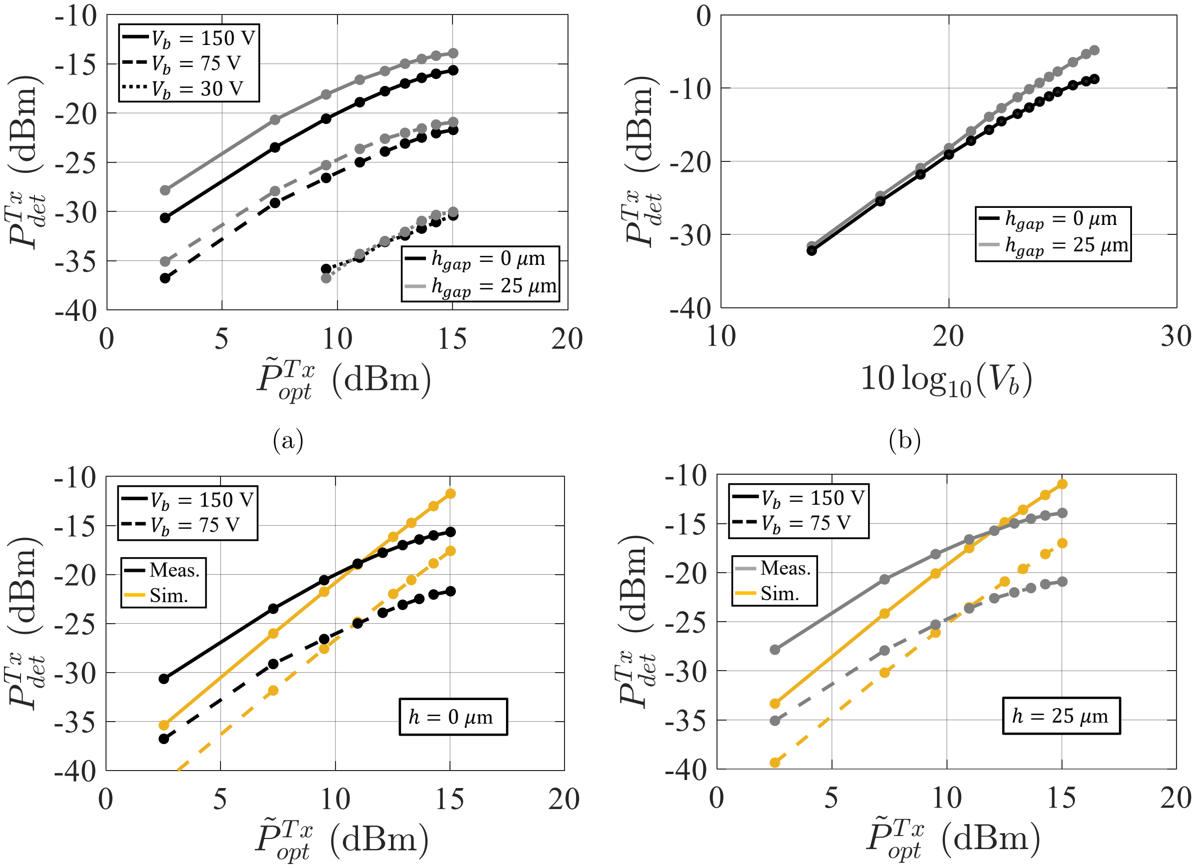

(a)

(b)

(c)

(d)

Figure D.4: Measurements and simulations of the radiated THz power P_{det}^{Tx} for PCCAs with and without the air gaps when using the setup in Fig. D.1. In the simulations, τ_c^{Tx} = 300 fs and τ_s^{Tx} = 8 fs. (a) Measured P_{det}^{Tx} versus $\tilde{P}_{opt}^{Tx}$. (b) Measured P_{det}^{Tx} versus $10\log_{10}(V_b)$. (c) Measured P_{det}^{Tx} compared to the simulations for the array without the air gap. (d) For the array with the air gap.

Appendix E

Design of Lens Antennas for Different Lens Materials

It was shown in Section 5.4 that a quartz lens with a resonant leaky-wave antenna (LWA) feed can well synthesis the reflector's focal field. In this appendix, we consider the lens antenna design for two other materials: plastic and silicon.

E.1 Lens Transmitted Geometrical-optics Fields

As mentioned in Section 5.4, for the central quartz lens antenna design, we need to conjugately match the patterns of the LWA feed with the transmitted geometrical optics (GO) fields on the FO sphere S_{FO}. Here we consider two other lens materials: high-density polyethylene (HDPE) and high-resistive silicon, with relative permittivity of $\varepsilon_r = 2.32$ and 11.9, respectively. The lens diameter is fixed as $D_l = 4\lambda_0$. For the silicon lens, we consider a standard quarter-wavelength parylene coating (same as the quartz lens), while this is not needed for the plastic lens.

The f-number of the lens, $f_{\#}^{l}$, is the parameter that should be co-designed with the LWA feed. $f_{\#}^{l}$ determines the truncation angle of the lens as well as the GO fields on the FO sphere, $\vec{E}_{ref}$. In the case of broadside incidence, to evaluate an estimation of $f_{\#}^{l}$ for different materials, we can approximate $\vec{E}_{ref}$ as the product between the airy pattern of the reflector and the transmitted GO fields of a plane wave, $\vec{E}_{PW}$, which was introduced in [16,38]. The latter field in the H-plane is plotted in Fig. E.1(a) until reaching the critical angles for three different materials and the resulting approximate $\vec{E}_{ref}^{app.}$ in the H-plane is shown in Fig. E.1(b) versus $f_{\#}^{l}$. As the material permittivity increases, $\vec{E}_{ref}^{app.}$ of the plastic lens has a sharper roll-off compared to that of the silicon lens, since the critical angle in plastic is closer to broadside than silicon, as indicated in Fig. E.1(a). Moreover, we can notice that as $f_{\#}^{l}$ decreases (increasing the lens truncation angle), the beam width of the silicon lens increases the most while that of the plastic lens changes slightly. The quartz lens behaves in between these two lenses. This means that we have more flexibility in

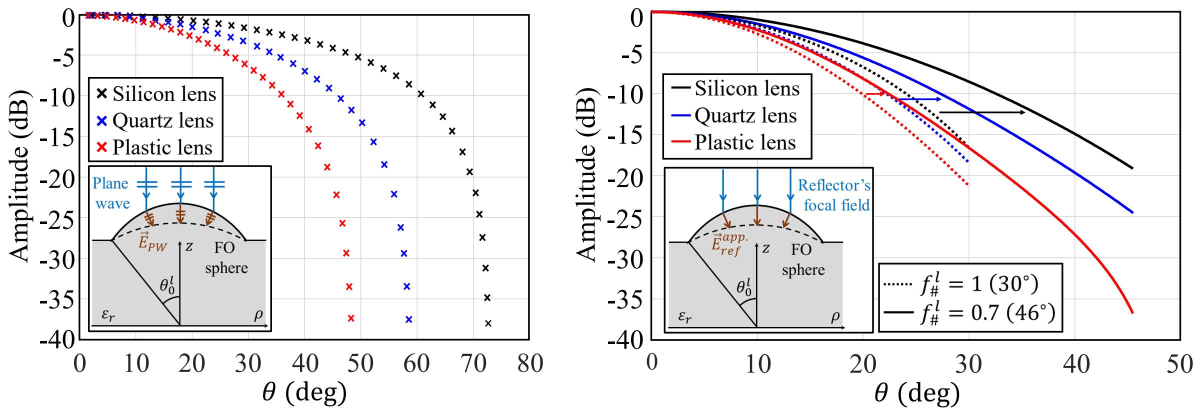

(a) (b)

Figure E.1: Comparison of the lens GO fields (in the H-plane) on the FO sphere for different materials when the incidence is (a) a broadside plane wave, and (b) the reflector's focal field. In (b), the lens GO fields are indicated as $\vec{E}_{ref}^{app.}$ since they are approximately evaluated.

selecting the f-number of the silicon lens to tune $\vec{E}_{ref}^{app.}$ than the other two lenses. This is important when considering the conjugate field-matching condition, because for example, the feed pattern of the plastic lens should be fixed to have a -10 dB width at about 22° as the maximum solid angle, whereas that of the silicon lens can varies from 25° to 35°.

E.2 Design of Leaky-wave Antenna Feeds

In the case of the silicon lens, the field radiated by the LWA through the air cavity, $\vec{E}_{LWA}$, is shown in the H-plane in Fig. E.2(a) by the dashed blue curve. It is very narrow compared to the lens GO field $\vec{E}_{ref}$ (black dashed curve) due to the dense medium, even when $f_\#^l$ is already increased to 1.28. To broaden $\vec{E}_{LWA}$ and achieve good amplitude matching, we can replace the air cavity by a plastic cavity with $\varepsilon_r^c = 2.55$ and height of $h_c = 0.5\lambda_d$ (wavelength in the medium). The resulting $\vec{E}_{LWA}$ is shown by the solid curves which are well matched with $\vec{E}_{ref}$ in both the amplitude and the phase [see Fig. E.2(b)]. Note that here the far field of the LWA is plotted for convenience, thus it looks slightly different from the near field shown in Fig. 5.2(c). Nevertheless, the -10 dB beam width is almost the same for both cases, thus the optimization procedure is the same. The optimized $f_\#^l = 1.28$ ($\theta_0 = 23°$) and the geometry of the double-slot iris is listed as follows: the iris angle is $\alpha = 65.5°$, the central distance between two slots is $\rho_0 = 0.38\lambda_0$, the slot width is $w = 0.15\lambda_0$, and the phase center of the feed is $\Delta_z = 0.63\lambda_0$ below the ground plane. Although the proposed stratification fulfills the conjugate field-matching condition, this structure leads to complexity when designing the impedance matching between the plastic cavity and the feeding waveguide which is filled with air. To achieve the best impedance matching, a quarter-wavelength transition inside the waveguide is required, which is complicated in practice.

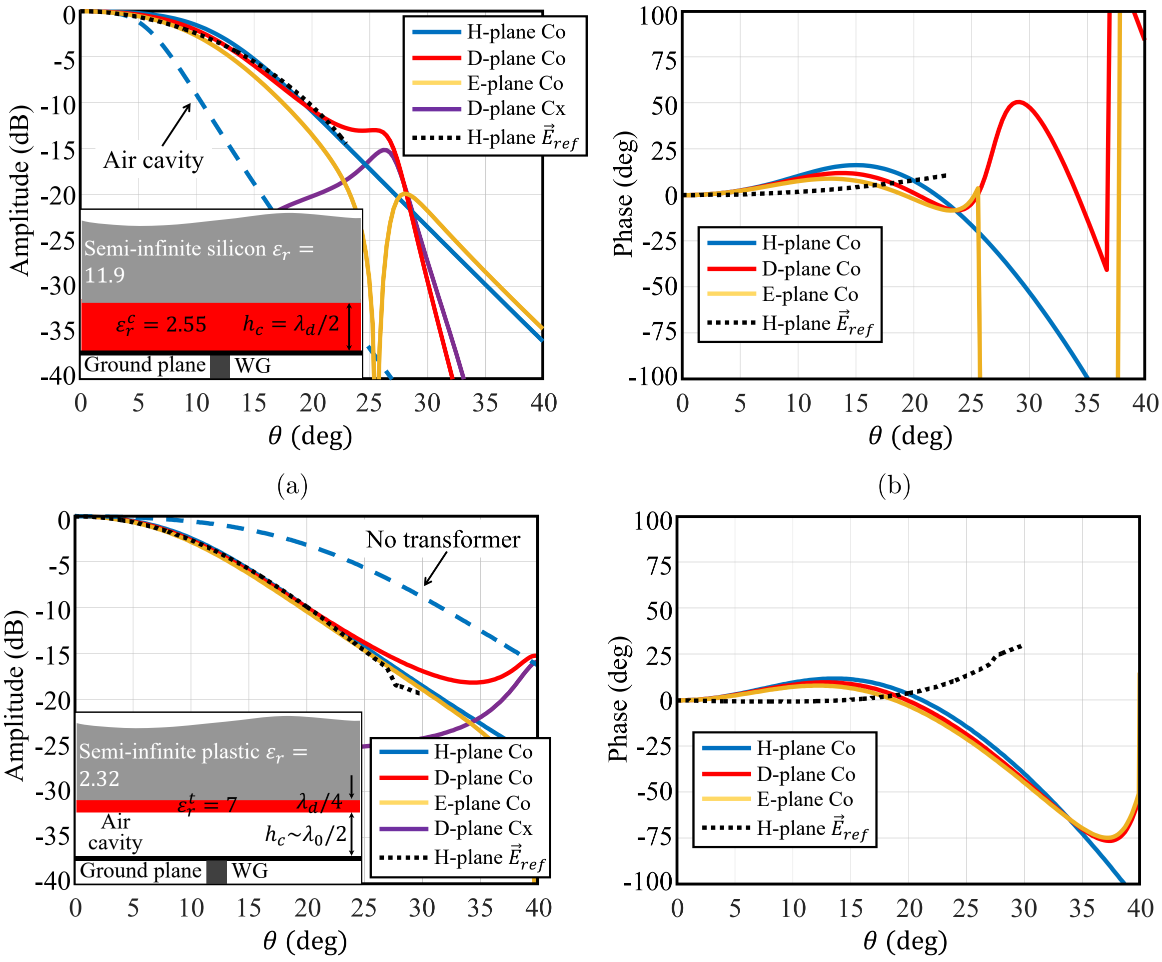

(a) (b)

(c) (d)

Figure E.2: Far-field patterns of the optimized LWA radiated inside a semi-infinite medium. (a) and (b) show the results for the silicon medium while (c) and (d) represent the plastic case. The stratifications are shown in the insets. In the H-plane, the lens GO field $\vec{E}_{ref}$ and the feed pattern when using only the air cavity are also shown for comparison.

On the contrary to the silicon lens, for the plastic lens with a resonant air cavity, the low permittivity contrast between the cavity and the plastic medium leads to a very wide far-field pattern which has -10 dB at about 30°, as shown by the dashed blue curve in Fig. E.2(c). To solve this, a quarter-wavelength transformation layer ($\varepsilon_r^t = 7$) is added between the air cavity and the plastic medium to alert the far-field pattern, as depicted in the inset in Fig. E.2(c). The resulting pattern is shown by the solid curves, showing very good matching with $\vec{E}_{ref}$. The optimized lens and feed geometries are listed as follows: $f_{\#}^l = 1$ (30°), $h_c = 0.485\lambda_0$ $\alpha = 65.5°$, $\rho_0 = 0.58\lambda_0$, the slot width is $w = 0.35\lambda_0$, and $\Delta_z = 0.85\lambda_0$.

To conclude, all types of lenses can fulfill the conjugate field-matching condition with proper design of lens and feed geometries. However, the feed designs of the silicon and the plastic lenses are more complex than that of the quartz lens shown in Section 5.2.

Bibliography

[1] O. J. Lodge and J. L. Howard, "On electric radiation and its concentration by lenses," *Proc. Phys. Soc. London*, vol. 10, no. 1, pp. 143, June 1888.

[2] D. B. Rutledge, D. P. Neikirk, and D. P. Kasilingam, "Integrated circuit antennas," *J. Infrared Milli. Waves*, vol. 10, pp. 1–90, 1983.

[3] G. M. Rebeiz, "Millimeter-wave and terahertz integrated circuit antennas," *Proc. IEEE*, vol. 80, no. 11, pp. 1748–1770, Nov. 1992.

[4] D. P. Neikirk, D. B. Rutledge, M. S. Muha, H. Park, and Chang-Xuan Yu, "Far-infrared imaging antenna arrays," *Appl. Phys. Lett.*, vol. 40, no. 3, pp. 203–205, Feb. 1982.

[5] D. F. Filipovic, G. P. Gauthier, S. Raman, and G. M. Rebeiz, "Off-axis properties of silicon and quartz dielectric lens antennas," *IEEE Trans. Antennas Propag.*, vol. 45, no. 5, pp. 760–766, May 1997.

[6] D. Grischkowsky, S. Keiding, M. van Exter, and C. Fattinger, "Farinfrared time-domain spectroscopy with terahertz beams of dielectrics and semiconductors," *J. Opt. Soc. Am. B*, vol. 7, no. 10, pp. 2006–2015, Oct. 1990.

[7] H. Harde and D. Grischkowsky, "Coherent transients excited by subpicosecond pulses of terahertz radiation," *J. Opt. Soc. Am. B*, vol. 8, no. 8, pp. 1642–1651, Aug. 1991.

[8] R. Al Hadi *et al.*, "A 1 k-pixel video camera for 0.7–1.1 terahertz imaging applications in 65-nm CMOS," *IEEE J. Solid-State Circuits*, vol. 47, no. 12, pp. 2999–3012, Dec. 2012.

[9] S. van Berkel, O. Yurduseven, A. Freni, A. Neto, and N. Llombart, "THz imaging using uncooled wideband direct detection focal plane arrays," *IEEE Trans. Terahertz Sci. Technol.*, vol. 7, no. 5, pp. 481–492, Sept. 2017.

[10] T. Nitta *et al.*, "Beam pattern measurements of millimeter-wave kinetic inductance detector camera with direct machined silicon lens array," *IEEE Trans. Terahertz Sci. Technol.*, vol. 3, no. 1, pp. 56–62, Jan. 2013.

[11] J. J. A. Baselmans *et al.*, “A kilo-pixel imaging system for future space based far-infrared observatories using microwave kinetic inductance detectors,” *A & A*, vol. 601, pp. A89, May 2017.

[12] X. Wu, G. V. Eleftheriades, and T. E. van Deventer-Perkins, “Design and characterization of single- and multiple-beam mm-wave circularly polarized substrate lens antennas for wireless communications,” *IEEE Trans. Microw. Theory Tech.*, vol. 49, no. 3, pp. 431–441, Mar. 2001.

[13] A. Artemenko, A. Maltsev, A. Mozharovskiy, A. Sevastyanov, V. Ssorin, and R. Maslennikov, “Millimeter-wave electronically steerable integrated lens antennas for WLAN/WPAN applications,” *IEEE Trans. Antennas Propag.*, vol. 61, no. 4, pp. 1665–1671, Apr. 2013.

[14] A. Mozharovskiy, A. Artemenko, O. Soykin, and R. Maslennikov, “Lens array antenna for 71–76/81–86 GHz point-to-point applications,” in *European Microw. Conf. (EuMC)*, London, UK, 2016, pp. 1560–1563.

[15] J. Ala-Laurinaho *et al.*, “2-D beam-steerable integrated lens antenna system for 5G *E*-band access and backhaul,” *IEEE Trans. Microw. Theory Tech.*, vol. 64, no. 7, pp. 2244–225, July 2016.

[16] M. Arias Campo, D. Blanco, S. Bruni, A. Neto, and N. Llombart, “On the use of fly’s eye lenses with leaky-wave feeds for wideband communications,” *IEEE Trans. Antennas Propag.*, vol. 68, no. 4, pp. 2480–2493, Apr. 2020.

[17] K. A. Shila and G. Mumc, “A millimeter-wave 2D beam steering antenna using extended hemispherical dielectric lens antenna subarrays,” *IEEE Access*, vol. 10, pp. 103065–103073, July 2022.

[18] B. G. Porter, L. L. Rauth, J. R. Mura, and S. S. Gearhart, “Dual-polarized slot-coupled patch antennas on Duroid with teflon lenses for 76.5-GHz automotive radar systems,” *IEEE Trans. Antennas Propag.*, vol. 47, no. 12, pp. 1836–184, Dec. 1999.

[19] B. Schoenlinner, X. Wu, J. P. Ebling, G. V. Eleftheriades, and G. M. Rebeiz, “Wide-scan spherical-lens antennas for automotive radars,” *IEEE Trans. Microw. Theory Tech.*, vol. 50, no. 9, pp. 2166–2175, Sept. 2002.

[20] F. A. Ghaffar, M. U. Khalid, K. N. Salama, and A. Shamim, “24-GHz LTCC fractal antenna array SoP with integrated Fresnel lens,” *IEEE Antennas Wirel. Propag. Lett.*, vol. 10, pp. 705–708, July 2011.

[21] K. F. Chang *et al.*, “77-GHz automotive radarsensor system with antenna integrated package,” *IEEE Trans. Compon. Packag. Manuf. Technol.*, vol. 4, no. 2, pp. 352–359, Feb. 2014.

[22] L. H. J. F. Beckmann and D. Ehrlichmann, "Optical systems for high-power laser applications: principles and design aspects," *Opt. Quantum Electron.*, vol. 27, no. 12, pp. 1407–1425, Dec. 1995.

[23] E. Gandini, A. Tamminen, A. Luukanen, and N. Llombart, "Wide field of view inversely magnified dual-lens for near-field submillimeter wavelength imagers," *IEEE Trans. Antennas Propag.*, vol. 66, no. 2, pp. 541–549, Feb. 2018.

[24] S. O. Dabironezare *et al.*, "A dual-band focal plane array of kinetic inductance bolometers based on frequency-selective absorbers," *IEEE Trans. Terahertz Sci. Technol.*, vol. 8, no. 6, pp. 746–756, Nov. 2018.

[25] D. F. Filipovic, S. S. Gearhart, and G. M. Rebeiz, "Double-slot antennas on extended hemispherical and elliptical silicon dielectric lenses," *IEEE Trans. Microw. Theory Tech.*, vol. 41, no. 10, pp. 1738–1749, Oct. 1993.

[26] N. Llombart, G. Chattopadhyay, A. Skalare, and I. Mehdi, "Novel terahertz antenna based on a silicon lens fed by a leaky wave enhanced waveguide," *IEEE Trans. Antennas Propag.*, vol. 59, no. 6, pp. 2160–2168, June 2011.

[27] M. Alonso-delPino, S. Bosma, C. Jung-Kubiak, G. Chattopadhyay, and N. Llombart, "Wideband multimode leaky-wave feed for scanning lens-phased array at submillimeter wavelengths," *IEEE Trans. Terahertz Sci. Technol.*, vol. 11, no. 2, pp. 205–217, Mar. 2021.

[28] S. Bosma, N. van Rooijen, M. Alonso-delPino, and N. Llombart, "A wideband leaky-wave lens antenna with annular corrugations in the ground plane," *IEEE Antennas Wirel. Propag. Lett.*, vol. 21, no. 8, pp. 1649–1653, Aug. 2022.

[29] D. R. Jackson and A. A. Oliner, "A leaky-wave analysis of the high-gain printed antenna configuration," *IEEE Trans. Antennas Propag.*, vol. 36, no. 7, pp. 905–910, July 1988.

[30] N. Llombart, A. Neto, G. Gerini, M. Bonnedal, and P. De Maagt, "Impact of mutual coupling in leaky wave enhanced imaging arrays," *IEEE Trans. Antennas Propag.*, vol. 56, no. 4, pp. 1201–1206, Apr. 2008.

[31] D. Blanco, E. Rajo-Iglesias, A. Montesano Benito, and N. Llombart, "Leaky-wave thinned phased array in PCB technology for telecommunication applications," *IEEE Trans. Antennas Propag.*, vol. 64, no. 10, pp. 4288–4296, Oct. 2016.

[32] CST Microwave Studio. Accessed: 2019. [Online]. Available: `http://www.cst.com`.

[33] Ansys HFSS. [Online]. Available: `https://www.ansys.com/products/electronics/ansys-hfss`.

[34] A. Neto, S. Maci, and P. J. I. de Maagt, "Reflections inside an elliptical dielectric lens antenna," *IEEE Proc. Microwaves, Antennas Propag.*, vol. 145, no. 3, pp. 243–247, June 1998.

[35] A. Neto, L. Borselli, S. Maci, and P. J. I. de Maagt, "Input impedance of integrated elliptical lens antennas," *IEEE Proc. Microwaves, Antennas Propag.*, vol. 146, no. 3, pp. 181–186, June 1999.

[36] N. Llombart, B. Blázquez, A. Freni, and A. Neto, "Fourier optics for the analysis of distributed absorbers under THz focusing systems," *IEEE Trans. Terahertz Sci. Technol.*, vol. 5, no. 4, pp. 573–583, July 2015.

[37] N. Llombart, S. O. Dabironezare, G. Carluccio, A. Freni, and A. Neto, "Reception power pattern of distributed absorbers in focal plane arrays: a Fourier optics analysis," *IEEE Trans. Antennas Propag.*, vol. 66, no. 11, pp. 5990–6002, Nov. 2018.

[38] H. Zhang, S. O. Dabironezare, G. Carluccio, A. Neto, and N. Llombart, "A Fourier optics tool to derive the plane wave spectrum of quasi-optical systems [EM programmer's notebook]," *IEEE Antennas Propagat. Mag.*, vol. 63, no. 1, pp. 103–116, Feb. 2021.

[39] V. Rumsey, "On the design and performance of feeds for correcting spherical aberration," *IEEE Trans. Antennas Propag.*, vol. 18, no. 3, pp. 343–351, May 1970.

[40] European Research Council Starting Grant (ERC-2014-StG LAA-THz-CC), Delft Univ. of Technol., Delft, the Netherlands. no. 639749, Oct. 2015. [Online]. Available: `https://cordis.europa.eu/project/id/639749/reporting`.

[41] G. C. Trichopoulos, H. L. Mosbacker, D. Burdette, and K. Sertel, "A broadband focal plane array camera for real-time THz imaging applications," *IEEE Trans. Antennas Propag.*, vol. 61, no. 4, pp. 1733–1740, Apr. 2013.

[42] P. U. Jepsen, D. G. Cooke, and M. Koch, "Terahertz spectroscopy and imaging – Modern techniques and applications," *Laser Photon. Rev.*, vol. 5, no. 1, pp. 124–166, Jan. 2011.

[43] N. M. Burford and M. O. El-Shenawee, "Review of terahertz photoconductive antenna technology," *Opt. Eng.*, vol. 56, no. 1, pp. 010901, July 2017.

[44] A. F. Bernardis, P. Sberna, A. Neto, and N. Llombart, "Signal to noise ratio budget of a pico-seconds pulsed radar system for stand-off imaging," in *44th Int. Conf. on Infrared, Milli., and Terahertz Waves (IRMMW-THz)*, Paris, France, 2019, pp. 1–2.

[45] D. A. Robertson *et al.*, "The CONSORTIS 16-channel 340-GHz security imaging radar," *Proc. SPIE*, vol. 10634, May 2018, Art. no. 1063409.

[46] K. B. Cooper, R. J. Dengler, N. Llombart, B. Thomas, G. Chattopadhyay, and P. H. Siegel, "THz imaging radar for standoff personnel screening," *IEEE Trans. Terahertz Sci. Technol.*, vol. 1, no. 1, pp. 169–182, Sept. 2011.

[47] H. Guerboukha, K. Nallappan, and M. Skorobogatiy, "Toward real-time terahertz imaging," *Adv. Opt. Photon.*, vol. 10, no. 4, pp. 843–938, Dec. 2018.

[48] E. Moreno, M. F. Fernández Pantoja, S. G. Garcia, A. R. Bretones, and R. G. Gómez Martin, "Time-domain numerical modeling of THz photoconductive antennas," *IEEE Trans. Terahertz Sci. Technol.*, vol. 4, no. 4, pp. 490–500, July 2014.

[49] N. Burford and M. El-Shenawee, "Computational modeling of plasmonic thin-film terahertz photoconductive antennas," *J. Opt. Soc. Am. B*, vol. 33, no. 4, pp. 748–759, Apr. 2016.

[50] O. A. Castaneda-Uribe, C. A. Criollo, S. Winnerl, M. Helm, and A. Avila, "Comparative study of equivalent circuit models for photoconductive antennas," *Opt. Express*, vol. 26, no. 22, pp. 29017–29031, Oct. 2018.

[51] A. Neto, N. Llombart, and A. Freni, "Time-domain modelling of pulsed photoconducting sources—Part I: The Norton equivalent circuit," *IEEE Trans. Antennas Propag.*, vol. 71, no. 3, pp. 2527–2535, Mar. 2023.

[52] Sang-Gyu Park, M. R. Melloch, and A. M. Weiner, "Analysis of terahertz waveforms measured by photoconductive and electrooptic sampling," *IEEE J. Quantum Electron.*, vol. 35, no. 5, pp. 810–819, May 1999.

[53] L. Duvillaret, F. Garet, J.-F. Roux, and J.-L. Coutaz, "Analytical modeling and optimization of terahertz time-domain spectroscopy experiments, using photoswitches as antennas," *IEEE J. Sel. Top. Quantum Electron.*, vol. 7, no. 4, pp. 615–623, July-Sept. 2001.

[54] T. K. Nguyen *et al.*, "Photoconductive dipole antennas for efficient terahertz receiver," *Opt. Commun.*, vol. 383, pp. 50–56, Jan. 2017.

[55] B. Chantraine-Bares, R. Sauleau, L. Le Coq, and K. Mahdjoubi, "A new accurate design method for millimeter-wave homogeneous dielectric substrate lens antennas of arbitrary shape," *IEEE Trans. Antennas Propag.*, vol. 53, no. 3, pp. 1069–1082, Mar. 2005.

[56] O. M. Haraz, A. Elboushi, S. A. Alshebeili, and A.-R. Sebak, "Dense dielectric patch array antenna with improved radiation characteristics using EBG ground structure and dielectric superstrate for future 5G cellular networks," *IEEE Access*, vol. 2, pp. 909–913, 2014.

[57] C.-X. Mao, S. Gao, and Y. Wang, “Broadband high-gain beam-scanning antenna array for millimeter-wave applications,” *IEEE Trans. Antennas Propag.*, vol. 65, no. 9, pp. 4864–4868, Sept. 2017.

[58] M. Khalily, R. Tafazolli, P. Xiao, and A. A. Kishk, “Broadband mm-wave microstrip array antenna with improved radiation characteristics for different 5G applications,” *IEEE Trans. Antennas Propag.*, vol. 66, no. 9, pp. 4641–4647, Sept. 2018.

[59] X. Gu *et al.*, “Development, implementation, and characterization of a 64-element dual-polarized phased-array antenna module for 28-GHz high-speed data communications,” *IEEE Trans. Microw. Theory Tech.*, vol. 67, no. 7, pp. 2975–2984, July 2019.

[60] X. Gu *et al.*, “A multilayer organic package with 64 dual-polarized antennas for 28GHz 5G communication,” in *2017 IEEE MTT-S Int. Microw. Symp. (IMS)*, Honolulu, HI, 2017, pp. 1899–1901.

[61] D. Liu, X. Gu, C. W. Baks, and A. Valdes-Garcia, “Antenna-in-package design considerations for Ka-band 5G communication applications,” *IEEE Trans. Antennas Propag.*, vol. 65, no. 12, pp. 6372–6379, Dec. 2017.

[62] A. Nafe, M. Sayginer, K. Kibaroglu, and G. M. Rebeiz, “2 × 64-element dual-polarized dual-beam single-aperture 28-GHz phased array with 2 × 30 Gb/s links for 5G polarization MIMO,” *IEEE Trans. Microw. Theory Tech.*, vol. 68, no. 9, pp. 3872–3884, Sept. 2020.

[63] D. Blanco, N. Llombart, and E. Rajo-Iglesias, “On the use of leaky wave phased arrays for the reduction of the grating lobe level,” *IEEE Trans. Antennas Propag.*, vol. 62, no. 4, pp. 1789–1795, Apr. 2014.

[64] F. Scattone, M. Ettorre, B. Fuchs, R. Sauleau, and N. J. G. Fonseca, “Synthesis procedure for thinned leaky-wave-based arrays with reduced number of elements,” *IEEE Trans. Antennas Propag.*, vol. 64, no. 2, pp. 582–590, Feb. 2016.

[65] J. C. R. Poirier, G. A. Morin, Y. M. M. Antar, and J. W. Moffat, “Millimetre-wave limited-scan array using small lenses,” in *IEEE Antennas and Propag. Soc. Int. Symp. (Cat. No.01CH37229)*, Boston, USA, 2001, vol. 2, pp. 823–826.

[66] G. Mumcu, M. Kacar, and J. Mendoza, “Mm-wave beam steering antenna with reduced hardware complexity using lens antenna subarrays,” *IEEE Antennas Wireless Propag. Lett.*, vol. 17, no. 9, pp. 1603–1607, Sept. 2018.

[67] S. Bosma, A. Neto, and N. Llombart, “On the near-field spherical wave formation in resonant leaky-wave antennas: application to small lens design,” *IEEE Trans. Antennas Propag.*, vol. 70, no. 2, pp. 801–812, Feb. 2022.

[68] D. R. Jackson, A. A. Oliner, and A. Ip, "Leaky-wave propagation and radiation for a narrow-beam multiple-layer dielectric structure," *IEEE Trans. Antennas Propag.*, vol. 41, no. 3, pp. 344–348, Mar. 1993.

[69] A. Neto, N. Llombart, G. Gerini, M. D. Bonnedal, and P. de Maagt, "EBG enhanced feeds for the improvement of the aperture efficiency of reflector antennas," *IEEE Trans. Antennas Propag.*, vol. 55, no. 8, pp. 2185–2193, Aug. 2007.

[70] G. Lovat, P. Burghignoli, and D. R. Jackson, "Fundamental properties and optimization of broadside radiation from uniform leaky-wave antennas," *IEEE Trans. Antennas Propag.*, vol. 54, no. 5, pp. 1442–1452, May. 2006.

[71] C. H. Tsao, Y. M. Hwang, F. Kilburg, and F. Dietrich, "Aperture-coupled patch antennas with wide-bandwidth and dual-polarization capabilities," in *1988 IEEE AP-S. Int. Symp., Antennas Propag.*, Syracuse, NY, USA, 1998, vol. 3, pp. 936–939.

[72] S. D. Targonski, R. B. Waterhouse, and D. M. Pozar, "Design of wide-band aperture-stacked patch microstrip antennas," *IEEE Trans. Antennas Propag.*, vol. 46, no. 9, pp. 1245–1251, Sept. 1998.

[73] A. Neto, N. Llombart, G. Gerini, and P. De Maagt, "On the optimal radiation bandwidth of printed slot antennas surrounded by EBGs," *IEEE Trans. Antennas Propag.*, vol. 54, no. 4, pp. 1074–1083, Apr. 2006.

[74] P. Burghignoli, "A leaky-wave analysis of the phase center in Fabry-Pérot cavity antennas," *IEEE Trans. Antennas Propag.*, vol. 60, no. 5, pp. 2226–2233, May. 2012.

[75] M. Yamazaki, E. T. Rahardjo, and M. Haneishi, "Construction of a slot-coupled planar antenna for dual polarisation," *Electron. Lett.*, vol. 30, no. 22, pp. 1814–1815, Oct. 1994.

[76] W. H. Syed, D. Cavallo, H. Thippur Shivamurthy, and A. Neto, "Wideband, wide-scan planar array of connected slots loaded with artificial dielectric superstrates," *IEEE Trans. Antennas Propag.*, vol. 64, no. 2, pp. 543–553, Feb. 2016.

[77] A. Deutsch, C. W. Surovic, R. S. Krabbenhoft, G. V. Kopcsay, and B. J. Chamberlin, "Prediction of losses caused by roughness of metallization in printed-circuit boards," *IEEE Trans. Adv. Packag.*, vol. 30, no. 2, pp. 279–287, May 2007.

[78] D. H. Auston, K. P. Cheung, and P. R. Smith, "Picosecond photoconducting Hertzian dipoles," *Appl. Phys. Lett.*, vol. 45, no. 3, pp. 284–286, Aug. 1984.

[79] R. Henri *et al.*, "Fabrication and characterization of an 8 × 8 terahertz photoconductive antenna array for spatially resolved time domain spectroscopy and imaging applications," *IEEE Access*, vol. 9, pp. 117691–117702, Aug. 2021.

[80] P. Benicewicz, J. Roberts, and A. Taylor, “Scaling of terahertz radiation from large-aperture biased photoconductors,” *J. Opt. Soc. Am. B*, vol. 11, no. 12, pp. 2533–2546, Dec. 1994.

[81] P. U. Jepsen, R. H. Jacobsen, and S. R. Keiding, “Generation and detection of terahertz pulses from biased semiconductor antennas,” *J. Opt. Soc. Am. B*, vol. 13, no. 11, pp. 2424–2436, Nov. 1996.

[82] M. Tani, S. Matsuura, K. Sakai, and S. Nakashima, “Emission characteristics of photoconductive antennas based on low temperaturegrown GaAs and semi-insulating GaAs,” *Appl. Opt.*, vol. 36, no. 30, pp. 7853–7859, Oct. 1997.

[83] I. Kostakis, D. Saeedkia, and M. Missous, “Terahertz generation and detection using low temperature grown InGaAs-InAlAs photoconductive antennas at 1.55 µm pulse excitation,” *IEEE Trans. Terahertz Sci. Technol.*, vol. 2, no. 6, pp. 617–622, Nov. 2012.

[84] N. Khiabani, Y. Huang, Y.-C. Shen, S. Boyes, and Q. Xu, “A novel simulation method for THz photoconductive antenna characterization,” in *Proc. European Conf. on Antennas and Propag. (EuCAP)*, Gothenburg, Sweden, 2013, pp. 751–754.

[85] A. Jooshesh, “Plasmonic-enhanced THz generation and detection using photoconductive antennas”, Ph.D. dissertation, Univ. of Victoria, Canada, 2016.

[86] B. Petrov, A. Fekecs, C. Sarra-Bournet, R. Arès, and D. Morris, “Terahertz emitters and detectors made on high-resistivity InGaAsP:Fe photoconductors,” *IEEE Trans. Terahertz Sci. Technol.*, vol. 6, no. 5, pp. 747–753, Sept. 2016.

[87] R. Smith, A. Jooshesh, J. Zhang, and T. Darcie, “Photoconductive generation and detection of THz-bandwidth pulses using near-field coupling to a free-space metallic slit waveguide,” *Opt. Express*, vol. 25, no. 22, pp. 26492–26499, Oct. 2017.

[88] D. V. Lavrukhin *et al.*, “Strain-induced InGaAs-based photoconductive terahertz antenna detector,” *IEEE Trans. Terahertz Sci. Technol.*, vol. 11, no. 4, pp. 417–424, July 2021.

[89] G. C. Loata, M. D. Thomson, T. Löffler, and H. G. Roskos, “Radiation field screening in photoconductive antennae studied via pulsed terahertz emission spectroscopy,” *Appl. Phys. Lett.*, vol. 91, no. 23, pp. 232506, Dec. 2007.

[90] C. W. Berry and M. Jarrahi, “Principles of impedance matching in photoconductive antennas,” *J. Infrared Milli. Terahertz Waves*, vol. 33, no. 12, pp. 1182–1189, Dec. 2012.

[91] N. Khiabani, Y. Huang, Y.-C. Shen, and S. Boyes, “Theoretical modeling of a photoconductive antenna in a terahertz pulsed system,” *IEEE Trans. Antenn. Propag.*, vol. 61, no. 4, pp. 1538–1546, Apr. 2013.

[92] R. Emadi, N. Barani, R. Safian, and A. Z. Nezhad, “Hybrid computational simulation and study of terahertz pulsed photoconductive antennas,” *J. Infrared Milli. Terahertz Waves*, vol. 37, no. 11, pp. 1069–1085, Aug. 2016.

[93] J. Prajapati, M. Bharadwaj, A. Chatterjee, and R. Bhattacharjee, “Circuit modeling and performance analysis of photoconductive antenna,” *Opt. Commun.*, vol. 394, pp. 69–79, July 2017.

[94] I. Malhotra, P. Thakur, S. Pandit, K. R. Jha, and G. Singh, “Analytical framework of small-gap photoconductive dipole antenna using equivalent circuit model,” *Opt. Quant. Electron.*, vol. 49, no. 10, pp. 334, Sept. 2017.

[95] G. J. Nissiyah and M. G. Madhan, “A simple equivalent circuit model of photoconductive dipole antenna for the study of Terahertz intensity modulation,” *Opt. Quant. Electron.*, vol. 53, no. 4, pp. 193, Mar. 2021.

[96] V. Rathinasamy, R. R. Thipparaju, E. N. F. Boby, and S. Mondal, “Numerical investigation and circuit analysis of interdigitated photoconductive antenna for terahertz applications,” *Opt. Quant. Electron.*, vol. 54, no. 4, pp. 239, Mar. 2022.

[97] A. Garufo, G. Carluccio, N. Llombart, and A. Neto, “Norton equivalent circuit for pulsed photoconductive antennas–Part I: Theoretical model,” *IEEE Trans. Antennas Propag.*, vol. 66, no. 4, pp. 1635–1645, Apr. 2018.

[98] A. F. Bernardis, P. M. Sberna, J. Bueno, H. Zhang, N. Llombart, and A. Neto, “Time-domain modelling of pulsed photoconducting sources–Part II: Characterization of a LT GaAs bow-tie antenna,” *IEEE Trans. Antennas Propag.*, vol. 71, no. 3, pp. 2536–2545, Mar. 2023.

[99] N. Llombart and A. Neto, “THz time-domain sensing: The antenna dispersion problem and a possible solution,” *IEEE Trans. Terahertz Sci. Technol.*, vol. 2, no. 4, pp. 416–423, July 2012.

[100] D. Grischkowsky, “Nonlinear generation of sub-psec pulses of THz electromagnetic radiation by optoelectronics-applications to time-domain spectroscopy,” *Front. in Nonlinear Opt.*, H Walther, N Koroteev, M O Scully (Eds.), CRC Press, 1993.

[101] S. Preu, “A unified derivation of the Terahertz spectra generated by photoconductors and diodes,” *J. Infrared Milli. Terahertz Waves*, vol. 35, no. 12, pp. 998–1010, Dec. 2014.

[102] A. Neto, S. Monni, and F. Nennie, “UWB, non dispersive radiation from the planarly fed leaky lens antenna–Part II: Demonstrators and measurements,” *IEEE Trans. Antennas Propag.*, vol. 58, no. 7, pp. 2248–2258, July 2010.

[103] E. Pancera, T. Zwick, and W. Wiesbeck, “Spherical fidelity patterns of UWB antennas,” *IEEE Trans. Antennas Propag.*, vol. 59, no. 6, pp. 2111–2119, June 2011.

[104] TERA K15, Menlo Systems, [Online]. Available: `https://www.menlosystems.com/products/thz-time-domain-solutions/terak15-terahertz-spectrometer`.

[105] TERA15-FC, Menlo Systems, [Online], Available: `https://www.menlosystems.com/assets/datasheets/THz-Antennas-and-Components/MENLO_TERA15FC-D-EN_2022-02-07_3w.pdf`.

[106] TICRA Tools GRASP, Accessed: 2020. [Online]. Available: `https://www.ticra.com/software/grasp`.

[107] J. Bueno, P. M. Sberna, A. Fiorellini-Bernardis, H. Zhang, A. Neto, and N. Llombart, "Fabrication and characterization of a leaky-lens photoconductive antenna on low temperature grown GaAs membranes," *IEEE Trans. Terahertz Sci. Technol.*, vol. 13, no. 5, pp. 431–439, Sept. 2023.

[108] A. Garufo, "Towards the engineering of pulsed photoconductive antennas", Ph.D. dissertation, Dept. Microelectronics, THz Sensing Group, Delft Univ. Technol., Delft, the Netherlands, 2017.

[109] M. J. Griffin *et al.*, "The Herschel-SPIRE instrument and its in-flight performance," *A & A*, vol. 518, no. L3, July 2010.

[110] J. Leech, B. K. Tan, G. Yassin, P. Kittara, and S. Wangsuya, "Experimental investigation of a low-cost, high performance focal-plane horn array," *IEEE Trans. Terahertz Sci. Technol.*, vol. 2, no. 1, pp. 61–70, Jan. 2012.

[111] E. Heinz *et al.*, "Progress in passive submillimeter-wave video imaging," *Proc. SPIE*, vol. 9078, June 2014, Art no. 907808.

[112] A. Dubok, A. Al-Rawi, G. Gerini, and A. B. Smolders, "Reflector synthesis for wide-scanning focal plane arrays," *IEEE Trans. Antennas Propag.*, vol. 67, no. 4, pp. 2305–2319, Apr. 2019.

[113] E. Gandini, J. Svedin, T. Bryllert, and N. Llombart, "Optomechanical system design for dual-mode stand-off submillimeter wavelength imagers," *IEEE Trans. Terahertz Sci. Technol.*, vol. 7, no. 4, pp. 393–403, July 2017.

[114] E. Gandini and N. Llombart, "Toward a real time stand-off submillimeter-wave imaging system with large field of view: quasi-optical system design considerations," *Proc. SPIE*, vol. 9462, May 2015, Art. no. 946205.

[115] R. Sauleau and B. Bares, "A complete procedure for the design and optimization of arbitrarily shaped integrated lens antennas," *IEEE Trans. Antennas Propag.*, vol. 54, no. 4, pp. 1122–1133, Apr. 2006.

[116] G. Godi, R. Sauleau, L. L. Coq, and D. Thouroude, "Design and optimization of three-dimensional integrated lens antennas with genetic algorithm," *IEEE Trans. Antennas Propag.*, vol. 55, no. 3, pp. 770–775, Mar. 2007.

[117] B. Chantraine-Bares and R. Sauleau, "Electrically-small shaped integrated lens antennas: a study of feasibility in Q-band," *IEEE Trans. Antennas Propag.*, vol. 55, no. 4, pp. 1038–1044, Apr. 2007.

[118] A. Rolland, M. Ettorre, A. V. Boriskin, L. Le Coq, and R. Sauleau, "Axisymmetric resonant lens antenna with improved directivity in Ka-band," *IEEE Antennas Wirel. Propag. Lett.*, vol. 10, pp. 37–40, Jan. 2011.

[119] T. Dang, J. Yang, and H.-X. Zheng, "An integrated lens antenna design with irregular lens profile," in *Proc. Global Symp. on Milli. Waves (GSMM)*, Harbin, China, 2012, pp. 212–215.

[120] T. Jaschke, B. Rohrdantz, and A. F. Jacob, "A flexible surface description for arbitrarily shaped dielectric lens antennas," in *German Microw. Conf. (GeMiC)*, Aachen, Germany, 2014, pp. 1–4.

[121] L. Mescia, P. Bia, D. Caratelli, M. A. Chiapperino, O. Stukach, and J. Gielis, "Electromagnetic mathematical modeling of 3D supershaped dielectric lens antennas," *Math. Probl. Eng.*, vol. 2016, pp. 8130160, Feb. 2016.

[122] C. C. Cruz, J. R. Costa, C. A. Fernandes, and S. A. Matos, "Focal-plane multibeam dual-band dielectric lens for Ka-band," *IEEE Antennas Wirel. Propag. Lett.*, vol. 16, pp. 432–436, 2017.

[123] S. O. Dabironezare, G. Carluccio, A. Freni, A. Neto, and N. Llombart, "Coherent Fourier optics model for the synthesis of large format lens based focal plane arrays," *IEEE Trans. Antennas Propag.*, vol. 69, no. 2, pp. 734–746, Feb. 2021.

[124] L. W. Mou, Y. J. Cheng, Y. F. Wu, M. H. Zhao, and H. N. Yang, "Design for array-fed beam-scanning reflector antennas with maximum radiated power efficiency based on near-field pattern synthesis by support vector machine," *IEEE Trans. Antennas Propag.*, vol. 70, no. 7, pp. 5035–5043, July 2022.

[125] F. Zernike, "Beugungstheorie des schneidenverfahrens und seiner verbesserten form, der phasenk ontrastmethode," *Physica*, vol. 1, no. 7-12, pp. 689–704, May 1934.

[126] A. N. Plastikov, "A high-gain multibeam bifocal reflector antenna with 40° field of view for satellite ground station applications," *IEEE Trans. Antennas Propag.*, vol. 64, no. 7, pp. 3251–3254, July 2016.

[127] E. Martinez de Rioja, J. A. Encinar, A. G. Pino, B. Gonzalez-Valdes, S. V. Hum, and C. Tienda Herrero, "Bifocal design procedure for dual-reflectarray antennas in offset

configurations," *IEEE Antennas Wirel. Propag. Lett.*, vol. 17, no. 8, pp. 1421–1425, Aug. 2018.

[128] *Heraeus Group*, Hanau, Germany. [Online]. Available: `https://www.heraeus.com/media/media/hca/doc_hca/products_and_solutions_8/optics/Data_and_Properties_Optics_fused_silica_EN.pdf`.

[129] *Laser Processing of Optical Components - LouwersHanique*. The Netherlands. [Online]. Available: `https://www.louwershanique.com/services/laser-processing`.

[130] X. Wang *et al.*, "28 GHz multi-beam antenna array based on a compact wideband 8 × 8 butler matrix," in *2018 IEEE AP-S. Int. Symp. Antennas Propag.*, Boston, MA, USA, 2018, pp. 2177–2178.

[131] N. Katzenellenbogen and D. Grischkowsky, "Efficient generation of 380 fs pulses of THz radiation by ultrafast laser pulse excitation of a biased metal-semiconductor interface," *Appl. Phys. Lett.*, vol. 58, no. 3, pp. 222–224, Jan. 1991.

[132] D. R. Bacon, J. Madéo, and K. M. Dani, "Photoconductive emitters for pulsed terahertz generation," *J. Opt.*, vol. 23, no. 6, pp. 064001, Apr. 2021.

[133] A. Garufo *et al.*, "Norton equivalent circuit for pulsed photoconductive antennas—Part II: Experimental validation," *IEEE Trans. Antennas Propag.*, vol. 66, no. 4, pp. 1646–1659, Apr. 2018.

[134] S. S. Prabhu, S. E. Ralph, M. R. Melloch, and E. S. Harmon, "Carrier dynamics of low-temperature-grown GaAs observed via THz spectroscopy," *Appl. Phys. Lett.*, vol. 70, no. 18, pp. 2419–2421, May 1997.

[135] M. C. Beard, G. M. Turner, and C. A. Schmuttenmaer, "Subpicosecond carrier dynamics in low-temperature grown GaAs as measured by time-resolved terahertz spectroscopy," *J. Appl. Phys.*, vol. 90, no. 12, pp. 5915–5923, Dec. 2001.

[136] V. Ortiz, J. Nagle, J.-F. Lampin, E. Péronne, and A. Alexandrou, "Low-temperature-grown GaAs: Modeling of transient reflectivity experiments," *J. Appl. Phys.*, vol. 102, no. 4, pp. 043515, Aug. 2007.

[137] A. Garufo *et al.*, "A connected array of coherent photoconductive pulsed sources to generate mW average power in the submillimeter wavelength band," *IEEE Trans. Terahertz Sci. Technol.*, vol. 9, no. 3, pp. 221–236, May 2019.

[138] *Sumipro*, Almelo, the Netherlands. [Online]. Available: `https://www.sumipro.nl`.

[139] M. Huiskes, "Towards the design of an imaging setup using photoconductive antennas", M.S. thesis, Dept. Microelectronics, THz Sensing Group, Delft Univ. Technol., Delft, The Netherlands, 2022.

Summary

Analysis and Design of Lens Antenna Systems for Applications at Millimeter and Sub-millimeter Wavelengths

In recent decades, dielectric lens antennas have been more and more adopted and developed for sensing and imaging applications at sub-millimeter (sub-mm) wavelengths because they can achieve high gain while keeping their physical size and weight acceptable at these wavelengths. More recently, as low-loss and low-cost lens materials have become available and the lens fabrication is becoming easier and more accurate, lens antennas are attracting more interests for variety of applications at millimeter (mm) wavelengths such as high-data-rate wireless communication and automotive radars. However, the analysis and design of lens antennas at mm and sub-mm wavelengths present different challenges. In this thesis, we propose to use a field correlation technique to analyze lens antennas in reception and then optimize their aperture efficiency for different scenarios. Based on this optimization methodology, three examples of lens antenna systems are described at 28 GHz, 180 GHz, and beyond 200 GHz for the applications of 5G communication, wide field-of-view security imaging, and future mm-resolution THz imaging, respectively. The proposed methodology and design provide possible solutions for the potential challenges and can be used as guidelines for designing lens antennas at mm and sub-mm wavelengths.

For 5G and beyond 5G communication systems, the research trend is on high-gain antennas with low-profile, low-cost, and less feeding elements. To meet these requirements, a sparse phased array in combination with a scanning lens array is proposed. The array element is a leaky-wave antenna (LWA) coupled to an elliptical lens. To reduce the cost, the LWA feed is designed in a PCB structure and the lens material is plastic which can be milled easily. By using the proposed field correlation methodology, the lens geometry is co-optimized with the feed for a limited physical size. It achieves good impedance matching of 22.7% relative bandwidth, and high lens aperture efficiency above 75% and 70% over the required frequency band for the cases of broadside and steering to ±10°, respectively. The grating lobes caused by the large array periodicity are suppressed by the directive lens element pattern thus the array achieves 27.5 dBi broadside gain at 28 GHz with only 16 elements. By displacing the lens array and steering the phased array at the same time, the proposed design is also capable of steering up to ±20° with less than 2 dB scan loss. Prototypes were fabricated and measured, showing very good agreement with the simulations. The proposed design can be easily scaled to other frequencies, array size,

and array elements thus it provides guidelines on the design of high-gain and low-profile lens antennas at mm wavelengths.

At sub-mm wavelengths, nowadays security imaging is gaining more attention as terroristic threats increase. The state-of-the-art THz radars can achieve decent lateral resolution; however, their range resolution is moderate (in centimeter range) since they only exploit limited absolute frequency bandwidth, in the order of tens of GHz. To meet the demands for future high-resolution imaging, THz time-domain spectroscopy systems are proposed for THz imaging since they can provide hundreds of GHz bandwidth. Such systems use photoconductive antennas (PCAs) as sources and receivers which are integrated with silicon lenses to generate and receive THz pulses when excited by pulsed laser sources. A PCA source has been extensively investigated; however, the propagation of the generated THz pulses along a quasi-optical (QO) link, including the effect of the receiver, has not been well modelled yet. As the result, the simulated detected THz pulses at the receiver have always been compared with the measurements using arbitrary units. This makes the design of PCA-based imaging systems difficult. In this thesis, such a QO link is accurately modelled by a link transfer function which is evaluated using the field correlation technique in combination with full-wave simulations, geometrical optics (GO), and physical optics (PO) approaches. The PCA receiver is modelled using a Norton equivalent circuit and its current generator is accurately evaluated using the link transfer function. The detected currents are then evaluated using the stroboscopic sampling of the modelled THz pulses. The same QO link has been measured and this is the first time that both the amplitude and the waveforms of the simulated detected currents are compared to the measurements, showing excellent agreement.

Finally, to facilitate the design of future PCA-based radar systems with arrays of PCA receivers, a focal plane array (FPA) of lens antennas coupled to a reflector is investigated. The challenge is to achieve wide field of view for such a system, which means that the edge lens element of the FPA should couple well to the reflector with a low scan loss. To achieve this, we propose to shape lens surfaces and synthesize the desired patterns that can best illuminate the reflector for large scanning angles. The field correlation technique is implemented on the lens aperture plane for this purpose. The incident reflector's focal field is calculated on this plane using the PO approach and the lens radiated field is evaluated using the GO approach. Both fields can be efficiently evaluated thus an optimization procedure is proposed for the lens shaping. An example shaped quartz lens combined with a LWA feed is designed at 180 GHz using this procedure and it can well couple to a parabolic reflector, achieving 50.5 dBi directivity up to 20.3° scanning. The scan loss is 2.6 dB which is much lower than the state-of-the art horn-based FPA. The shaped lens antenna was fabricated and its measured far-field performance is in excellent agreement with the simulations. The proposed FPA provides design rules for future PCA-based imaging systems. In addition, the lens shaping concept and the optimization procedure are applicable for different lens materials and can be extended to other applications which require different patterns to be synthesized.

Samenvatting

Analyse en ontwerp van lens antenne systemen voor toepassingen op millimeter en submillimeter golflengten

In de afgelopen decennia zijn diëlektrische lensantennes steeds meer ontwikkeld en gebruikt voor detectie en beeldvorming toepassingen op sub-millimeter golflengten vanwege de hoge versterking die bereikt kan worden, terwijl tegelijkertijd hun fysieke grootte en gewicht aanvaardbaar kunnen worden gehouden bij deze golflengten. Omdat er recentelijk relatief goedkope materialen voor lenzen met een lage verliesfactor beschikbaar zijn gekomen en de fabricage van lenzen gemakkelijker en nauwkeuriger wordt, trekken lensantennes interesse voor een verscheidenheid aan toepassingen bij millimetergolflengtes (mm), zoals draadloze communicatie met hoge datasnelheden en automotive radars. De analyse en het ontwerp van lensantennes bij millimeter (mm) en sub-millimeter (sub-mm) golflengtes brengen echter verschillende uitdagingen met zich mee. In dit proefschrift stellen we voor om een veldcorrelatietechniek te gebruiken om lensantennes als ontvanger te analyseren en vervolgens hun apertuur-efficiëntie te optimaliseren voor verschillende scenario's. Op basis van deze optimalisatiemethodologie worden drie voorbeelden van lensantennesystemen beschreven bij 28 GHz, 180 GHz en meer dan 200 GHz voor respectievelijk de toepassingen van 5G-communicatie, beveiligingsbeeldvorming met een breed gezichtsveld en toekomstige beeldvorming met millimeterresolutie in het terahertz (THz) bereik. De voorgestelde methodologie en het ontwerp bieden mogelijke oplossingen voor de potentiële uitdagingen en kunnen worden gebruikt als richtlijnen voor het ontwerpen van lensantennes bij millimeter (mm) en sub-millimeter (sub-mm) golflengtes.

Voor 5G en toekomstige communicatiesystemen richt de onderzoekstrend zich op antennes met een hoge versterking, een laag profiel, lage kosten en minder voedingselementen. Om aan deze eisen te voldoen, wordt voorgesteld om een schaarse fase-gestuurde antenne array te combineren met een gestuurde lens array. Het arrayelement is een lekgolfantenne (LWA) gekoppeld met een elliptische lens. Om de kosten te verlagen, is de lekgolfantenne ontworpen in een PCB-structuur en is het lensmateriaal plastic dat gemakkelijk gefreesd kan worden. Door de voorgestelde veldcorrelatiemethodologie te gebruiken, wordt de lensgeometrie samen met de voeding geoptimaliseerd voor een beperkte fysieke grootte. Een goede impedantieaanpassing wordt bereikt met een relatieve bandbreedte van 22.7% en een hoge apertuur-efficiëntie van de lens boven de 75% en 70% over de vereiste frequentieband voor straling in de normaalrichting en gestuurd naar ±10°, graden, respectievelijk.

De grating lobes veroorzaakt door de schaarse opstelling van de array worden onderdrukt door de nauwe stralingsbundel van het lens element, waardoor de array 27.5 dBi stralingsdichtheid bereikt bij 28 GHz met slechts 16 elementen. Door de lens array te verschuiven en tegelijkertijd de fase-gestuurde array te sturen, is het voorgestelde ontwerp ook in staat om te sturen tot ±20° graden met minder dan 2 dB stuurverlies. Prototypes zijn vervaardigd en gemeten, waarbij een zeer goede overeenstemming met de simulaties werd aangetoond. Het voorgestelde ontwerp kan eenvoudig worden geschaald naar andere frequenties, array-groottes en array-elementen, en biedt daarmee richtlijnen voor het ontwerpen van laagprofiel lensantennes met hoge stralingsdichtheid bij millimetergolflengtes.

Bij sub-mm golflengtes krijgt beveiligingsbeeldvorming tegenwoordig meer aandacht door het toenemende aantal terroristische dreigingen. De state-of-the-art THz-radars kunnen een redelijke laterale resolutie bereiken; echter, hun bereikresolutie is matig (in de orde van centimeters), aangezien ze slechts beperkte absolute frequentiebandbreedte benutten, in de orde van tientallen GHz. Om te voldoen aan de eisen voor toekomstige beeldvormingssystemen met hoge resolutie, worden THz tijd-domein spectroscoopsystemen voorgesteld voor THz-beeldvorming, omdat ze honderden GHz bandbreedte kunnen bieden. Dergelijke systemen maken gebruik van fotoconductieve (PCA) antennes als bronnen en ontvangers, die geïntegreerd zijn met siliciumlenzen om THz-pulsen te genereren en ontvangen wanneer ze worden geëxciteerd door gepulste laserstraling. PCA bronnen zijn uitgebreid onderzocht; echter is de propagatie van de gegenereerde THz-pulsen langs een quasi-optische (QO) verbinding, inclusief het effect van de ontvanger, nog niet goed gemodelleerd. Als gevolg daarvan zijn de gesimuleerde gedetecteerde THz-pulsen bij de ontvanger altijd vergeleken met metingen in arbitraire eenheden. Dit maakt het ontwerpen van beeldvormingssystemen die berusten op het gebruik van PCAs moeilijk. In deze scriptie wordt een dergelijke quasi-optische (QO) verbinding nauwkeurig gemodelleerd met behulp van een transferfunctie die wordt geëvalueerd met behulp van de veldcorrelatietechniek in combinatie met volledige golfsimulaties, geometrische optica (GO) en fysische optica (PO) benaderingen. De PCA-ontvanger wordt gemodelleerd met behulp van een Norton equivalente schakeling waarvan de stroomgenerator nauwkeurig geëvalueerd wordt met behulp van de transferfunctie. De gedetecteerde stromen worden vervolgens geëvalueerd met behulp van de stroboscopische bemonstering van de gemodelleerde THz-pulsen. Dezelfde QO-verbinding is gemeten, en dit is de eerste keer dat zowel de amplitude als de golfvormen van de gesimuleerde gedetecteerde stromen worden vergeleken met de metingen, met uitstekende overeenkomst.

Tot slot wordt, om het ontwerpen van toekomstige radar systemen met PCA-ontvangers in arrays te vergemakkelijken, een focal plane array (FPA) van lensantennes gekoppeld aan een reflector onderzocht. De uitdaging is om een breed gezichtsveld te bereiken voor een dergelijk systeem, wat betekent dat het lenselement aan de rand van de FPA goed moet koppelen aan de reflector met een laag stuurverlies. Om dit te bereiken, stellen we voor om lensoppervlakken te vormen om stralingspatronen te synthetiseren die het beste de reflector kunnen belichten voor grote sturingshoeken. De veldcorrelatietechniek wordt voor dit doel geïmplementeerd op de apertuur van de lens. Het invallende focaal veld van de reflector wordt op dit vlak berekend met behulp van de PO-benadering, en het uitgestraalde veld van de lens wordt geëvalueerd met behulp van de GO-benadering. Beide velden kunnen efficiënt worden geëvalueerd. Daarom wordt een optimalisatieprocedure voorgesteld voor het vormgeven van de lens. Als voorbeeld wordt een gevormde kwartslens gecombineerd met een lekgolfantenne-voeding ontworpen op 180 GHz met behulp van deze procedure, welke goed kan koppelen aan een parabolische reflector, met een stralingsdichtheid van 50.5 dBi tot 20.3° graden sturen. Het stuurverlies bedraagt 2.6 dB, wat veel lager is dan de FPA's op basis van hoorns die momenteel beschikbaar zijn. De gevormde lensantennes is vervaardigd en de gemeten verre-veldprestaties zijn in uitstekende overeenstemming met de simulaties. De voorgestelde FPA biedt ontwerprichtlijnen voor toekomstige beeldvormingssystemen op basis van PCAs. Bovendien is het concept van lensvorming en de optimalisatieprocedure toepasbaar voor verschillende lensmaterialen en kan worden uitgebreid voor andere toepassingen waarbij andere stralingspatronen moeten worden gesynthetiseerd.

List of Publications

Journal Papers

J1. H. Zhang, S. O. Dabironezare, G. Carluccio, A. Neto, and N. Llombart, “A Fourier optics tool to derive the plane wave spectrum of quasi-optical systems [EM Programmer’s Notebook],” *IEEE Antennas Propagat. Mag.*, vol. 63, no. 1, pp. 103-116, Feb. 2021.

J2. H. Zhang, S. Bosma, A. Neto, and N. Llombart, “A dual-polarized 27 dBi scanning lens phased array antenna for 5G point-to-point communications,” *IEEE Trans. Antennas Propag.*, vol. 69, no. 9, pp. 5640-5652, Sept. 2021.

J3. A. F. Bernardis, P. M. Sberna, J. Bueno, H. Zhang, N. Llombart, and A. Neto, “Time-domain modelling of pulsed photoconducting sources—Part II: Characterization of an LT GaAs bow-tie antenna,” *IEEE Trans. Antennas Propag.*, vol. 71, no. 3, pp. 2536-2545, Mar. 2023.

J4. J. Bueno, P. M. Sberna, A. Fiorellini-Bernardis, H. Zhang, A. Neto, and N. Llombart, “Fabrication and characterization of a leaky-lens photoconductive antenna on low-temperature grown GaAs membranes,” *IEEE Trans. Terahertz Sci. Technol.*, vol. 13, no. 5, pp. 431-439, Sept. 2023.

J5. H. Zhang, N. Llombart, J. Bueno, A. Freni, and A. Neto, “Time-domain equivalent circuits for the link modelling between pulsed photoconductive sources and receivers,” *IEEE Trans. Terahertz Sci. Technol.*, under review.

J6. H. Zhang, S. O. Dabironezare, J. J. A. Baselmans, and N. Llombart, “Focal plane array of shaped quartz lenses for wide field-of-view submillimeter imaging systems,” *IEEE Trans. Antennas Propag.*, doi: 10.1109/TAP.2023.3334391.

Conference Papers

C1. H. Zhang, S. O. Dabironezare, G. Carluccio, A. Neto, and N. Llombart, “A GO/FO tool for analyzing quasi-optical systems in reception,” in *44th Int. Conf. on Infrared, Millimeter, and Terahertz Waves (IRMMW-THz)*, Paris, France, 2019, pp. 1-2.

C2. S. Bosma, H. Zhang, A. Neto, and N. Llombart, “Near-field beamforming in leaky-wave resonant antennas,” in *Proc. European Conf. on Antennas and Propag. (EuCAP)*, Copenhagen, Denmark, 2020.

C3. H. Zhang, S. Bosma, A. Neto, U. Imberg, and N. Llombart, “On the design of a 27-dBi phased array for 5G point-to-point communications,” in *Proc. European Conf. on Antennas and Propag. (EuCAP)*, Copenhagen, Denmark, 2020.

C4. S. Bosma, H. Zhang, A. Neto, and N. Llombart, “Near-field analysis of leaky-wave lens array feeds,” in *2020 IEEE AP-S. Int. Symp. Antennas Propag.*, Montreal, Canada, 2020.

C5. H. Zhang, S. O. Dabironezare, M. Zhang, and N. Llombart, “Design of wide-scan lens based focal plane arrays for sub-millimeter imaging systems,” in *Proc. European Conf. on Antennas and Propag. (EuCAP)*, Dusseldorf, Germany, 2021.

C6. H. Zhang, S. Bosma, A. Neto, U. Imberg, and N. Llombart, “High gain phased lens array for 5G fixed wireless access points,” in *Proc. European Conf. on Antennas and Propag. (EuCAP)*, Dusseldorf, Germany, 2021.

C7. H. Zhang, S. O. Dabironezare, and N. Llombart, “Design of wide field-of-view imagers based on focal plane arrays of leaky-wave lenses,” in *2021 IEEE AP-S. Int. Symp. Antennas Propag.*, Singapore, 2021.

C8. A. F. Bernardis, H. Zhang, P. Sberna, J. Bueno, A. Neto, and N. Llombart, “On the power radiated by photo conductive sources,” in *46th Int. Conf. on Infrared, Millimeter, and Terahertz Waves (IRMMW-THz)*, Chengdu, China, 2021, pp. 1-1.

C9. H. Zhang, A. Neto, and N. Llombart, “On the modelling of the quasi-optical coupling between two photoconductive antennas under pulsed laser illumination,” in *46th Int. Conf. on Infrared, Millimeter, and Terahertz Waves (IRMMW-THz)*, Chengdu, China, 2021, pp. 1-2.

C10. H. Zhang, S. O. Dabironezare, M. Zhang, and N. Llombart, “Design of lens based focal plane arrays for wide field-of-view imagers at sub-millimeter wavelengths,” in *46th Int. Conf. on Infrared, Millimeter, and Terahertz Waves (IRMMW-THz)*, Chengdu, China, 2021, pp. 1-2.

C11. H. Zhang, A. Neto, J. Bueno, P. Sberna, and N. Llombart, “On the modelling of a quasi-optical link between two photoconductive antennas under pulsed laser illumination,” in *Proc. European Conf. on Antennas and Propag. (EuCAP)*, Madrid, Spain, 2022.

C12. J. Bueno, M. Huiskes, H. Zhang, P. M. Sberna, N. Llombart, and A. Neto, “A leaky enhanced photo-conductive connected array for efficient generation of THz power,” in *Proc. European Conf. on Antennas and Propag. (EuCAP)*, Madrid, Spain, 2022.

C13. J. Bueno, M. Huiskes, H. Zhang, P. M. Sberna, N. Llombart, and A. Neto, “A leaky enhanced photo-conductive connected array for broadband generation of THz power,” in *47th Int. Conf. on Infrared, Millimeter, and Terahertz Waves (IRMMW-THz)*, Delft, the Netherlands, 2022, pp. 1-2.

C14. H. Zhang, A. Neto, J. Bueno, P. Sberna, and N. Llombart, “Comparison of receiver performance between bow-tie and leaky-wave based photoconductive antennas,” in *47th Int. Conf. on Infrared, Millimeter, and Terahertz Waves (IRMMW-THz)*, Delft, the Netherlands, 2022, pp. 1-2.

C15. H. Zhang, N. Llombart, A. Freni, and A. Neto, “Frequency-domain Norton resistance for pulsed photoconductive antennas,” in *Proc. European Conf. on Antennas and Propag. (EuCAP)*, Florence, Italy, 2023.

C16. H. Zhang, J. Bueno, P. Sberna, N. Llombart, and A. Neto, “Experimental setup for the characterization of a quasi-optical link between two pulsed photoconductive antennas,” in *Proc. European Conf. on Antennas and Propag. (EuCAP)*, Florence, Italy, 2023.

C17. H. Zhang, S. O. Dabironezare, and N. Llombart, “A shaped quartz lens antenna for wide scanning sub-millimeter imaging systems,” in *48th Int. Conf. on Infrared, Millimeter, and Terahertz Waves (IRMMW-THz)*, Montreal, Canada, 2023, pp. 1-2.

C18. H. Zhang, J. Bueno, P. Sberna, N. Llombart, and A. Neto, “On the experimental characterization of generated and received pulses of photoconductive antennas,” in *48th Int. Conf. on Infrared, Millimeter, and Terahertz Waves (IRMMW-THz)*, Montreal, Canada, 2023, pp. 1-2.

Thesis Co-supervised

T1. S. S. Nerkar, “GUI for system dimensioning and QO channel analysis of pulsed pico-second radar,” M.S. thesis, Dept. Microelectronics, THz Sensing Group, Delft Univ. Technol., Delft, The Netherlands, Oct. 2021.

T2. M. Huiskes, “Towards the design of an imaging setup using photoconductive antennas,” M.S. thesis, Dept. Microelectronics, THz Sensing Group, Delft Univ. Technol., Delft, The Netherlands, Oct. 2022.

Nominations

N1. Nomination for the “Best Electromagnetics Award” in the European Conference on Antennas and Propagation (EuCAP), Florence, Italy, 2023, with the paper **C15** listed in the conference publications.

Propositions Accompanying the Doctoral Thesis

1. The field correlation technique is very powerful and efficient for co-optimizing lens-feed geometries. (This proposition pertains to this dissertation)

2. Focal plane arrays with shaped lens antennas are promising architectures for achieving wide field-of-view imaging. A shaped quartz lens with a leaky-wave feed was demonstrated for the first time to achieve better scanning performance than a horn antenna. (This proposition pertains to this dissertation)

3. In a THz time-domain system, the link transfer function between a photoconductive antenna (PCA) source and a PCA receiver has been accurately characterized. Therefore, the simulated detected currents in both amplitude and waveforms can be compared to the measurements for the first time. This allows for the design of future PCA-based imaging systems. (This proposition pertains to this dissertation)

4. It is better to think and reflect more on the results you got, instead of doing endless measurements looking for the perfect results. Only if you can clearly explain the results, others can help you find and solve the problems.

   Paraphrased from discussions with Prof. Nuria Llombart, Delft University of Technology.

5. Your prototypes and measurements cannot always meet your expectations. The important thing is to find the reasons behind the disagreement. This helps you learn more and gain more experiences, which is valuable.

6. It may sound old-fashioned, but the only way to get your work done is to devote yourself to what you are doing. Smartphones and the Internet are the major obstacles for your work.

7. It is important to make proper work plans and leave some buffer time. Well-organized workflow improves productivity.

8. Attending conferences is an important part of the Ph.D. journey. You can gain more confidence when you see what others have done.

9. Work-life balance is very important to maintain your productivity and enthusiasm. Do not waste your holidays and try to throw all things behind when you relax.
10. The Ph.D. journey expands your horizon, but sometimes it can be frustrating and exhausting, especially when you are in a foreign country. Nevertheless, when you are close to the end and look back, you will be proud of yourself since you have achieved so many things. All you have experienced will have an influence on your future career and this journey will definitely be a precious treasure in your life.

These propositions are considered opposable and defendable, and as such have been approved by the promotors Prof. dr. N. Llombart and Prof. dr. A. Neto.

About the Author

Huasheng Zhang was born on June 16th, 1994 in Urumqi, China. He received the B.Eng. degree (cum laude) in electronic information engineering from the Beihang University, Beijing, China, in 2016, and the M.Sc. degree (cum laude) in electrical engineering from the Delft University of Technology, Delft, the Netherlands (TU Delft), in 2018. He is currently working toward his Ph.D. degree at the THz Sensing Group in the Microelectronics department of the Electrical Engineering, Mathematics and Computer Science (EEMCS) faculty at Delft University of Technology, Delft, the Netherlands.

His Ph.D. topic is on the analysis and design of lens antenna systems for applications at millimeter and sub-millimeter wavelengths. This research has been carried out under the supervision of Prof. Nuria Llombart and Prof. Andrea Neto as promotors. This project has been supported by the European Research Council (ERC) starting grant. The research has resulted in six journal publications and eighteen proceedings in international conferences.

His research interests include analyzing and designing leaky-wave antennas, lens antennas, photoconductive antennas, and quasi-optical systems at millimeter and sub-millimeter wavelengths, and high-frequency electromagnetic analysis techniques.

During his Ph.D., he has co-supervised two M.Sc. students (Delft University of Technology, THz sensing group).

Acknowledgements

This work could have never been done without the great support, supervision, and guidance of many people. It is my great pleasure to work in the THz Sensing Group with all the brilliant people around me. I am very grateful for the substantial support from my family my friends, and my colleagues. You carry me this far to make this journey finished. First of all, I would like to thank my promotors Prof. Nuria Llombart and Prof. Andrea Neto. You have given me the best supervision and I really appreciate it.

Nuria, I have learnt so many things from you during this journey. You are a very knowledgeable person at the top of your field. I am always impressed by how much you know, how experienced you are, and how many things you can deal with in parallel. You are strict with details but also have clear big pictures, and this is what I am pursing and will continue. When I have problems, you are always patient to help me out and guide me toward the correct directions. Sometimes I got lost in my work or future. But by talking with you, I can always refresh myself and become more confident. In the last year of my project, I was quite frustrated with the measurements of PCAs. You encouraged me and told me to think and reflect more before actions. Step by step, I finished the measurements and finally reach the end of the journey. You have also taught me how to present research results, which is very valuable and will definitely benefit me in the future.

Andrea, I have also learnt a lot from you. In my mind, you are the person who basically knows everything in the field and has so much experience. You can always propose fresh ideas during meetings and discussions which are very helpful. When I have questions, you are always happy to discuss with me until we solve them. There were several times when we wrote or modified papers together. I was impressed by how fast and good you could finish writing, and my writing skills was gradually improved during such collaboration. You are always energetic and encouraging so I am always inspired by you. I really enjoy the small talks that you share during the lunch and coffee time, from which I know many interesting things. Recently, thanks to your recommendation during a seminar, I successfully got my first interview. I really appreciate this.

I would like to thank the rest of the group members. Thank you, Prof. Angelo Freni, Dr. Daniele Cavallo, Dr. Ioan Lager, and Dr. Maria Alonso-delPino for your help on my study. I really enjoy the discussions with you.

Juan, thank you for your tremendous support in the last two years. I can never finish the PCA measurements without your help. You taught me how to work properly and systematically in the lab, and your suggestions were very helpful. You are an interesting person and I always feel relaxed when you tell a joke.

Shahab, you supervised my master project, and from then until now, you really taught me many things and helped me a lot. You are a good friend to share gossips with but also an excellent colleague to work with. Because of your help and insistence, I can finally finish the shaped lens project. We really did an excellent work and I am proud of ourselves.

For other colleagues and friends, Giorgio, Darwin, Marta, Alejandro, Sjoerd, Arturo, Sven, Ralph, Cristina, David, Paolo, Alessandro, Sebastian, and other new Ph.D. students, I am really lucky and happy to meet you and work with you. Daily conversations and discussions with you make me feel at home in the group.

A special thank to Prof. Jochem Baselmans, without your support on the shaped lens project, that work will never be done and the last chapter of the thesis will never be finished.

I would also like to specially thank Martijn Huiskes for helping me translate the summary to Dutch.

Thank you my friends, Li Yin, Heqiao, Chuyue, Zhengzheng, Ziqiao, Shuchen, for your support during these years. It is always relaxing to hang out and chat with you.

To my family members, thank you for your encouragement, consolation, share of happiness and unconditional support. Thank you my sister Yifan and your husband Hailong. It is so reassuring to have you here in the Netherlands. You have really helped me a lot to survive here and I am very happy and enjoyable to have catch up with you.

Finally, to my dear parents:

致我亲爱的父母，感谢你们在这四年半里对我毫无条件的支持，在我遇到困难的时候开导我，安慰我，给我能量；在我开心的时候祝贺我，陪我一起开心。 虽然身处异国他乡，你们每周都会和我打电话， 聊聊生活的点滴和最近的情况，这让我很安心，让我有回家的感觉。 虽然要一个人在这里面对很多，但我知道，我身后永远有你们作为我最坚强的后盾，对我毫无保留的帮助，支持，和付出。很难想象没有你们的鼓励我能走到现在，谢谢你们的爱让我勇往直前没有顾虑，爱你们！ -华盛